



<https://theses.gla.ac.uk/>

Theses Digitisation:

<https://www.gla.ac.uk/myglasgow/research/enlighten/theses/digitisation/>

This is a digitised version of the original print thesis.

Copyright and moral rights for this work are retained by the author

A copy can be downloaded for personal non-commercial research or study,
without prior permission or charge

This work cannot be reproduced or quoted extensively from without first
obtaining permission in writing from the author

The content must not be changed in any way or sold commercially in any
format or medium without the formal permission of the author

When referring to this work, full bibliographic details including the author,
title, awarding institution and date of the thesis must be given

Enlighten: Theses

<https://theses.gla.ac.uk/>
research-enlighten@glasgow.ac.uk

**Modelling of Photonic Band Gap Materials
For mm-wave & Optical Applications.**

**A thesis for the degree of
Doctor of Philosophy (Ph.D.),
submitted to the Faculty of Engineering,
University of Glasgow**

by

Andrew Lawrence Reynolds

September 2000

© Andrew L. Reynolds 2000

ProQuest Number: 10644197

All rights reserved

INFORMATION TO ALL USERS

The quality of this reproduction is dependent upon the quality of the copy submitted.

In the unlikely event that the author did not send a complete manuscript and there are missing pages, these will be noted. Also, if material had to be removed, a note will indicate the deletion.



ProQuest 10644197

Published by ProQuest LLC (2017). Copyright of the Dissertation is held by the Author.

All rights reserved.

This work is protected against unauthorized copying under Title 17, United States Code
Microform Edition © ProQuest LLC.

ProQuest LLC.
789 East Eisenhower Parkway
P.O. Box 1346
Ann Arbor, MI 48106 – 1346

GLASGOW
UNIVERSITY
LIBRARY

12020-Copy 2

Abstract

The properties of 1-, 2- and 3- dimensional periodic structures, generically known as photonic crystals, are examined using the transfer matrix technique with a view to application in the mm-wave and optical domains. Periodic structures are now well acknowledged in their ability to control the propagation of electromagnetic radiation. Through careful design of crystal lattice parameters and consideration of the materials used in fabrication, periodic materials are known to display gaps in their dispersion relation where there are no allowed modes or states: the photonic band gap, such that any impinging electromagnetic wave will be reflected regardless of its incidence angle or polarisation.

Within the first half of this work several structures and approaches are examined, with the objective of finding a truly 3-dimensional photonic band gap for use as an antenna substrate. In the process, through careful investigation, many design considerations are highlighted, such that some structures are shown to be successful in achieving this goal, while other structures are shown to be inadequate.

In the second half of this work the analysis moves away from the search for the complete photonic band gap by examining incomplete band gaps and the influence of various defects and alterations that may be incorporated into photonic crystal structures. These alterations or the inclusion of intentional defects are set to play a significant role in the marriage between photonic crystals and current day optoelectronic and mm-wave components.



Acknowledgements

I would like to express my sincere gratitude to many people and organisations who were instrumental in the successful outcome of this work. I regard the time in which I carried out this work as some of the most enjoyable and challenging I have encountered.

First and foremost I would like to thank my supervisor Professor John Arnold for encouraging and permitting me to carry out my work at the University of Glasgow. I would like to express my most sincere thanks for the useful discussions, telephone conversations and emails especially when I was abroad, due to the freedom he allowed me in working collaboratively with other institutions.

I would also like to especially thank Doctor Peter De Maagt. Peter was responsible for introducing and spawning my interest in the field of photonic crystals when I was a graduate trainee within the Antenna Section of the European Space Agency Research and Technology Centre, ESTEC. Over the last few years I have really learned to appreciate his questioning and corrections in our continued collaborative work together and I value our friendship. I would also like to thank Peter for giving me the opportunity to return to the division once again during this work. I greatly miss all of my friends and colleagues within the electromagnetics and other divisions of the agency, Peter, Gerry, George, Willy, Bertram, Pedro, Antonio, Peter Rinous, Arturo and Inigo to name but a few, with whom I had the pleasure of working, sharing the stress of the day over lunches, and of course the occasional beer from Maxwell the fridge.

To my friends in the Mad Cows football team, the rugby club and other clubs and teams within ESTEC there are countless happy memories which I will forever cherish. I extend a special thanks to Sean and Lena Clarke, John and Marjan Henwood, Elise Maury, Chris and Petra Sandford, Jens and Oddrun Scheiman, David Munn for their incredible discussions, acts of generosity and all the parties that helped me keep my sanity during the tougher times.

My time in France in sunny Montpellier was made possible through an invitation by Doctor David Cassagne. There is little further I can say to reiterate my appreciation for the opportunity to work with David and Professor Christian Jouanin. For the first time in my life I spent a warm winter beside the Mediterranean, a truly unforgettable experience.

To Doctor Ulf Peschel my sincerest thanks for all the technical feedback and understanding that you gave me during the time in which we were in Glasgow and also for the opportunity to work within the group in Jena, Germany.

Related to my time in DERA Malvern I would like to thank Doctor Terence Shepherd for making the whole the CASE award possible and for all the useful discussions that we had together. On the same note I would also like to thank Doctor Richard Amos and Doctor John Roberts for all their useful discussions, feedback and assistance. To my office mates Rich, Dave, Andy and Brian a special thanks for such a lively office.

Finally I dedicate this thesis to my family. To my sister Kathryn, my mother and father Eileen and Lawrence Reynolds who through all of this have tolerated me and provided the love and moral support that have seen this work through to completion. This is for you.

Foreword

During the course of this work the transfer matrix method program, as documented and distributed by Professor Bell, Professor Pendry and Dr. Ward from the Condensed Matter Group of Imperial College's Science Technology and Medicine department, ICSTM, has been modified significantly. Consequently in February 2000, with the kind permission of Imperial College, I started to distribute a free Windows® executable version of the code incorporating many new features, a graphical user interface, renditions of the crystals in virtual reality, diffraction capability amongst others. Since then, over 250 people have registered their downloads of the executable file and consequently several institutions have invested in dedicated computer facilities to run it.

I would like to reiterate my thanks to Professor John Pendry for allowing me to distribute the code and to promote the transfer matrix method. I would also like to thank Dr. Yurii Vlasov currently with NEC's research institute in Princeton, New Jersey, USA, and Dr. Jonathan Dowling from the Jet Propulsion Laboratory in Pasadena, California, USA for the interest that they created in my work through emails and links to my web site.

Collaborative Institutions

Defence Evaluation Research Agency:

Dr. Terence Shepherd:

DERA Malvern, St. Andrew's Road, Malvern, Worcs, WR14 3PS, England U.K. Work was carried out as part of a E.P.S.R.C. CASE agreement between the University of Glasgow and DERA.

European Space Research and Technology Centre, ESTEC

Dr. Peter de Maagt:

Electromagnetics Division, European Space Research and Technology Centre, ESTEC, P.O. Box 299, 2201 AG Noordwijk, The Netherlands. Microwave and mm-wave photonic band gap material research conducted with assistance from the European Space Agency's Research & Technology Centre under contract SRON STS-KJW-96/067.

Semiconductor Group, University of Montpellier II

Dr. David Cassagne:

Groupe d'Etude des Semiconducteurs, CC074, Universite de Montpellier II, Place Bataillon, 34095 Montpellier Cedex 05, France. Work on colloidal crystals carried out as part of the European funded contract PHOBOS.

Friedrich-Schiller Institute, University of Jena

Dr. Ulf Peschel:

Friedrich-Schiller-Universitat Jena, Max-Wien-Platz 1, 07743 Jena, Germany

“And God said, “let there be light,” and there was light”

Genesis 1:3

So we strive to harness, emulate and control it.....

CHAPTER 1	
<i>Introduction</i>	1
<i>Overview</i>	1
History & Application	2
<i>Antenna Applications</i>	3
<i>Optical Applications</i>	3
Initial concepts	5
<i>Describing Lattices</i>	6
<i>The bulk medium dispersion relation</i>	7
<i>Elementary Bragg stack</i>	9
Chapter Aims and Objectives	10
CHAPTER 2	
<i>Omni-directional Reflecting Bragg Stacks</i>	17
<i>Overview</i>	17
Omnidirectional reflectance from 1-dimensional dielectric films.	18
Silicon and Kapton Bragg Stack	19
<i>Explanation</i>	22
<i>Block Medium Band Structures</i>	22
<i>Allowed propagation state restrictions due to Snell's law</i>	23
Full angular transmittance characterisation of the Bragg Stack	28
<i>Excitation from an air medium</i>	28
<i>Bragg Stack Rotational Symmetry</i>	28
<i>Excitation from a silicon medium</i>	29
Conclusion	30
CHAPTER 3	
<i>Photonic Crystal Sandwich</i>	31
<i>Introduction</i>	31
Issues related to the structure	32
Initial Design Parameters for 80GHz	33
<i>Simple hexagonal lattice of air holes in silicon</i>	34
<i>Interim Conclusion</i>	35
Bragg Stack Response	36
<i>Important Point concerning lattice constants</i>	36
<i>Quick reference normalised frequencies</i>	37
<i>Bragg stack wave incidence from air</i>	37
<i>Bragg stack wave incidence from silicon</i>	38
<i>Brewster Angle</i>	40
<i>Discussion</i>	40
3 dimensional verification	41
Normal incidence into the side of the crystal	43
<i>Angular analysis within the periodic hexagonal plane of the dielectric sandwich structure</i>	44
Conclusion: Dielectric sandwich with solid interspatial layer	45
CHAPTER 4	
<i>Drilled Bragg stacks</i>	47
<i>Introduction</i>	47
Scope	48
<i>Slab Waveguides</i>	48
<i>Objective</i>	49

Filling Ratio Evolution	50
Square lattice of drilled holes	52
<i>Normal end-fire incidence in the periodic square lattice plane</i>	52
Estimation of the effective dielectric constant	54
<i>Angular effective medium transmission response: waves incident from air</i>	56
<i>Angular effective medium transmission response: non radiative modes included</i>	56
<i>Effective Medium Overview</i>	57
3-dimensional characterisation of the structure with a square lattice	58
<i>Incidence from air</i>	59
<i>Conclusion</i>	60
CHAPTER 5	
<i>Interleaved 2D lattices creating fully 3D Photonic Crystals</i>	63
<i>Overview</i>	63
Introduction	64
Interleaved 2-dimensional lattices	65
Numerical results	66
Characterisation and application of a 94GHz Woodpile	70
<i>Measured Response</i>	71
Angular Performance	73
Antenna Radiation Response	74
<i>Summary of Measured Response</i>	75
<i>Case 1: Antenna without PBG</i>	75
<i>Case 2: Antenna & feed aligned over gap</i>	76
<i>Case 3 & Case 4</i>	76
<i>Summary</i>	76
Conclusion	79
CHAPTER 6	
<i>Membrane Analysis</i>	81
<i>Introduction</i>	81
2-Dimensional Lattices with Membranes	82
Substrate Modes	84
94GHz 2-Dimensional System: Single Layer	86
<i>Silicon Membranes: Normal Incidence</i>	86
<i>Kapton Membranes: Normal Incidence</i>	87
<i>Comparative performance: single layer kapton & silicon membranes</i>	87
<i>Convergence</i>	89
Experimental Verification	90
Angular Response Γ_X Orientated Crystal	93
<i>Perfect Crystal: no membrane</i>	93
<i>Influence of kapton & silicon membranes</i>	94
<i>Comparative Performance & Conclusion</i>	97
CHAPTER 7	
<i>Tuning Planar Cavity</i>	101
<i>Abstract</i>	101
Introduction	102
Structure	102

Perfect Crystal	104
Planar Cavity Defect	106
Conclusion	109
CHAPTER 8	
<i>Localised Defects in Hexagonal Photonic Crystals</i>	111
<i>Introduction</i>	111
Motivation	112
Hexagonal Lattice Definitions	114
<i>The perfect crystal</i>	114
<i>Perfect Crystal Results</i>	115
Defects: One in every two, Γ K & Γ M	116
Defects: One in every three, Γ K & Γ M	117
Superlattice evolution	119
<i>Applications</i>	120
CHAPTER 9	
<i>Opal Colloidal Crystals</i>	123
<i>Introduction</i>	123
Motive	124
<i>Aims & Objectives</i>	125
Crystal types	126
<i>Normal / Bare opal</i>	126
<i>Inverted opal</i>	126
<i>Coated opal</i>	126
<i>Sintered opal</i>	126
Unit Cell Approach	127
<i>Conventional Cell</i>	127
<i>Split Cell</i>	129
<i>Matrix Processing Time Considerations</i>	130
Bare Opal	130
<i>Transmission along the [100] direction</i>	130
<i>Transmission along the [111] direction.</i>	131
<i>Comparison of response in the [100] and [111] directions</i>	132
Coated Opal	133
<i>Comments on Coatings</i>	133
<i>Transmission along the [100] direction</i>	134
<i>Transmission along the [111] direction</i>	137
Sintered Opal	138
<i>Comments on implementation</i>	138
<i>Transmission along the [100] direction</i>	139
<i>Transmission along the [111] direction</i>	140
Conclusion	141
CHAPTER 10	
<i>Optical characterisation of shear ordered colloidal crystals</i>	143
<i>Introduction</i>	143
Building The Crystal	144
<i>Theoretical representation of the crystal</i>	144
<i>Fabrication using shear alignment</i>	145

<i>Emulating the experiment</i>	145
Diffraction	146
<i>Diffraction Limit</i>	147
<i>Normal Incidence</i>	147
<i>Off-Normal Incidence</i>	149
Diffraction resultant from the $\langle 111 \rangle$ surface plane	150
<i>Diffraction through the colloid</i>	151
<i>Twinned Opal</i>	154
Optical characterisation of a shear ordered colloidal crystal	155
<i>The measurement set-up</i>	157
Conclusion	162
CHAPTER 11	
<i>Summary, Conclusions and Future Considerations</i>	165
<i>Summary & Conclusions</i>	165
<i>Future considerations</i>	167
CHAPTER 12	
<i>Consequent publications</i>	169
CHAPTER 13	
<i>Bibliography</i>	171
Appendix A	
<i>The dispersion relation</i>	175
The Dispersion Relation.....	176
<i>Point of Interest</i>	177
Appendix B	
<i>The Transfer Matrix Method</i>	179
The Transfer Matrix & Co-ordinate Definitions.....	180
Formulating the calculation.....	180
<i>Discretizing Maxwell's equations</i>	181
<i>Fourier Transforms</i>	182
<i>Approximating the k-vector</i>	183
<i>Expanded Maxwell's equations</i>	184
<i>Real space difference equations</i>	185
Boundary conditions	187
Polarisation & the plane wave basis.....	188
<i>Polarisation relative to the surface normal</i>	188
<i>General polarisation definitions</i>	189
<i>Normal incidence</i>	190
<i>S- or TE- Polarisation waves from + infinity</i>	190
<i>P- or TM- Polarisation waves from + infinity</i>	191
<i>Waves arriving from - infinity</i>	191
<i>Off-normal incidence</i>	191
<i>S- or TE- Polarisation waves from + infinity</i>	191
<i>P- or TM- Polarisation waves from + infinity</i>	192
<i>Waves arriving from - infinity</i>	193
Calculating the reflection and transmission coefficients	193
<i>Unitary transformation</i>	193

<i>Transmission and reflection from a slice</i>	194
<i>Transmission and reflection from a block.</i>	196

Appendix C

<i>Polarmetric scattering from opal colloid photonic crystals.....</i>	197
Motivation	197
<i>Polar Spherical Co-ordinates</i>	198
The experimental set-up	199
<i>Rotation in a plane.</i>	200
<i>Rotation in the plane relative to the colloid</i>	201
<i>Issues related to the Translight program</i>	205



Introduction

Visualisation of 1-, 2-, 3-dimensional photonic crystals.	2
Generic 2-dimensional periodic lattice.	6
Brillouin zones for square and hexagonal lattices	7
Bulk air response.	8
Band diagram response	9
Band diagram and transmission response for a simple Bragg stack.	10
A picture of a simple Bragg stack	10
A picture of the 'dielectric sandwich'	11
Drilled Bragg stack	12
Woodpile structure with a semi transparent membrane.	12
A piece of hexagonal lattice with defects introduced.	14
Scanned Electron Micrograph of an opal colloid.	15

Omni-directional Reflecting Bragg Stacks

Schematic of a Bragg stack being illuminated by incoming plane wave at an arbitrary angle.	18
Transmission Response (left) and specific angle response (right)	19
Transmission Response for a Bragg Stack made from Silicon and Kapton	21
Transmission as a function of external angle for TE and TM polarisations	21
Allowed bands within solid dielectric blocks.	22
Allowed Internal Angles of Propagation within a Bragg Stack	23
Transmission Response for a Bragg Stack made from Silicon and Kapton embedded in Silicon.	24
Internal Transmission Modes for a Bragg Stack made from Silicon and Kapton.	26
TE & TM transmission evolution as a function of embedding medium dielectric constant.	27
External Transmittance Response for the Silicon / Kapton Bragg Stack	28
Internal Transmittance Response for the Silicon / Kapton Bragg Stack	29

Photonic Crystal Sandwich

Schematic of dielectric 'sandwich' structure.	31
Hexagonal Lattice Definitions	33
Hexagonal lattice; waves impinge from air	34
Hexagonal lattice; waves start from silicon	35
Generic Illustrations of a Bragg Stack & Sandwich Structure	36
Bragg Stack: External TE & TM transmission response $\epsilon_{\text{initial}}=1.00$	38
Bragg stack transmission response, waves start from silicon $\epsilon_{\text{initial}}=11.7$	39
Bragg stack transmission response, waves start in $\epsilon_{\text{initial}}=4.18$	40
Normal incidence transmission response for the 3-dimensional structure.	41
Normal incidence response for a 1-dimensional Bragg stack	42
TE and TM response for side incidence into the sandwich structure.	43
Angular transmission analysis for side incidence.	44

Drilled Bragg stacks

Patent Structure: Bragg Stack with a hexagonal lattice of air cylinders.	48
Filling Ratio Evolution for the square and hexagonal lattices	50
Comparative TM transmission for the square and hexagonal lattice drilled through a Bragg Stack.	51
Transmission Response for normally incident plane wave on the side of structure.	52
Gap maps for a square lattice of air holes in silicon.	53
Evolution of the Square Lattice with Dielectric Constant	54
Normal in-plane incidence response for a 2-dimensional square lattice	55
Effective medium square lattice transmission response; waves incident from air.	56
Internal TE & TM Transmission Response; Square Lattice	57
Transmission response for planes waves launched from air.	59
Transmission response for planes waves launched from silicon.	60

Interleaved 2D lattices creating fully 3D Photonic Crystals

2-dimensional square lattices	65
Maximum transmission for 2-dimensional bar lattices	66
Transmission for Angular Sweep of Case 1 & Case 2 Lattices	67
Optimum Angle of Interleave	68
Interleaved Bar Unit Cell	69
Woodpile Frequency Response	69
Woodpile Mid Gap Transmission	70
Photograph & Schematic of the 94GHz Woodpile	71
Theoretical Transmission Response	71
Measured & Theoretical Response for the 94GHz Woodpile.	72
Angular response for 4 Cells @94GHz: Waves impinge from air	73
Angular response for 4 Cells @94GHz: Waves impinge from silicon	74
Schematic of the measurement scenarios.	75
Measured Antenna Responses at 94GHz	78

Membrane Analysis

General visualisation of a membrane placed over a lattice of 2-dimensional dielectric bars.	82
Polarisation & Lattice Definitions	82
Number of wavelengths inside a membrane for Air, silicon and kapton.	84
Substrate Modes in silicon and kapton Membranes.	85
Various silicon membranes placed on a single layer of periodic dielectric bars for 94GHz system.	86
Kapton membrane analysis	87
Relative Difference curves for silicon and kapton membranes.	88
Cell & Convergence Plot for a 25um kapton membrane using different meshes.	89
Γ X Lattice: Measured and theoretical TM response.	91
Γ M Lattice: Measured and theoretical TM response.	92
Perfect crystal angular transmission response	93
TM band structure.	94
100 μ m silicon Membrane response on the otherwise perfect crystal	95
Difference in TM Transmission	97
Surface wave excitation.	99

Tuning Planar Cavity

Schematic & picture of the photonic crystal.	103
Perfect crystal response.	104
TM Band structure, perfect crystal.	105
In & Out of Plane Angular Response.	106
Cavity transmission, normal incidence.	107
TM Defect In- & Out of plane response.	108
Angular xz-plane transmission response.	109

Localised Defects in Hexagonal Photonic Crystals

A planar defect introduced into a hexagonal lattice photonic crystal.	113
Section of Hexagonal lattice showing the two propagation directions studied.	114
"Cells" used to built the perfect and hexagonal lattices.	114
Perfect Crystal: TM Polarisation Response for the Γ and Γ M directions.	115
Periodic Defects: One in every two, Γ K & Γ M.	116
Periodic Defects: One in every three, Γ K & Γ M.	117
Closer look at 1 in 3 defects in the Γ M lattice direction.	118
Evolution for superlattice spacing.	119
An idea for a Y-Splitter	120

Opal Colloidal Crystals

SEM Micrograph of a shear ordered PMMA Opal	123
The face centred cubic cell.	124
Opal [111] and [100] surface truncations.	125
Sintered & Inverted opal	127
Front, Conventional, and Rear Cells to construct opal [100]	128
Split Cell opal [100]	129
Split Cell opal [111]	129
Band structure & [100] transmission response.	130
Band structure & [111] transmission response.	132
Transmission as a function of thickness	133
10% Coated opal [100]	135
[100] Evolution for various coating thicknesses	136
[100] Transmission against thickness for various coatings.	136
[111] Evolution as a function of coating thickness.	137
[111] Transmission versus thickness for various coatings.	138
[100] The effect of Sintering	139
[100] Transmission versus thickness as a function of sintering.	140
[111] Evolution of Transmission as a function of sintering level.	140
[111] Transmission versus crystal thickness as a function of the sintering level.	141

Optical characterisation of shear ordered colloidal crystals

Generic ABC Colloid	143
<111> plane within the cubic crystal lattice	144
Shear Alignment	145
PMMA & Octanol <111> surface transmission	146
Diffracted Orders resultant from a normally incident wave.	147
Off normal incidence diffraction.	149
Two possible orientations of the <111> surface plane.	150
Code generated diffracted orders.	152
Diffraction patterns for ABC and ACB f.c.c colloids	152
Measurements on shear aligned opals	153
Diffracted order intensity for an ABC colloid.	154
Twinned Opal Intensity responses.	154
The experimental set-up	155
Bragg spot intensity profiles as a function of incidence angle.	156
Bragg spot intensity profile for a twinned f.c.c. as a function of incidence angle.	157
Experimental data for the twinned f.c.c. PMMA colloid in Octanol	158
Gray scale map of the optical scattering of a twinned f.c.c. colloidal crystal.	159
3-dimensional colour map of the optical scattering of a twinned f.c.c. colloidal crystal.	159
The zero, first and second TM orders predicted by the TMM code.	160
Experimental intensity of the first order Bragg spot.	161
Theoretical intensity of the first order Bragg spot.	161

The dispersion relation

The light line	176
----------------	-----

The Transfer Matrix Method

Cartesian co-ordinate system for a generic periodic structures.	180
Simplified Flow Chart of Program Operation.	181
A wave incident on to the right hand side of a slice of material	194
A wave incident on to the left side of a slice of material	195

Polarmetric scattering from opal colloid photonic crystals

Spherical Polar Co-ordinates.	198
Rotation in a plane	200
Schematic of an Opal Colloid $\langle 111 \rangle$ Surface	201
$\langle 111 \rangle$ plane within the cubic crystal lattice	202

Overview

Periodic structures are now well acknowledged in their capability to control the propagation of electromagnetic waves. In 1987 perfect periodic structures demonstrated in the work of Yablonovitch [1] and John [2] were shown to display ranges of frequency where propagation was forbidden for a given, or for every direction. These structures, regardless of their operational frequency and dimensionality, are now generically called photonic crystals. The forbidden frequency range is called the photonic band gap, PBG, and is said to be complete if a PBG exists for all polarisations and all propagation directions.

Photonic crystals are characterized by three parameters the spatial period, the fractional volume of the constituent materials and their dielectric constants, the ratio between which is the dielectric contrast. By properly selecting these parameters, gaps in the electromagnetic dispersion relation can be created within which propagation is forbidden. Dimensionality relates the number of dimensions within which periodicity has been introduced into the structure. Photonic crystals can therefore be either one, two or three dimensional with the band gap respecting the dimensionality. Examples of one, two and three dimensional photonic crystals are shown in Figure 1.1 overleaf. Bragg stacks are the classic example of one dimensional photonic crystals.



Figure 1.1 Visualisation of 1-, 2-, 3-dimensional photonic crystals.

1.1: History & Application

Possible applications of photonic crystals can be found across the electromagnetic spectrum. Depending on the intended application the periodic spacing of the crystal can range dramatically in size. For applications in the mm-wave regime the structures can be made with standard machining and micro machining techniques. Yablonovite, the three cylinder structure [1] named after Eli Yablonovitch, was one of the first structures to be demonstrated to have a complete 3-dimensional photonic band gap. While initial demonstration of photonic band gap properties was carried out at microwave and millimetre wave frequencies, attention quickly focused on optical applications. The physical dimensions of photonic crystals are scalable such that the resultant crystals can be applied to a wide range of frequencies.

For some optical applications the periodicity that can be manufactured is limited by today's fabrication technology and associated resolution. Micro-machining, photo-, stereo-, holographic and electron-beam lithography are a few of the common fabrication techniques that can be used to manufacture photonic crystals. These fabrication techniques continue to evolve such that the challenges and limitations imposed today will most likely have been addressed or superseded by more advanced processes in another few years. While some limitations are imposed by lithographic techniques self organising crystals, which form colloids, operating at optical frequencies can be made by chemical deposition.

While the dispersion curves for photonic crystals often show gaps for both polarisations they do not necessarily overlap. Initial and continued emphasis has been placed on structures where there is a common gap for both polarisations. Such gaps are called absolute photonic band gaps and the forbidden region extends to cover all propagation directions for

a range of frequencies. Such structures can be used for a variety of applications inclusive of substrates for antenna systems [3].

Antenna Applications

In the present European Space Agency earth observation studies, millimetre and sub millimetre limb-sounding instruments such as MASTER+, SOPRANO, PHYRAMID, are already using frequencies up to 1THz. This frequency band also has applications related to astronomical missions, FIRST, PLANCK, where the frequency range may extend over and above 3THz [4]. As the intended operation frequencies increase, the physical size of the system front end and associated components reduces. The integration of an antenna system and associated circuitry such as the mixer, local oscillator etc. onto a single substrate is therefore advantageous and is made possible using current micro-machining and lithographic techniques.

By using planar antenna systems in conjunction with semiconductor substrates the possibility of coupling to parasitic substrate modes becomes a distinct reality, detracting from the overall radiation efficiency of the antenna. An antenna prefers to radiate into the substrate medium rather than air by a factor of $\epsilon^{3/2}$, where ϵ is the substrate dielectric constant [5]. This means that for a bulk silicon substrate only about 4% of the power is radiated into free space.

The reasons which cause substrate mode coupling are well known, and several techniques can be employed to minimize such losses while maintaining the small size and versatility of the original device. Since photonic crystals can be designed to forbid the propagation of electromagnetic waves they in essence reflect any impinging electromagnetic radiation. It was in 1946 that Purcell [6] first suggested that a mirror would alter the emission properties of a dipole. By integrating an antenna onto the surface of a photonic crystal the antenna is unable to radiate into the photonic crystal substrate, negating the possibility of coupling to the parasitic substrate modes and increasing the radiation efficiency significantly.

Optical Applications

For applications in the optical regime, where the periodicity is smaller, fabrication issues are much more complex. By extending the periodicity of structures to three dimensions and

ensuring sufficient dielectric contrast then optical propagation can be controlled or entirely suppressed in all three dimensions. Opportunities to control spontaneous emission using photonic crystals offer vast potential in drastically improving laser design in reducing threshold and increasing efficiency. Not all applications require three dimensional photonic crystals, many applications in the optical and other domains can be addressed by one or two dimensional photonic crystals. The vertical cavity laser or VCSEL exemplifies the application of a one dimensional photonic crystal in so far as the periodic modulation of material index defines the lasing cavity.

An excellent review of the motivations behind the driving forces of photonic crystal and future perspectives has been provided by Krauss [7], as much of the way society currently illuminates its life is vastly inefficient:

“it is still surprising that we still rely mainly on such archaic light sources as the incandescent light bulb or on fluorescent strip-lights, particularly since these light sources typically waste 80-95% of the electrical energy input.”

Light emitting diodes, LEDs, as currently manufactured also suffer from the same wastage problems. While the devices have very high internal quantum efficiency, in excess of 90%, much of the light is trapped within the material with only a few percent escaping. The trapping mechanisms are not dissimilar to those experienced by the conventional integrated planar antenna systems discussed in the previous section. Once again photonic crystal substrates offer vast potential in overcoming the wastage hurdle.

Photonic crystals are not limited in application to addressing the wastage in light emitting devices or suppressing substrate modes for antenna applications. The explosive growth of the internet has resulted in considerable pressure on the telecommunications network back bone as it tries to meet the current day demands for bandwidth and high speed data transfer rates. Consequently there is a large need for completely integrated photonic chips. These chips would work entirely with light, offering light speed performance, and would maintain the same functionality as their electronic counterparts, which consist of millions of transistors, in a much smaller chip. Such chips could integrate all the elements of larger optoelectronic systems onto a single chip including emitters, waveguides and couplers etc. One of the fundamental elements of such a integrated system would be the interconnecting waveguides. While photonic crystals may be used to enhance the efficiency

of the emitters and other devices, waveguides can also be made using photonic crystals. For example, a guiding region can be introduced by inserting a continuous cavity through an otherwise perfect crystal. Within such waveguides light can be turned around corners at length scales comparable to the wavelength of the light itself [8].

1.2: Initial concepts

As in any technological field, many of the initial demonstrations involved experimental demonstration of the ideas due to the lack of reliable prediction techniques. As the potential for photonic crystals was rapidly realised the development of theoretical methods was quick to follow. The description of electromagnetic waves in pure photonic crystals involves the solution of Maxwell's equations in periodic media. Over the last few years several techniques have emerged which allow us useful insight into different properties of the crystals providing essential pre fabrication and experimental data. There are a few numerical models that are used in modelling photonic crystals, Order N, Finite Difference Time Domain, F.D.T.D., Plane Wave Method, P.W.M. and the Transfer Matrix Method, T.M.M. Each of the methods can provide useful and different insight into the properties of photonic crystals.

The Plane Wave Method is used extensively to compute the band structure with the assumption that the structure is infinite in extent. The Order N method utilises mode orthogonality to decrease computation times and can be used to compute the Density of States, D.O.S., as well as the band structure for infinite structures. The Transfer Matrix Method imposes two periodic boundary conditions and allows the computation transmission and reflection co-efficient for finite thickness structures. Finite Difference Time Domain is well suited to applications where truly finite structures are required and has the added advantage of being able to compute the response for point sources within the structure, pulse response as opposed to plane waves, and could also include active elements such as antennas. Each of the methods has inherent advantages and disadvantages and each provides different information. The applicability of one method over another depends primarily on which analysis provides the most useful information.

Describing Lattices

Many of the numerical methods exploit the inherent periodicity of the structures. In 1946 Brillouin [9] wrote an authoritative text concerning wave propagation in periodic structures. As crystals have small unit cells that repeat throughout the structure the crystals can be described by a set of primitive direct lattice vectors. These vectors describe the distances and directions required to translate between similar points and can be applied to 1-, 2- or 3-dimensional lattices, see Figure 1.2 on page 6.

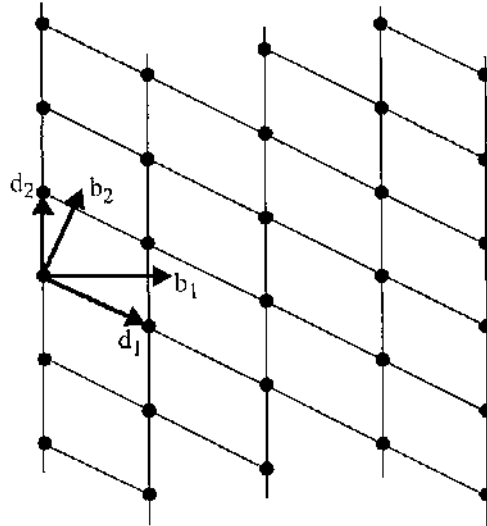


Figure 1.2 Generic 2-dimensional periodic lattice.

There is also a reciprocal lattice that is simply related to the direct lattice through the Kronecker delta matrix:

$$(b_j \cdot d_k) = \delta_{jk} \quad (1.1)$$

For 2-dimensional lattices the orthogonality between the direct and reciprocal lattice vectors is easily understood and can be seen clearly from Figure 1.2. In 3-dimensional systems the equations extend by simply making use of the vector triple product such that the reciprocal lattice vectors b_j are related to the direct lattice vectors d_j through Equation 1.2.

$$\begin{aligned} b_1 &= \frac{d_2 \times d_3}{d_1 \cdot (d_2 \times d_3)} \\ b_2 &= \frac{d_3 \times d_1}{d_2 \cdot (d_3 \times d_1)} \\ b_3 &= \frac{d_1 \times d_2}{d_3 \cdot (d_1 \times d_2)} \end{aligned} \quad (1.2)$$

By moving from the direct to reciprocal lattice we move from a real space to a k -space description of the lattice. Within reciprocal space the Brillouin zone can be constructed, this is a region in k -space that is constructed by perpendicular bisectors from an origin point to the neighbouring reciprocal lattice points. Examples of Brillouin zones for square and hexagonal lattices are shown by the shaded areas in Figure 1.3.

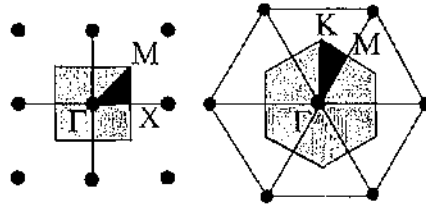


Figure 1.3 Brillouin zones for square and hexagonal lattices

The main Brillouin zone is shown by the lightly shaded region and the irreducible zone is shaded with black. The labelling for the zones has also been shown.

Within the Brillouin zone there is a smaller region, called the irreducible Brillouin zone. This smaller zone can be rotated and repeated as many times as necessary to fill the larger Brillouin zone. In essence the information that can be obtained from the irreducible Brillouin zone characterises the performance over the whole Brillouin zone, facilitating the analysis.

The bulk medium dispersion relation

The dispersion relation for a bulk medium is one of the most important equations pertinent to photonic crystals. The dispersion equation relates angular frequency, material refractive index, the speed of light in a vacuum and the k -vector, see Equation 1.3, where n is the refractive index of the material, c_0 is the speed of light in a vacuum, f is the frequency, ω is the angular frequency and λ is the wavelength.

$$\begin{aligned} c_0 &= n f \lambda \\ c_0 &= \frac{n 2 \pi f \lambda}{2 \pi} \quad (1.3) \\ \omega n &= c_0 k \end{aligned}$$

The final expression is the most commonly known form of the dispersion relation, further details relating to the dispersion relation can be found in Appendix A.1 on page 176. By changing the components of the k -vector the magnitude and direction can be altered such that the allowed modes within the irreducible Brillouin zone can be characterised, indeed this technique is known as the plane wave method [10]. On examining a “picce” of air using Equation 1.3 the artificial boundaries imposed allow the response to be

characterised. As the refractive index of air is $n_{\text{air}}=1.0$ the dispersion relation in Equation 1.3 is also known as the light line. Figure 1.4 shows the light line relating normalised frequency to the k -vector.

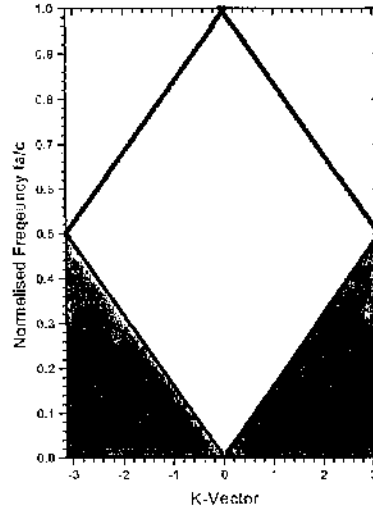


Figure 1.4 Bulk air response.

Shaded area below the light line corresponds to evanescent modes.

The piece of air has been normalised such that the k -vector has units of π/a , where a is the spatial period of the lattice commonly known as the lattice constant. The shaded areas below the line in Figure 1.4 relate to evanescent modes and the line folds back in to form the distinctive diamond shape due to the artificial boundary imposed. Using Equation 1.3, only the gradient of the line is altered for materials other than air. Normalised frequency, given by Equation 1.4 below, is frequently used such that for dispersionless materials the units become dimensionless and consequently can be scaled to any application.

$$\text{Normalised Frequency} = \frac{fa}{c} = \frac{a}{\lambda} \quad (1.4)$$

Elementary Bragg stack

Elementary Bragg stacks are 1-dimensional photonic crystals that are made from two materials which periodically repeat. By introducing a second material into a bulk material there is a considerable change in the behaviour of the structure. At each dielectric boundary waves are both transmitted and reflected a well known phenomena governed by Fresnel's equations. If the ratio of material thicknesses and dielectric constants is chosen correctly, sizeable gaps in the dispersion or band diagram can be created. Figure 1.5 shows the band diagram for a homogeneous medium $\epsilon_r=12.96$, the familiar diamond shape described by Equation 1.3 on the left, and the band diagram with $0.1a$ air slices introduced into the bulk medium on the right, where a is the period lattice constant.

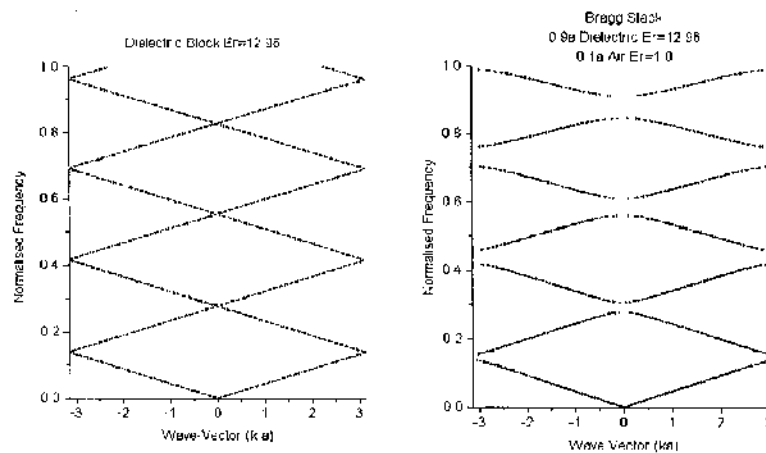


Figure 1.5 Band diagram response

Left: The band diagram response for a bulk medium of $\epsilon_r=12.96$. *Right:* Response for a Bragg stack made from 10% air, and 90% material $\epsilon_r=12.96$.

For the right inset response there are small ranges in normalised frequency where there are no allowed bands, examples of the photonic band gap. If the ratio of air to the other material is altered such that the air layer is $0.7a$, then much larger gaps are opened [11]. The band diagram and the transmission response for five periods for a wave impinging in the

transverse (normal) direction to the top of the stack calculated using the transfer matrix technique and are shown in Figure 1.6.

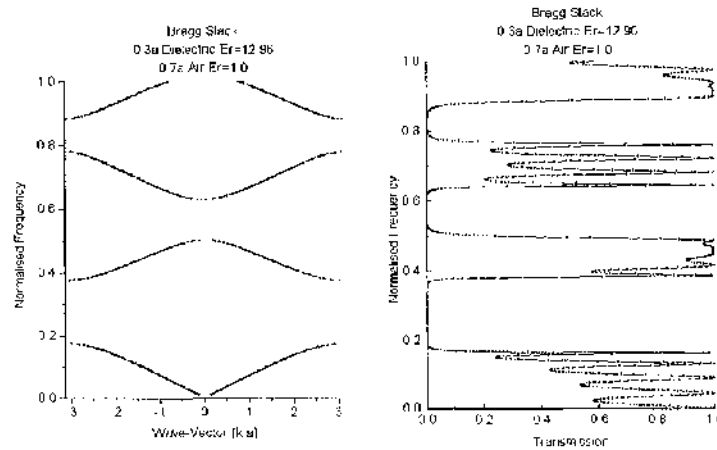


Figure 1.6 Band diagram and transmission response for a simple Bragg stack.

The Bragg stack is made from $0.7a$ air and $0.3a$ $\epsilon_r=12.96$. The example shown can be compared directly with the results presented in [11]. Transmission response shown for a crystal thickness, $L=5a$, where a is the periodic lattice constant.

The response of structures is highly dependent on the direction and polarisation of the impinging wave. Figure 1.6 shows that a large photonic band gap exists for a normally incident plane wave onto the stack while in another direction there may not exist a band gap region at all. Under certain circumstances Bragg stacks can display omni directional reflectance, that is to say that there are complete band gaps regardless of polarisation. This is an idea that would at first contradict the known transmission due to the Brewster angle and is investigated further in Chapter 2.

1.3: Chapter Aims and Objectives

The first four chapters deal with the characterisation of 1- and 2- dimensional photonic crystals. The objectives within these chapters is to examine the applicability of the structures as omni directional reflectors, that is to say that the structures should not allow propagation for any polarisation or incidence angle.



Figure 1.7 A picture of a simple Bragg stack

Within chapter 2 simple 1-dimensional Bragg stacks are examined. The transmitted level through optimised Bragg stacks is investigated as a function of polarisation and incidence angle for various materials. By considering Snell's Law, which states the relationship between the impinging wave incidence angles and the transmitted or reflected angles, it is shown that Bragg stacks, under particular circumstances, display omni directional reflection. It is also demonstrated that the circumstances under which omni directional reflectance occurs are somewhat limiting, in that waves are free to propagate, not least due to the Brewster angle, in other directions when the criteria required for omni-directional reflectance are removed.

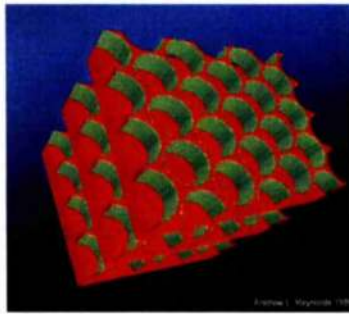


Figure 1.8 A picture of the 'dielectric sandwich'

Chapter 3 builds on the idea of using a Bragg stack as the base mechanism for a proper 3-dimensional reflector. For a given operational frequency, an optimised 2-dimensional lattice of air holes is introduced into a finite thickness high refractive index slab of material, such as silicon, to suppress any lateral propagation of waves at the operational frequency. The introduction of correctly sized holes is sufficient to create a full photonic band gap within the periodic plane of the slab, while simultaneously serving to reduce the effective or average weighted index of the slab significantly. This reduction in effective index is then used in creating a periodic modulation in refractive index in the plane transverse to the slab by sandwiching the perforated slice between two pieces of the same bulk material, see Figure 1.8. Consequently the structure formed is a pseudo 2+1-dimensional structure. The thickness of each slab can also be controlled to give optimal reflectance for the operational frequency. However, the refractive index contrast between the bulk material and the effective index of the perforated layer is shown to be insufficient to open a full 3-dimensional band gap.

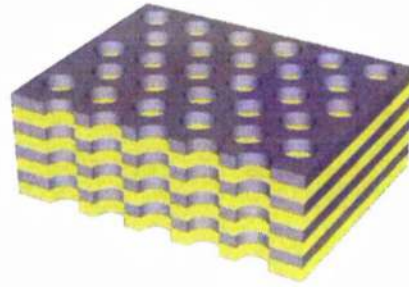


Figure 1.9 Drilled Bragg stack

Reproduced with the kind permission of Dr. Peter de Maagt, ESTEC

Chapter 4 extends the thinking of Chapter 3 by using two different materials to form the stack and also extends the holes straight through stack, see Figure 1.9. This facilitates fabrication considerably and the idea has been patented by the European Space Agency. For the materials examined the response of the 1-dimensional stack is optimised for the operational frequency before the holes are introduced. Incidence onto the side of the stack presents a stratified medium to any impinging waves which are consequently free to propagate along the stratifications.

The introduction of air holes serves to kill these propagating modes, and various hole sizes are examined for both square and hexagonal lattice patterns. Both patterns degrade the performance of the Bragg stack, as the effective index of each layer of the stack is reduced. The final systems examined take into account for the trade off between the degradation in the stack performance due to the introduction of the holes from the initially optimised Bragg stack and the lack of lateral mode propagation if the holes are not introduced. It is concluded that for the range of materials studied, that this 2+1-dimensional structure also has insufficient symmetry to display full 3-dimensional photonic band gap behaviour for both polarisations.

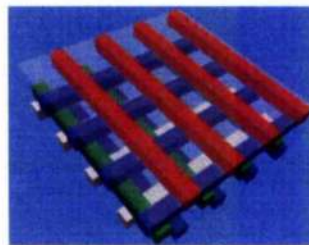


Figure 1.10 Woodpile structure with a semi transparent membrane.

Chapter 5 demonstrates that interleaving two, 2-dimensional photonic crystal lattices to make a woodpile structure, see Figure 1.10, results in the successful creation of a full 3-dimensional photonic band gap. It is shown by examining the transmission properties, that the strong polarisation discrimination exhibited by the constituent 2-dimensional sub lattices in their respective stop-bands leads to a completely 3-dimensional photonic band gap crystal in all polarisations when the two sub-lattices are interleaved. Many of the properties of the resultant 3-dimensional photonic crystal can be predicted directly from a knowledge of the properties of the sub-lattices thereby radically reducing the computational cost of their determination. The chapter then examines the properties of a previously published woodpile structure for an operational frequency of 94GHz. The examination verifies the transmitted levels through the crystal for various crystal thicknesses using both theoretical and measurement techniques and also confirms the existence of the full 3-dimensional photonic band gap. The performance of a slot antenna placed onto the surface of the crystal is also presented.

Chapter 6 examines the influence of placing a dielectric membrane with translational invariance over the top layer of an underlying 2-dimensional photonic crystal. It is known that membranes themselves are capable of supporting substrate modes, through total internal reflection, and in conjunction with the underlying crystal, may also support surface modes where the mode evanescently decays on either side of the surface. The chapter examines the transmission performance of several membranes, both experimentally and theoretically, for a range of membrane materials, thicknesses and for two underlying geometries of photonic crystal. It is demonstrated that the combination of the membrane and top layer of photonic crystal can result in the excitation of surface waves but for application at the chosen operational frequency of 94GHz such surface waves are not excited.

Chapter 7 introduces a planar cavity defect into an otherwise perfect 2-dimensional photonic crystal. The structure is then examined theoretically and the resonance created by the supported mode in the cavity displays strong impinging wave incidence angle dependence. Measurements confirm the findings and such cavities have already been shown to increase the directivity of a resonant antenna that is placed within the cavity.

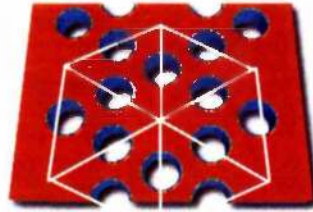


Figure 1.11 A piece of hexagonal lattice with defects introduced.

Chapter 8 examines the influence of introducing a superlattice of defects into an otherwise perfect hexagonal lattice of air holes in dielectric. The defects are created by filling in the air hole at the defect sites in the high symmetry axis of the crystal, see Figure 1.11. The coupling between neighbouring defects is examined as a function of distance and direction of propagation within the lattice.

For defects that are introduced at every second lattice site, as shown in Figure 1.11, the coupling is strong and there is a band of allowed resonance frequencies with a distinct difference in performance depending on the direction of propagation. As the distance between the defect lattice sites is increased the coupling between defect sites reduces at a much faster rate than expected. This is identified by the rapid narrowing of the band of resonance frequencies.

Defect coupling can also be used as the mechanism to form waveguides, also known as coupled resonance optical waveguides, CROWs. Such waveguides make use of the inherent symmetry of the lattice to allow light to be guided around corners without the inherent bend loss or reflections encountered by conventional techniques. In the conclusion of the chapter a simple idea for a wavelength dependent optical waveguide splitter is presented.

Chapters 9 and 10 examine the properties of opal colloidal crystals. These crystals operate in the optical domain and consequentially small sized particles are required to build the crystal. The crystals are manufactured using various techniques but most are fabricated

by taking advantage of the fact the crystals self organise to form face centred cubic, f.c.c., lattice formations, see Figure 1.12.

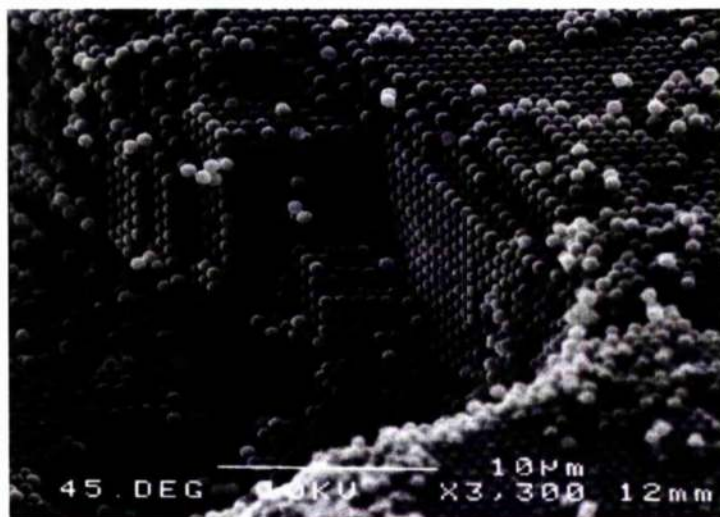


Figure 1.12 Scanned Electron Micrograph of an opal colloid.
Reproduced with the kind permission of Dr. Richard Amos, DERA

Chapter 9 examines the transmitted level through the crystal for two of the main crystal surface truncations, the $\langle 100 \rangle$ and $\langle 111 \rangle$ planes. The transmission through the crystal is investigated as a function of various crystal parameters. The properties of the photonic band gap region are compared for two distinct directions of propagation, the $[100]$ and $[111]$ directions, for silica based opals as functions of dielectric coating placed around the non touching areas of the spheres, for sintering a thermal process that shrinks and stabilises the crystal, and as a function of total crystal thickness.

Chapter 10 examines the information that can be obtained optically by examining the intensity and the intensity profiles as a function of incidence angle, of the diffracted orders generated by a laser beam probing the colloidal crystal. Both the intensity and its profile provide definitive information concerning the stacking sequence and purity of the sample under test, in effect defining optical signatures for the structure.

Chapter 11 summarises the findings and concludes this thesis.

Omni-directional Reflecting Bragg Stacks

Overview

Considerable work has been spent during the last decade in developing periodic structures that display electromagnetic rejection bands, the so called 'photonic band gaps' (PBG). For certain applications the PBG must be completely three dimensional and absolute, both TE and TM polarised waves should be rejected for all angles of incidence. In the field of optics (anti)-reflection coatings have been studied for some time and are well understood [12-15]. Recently the understanding that omni-directional reflection can be achieved, under specific criteria, with simple 1-dimensional periodic structures commonly known as Bragg stacks [16-20], has resurfaced and is changing the approach to certain problems.

The most important issue for deciding the applicability and usability for these omni-directional reflecting structures is that the excitation source must be far enough away from the initial dielectric boundary so that no evanescent wave coupling can occur [16]. When a radiating source is placed in close proximity to a boundary then power between the two can be exchanged if the evanescent fields between the two overlap to a significant extent. Evidently the coupling between the two can be significantly reduced by increasing the distance between them.

A fundamental point that is of vital importance is that the band structure for the crystal need not necessarily display a complete photonic band gap;

the condition for omni-directional reflectance is that there be no allowed states internal to the crystal to which any external incoming illuminating wave can couple.

2.1: Omnidirectional reflectance from 1-dimensional dielectric films.

The light line for any ambient medium can be projected onto the allowed modes of a photonic crystal. For a given frequency or range of frequencies if the area bounded by this light line contains a region where there are no modes then the structure will display omnidirectional reflectance.

The transfer matrix method, TMM, as suggested by Pendry and Bell [21] illuminates the structure under study with a defined frequency plane wave from a user definable reference medium. The rotational symmetry of 1-dimensional structures, assuming that the structure is infinite in the xy - plane, see Figure 2.1, simplifies the analysis of the omni-directional reflectance by reducing the forward hemispherical sweep required for 2-dimensional and 3-dimensional structures. Complete characterisation can be achieved for a 1-dimensional structure by sweeping any plane parallel to the surface normal, i.e. the xz -plane in Figure 2.1. By scanning the incident plane wave control vectors to cover this plane the reflectance can be investigated.

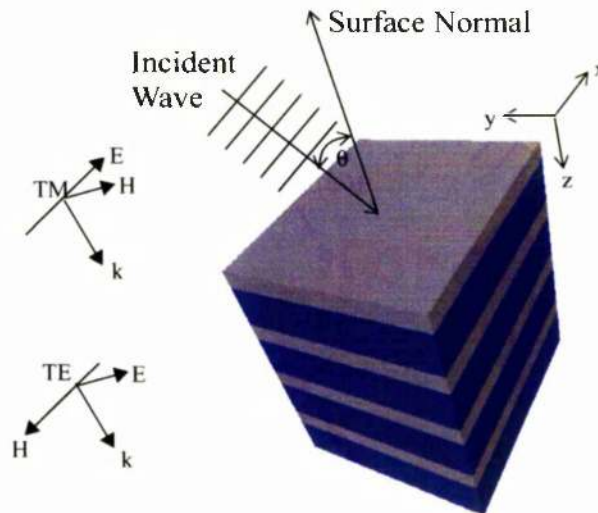


Figure 2.1 Schematic of a Bragg stack being illuminated by incoming plane wave at an arbitrary angle.

For verification purposes the structures presented by Winn et al. [16] were analysed using the transfer matrix method, TMM. The structure studied was made by stacking pairs of layers where each layer was quarter wave length thick. The materials used to make the

stack had refractive index $n_1=3.4$ and $n_2=1.7$ and the impinging plane waves were assumed to start from an air medium. The order of the materials makes no difference after the initial boundary between the ambient medium and the stack. Analysis was carried out for normal incidence, 45° and 89° and found to be in good agreement with the published results.

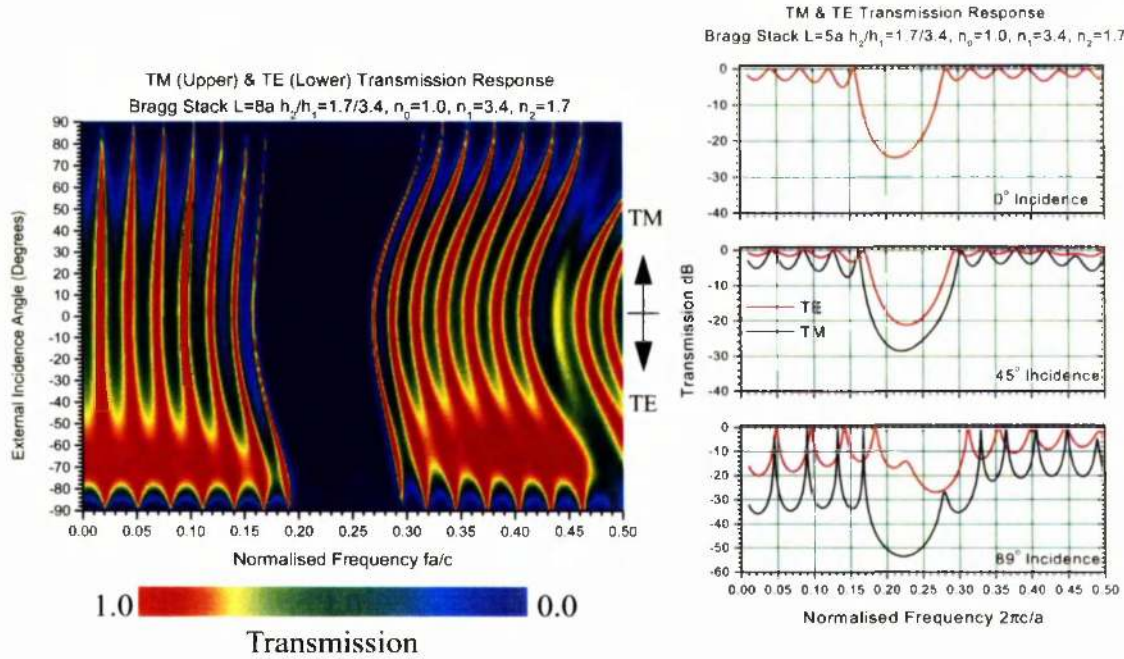


Figure 2.2 Transmission Response (left) and specific angle response (right)

Left: The transmission response for TM (upper half) and TE (lower half) polarisations plotted as a function of external incidence angle for a four pair quarter wave stack of two materials refractive index $n_1=3.4$ and $n_2=1.7$. *Right:* Specific angle response for a ten film stack of the same materials for TM and TE polarisations, this thickness has been shown for literature comparative purposes. **NOTE:** While the responses shown above have the same constituent stack parameters the crystals have a different number of total periods.

For normal incidence onto the surface of the Bragg stack the TE and TM polarisations are not distinguishable due to the rotational symmetry of the stack, but for off-normal incidence the response for each polarisation is quite different. The normal incidence condition defines the upper band edge, the lower band edge being set by the oblique incidence condition of the TE response curve. Increasingly oblique incidence results in a decrease in transmitted level for the TM polarisation while the converse applies for TE polarised waves.

2.2: Silicon and Kapton Bragg Stack

Two common and inexpensive materials with a large difference in dielectric constant are silicon and kapton. The relative dielectric constant (refractive index) for silicon is $\epsilon_r=11.7$

($n=3.42$) and for kapton $\epsilon_r=3.7$ ($n=1.92$) at radio frequencies and it is assumed that the materials are dispersionless. Kapton is a strong polymer material that is frequently metalised and used as a thermal and radiation shield for satellites. The contrast between these materials is sufficient to open an omnidirectional reflecting band gap when the stack is illuminated by waves impinging from air. The optimum choice of layer thickness constituting the stack is not far off the quarter wavelength mark, the optimal stack is constructed such that $h_2/a=0.38$ where h_2 is the thickness of silicon and $a=h_2+h_1$. Quarter wave Bragg stacks can be easily designed by using Equation 2.1 below where a is the lattice constant, λ is the free space wavelength, n_1 and n_2 are the refractive indices of the materials of the stack. The thickness of each layer is expressed as t_1 (t_2) for the n_1 (n_2) layer.

$$\begin{aligned} \text{Lattice Constant } a &= \frac{\lambda}{4} \left(\frac{1}{n_1} + \frac{1}{n_2} \right) \quad \text{where } a = t_1 + t_2 \\ \frac{t_1}{a} &= \frac{n_2}{n_1 + n_2} \quad \frac{t_2}{a} = \frac{n_1}{n_1 + n_2} \end{aligned} \quad (2.1)$$

The omnidirectional response for the optimal stack is shown in Figure 2.3 on page 21 for transmission through eight layer pairs. The calculation stops in the final layer of the structure and does not assume an underlying substrate. The omnidirectional gap can be seen to extend from a normalised frequency, defined by Equation 1.4 on page 8, of $fa/c=0.185$ to approximately $fa/c=0.235$, a gap / mid gap ratio of approximately 24%.

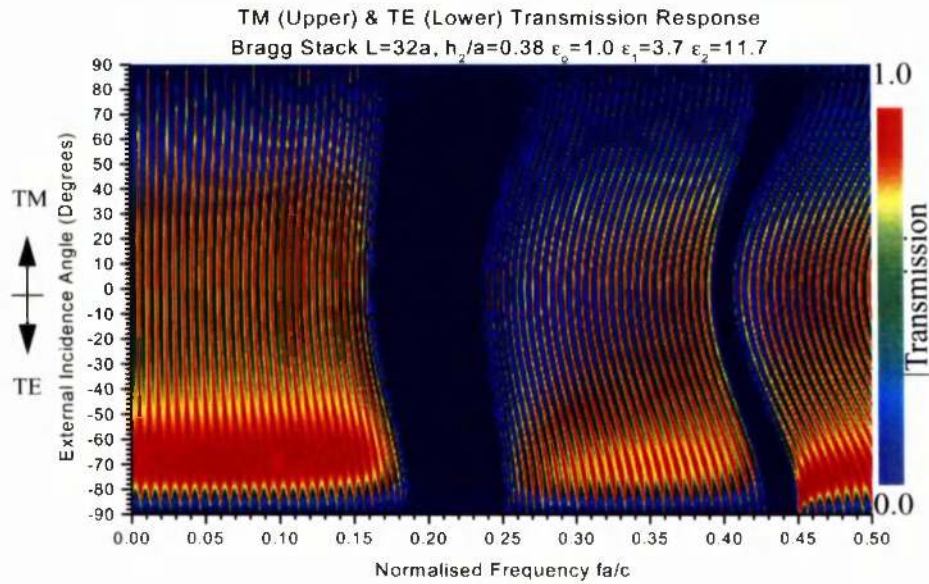


Figure 2.3 Transmission Response for a Bragg Stack made from Silicon and Kapton

The stack has been optimised to give the largest omnidirectional reflection. TM (TE) polarised waves are shown in the top (bottom) half of the figure and the response is shown for a finite thickness crystal thirty-two periods thick.

As previously stated the normal incidence condition defines the upper band edge, the lower band edge being set by the oblique incidence condition of the TE response curve. This is observable in Figure 2.3 and Figure 2.4. While the increase in transmitted level for the TE polarised waves for increasingly oblique incidence is significant, some 40dB for a 32 pair layer Bragg stack as shown in Figure 2.4, it still does not negate the omnidirectional reflectance of the structure.

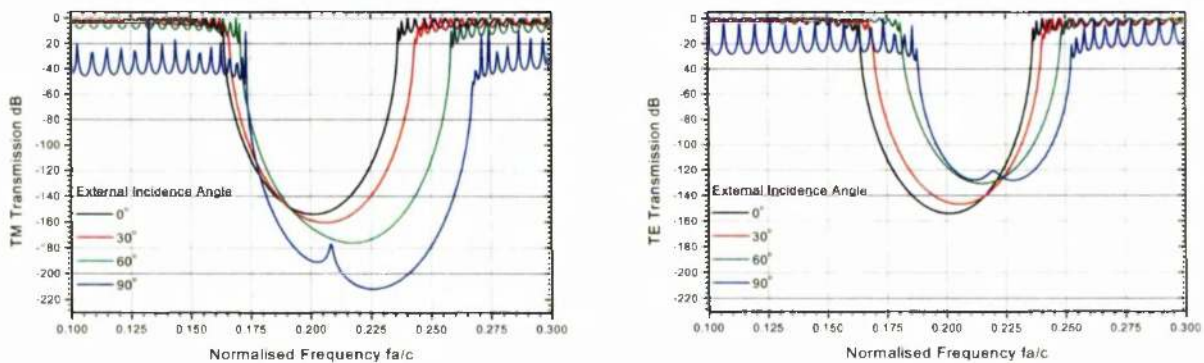


Figure 2.4 Transmission as a function of external angle for TE and TM polarisations

Transmission response from a Bragg stack made from silicon and kapton, $h_2/a=0.38$, for externally incident plane waves, i.e. incident from an air medium.

Explanation

Chigrin [18] has provided an excellent overview of omnidirectional reflectance, the main point of which is re-iterated here. When a plane wave illuminates the 1-dimensional Bragg stack the tangential component of the k -vector remains constant throughout the crystal due to interface matching boundary conditions given by Equation 2.2. The refractive index of the current medium is given by n , ω is the angular frequency, c is the speed of light in a vacuum and α is the external incidence angle of the plane wave in the stack.

$$|k_{\text{parallel}}| = \left(\frac{n\omega}{c}\right)\sin\alpha \quad (2.2)$$

The allowed values for the parallel component of the k -vector lie between zero for normal incidence and $(n\omega)/c$ for oblique incidence. Any other values for the parallel vector are evidently outside the allowed range and, in most instances, can be disregarded.

Block Medium Band Structures

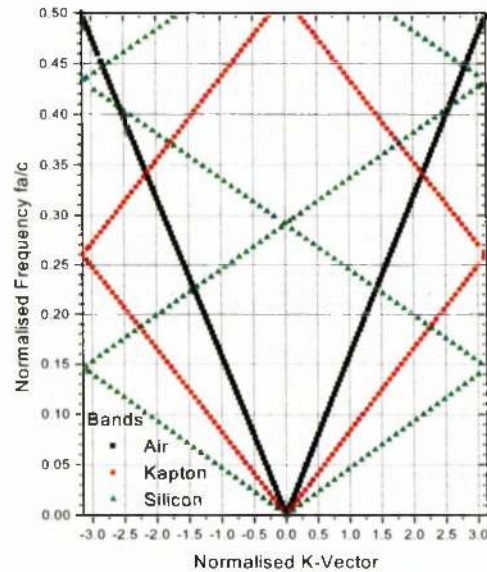


Figure 2.5 Allowed bands within solid dielectric blocks.

Figure 2.5 shows the allowed bands for individual dielectric blocks of air, kapton $\epsilon_r=3.7$, and silicon $\epsilon_r=11.7$. The cells that were analysed were normalised such that the k -vector varies between $\pm\pi$. The significance of the refractive index in Equation 2.2 can be seen in the gradient of the resultant bands. At a given frequency an increase in the refractive index

of the material increases the value of the parallel k -vector for any fixed angle generating a resultant decrease in the gradient of the line.

Any of these ambient medium curves can be drawn onto the allowed bands of a photonic crystal. Any regions below the line defined by Equation 2.3 are evanescent and can be disregarded. Therefore for an ambient medium of air, any bands within a photonic crystal that are below the black line composed of squares in Figure 2.5 can be ignored as no wave starting in the air medium can couple to them. This reference medium projection is demonstrated in Figure 2.7 on page 24 for an air reference medium and a Bragg stack.

In general a Bragg stack may display omnidirectional reflectance when the host medium has a refractive index which is less than the smallest index of the stack materials. When the stack is embedded in the same material as the largest refractive index of the constituent materials there is no omnidirectional reflectance, this a direct result of the Brewster angle.

Allowed propagation state restrictions due to Snell's law

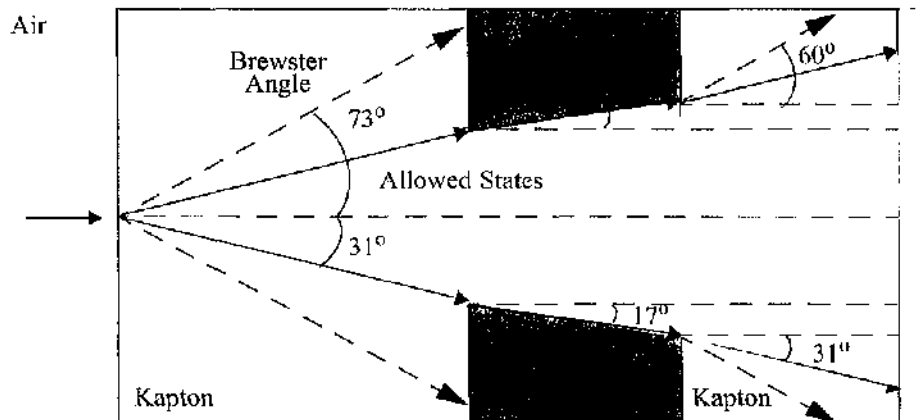


Figure 2.6 Allowed Internal Angles of Propagation within a Bragg Stack

A sketch of the range of allowed internal angles of propagation are shown in white for incoming incident waves from air, $n_{\text{kapton}}=1.92, n_{\text{silicon}}=3.42$.

A wave incident at the Brewster angle, of the correct polarisation, for a given dielectric boundary is completely transmitted. If multiple boundaries using different materials are used then Snell's law, Equation 2.3, allows accurate prediction of transmitted wave angles given any initial incidence angle. Snell's law relates the incidence angle θ_i in material n_1 to the transmitted angle θ_t in material n_2 , both angles are measured from the surface normal of the interface plane between the two materials.

$$n_1 \sin \theta_i = n_2 \sin \theta_t \quad (2.3)$$

Using the kapton / silicon stack in an air medium, illustrated in Figure 2.6, an obliquely incident wave from air will have a transmitted angle of approximately 31° within the first kapton layer. As the Brewster angle for the following kapton-silicon boundary requires an incident wave angle within the kapton layer of 60° transmission due to the Brewster angle is not achievable when the wave impinges externally onto the stack.

Therefore for the kapton / silicon dielectric boundary we need only consider the allowed incidence range, $0 \leq \theta \leq \pm 31^\circ$, which results in an even narrower range of allowed propagation angles within the silicon layer $0 \leq \theta \leq \pm 17^\circ$. The Brewster angle for a silicon / kapton boundary is 29° , larger than the allowed propagating wave range, ensuring that transmittance through the structure due to the Brewster angle for either dielectric boundary case cannot occur. Re-ordering of the layers, i.e. silicon- kapton as opposed to kapton-silicon, does not alter the response of the structure.

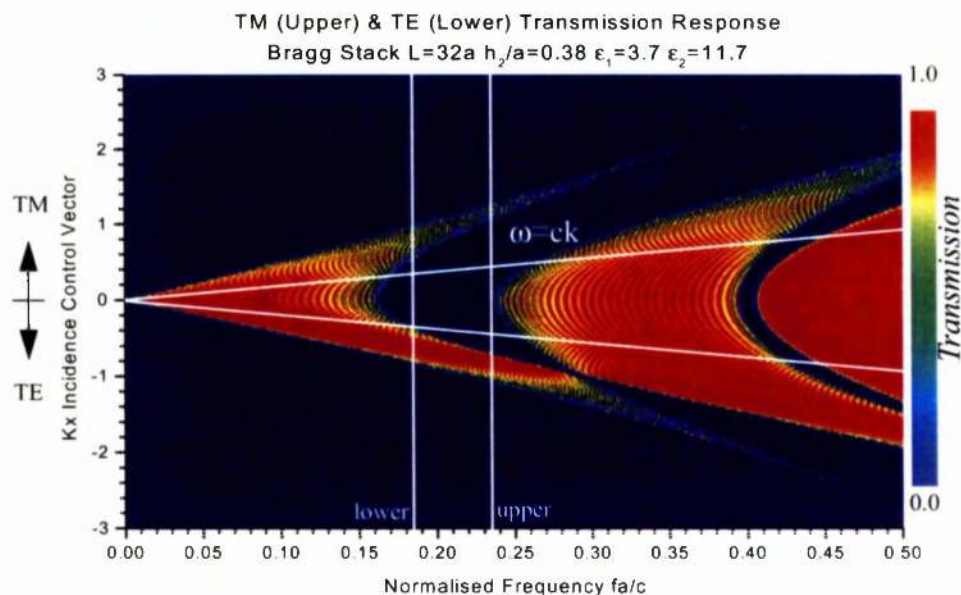


Figure 2.7 Transmission Response for a Bragg Stack made from Silicon and Kapton embedded in Silicon.

The transmission response for TM (TE), upper (lower) half of the figure plotted against the incidence control vector k_x . The response shown is for a 32 layer pair stack.

Figure 2.7 shows the transmission response for the silicon / kapton Bragg stack embedded in a silicon background medium where the silicon layer is 0.38 of the periodic lattice constant. This value was chosen to optimise the omni-directional reflectance using

the analytical solution presented by Chigrin [18]. By using a silicon reference medium there is no restriction over the allowed angle range. The free space light line, $\omega = ck$, has been projected onto the diagram. The information encompassed within the cone represents the k -space that can be excited from an air reference medium, $n=1.0$. The line can easily be adjusted for any reference medium by altering the refractive index n as $\omega n = ck$. The region encompassed *within* the central trapezoid in Figure 2.7 has no transmission for either polarisation and as this region represents all angles that can be excited externally for the stack zero transmission indicates omnidirectional reflectance.

The TE polarisation has a point where the upper and lower bands touch at values of (approximately) k -vector $= -1.0$, $fa/c = 0.29$. This point is related to the Brewster angle and the value in degrees can be calculated by Equation 2.4 on page 26. Using a refractive index for silicon $n = 3.42$ and for kapton $n = 1.92$ the resultant Brewster angle assuming that silicon is the initial or reference medium is 29.3° . The response in Figure 2.7 has been re-plotted as a function of normalised frequency against angle in degrees in Figure 2.8 to allow confirmation of the Brewster angle point. For more information concerning the dispersion relation consult Appendix A on page 175.

The response of the stack embedded in an air medium is shown in Figure 2.3 on page 21 for an eight layer pair stack. (Figure 2.8 shows the transmission response for 32 layer pairs)

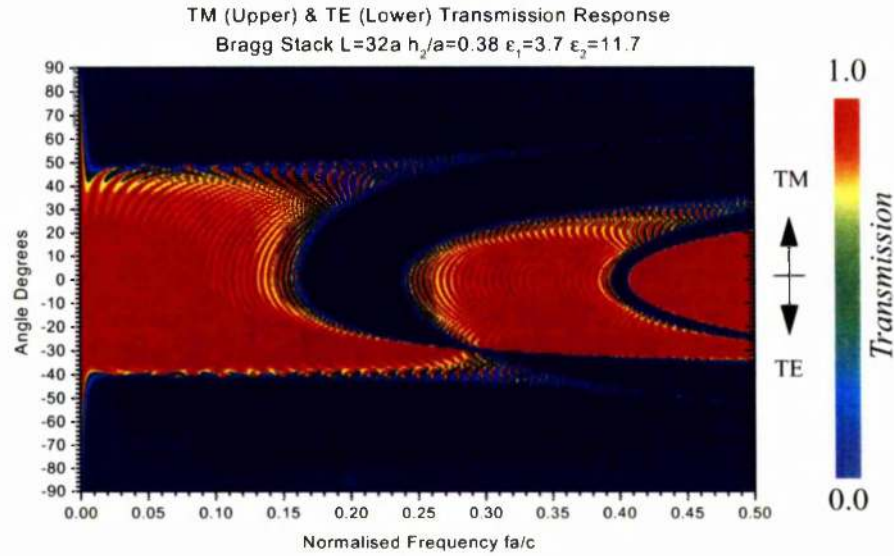


Figure 2.8 Internal Transmission Modes for a Bragg Stack made from Silicon and Kapton.

The transmission response for TM (TE), upper (lower) half of the figure plotted against the internal angle. The response is shown for a 32 layer pair stack.

Examining a range of embedding mediums starting from air and rising in value decreases the Brewster angle, Equation 2.4 where n_1 and n_2 are the refractive indexes of the materials before and after the boundary respectively.

$$\tan\theta_{brewster} = \frac{n_2}{n_1} \quad (2.4)$$

Figure 2.9 on page 27 shows the TE and TM polarised wave transmission response for a Bragg Stack when the reference medium dielectric constant is altered. The parameters of the stack remain unaltered, $h_2/a=0.38$ where $\epsilon_{r2}=11.7$ and $\epsilon_{r1}=3.7$, only the reference medium from where the plane wave is incident is altered.

The TM transmission response clearly improves as the refractive index of the embedding medium is increased, demonstrated by the gap region widening. For the TE polarisation the converse situation is found. Initially there is a complete gap when the structure is embedded in air, but as the reference medium increases in dielectric constant value the Brewster angle closes the gap. For a stack embedded in a reference medium of kapton, $\epsilon_r=3.7$, the Brewster

angle can be easily calculated for the silicon interface $\epsilon_r=11.7$ using Equation 2.4, and visually verified from the lower inset of Figure 2.9 at approximately -60° .

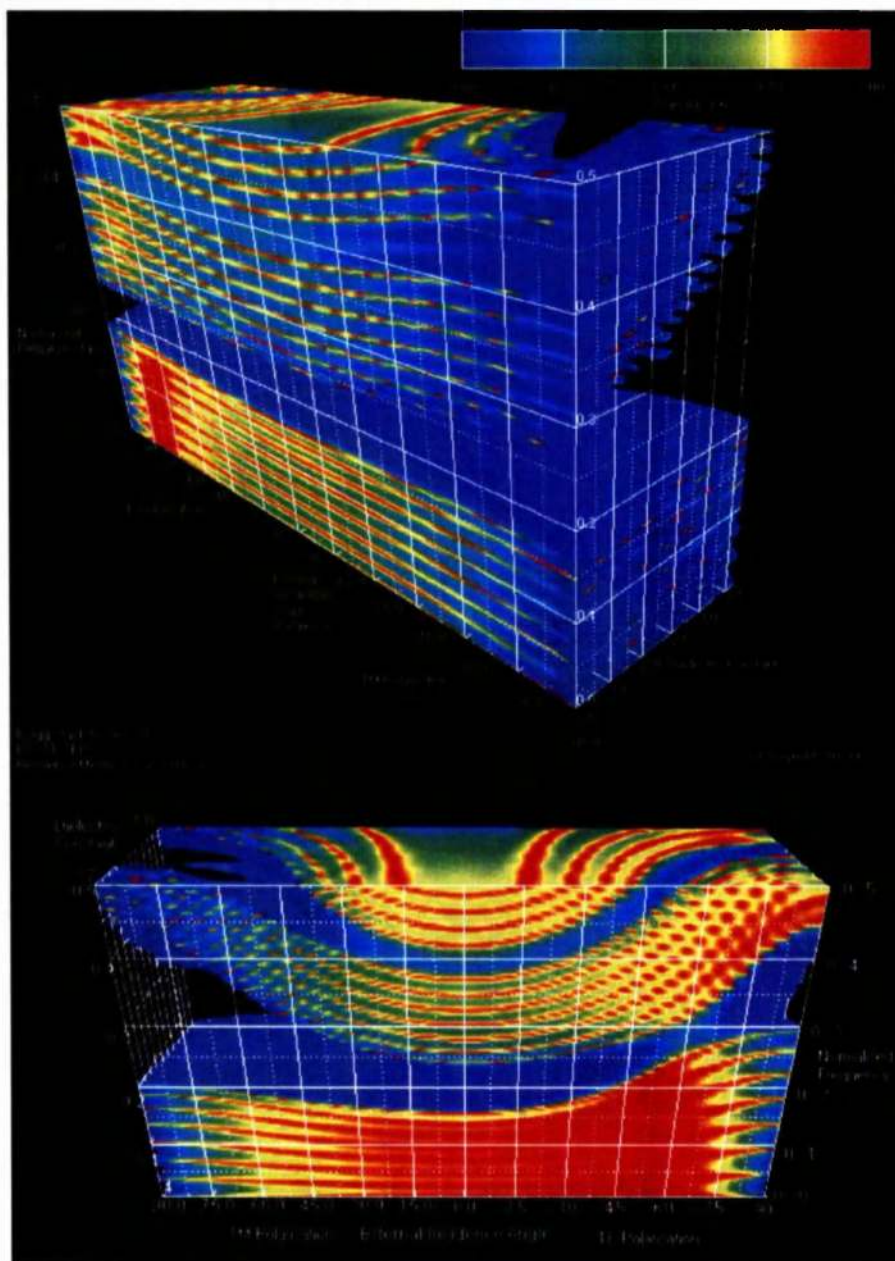


Figure 2.9 TE & TM transmission evolution as a function of embedding medium dielectric constant.

The TE and TM polarisation transmission response as a function of the embedding medium. The parameters of the stack remain unaltered, $h_2/a=0.38$ where $\epsilon_{r1}=3.7$ and $\epsilon_{r2}=11.7$. The TM transmission response improves as the embedding medium constant is increased as the gap region widens, while for the TE polarisation the Brewster angle can be seen closing the gap as the reference medium dielectric constant increases. The two figures show the same information from difference perspectives.

2.3: Full angular transmittance characterisation of the Bragg Stack

Excitation from an air medium

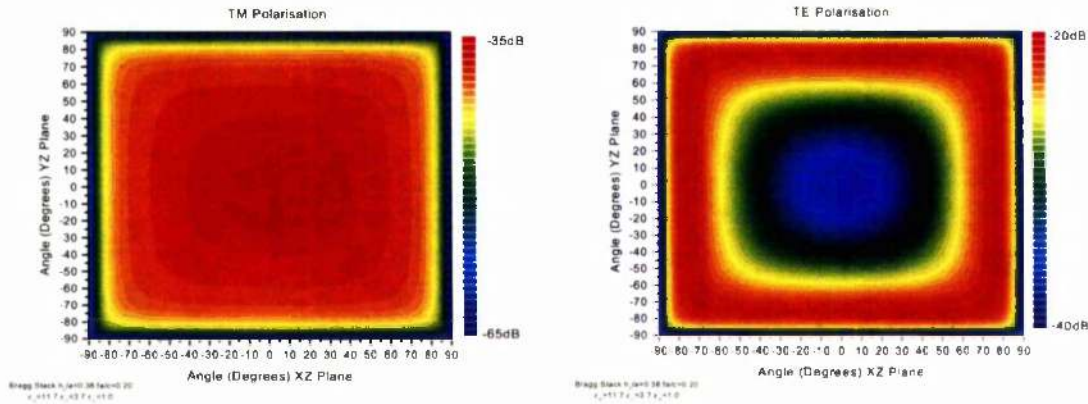


Figure 2.10 External Transmittance Response for the Silicon / Kapton Bragg Stack

TE & TM transmittance plots for the full forward hemisphere of available incidence angles on to the top of the Bragg Stack. The incident waves are from an air medium. The stack was a silicon / kapton stack $h_2/a=0.38$, where $\epsilon_{r2}=11.7$ (silicon) and $\epsilon_{r1}=3.7$ (kapton). The analysis has been carried out a normalised frequency of $fa/c=0.20$. Normal incidence, i.e. parallel to the surface normal of the stack is found at the central point within both insets where both the xz - and yz - angles are zero valued.

Figure 2.10 shows the transmittance through an eight layer pair Bragg stack for incident plane waves originating from an air medium. The TE polarisation has the highest transmission co-efficient, -20dB at close to oblique incidence, while the TM polarisation has -35dB as the highest transmission co-efficient at normal incidence on to the top of the stack. The TM polarisation transmitted level decreases at increasingly oblique incidence, normal incidence is located at the central point of the insets in Figure 2.10 where the xz and yz angles are both zero. The TE polarisation transmitted level increases away from normal incidence from the lowest value of transmission at normal incidence to the highest value at close to oblique incidence.

Bragg Stack Rotational Symmetry

There is much repetition in the transmission data shown in Figure 2.10. At first appearance by splitting the angular characterisation into quadrants each quadrant is simply related to another by mirror symmetry about the zero xz - and yz - angle lines. However as the stack possesses full rotational symmetry in the xy -plane, if Figure 2.10 was plotted using the k -vector component as opposed to the angle in degrees, then the responses would have rotational symmetry. Consequently it is sufficient to perform an angular scan from normal

incidence to oblique incidence in any one direction over the surface plane to characterise the full forward hemispherical incidence response of the structure.

This is an attribute that can be used to reduce the calculation times that are involved in characterising these structures. However, when further elements are introduced into the structure which break the complete rotational symmetry, then full angular analysis is required.

Excitation from a silicon medium

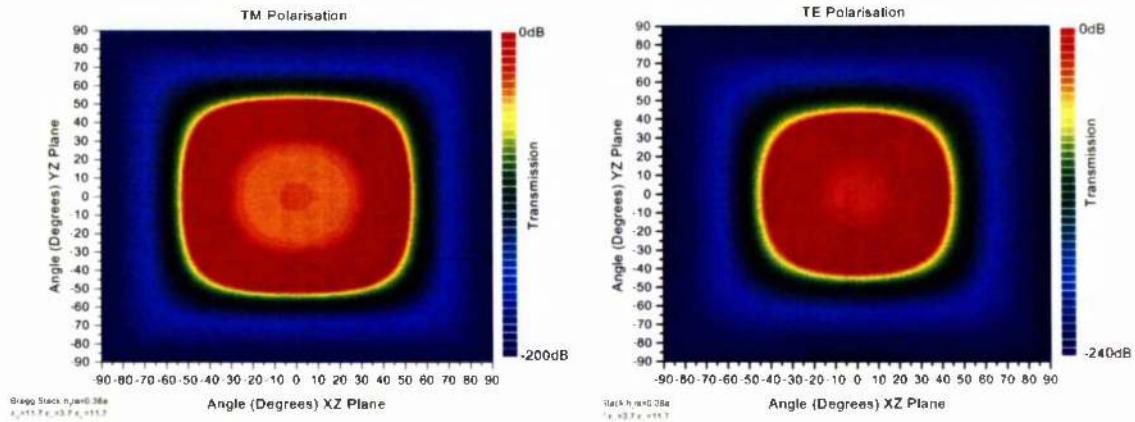


Figure 2.11 Internal Transmittance Response for the Silicon / Kapton Bragg Stack

TE & TM transmittance plots for the full forward hemisphere of available incidence angles on to the top of the Bragg Stack. The incident waves are from an air medium. The stack was a silicon / kapton stack $h_2/a=0.38$, where $\epsilon_{r2}=11.7$ (silicon) and $\epsilon_{r1}=3.7$ (kapton). The analysis has been carried out a normalised frequency of $fa/c=0.20$.

Figure 2.11 shows the transmittance through an eight layer pair Bragg stack. Both the TE and TM polarised waves have complete transmittance through the stack for certain ranges of angles. The plane waves impinging on the structure originate from a silicon medium, therefore the restrictions on allowed internal propagation angles due to Snell's Law are not applicable (See "Allowed propagation state restrictions due to Snell's law" on page 23.). Both polarisations increase in their transmission level from their normal incidence value to complete transmission before the transmitted level drops dramatically to over -200dB for angles close to oblique incidence.

2.4: Conclusion

By using Snell's Law all propagation angles at a dielectric interface boundary can be calculated for any incident wave. This allows accurate prediction of the range of angles within the second material. By careful choice of stack and ambient materials the Brewster angle for the Bragg stack dielectric material interfaces can be made unobtainable, resulting in an omni directional band gap. It has been demonstrated that Bragg stacks are capable of displaying omni-directional reflectance for both TE and TM polarised waves. The condition required is that waves impinge onto the top of the stack from a medium that is different and smaller in refractive index value than that of either of the constituent stack materials. Evidently stacks that utilise air as one of the constituent materials will not display omni-directional reflectance due to transmission at the Brewster angle. Furthermore the wave source must be spatially distant from the stack such that no coupling via evanescent waves may occur at the surface of the stack.

For device application, evanescent coupling places serious limitations on the usage of omnidirectional films. To use such a reflector for antennae, which may involve placing antennae either on the surface or within the stack, coupling via this mechanism would undoubtedly occur, resulting in parasitic losses such as substrate modes. By introducing further periodicity into the structure, such as a 2-dimensional periodic lattice within the stack, these substrate modes may be suppressed giving rise to a true 3-dimensional photonic band gap. This is investigated in the following two chapters.

Introduction

Combining 1-dimensional and 2-dimensional photonic crystals may present the opportunity to create a 3-dimensional photonic crystal. The idea is to construct a dielectric Bragg mirror constructed with, at minimum, two effective dielectric constant materials which, while not considered here, could include metals. Metals could prove useful, depending on the operational frequency, due to their large dielectric constants. However modelling of metallic structures requires careful choice of the spatial sampling mesh to ensure correct sampling of the wave fields which decay on much shorter length scales than their dielectric counter parts.

One or more of the periodic layers in the Bragg stack will be etched with a 2-dimensional photonic crystal lattice in an attempt to suppress laterally propagating substrate modes.

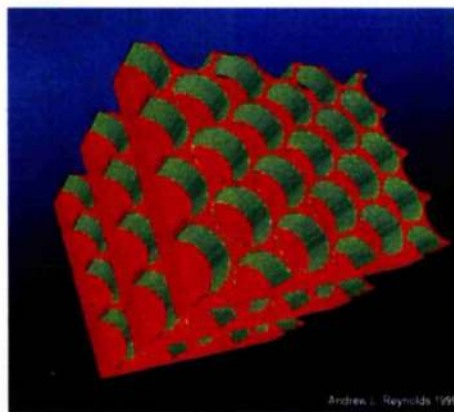


Figure 3.1 Schematic of dielectric 'sandwich' structure.
Each pair of solid and perforated layers has been separated with air to aid visualisation.

The idea is shown conceptually in Figure 3.1 with three layer pairs, each pair employing a single solid layer. The layers have been separated to aid visualisation only.

3.1: Issues related to the structure

As discussed in the previous chapter Bragg stacks are created by repetitively stacking at least two layers to form a periodic structure. For the “sandwich” structure at least one of the constituent layers will be perforated with a 2-dimensional photonic lattice. As the 2-dimensional photonic lattice will reduce the effective dielectric constant of that particular layer the stack can be made from a single material. The dielectric contrast between the layers required to observe the Bragg effect is then provided by the reduction of the effective dielectric constant of perforated layer through the introduction of the 2-dimensional photonic lattice with that of the solid layer.

By introducing a 2-dimensional photonic lattice into one of the layers it is hoped that suppression of substrate modes can also be achieved at the intended operational frequency. The 2-dimensional photonic lattices could also be shifted relatively to each other to construct face centred cubic, f.c.c., and body centred cubic, b.c.c., lattices which may negate the usage of the solid inter-spatial layer, but initially the response of the structure using a solid interspatial layer is investigated. The structure has many degrees of freedom and the investigation starts by studying the achievable photonic band gap in a pure 2-dimensional triangular photonic crystal. Thereafter the analysis incorporates this crystal as one of the periodic layers into a Bragg stack and the resultant performance is investigated.

Assuming that the materials behave in a linear form, the effective index for a hexagonal lattice is expressed in Equation 3.1, $\epsilon_{\text{effective}}$ is the resultant effective dielectric constant, $\epsilon_{\text{feature}}$ is the dielectric constant of the feature used in the lattice, $\epsilon_{\text{refmedium}}$ is the reference dielectric constant and f is the filling fraction.

$$\epsilon_{\text{effective}} = f \cdot \epsilon_{\text{feature}} + (1 - f) \cdot \epsilon_{\text{refmedium}} \quad (3.1)$$

The formula for deriving the filling fraction, f , for a hexagonal lattice consisting of cylinders, assuming that the radius to lattice spacing ratio does not exceed $r/a=0.5$, is expressed in Equation 3.2.

$$\text{Filling fraction } f = \frac{2\pi}{\sqrt{3}} \cdot \left(\frac{r}{a}\right)^2 \quad (3.2)$$

The hexagonal lattice appears as more promising than the square lattice as there is an operation region where a complete band gap for both TE and TM polarised waves exists for air cylinders in dielectric substrate [8]. There is a further advantage in using the hexagonal lattice because the complete gap occurs when the ratio of the radius to the lattice constant is relatively large, around $r/a=0.45$. Using the formula in Equation 3.2 a value of $r/a=0.45$ reduces the effective index of an isolated silicon wafer substantially. When this wafer is then integrated into the sandwich structure, which consists of a solid silicon layer and the perforated silicon layer, the reduced effective index of the perforated layer will aid the omni-directional reflectance properties.

3.2: Initial Design Parameters for 80GHz

An operational frequency of 80GHz was chosen as the W-band network analyser has a measurement range from 67-110GHz. The optimum r/a value for the hexagonal lattice was investigated and $r/a=0.44$, $a=1500\mu\text{m}$ were found to provided gap region at 80GHz for a hexagonal lattice for ΓM plane wave incidence, see Figure 3.2.

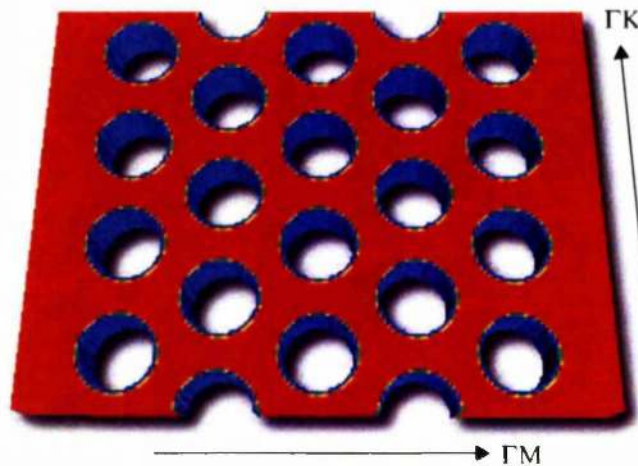


Figure 3.2 Hexagonal Lattice Definitions

A schematic of a hexagonal lattice of air holes in a dielectric medium showing the commonly known reciprocal space lattice directions.

Simple hexagonal lattice of air holes in silicon

Angular investigation of impinging plane waves was carried out with the plane waves arriving from both silicon and air media to remove any limitations over excitable k -space, the silicon response being of greater significance as this characterises all the internal modes of the structure. Figure 3.3 and Figure 3.4 on page 35 show the TE and TM transmission responses for incident waves commencing in air and in silicon respectively. Normal incidence is for end fire incidence, i.e. within the periodic plane, for the ΓM direction.

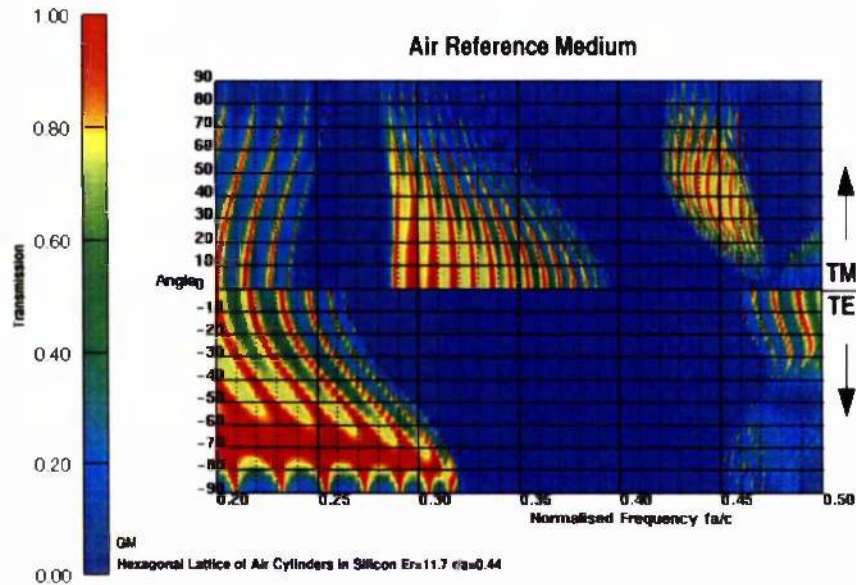


Figure 3.3 Hexagonal lattice; waves impinge from air

Hexagonal lattice of air cylinders in silicon $\epsilon_r=11.7$ $r/a=0.44$, $a=1500\mu\text{m}$, ΓM orientation for normal incidence. Wave propagated through a thickness of crystal $L=16a'$ where $a'=a\sqrt{3}$

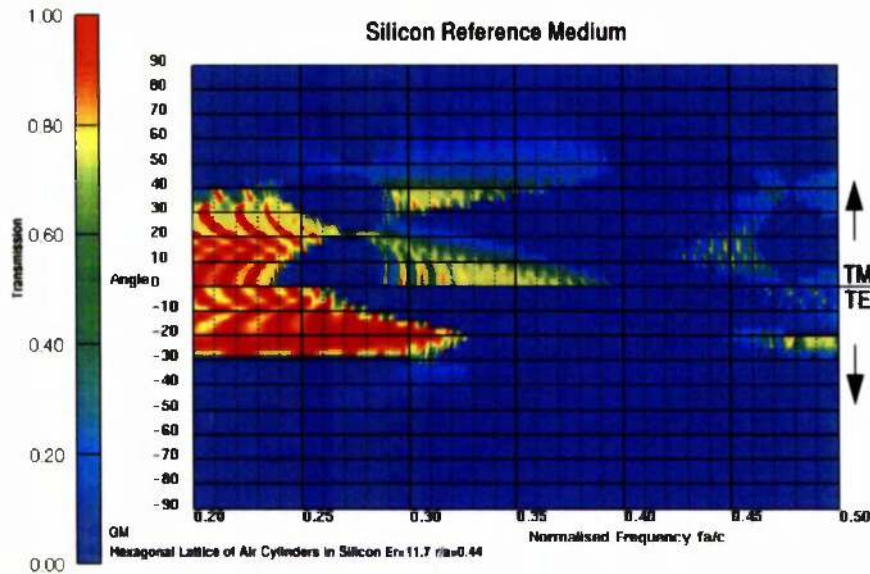


Figure 3.4 Hexagonal lattice: waves start from silicon

Hexagonal lattice of air cylinders in silicon $\epsilon_r=11.7$ $r/a=0.44$, $a=1500\mu\text{m}$, TM orientation for normal incidence. Wave propagated through a thickness of crystal $L=16a$ where $a'=a\sqrt{3}$

Both Figure 3.3 and Figure 3.4 show the TE and TM polarisations plotted on the same figure. The TM polarisation has been plotted on a positive incidence angle scale while the TE polarisation response has been plotted on the negative angle scale. This has been done merely to show both sets of information on the same graph and to ascertain whether there is a range in normalised frequency where there is no transmission for both polarisations.

Both Figure 3.3 and Figure 3.4 show that there is a complete band gap in the normalised frequency range from 0.395-0.420 for both TE and TM polarised waves. Figure 3.3, which assumes that the waves start from air, shows the existence of a complete photonic band gap for the TM polarisation in the normalised frequency range 0.26-0.28. Examination of this range when the waves start within silicon, Figure 3.4, show that this gap is indeed complete as the gap does not close. Consequently the gap seen in the 0.395-0.420 normalised frequency range is a complete photonic band gap for all directions within the 2-dimensional plane for both TM and TE polarised waves.

Interim Conclusion

The utilisation of a hexagonal lattice of air cylinders in silicon can be used to design a photonic crystal with a complete band gap for TE and TM polarised waves. This has been demonstrated for a system for suggested usage at 80GHz by setting the lattice constant to 1500 μm and employing an optimised radius to lattice constant ratio $r/a=0.44$. Utilisation of

the effective medium formula in Equation 3.2 on page 33, derives an effective dielectric constant for the 2-dimensional hexagonal photonic crystal of $\epsilon_r=4.18$. This effective dielectric constant is used in the next section in the Bragg stack calculations.

3.3: Bragg Stack Response

Using the effective dielectric constant computed for the hexagonal lattice with $r/a=0.44$, $\epsilon_r=4.18$ and bulk silicon $\epsilon_r=11.7$ a Bragg stack can be optimised for operation at 80GHz by tailoring the layer thickness. An illustration of a generic Bragg stack is shown on the left of Figure 3.5, the Bragg stack could be considered as an effective illustration of the dielectric sandwich structure shown on the right.

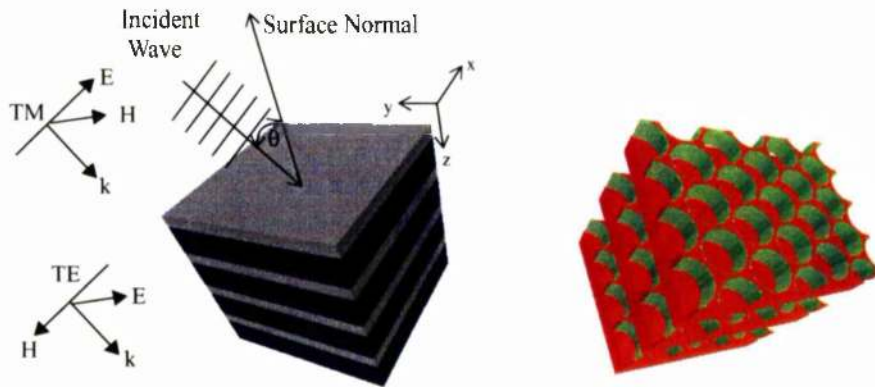


Figure 3.5 Generic Illustrations of a Bragg Stack & Sandwich Structure

Left: Bragg stack structure with TE/TM, surface normal and co-ordinate axis definitions, Right: Proposed dielectric sandwich structure.

In this instance the dielectric sandwich structure is constituted entirely from silicon but with one of the periodic layers reduced in effective dielectric constant by introducing a 2-dimensional photonic crystal. Utilising the effective dielectric constant of the perforated layer in conjunction with a solid silicon layer, near optimal performance can be obtained by setting each layer thickness to a quarter wavelength, $\lambda/4$, such that the period of the lattice, a , is $\lambda/2$. The lattice constant for the Bragg stack can be calculated using Equation 2.1 on page 20.

Important Point concerning lattice constants

The operational frequency has been defined as 80GHz. The lattice constant for the Bragg stack *is not the same* as that used within the hexagonal lattice calculations. Calculation of the lattice constant for the Bragg stack, assuming quarter wavelength thickness for the two layers as defined in Equation 2.1 on page 20, results in a lattice constant $a=733\mu\text{m}$. This

results in layer thickness to lattice constant ratios of $t_2/a=0.3736$ and $t_1/a=0.6264$. Consequently the normalised operational frequency of 80GHz for the Bragg stack is $fa/c=0.195$, and not $fa/c=0.40$, as was the case for the 2-dimensional hexagonal photonic crystal. A quick reference table of normalised frequencies for both the Bragg stack and hexagonal lattice constants is provided in Table 3.1.

Quick reference normalised frequencies

Frequency GHz	Normalised Frequency fa/c	
	$a=1500\mu\text{m}$	$a=733\mu\text{m}$
60	0.300	0.1466
65	0.325	0.1588
70	0.350	0.1710
75	0.375	0.1832
80	0.400	0.1955
85	0.425	0.2077
90	0.450	0.2199

Table 3.1 Quick reference normalised frequency.

Bragg stack wave incidence from air

The Bragg stack transmission was investigated as a function of incidence angle by illuminating the top of the structure as shown pictorially in Figure 3.5 on page 36. The plane waves are launched from an air medium external to the stack. The following calculations assume a truly 1-dimensional stack made from two dielectric materials,

$\epsilon_{r1}=4.18$ and $\epsilon_{r2}=11.7$ with $t_2/a=0.3736$. The transmission response for TE and TM polarised waves is shown in Figure 3.6.

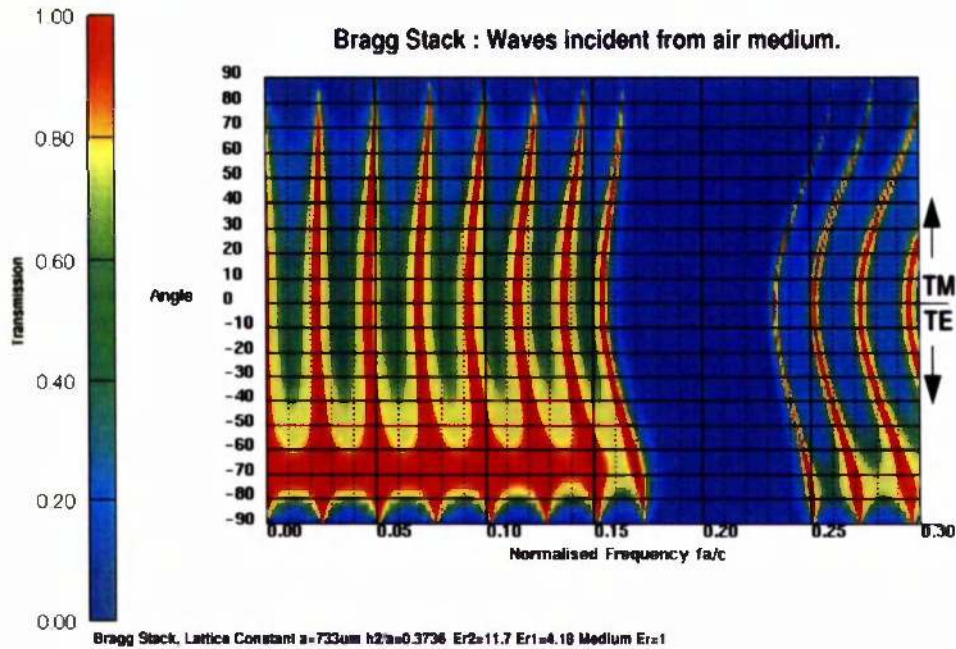


Figure 3.6 Bragg Stack: External TE & TM transmission response $\epsilon_{\text{initial}}=1.00$

The TE, (TM) transmission responses plotted on the upper, (lower) half of the diagram. The plot shows the transmission response plotted as a function of incidence angle and normalised frequency. NOTE: due to the rotational symmetry of the structure the TE and TM polarisations are indistinguishable for normal incidence. The stack was made from two dielectric materials, $\epsilon_{r1}=4.18$ and $\epsilon_{r2}=11.7$, lattice constant $a=733\mu\text{m}$ with $t_2/a=0.3736$, total thickness $L=8a$.

Figure 3.6 demonstrates that there is a complete gap for both polarisations in the normalised frequency range 0.18-0.23. This gives a gap to mid gap ratio $f/\Delta f=0.243$, some 24%, with a central operational frequency of 84GHz using the band extremities to generate the mid point. The TE polarisation can be used to obtain both the upper and lower band edge extremities, the normal or 0° degree angle condition sets the upper band edge at a normalised frequency of $fa/c=0.23$, while the oblique incidence condition, the absolute angle being 90° , sets the lower band edge of $fa/c=0.18$.

By removing the assumption that the plane waves impinge from air and assuming that they start from within silicon, the stack can be fully characterised and the Brewster angle observed, (see the following section “Bragg stack wave incidence from silicon”).

Bragg stack wave incidence from silicon

Removing the assumption that the plane waves impinge onto the Bragg stack from an ambient medium different to the constituent materials of the stack allows us to characterise

the stack more thoroughly. Transmission of the TE polarised wave due to the Brewster angle can be more clearly seen where the upper and lower bands touch. A Brewster angle exists for any boundary between two dielectric materials. As discussed previously omnidirectional reflectance [16-19] is obtained by limiting the internal propagation angles within a structure stack to values below the Brewster angle. This is achieved by Snell's law by introducing a third material which acts as the initial or reference medium with a lower refractive index than the stack materials.

A wave starting in this initial medium will experience a reduction in propagation angle upon entry into the first layer of the Bragg stack due to Snell's law. If the materials are selected correctly then the resultant angular propagating range can exclude the Brewster angle and therefore transmission due to the Brewster angle can never occur.

The TE and TM polarised wave transmission response for waves that start in silicon as a reference medium is shown in Figure 3.7. The transmission response has been plotted as a function of normalised frequency and incidence angle. The TM polarised wave has been plotted on the upper half of the figure while the lower half shows the TE polarisation. The angular range merely runs from -90 to +90 so that both TE and TM polarised waves can be shown on the same diagram.

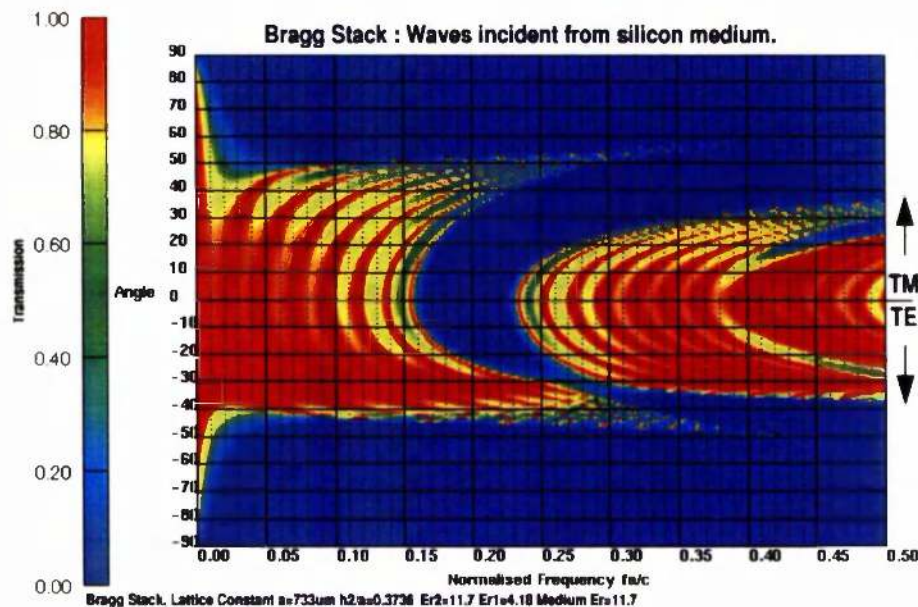


Figure 3.7 Bragg stack transmission response, waves start from silicon $\epsilon_{\text{initial}}=11.7$

The TE, (TM) transmission responses plotted on the upper, (lower) half of the diagram. The plot shows the transmission response plotted as a function of incidence angle and normalised frequency. NOTE: due to the rotational symmetry of a 1-dimensional Bragg stack the TE and TM polarisations are indistinguishable for normal incidence. The stack was made from two dielectric materials, $\epsilon_{r1}=4.18$ and $\epsilon_{r2}=11.7$, lattice constant $a=733\mu\text{m}$ with $t_2/a=0.3736$, total thickness $L=8a$.

Brewster Angle

The Brewster angle is defined in Equation 2.4 on page 26. For the situation shown in Figure 3.7 when the waves were initiated within a silicon medium $n_1 = \sqrt{11.7}$, $n_2 = \sqrt{4.18}$ giving a resultant Brewster angle of 30.8° . This can be clearly seen in Figure 3.7 on page 39 for the TE polarisation at the point where the two bands touch.

When the embedding material is changed such that $n_1 = \sqrt{4.18}$, $n_2 = \sqrt{11.7}$ then the Brewster angle changes to 59.1° . To provide verification and to further test the model capabilities, this scenario was also investigated and the results are shown in Figure 3.8. The increase in transmission can be clearly seen at the desired angle, again at the point where the TE bands touch.

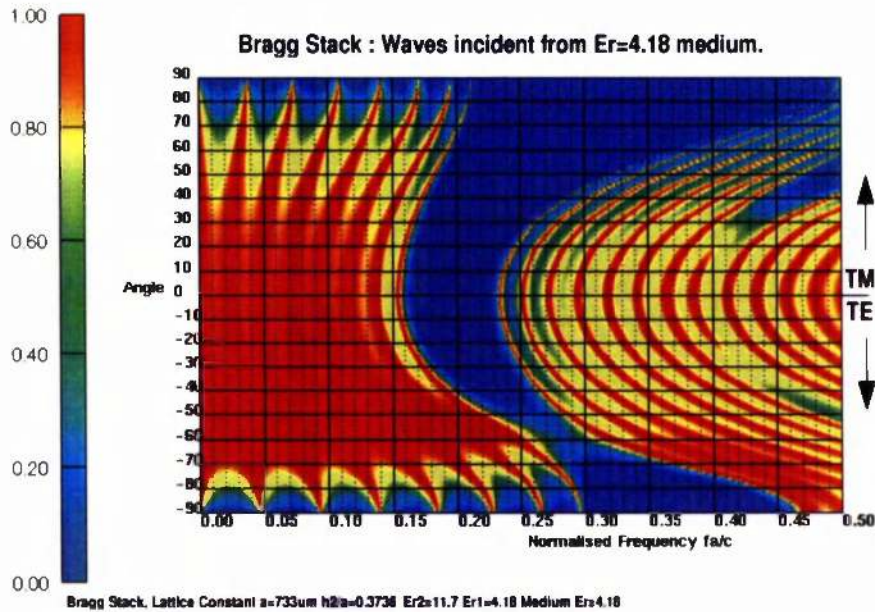


Figure 3.8 Bragg stack transmission response, waves start in $\epsilon_{\text{initial}}=4.18$

The TE, (TM) transmission responses plotted on the upper, (lower) half of the diagram. The plot shows the transmission response plotted as a function of incidence angle and normalised frequency. NOTE: due to the rotational symmetry of a 1-dimensional Bragg stack the TE and TM polarisations are indistinguishable for normal incidence. The stack was made from two dielectric materials, $\epsilon_{r1}=4.18$ and $\epsilon_{r2}=11.7$, lattice constant $a=733\mu\text{m}$ with $t_2/a=0.3736$, total thickness $L=8a$.

Discussion

When considering that the Bragg stack is illuminated from an air reference medium there is a sizeable photonic band gap with some 24% useable band width at 80GHz. Assuming that the waves are incident from air does not characterise all of the allowed directions that can propagate within the structure. For these initial Bragg stack calculations homogeneous

dielectric layers have been assumed with dielectric constants that have been derived from effective medium formulae (Equation 3.2 on page 33).

The Brewster angle exists for every simple dielectric layer boundary, and transmission through a 1-dimensional Bragg stack is therefore always possible. Therefore without limitation such a structure will never possess a complete photonic band gap for all internally and externally excitable directions. However a 1-dimensional Bragg stack calculation does not take into account the possibility of suppressed transmission due to the embedded 2-dimensional photonic crystal which also helps to negate the Brewster angle leakage. To verify this full 3-dimensional calculations are required and discussed in the next section; “3 dimensional verification” on page 41.

3.4: 3 dimensional verification

The 3-dimensional sandwich structure was analysed by plane waves at normal incidence onto the top of the structure, i.e. parallel to the surface normal of the stack. The results are shown in Figure 3.9 for either the TE or TM polarised waves for several crystal thicknesses. The inset is labelled transmission but is valid for either TE or TM polarised waves due to the three fold rotational symmetry of the structure.

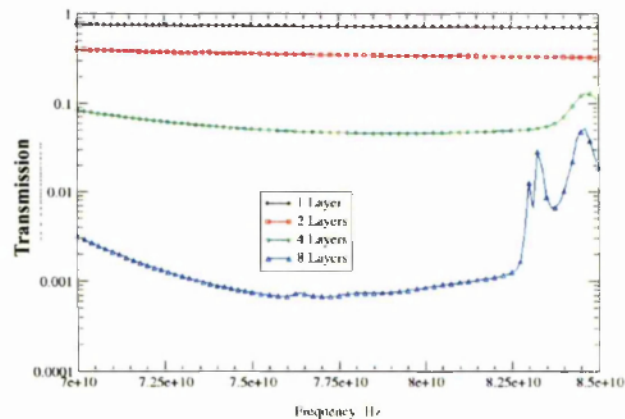


Figure 3.9 Normal incidence transmission response for the 3-dimensional structure.

TM or TE polarised wave transmission response for the full 3-dimensional dielectric sandwich structure made from silicon with a hexagonal pattern of holes removed in the perforated layer, hole size is $r/a=0.44$, $a=1500\mu\text{m}$. The Bragg stack has been optimised for 80GHz operation and the layer thickness $t_2/a=0.3736$ with $a=733\mu\text{m}$. TM and TE transmission responses are the same for normal incidence due to the three fold symmetry of the hexagonal lattice.

By comparing Figure 3.9 with Figure 3.10 on page 42, which shows the 1-dimensional effective index model response for the same incidence, (normal incidence onto the top of the stack), the differences between the full 3-dimensional model and the 1-dimensional

Bragg stack model can be seen. At this stage it is noteworthy that both the 1-dimensional and 3-dimensional model show significant, but different attenuation, for similar thicknesses of crystal due to Bragg reflection.

Consequently the assumption concerning the effective dielectric constant of the perforated layer used within the 1-dimensional model is inappropriate. The choice of dielectric constant in the 1-dimensional model results in a decrease in the transmitted level when compared to the 3-dimensional model results for normal incidence. This indicates that the effective dielectric constant calculated for the perforated layer is too small in value and an increase in this value decreases the dielectric contrast within the stack and weakens the Bragg stack effect increasing transmission.

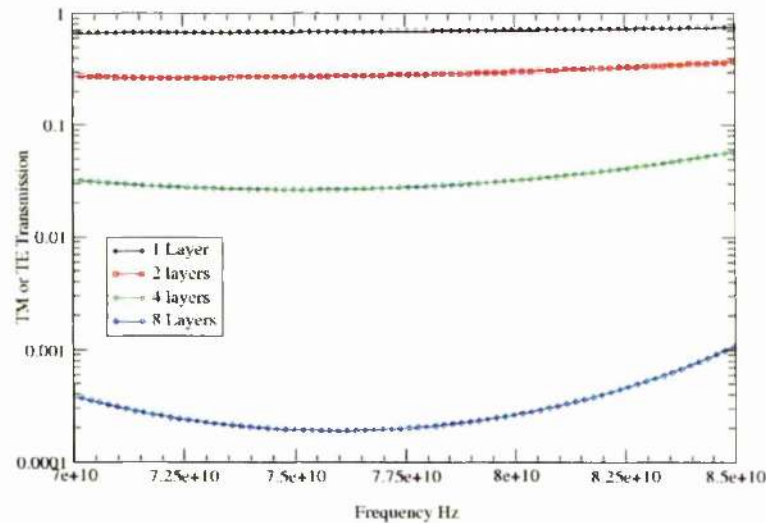


Figure 3.10 Normal incidence response for a 1-dimensional Bragg stack

Stack parameters, $\epsilon_1=11.7$, $\epsilon_2=4.18$, thickness $t_2/a=0.3736$ where $a=733\mu\text{m}$. As the transmission analysis has been performed at normal incidence the TE and TM transmission response curves are identical.

3.5: Normal incidence into the side of the crystal

The crystal was re-orientated so that normal incidence relates to waves that impinge onto the side of the crystal such that the waves propagate parallel to the layers, i.e. parallel to the periodic plane of the hexagonal perforated layer. The TE and TM transmission results are shown in Figure 3.11 for a finite thickness crystal $L=8a'$ where $a' = 8\sqrt{3}a$.

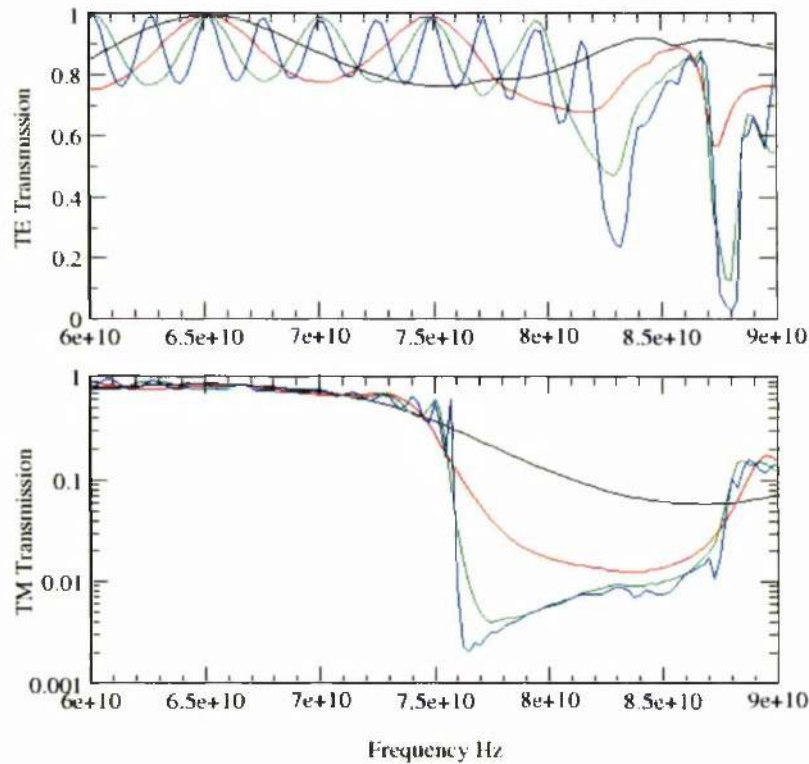


Figure 3.11 TE and TM response for side incidence into the sandwich structure.

Structure: Full 3-dimensional dielectric sandwich structure made from silicon with a hexagonal pattern of holes removed in the perforated layer, hole size is $r/a=0.44$, $a=1500\mu\text{m}$. The Bragg stack has been optimised for 80GHz operation and the layer thickness $t_2/a=0.3736$ with $a=733\mu\text{m}$, and the total crystal thickness $L=8a'$ where $a'=8\sqrt{3}a$

In contrast to the results for the “Simple hexagonal lattice of air holes in silicon” on page 34 the transmission results for the full 3-dimensional calculation are quite different. For normal end fire incidence onto the side of the structure the TM polarisation shows photonic band gap behaviour due to the periodic hexagonal pattern of holes $r/a=0.44$ that have been introduced into one of the layers that form the stack. Furthermore the width of the photonic band gap for the TM polarisation is quite wide, ranging from 76GHz to 88GHz, a width of 12GHz.

Conversely the TE polarisation has a normal transmission response that is remarkably poor in comparison when compared with its 2-dimensional counterpart (Figure 3.4 on

page 35). There appear to be two regions where possible band gaps are opening, both of which are narrow band, 82-84GHz and 87-89GHz. The TE and TM responses for the sandwich structure are almost the reverse of what was expected, in that the expected results were a wide band response for TE polarised waves and a narrower band for TM polarised waves. It turns out that these two gaps are independent and further investigation of their response was carried out by scanning the angle within the periodic plane of the hexagonal lattice; the results are presented within the next section.

Angular analysis within the periodic hexagonal plane of the dielectric sandwich structure

The transmission response for the structure was studied with waves incident onto the side of the structure and scanned parallel to the hexagonal lattice. The response is shown in Figure 3.12.

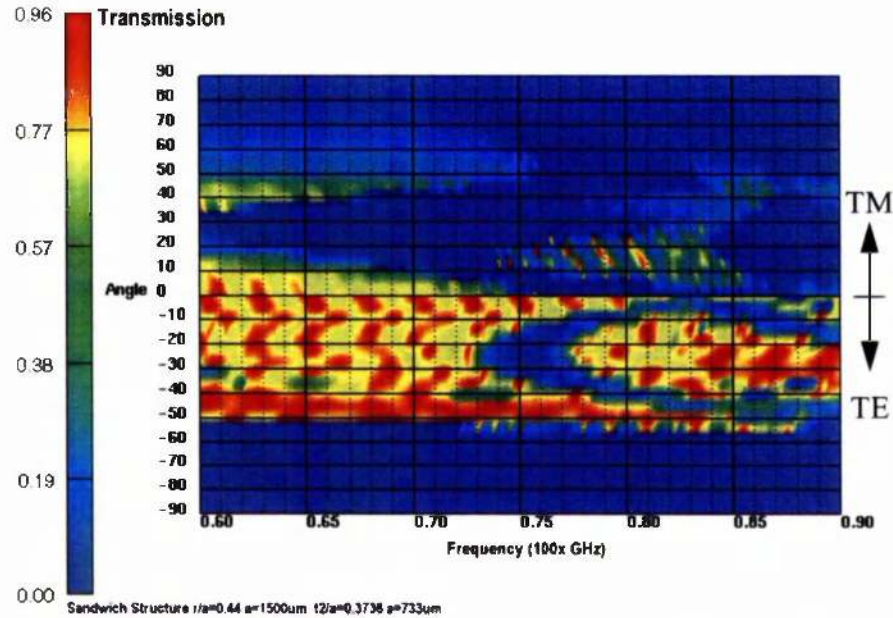


Figure 3.12 Angular transmission analysis for side incidence.

Structure: Full 3-dimensional dielectric sandwich structure made from silicon with a hexagonal pattern of holes in the perforated layer, hole size is $r/a=0.44$, $a=1500\mu\text{m}$. The Bragg stack has been optimised for 80GHz operation and the layer thickness $t_2/a=0.3736$ with $a=733\mu\text{m}$, and the total crystal thickness $L=8a'$ where $a'=8\sqrt{3}a$. The transmitted level is shown as a function of incidence angle against normalised frequency with $0-90^\circ$ relating to TM polarised waves where $-90-0^\circ$ relates to TE polarised waves.

Both the TM and TE polarisations show that there is no complete photonic band gap for the operational design frequency of 80GHz. The pattern of the bands is reassuring when compared to Figure 3.4 on page 35 as it had been noted in the previous section that the polarisation response had been substantially different to that expected, see “Normal incidence into the side of the crystal” on page 43.

When comparing Figure 3.12 with Figure 3.4 on page 35 and taking note of the differing x -axis frequency scales, both the TM and TE polarisation band gaps have closed. For both polarisations the upper and lower band edges of the gap shown in Figure 3.4 have moved towards each other, closing the photonic band gaps and negating the intended effect of substrate mode suppression.

3.6: Conclusion: Dielectric sandwich with solid interspatial layer

The transmission analysis has shown that there is no complete band gap for either TE or TM polarised waves which propagate parallel to layer interfaces. The solid layer between and in conjunction with the perforated layers is providing a medium for the waves to travel through. As there is always transmission through a Bragg stack for TE polarised waves due to the Brewster angle, assuming that these directions can be excited, it is not surprising that the sandwich structure with the solid interspatial layer does not possess a full photonic band gap. Higher index materials may provide a possible solution to this problem as the Brewster angle could be forced to larger angle values. This would ensure that any transmission into a perforated layer due to the Brewster angle would then be killed by the photonic band gap effect within the layer. Utilisation of different shaped scatterers has already been investigated by Baba [22] and while found to alter the in-plane response the sensitivity of the response has been clearly shown to be dependent on the lattice adopted rather than the scatter shape.

The results also indicate that there is insufficient symmetry within the structure to open a full photonic band gap. This suggests that the solid interspatial layer should be removed and perforations are required in all layers in conjunction with adjacent layer shifting to form face centred cubic, f.c.c., and face centred tetragonal, f.c.t., lattice variants which can display full photonic band gap behaviour.

Introduction

In the previous chapter, “Photonic Crystal Sandwich” on page 31 a photonic crystal was made from a single material by sandwiching a 2-dimensional slab of photonic crystal between sheets of solid dielectric material. The structure was then repetitively stacked to form a Bragg stack. The photonic crystal served two purposes: firstly to aid in the formation of the Bragg stack as the crystal layer has a lower refractive index than the bulk material due to the periodic hole pattern; and secondly it was hoped that the photonic crystal would suppress any laterally allowed substrate modes that otherwise propagate within a stack. However while parameters were carefully chosen to optimise structure performance the suppression of the substrate modes did not occur.

The structure patented by ESTEC¹ extends this train of thought by utilising two materials for the Bragg stack and extends the lattice of holes straight through the structure facilitating fabrication, see Figure 4.1 on page 48. In this chapter the analysis characterises the transmittance of such a PBG material which consists of periodic air cylinders arranged in a square or hexagonal lattice which have been drilled through a repeating stack of two periodically alternating and differing materials.

1. European Space Research and Technology Centre, ESTEC, located in Noordwijk, The Netherlands.

4.1: Scope

There are many permutations of parameters that define the structure; the type of the lattice that can be drilled through the stack, the size of the drilled features, and the ratio of materials that form the periodic stack itself. Analysis could be extended to other shapes etched through the stack, such as bars or triangles, which have been shown by Baba to alter the response of the photonic band gap performance within the periodic plane [22].

As the structure is constructed by stacking alternating sheets of materials, the thickness of each individual layer could also be adjusted in an attempt to obtain ultra wide band performance. If the feature sizes in each layer pair were also altered then this technique would not be dissimilar to that suggested by Agi [23] who stacked different PBG crystals. However, this type of construction would detract from the simplicity of the structure.

An antenna placed on the surface of the crystal will undoubtedly interact with the substrate and incorrect design may cause coupling and excitation to either or both substrate and surface modes. The inclusion of the correct size of holes and lattice type should ensure that substrate modes are suppressed.

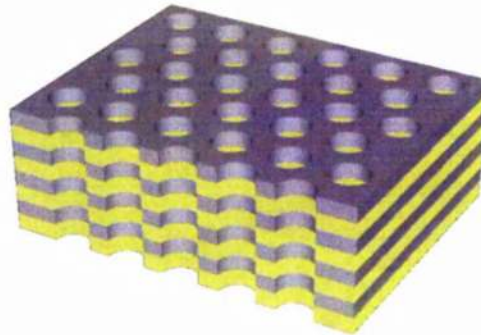


Figure 4.1 Patent Structure: Bragg Stack with a hexagonal lattice of air cylinders.

Picture courtesy of Peter De Maagt, ESTEC

Slab Waveguides

Simplistically guided mode propagation in a homogeneous slab of material is governed by the critical angle between the slab material and any boundary material. Waves propagating at angles above the critical angle are reflected at the dielectric boundary and guided along the layer by total internal reflection, T.I.R. The materials used in the analysis of the structure are silicon and kapton, $\epsilon_{\text{silicon}}=11.7$ and $\epsilon_{\text{kapton}}=3.4$.

From Snell's law, Equation 2.3 on page 23, the critical angle for T.I.R. between silicon and kapton is 34.2° , between kapton and air is 31.3° , and between silicon and air is 17.0° . A wave initiated within the stack will therefore only pass from one layer to another if these incidence angles are not exceeded. These T.I.R. substrate modes can be killed by employing a 2-dimensional lattice of dielectric holes in each layer. The photonic crystal should therefore still operate at that the largest T.I.R. out of plane propagation angle, for any relevant material boundary combination, the silicon kapton boundary in this instance. The choice of lattice pattern, feature size and constituent materials directly influence the performance of the structure.

The angles which will give rise to total internal reflection are known for any arbitrary choice of materials. Consequently the 2-dimensional PBG crystal should work over these out of plane propagation angles. The 2-dimensional PBG response degrades as the out of plane component grows. Brewster angles for different material boundaries can also be calculated providing useful information to aid in the design of the crystal. Utilising Snell's law, Equation 2.3 on page 23, the path of any incident plane wave can be traced through the structure, such issues have already been addressed in many standard optics textbooks and thin film work [12-15].

It has already been shown that e.m. waves concentrate the majority of their power in high dielectric constant regions [8]. Within the silicon / kapton stack the higher dielectric constant material is silicon and the consequent analysis considers a square and hexagonal lattice of air holes introduced into the structure. Drilling a pattern of holes through the stack reduces the effective dielectric constant, shifts the central frequency and alters the angular response of the structure.

Objective

The objective is to design a photonic crystal with a complete PBG by drilling air cylinders through an optimised Bragg stack made from silicon and kapton. The air cylinders should be arranged in a lattice configuration that displays complete PBG behaviour within the periodic plane i.e. circular cross sectional plane of the cylinders, but without excessively compromising the performance of the Bragg stack. The PBG should continue to operate for the range of out of plane angles resulting from T.I.R. within the structure as discussed previously.

Initially the transmittance is studied for an incident plane wave onto the top of the structure, i.e. parallel with the surface normal of the Bragg stack, see Figure 4.3 overleaf. Thereafter the response is studied for a wave incident parallel to the periodic plane of the air cylinders i.e. perpendicular to the stacking axis of the Bragg stack. The Bragg stack that has been modelled is made from silicon and kapton and has been optimised for omni-directional reflectance, see “Silicon and Kapton Bragg Stack” on page 19.

4.2: Filling Ratio Evolution

For both the square and hexagonal lattices the amount of material that will be removed from the stack will directly influence the response. For an increasing hole radius to lattice spacing ratio r/a , the hexagonal lattice unit cell has progressively more material removed than for the square lattice. Equation 4.1 and Equation 4.2 express the filling ratios for the hexagonal and square lattices. Both equations are valid so long as the ratio of the radius of the cylinders, r , to the lattice spacing, a , does not exceed $r/a < 0.5$.

$$\text{Hexagonal Lattice Filling Ratio } FR = \frac{2\pi}{\sqrt{3}} \left(\frac{r}{a}\right)^2 \quad (4.1)$$

$$\text{Square Lattice Filling Ratio } FR = \pi \left(\frac{r}{a}\right)^2 \quad (4.2)$$

The evolution curve for the filling ratio as a function of radius size is shown in Figure 4.2

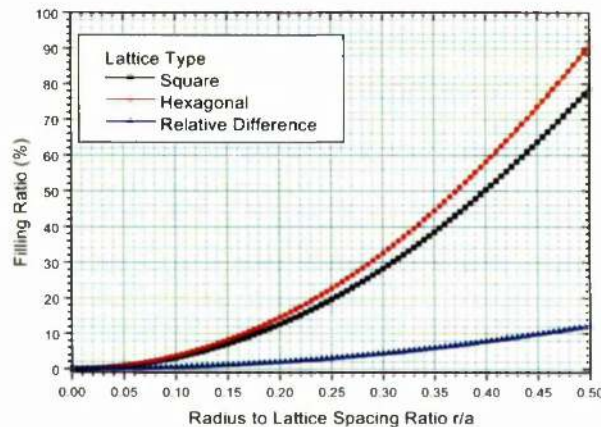


Figure 4.2 Filling Ratio Evolution for the square and hexagonal lattices

The filling ratio plotted as a function of the radius to lattice spacing ratio r/a for generic square and hexagonal lattice types. The relative difference between the two lattice type curves is also shown.

For low filling ratios the square and hexagonal response curves are similar but as the feature size increases the difference between the curves becomes progressively more apparent. These trends are reflected directly in the comparative transmission response curves of Figure 4.3.

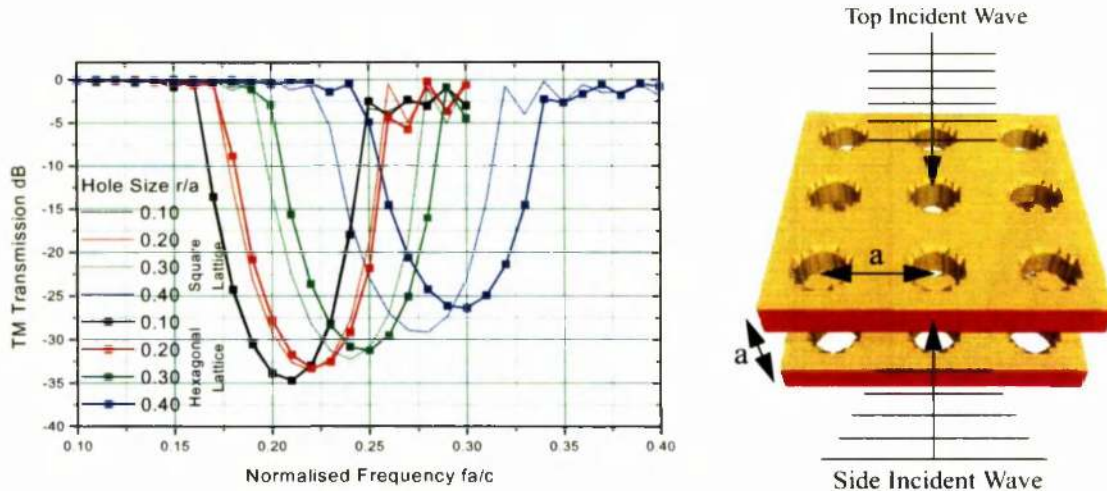


Figure 4.3 Comparative TM transmission for the square and hexagonal lattice drilled through a Bragg Stack.

Left: The solid (dashed) lines represent the transmission for a normal incidence plane wave onto the top of the Bragg stack with a hexagonal (square) pattern of air cylinders drilled through the stack. The transmission performance for the hexagonal pattern degrades faster than for the square lattice as for the same radius size more volume per unit cell is removed. *Right:* Schematic of the stack with a square lattice of air cylinders showing plane waves incident from the top and side onto the stack. Material between the layers has been removed to aid visualisation.

When a normally incident plane wave illuminates the structure, the introduction of a square or hexagonal lattice of air cylinders shifts and degrades the first order band gap of the structure. The dashed, (solid) lines in Figure 4.3 show the TM or TE transmission response for various sizes of air cylinders in a square (hexagonal) lattice drilled through the stack. For normal incidence the TE and TM polarisations are indistinguishable due to the four-fold symmetry of the structure. However away from normal incidence the two polarisations behave differently.

As the air cylinder size increases the transmitted level through the structure increases and the central band frequency increases, a sign that the effective index of the stack is reducing. This is expected behaviour as both constituent materials of the stack have larger dielectric constants than that of air, and the extraction of material to form the lattice of cylinders will reduce the effective index of the stack.

4.3: Square lattice of drilled holes

Normal end-fire incidence in the periodic square lattice plane

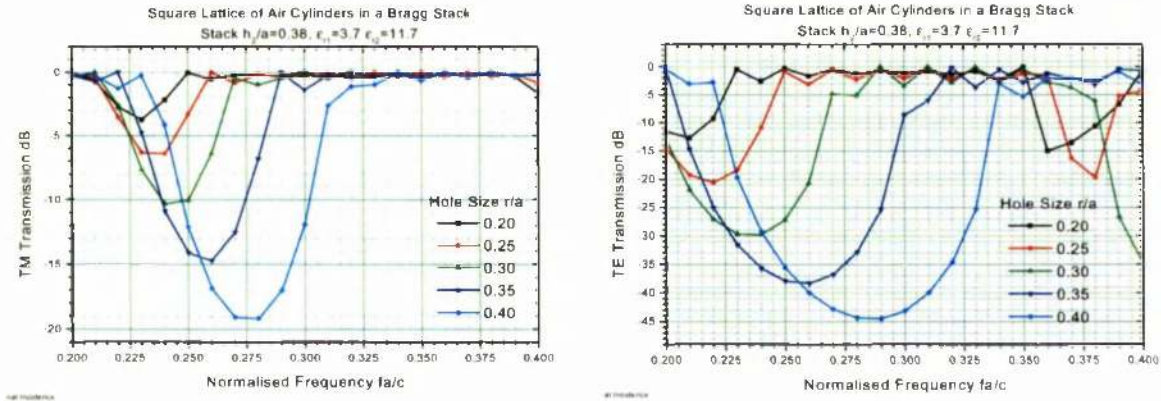


Figure 4.4 Transmission Response for normally incident plane wave on the side of structure.

The transmission response in dB, for TM (TE) polarised waves shown on the left (right) as a function of the radius size of the square lattice of cylinders that has been drilled through the periodic stack. The response shown is for eight periods of cylinders.

Before any cylinders are introduced into the structure a wave incident onto the side of the stack encounters a stratified medium with no periodicity in the propagation plane. The stratification is transverse to the direction to propagation and given the choice of materials acts as a stacked set of slab waveguides. Consequently both TE and TM polarised waves are transmitted through the structure.

Once cylinders are drilled into the structure and the radius size is gradually increased, band gap regions develop as periodic scatterers have now been introduced into the system. Figure 4.4 shows that for an increasing size of cylinder both the attenuation in the band gap region as well as the central band gap frequency increase. The information shown in Figure 4.4 is for one direction only, recall that the gap has a strong angular dependence, see “Angular effective medium transmission response: waves incident from air” on page 56.

Complete band gap in a square lattice of air holes in dielectric

To evaluate the presence of a complete band gap for either polarisation a full angular analysis must be made. By calculating the maximum allowed transmission for a range of frequencies for any angle and also scanning the filling ratio, a photonic band gap map is created. The gap maps for a square lattice of air holes in silicon, $\epsilon_r=11.4$, are shown for TE and TM polarised waves in Figure 4.5. By locating regions in the gap map of near zero transmission for both polarisations, any regions that overlap define complete photonic band

gaps. For the square lattice of cylindrical holes in bulk silicon it is not until the radius size is some 0.45 of the lattice constant that a small complete TE and TM band gap opens.

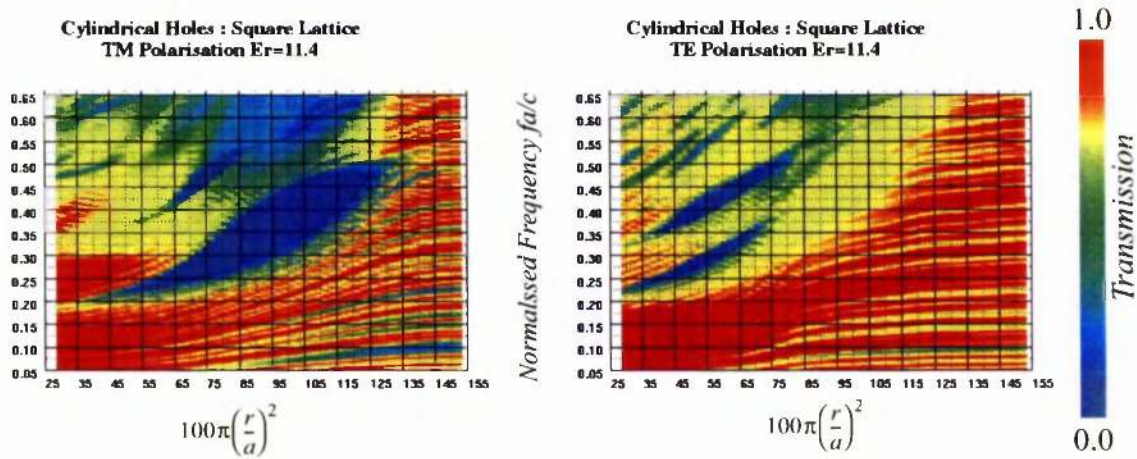


Figure 4.5 Gap maps for a square lattice of air holes in silicon.

The maximum transmission response for TM (left) and TE (right) polarised waves for a full angular in plane scan plotted as a function of filling ratio and normalised frequency. Note: when $r=a/2$ neighbouring cylinders begin to touch and when $r = a/(\sqrt{2})$ the cell cylinders completely fill the unit cell.

The drilled Bragg stack consists of a stack of two different materials with an effective index smaller than that of a similar lattice in bulk silicon. Therefore while a similar cylinder radius to lattice constant ratio, r/a , may also open a full gap in the drilled Bragg stack structure the normalised operational frequency will be different due to the scaling properties of Maxwell's equations for bulk media.

If the structure were to be used in conjunction with an antenna then the embedding host medium could be considered to be air as only the radiative modes couple to and from air. Following the arguments presented for the omni directional reflecting Bragg stacks, there is a very evident performance difference between the response of the structure from air relating to the radiative coupling modes, and the modes that can be excited internally within the stack.

This is of substantial significance to the analysis concerning the response of the structure within the periodic plane of the cylinders. If the analysis is limited to the modes which can radiate, it is easier to match the band gap response to that of the substrate modes within the stack. Conversely considering all allowed substrate modes, not just the radiative coupling modes, makes the gap matching task more elusive.

4.4: Estimation of the effective dielectric constant

From the calculations shown in Figure 4.3 and Figure 4.4 an air hole radius to lattice spacing ratio $r/a=0.40$ is chosen. This value is a compromise between the opposing trends in transmission response. As the air hole cylinder size increases the Bragg stack response degrades, Figure 4.3, while enhancing the periodic plane response. At a radius / lattice spacing constant $r/a=0.40$, the band gap response for normally incident TE and TM polarised plane waves incident on to the top and side of the structure is relatively well matched in normalised frequency. Normal incidence onto the top of the stack at this radius size results in a TE/TM gap with maximum attenuation of -30dB for a gap ranging in normalised frequency from 0.225-0.325. Incidence within the periodic plane of cylinders has a TM gap, -20db, $fa/c=0.225-0.310$, and a TE gap, -45db, $fa/c=0.225-0.335$.

To estimate the effective dielectric constant for the structure, analysis of a square lattice of air holes in a 2-dimensional photonic crystal was carried out for a range of dielectric materials. To attain an estimation, the upper and lower band edges for the 3-dimensional square lattice structure are matched with the corresponding band edges for the 2-dimensional square lattice transmission response curves shown in Figure 4.6. The TE and TM polarisation transmission responses for a square lattice of air cylinders in dielectric radius $r/a=0.40$ for a range of dielectric materials are shown in Figure 4.6.

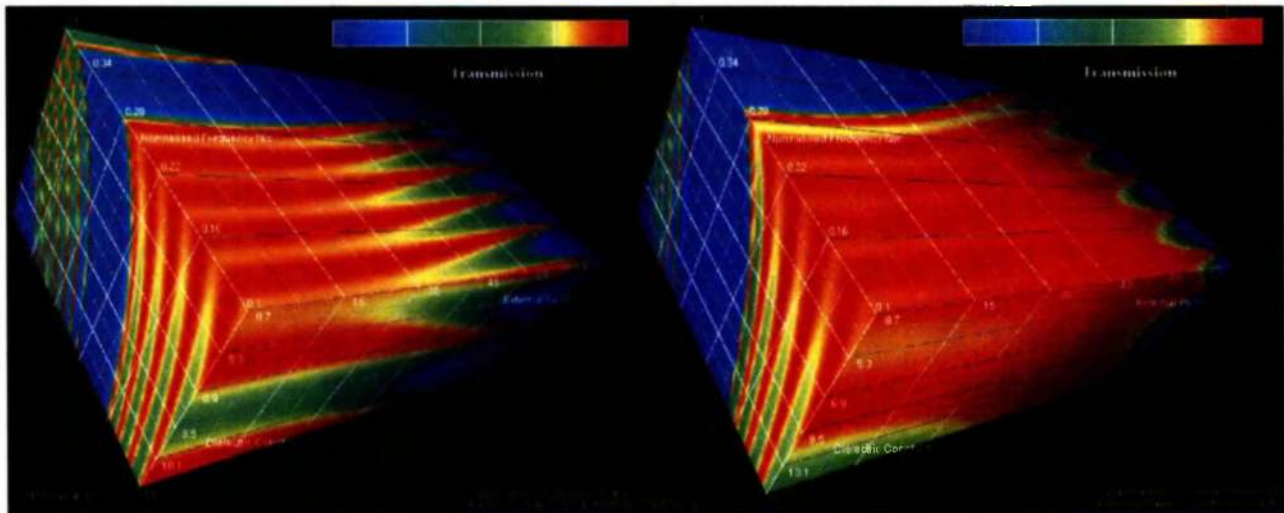


Figure 4.6 Evolution of the Square Lattice with Dielectric Constant

The TM (TE) Polarisation transmission response shown on the left (right) for a square lattice of air cylinders $r/a=0.40$ in a varying dielectric medium. The plots show the response as a function of incidence angle for a plane wave starting in an air medium.

Matching the response curves for the square lattice $r/a=0.40$ patent structure curves suggests an effective dielectric constant for the stack of $\epsilon_{\text{effective}}=5.6$. The curves relating to

the $r/a=0.40$ from Figure 4.4 on page 52 for 3-dimensional analysis can be compared with Figure 4.7.

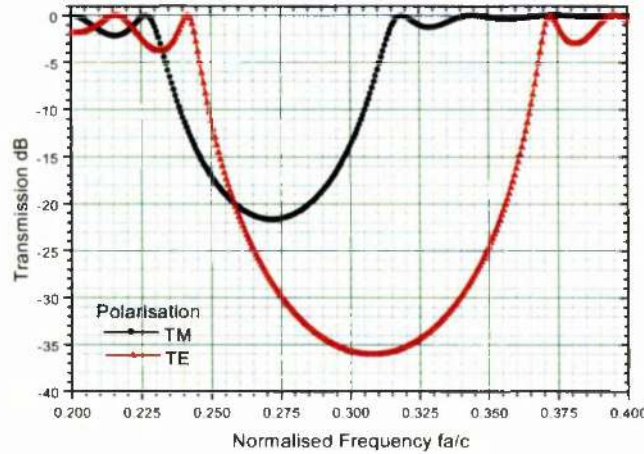


Figure 4.7 Normal in-plane incidence response for a 2-dimensional square lattice

The TM and TE transmission responses for normal incidence onto a square lattice or air holes using an 'effective medium' dielectric constant of 5.6. The air holes were chosen to have a radius to lattice spacing ratio $r/a=0.45$, $L=8a$.

The effective medium is in relatively good agreement with the transmission analysis carried out at normal incidence in the periodic square lattice plane. The TM polarised wave has both the upper and lower band edges and a comparable profile to the 3-dimensional structure calculation. The TE polarised wave has a similar band width but has up-shifted in normalised frequency and does not have such a strong attenuation profile in the band gap for the effective medium calculation. This is indicative of under estimation in the value of the effective dielectric constant. The angular performance of the effective medium is shown in Figure 4.8.

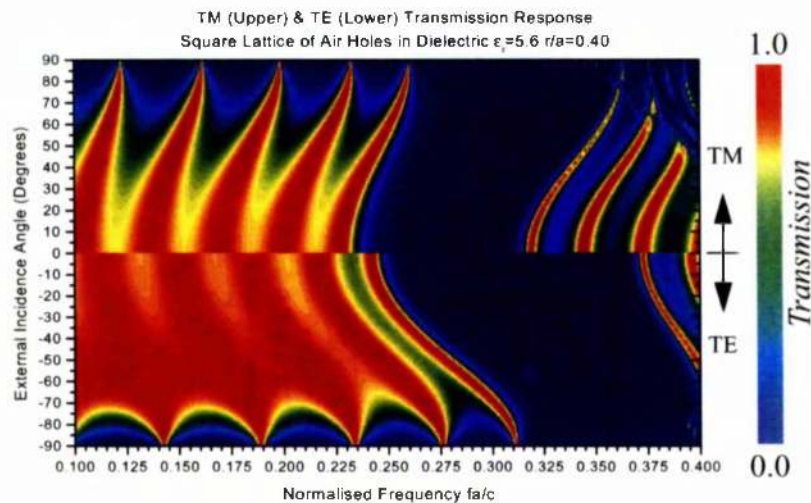
Angular effective medium transmission response: waves incident from air

Figure 4.8 Effective medium square lattice transmission response: waves incident from air.

The TM (Upper) and TE (Lower) transmission response for a square lattice of cylindrical air holes in dielectric $\epsilon_r=5.6$ for plane waves incident within the periodic plane onto the structure from an air medium. The radius of the cylinders is related to the lattice constant a , such that $r/a=0.40$.

From the effective medium angular characterisation plot, Figure 4.8, there is a very small range of normalised frequencies where there is near zero transmission for both TE and TM polarised waves. This small gap will most likely close when the internally excitable modes that are otherwise evanescent in air i.e. non radiating, are taken into account, such that there will be no full photonic band gap within the periodic square lattice plane of this structure.

The structure is further examined by removing the assumption that the response is limited to the k -space excitable from air. By limiting the excitation range to angles excitable from air, not all allowed propagation directions within the crystal are examined. This exclusion is significant for any radiating source located on, internally or within close proximity to the photonic crystal. Examination of these ‘internal’ modes of the crystal are discussed in the next section.

Angular effective medium transmission response: non radiative modes included

The internal response for the same crystal displays different behaviour as the angular boundary imposed by the air ambient medium is removed. The new response curves encompass the same information as that shown in Figure 4.8 on page 56 but assume that the plane waves are launched from within bulk silicon, removing the k -space limitation. This

issue has already been discussed in detail, See “Allowed propagation state restrictions due to Snell’s law” on page 23.

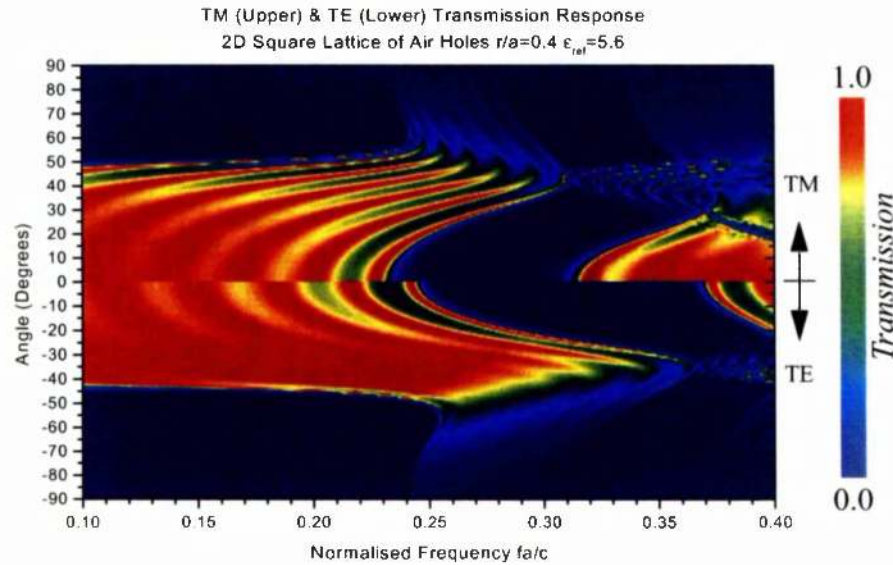


Figure 4.9 Internal TE & TM Transmission Response; Square Lattice

The TM (Upper) and TE (Lower) transmission response for a square lattice of cylindrical air holes in dielectric $\epsilon_r=5.6$ for plane waves incident onto the structure from a bulk reference medium $\epsilon_r=5.6$. The radius of the cylinders is related to the lattice constant a , such that $r/a=0.40$. There is not a complete photonic band gap for either polarisation.

Comparing the responses for the effective medium systems between Figure 4.8 on page 56 and Figure 4.9, the latter shows no overlapping region that encompasses every angle for a single frequency where either polarisation or more importantly both polarisations show near zero transmission. This means that there is no complete ‘internal’ band gap available for the structure for these choice of materials as other analysis has also confirmed [8].

Effective Medium Overview

The photonic band gap regions of the ‘effective’ structure have strong directional dependence, and the goal of aligning the in-plane 2-dimensional response with the Bragg stack must not be forgotten. The value of $r/a=0.40$ was chosen in an attempt to obtain optimal performance for the 2-dimensional photonic crystal. Examining the response curves shown in Figure 4.4 on page 52 shows that both the TE and TM polarisations share a lower band edge normalised frequency of $fa/c=0.225$. This is slightly higher than required to match the mid gap Bragg stack response that is shown in Figure 2.3 on page 21. By reducing the air hole size in the lattice the band gap will reduce in frequency, helping to

align the systems responses. Therefore a radius to lattice spacing ratio of $r/a=0.30$ was chosen to help align the 2-dimensional crystal transmission response with that of the stack.

4.5: 3-dimensional characterisation of the structure with a square lattice

The transmission performance for the structure with a square lattice of air holes drilled through it was characterised for the full range of angles aided by the symmetric properties of the structure. A full forward hemispherical sweep of angles onto the top of the structure can be reduced to a sweep of one quadrant of the hemisphere due to the discrete rotational symmetry of the structure. Successive rotation of the incident plane wave in 90° steps results in the same performance, see “Bragg Stack Rotational Symmetry” on page 28 for a brief discussion on symmetry issues.

Following the discussions and conclusions in the “Effective Medium Overview” on page 57 the stack’s transmittance was analysed as a function of angle for a single frequency. The holes were drilled in a square lattice formation, $r/a=0.30$, though the stack and analysis was carried out at a normalised frequency of $fa/c=0.25$. These figures were chosen as a direct result of the previous 3-dimensional analysis for incidence onto the top of the structure, see Figure 4.3 on page 51 and in an attempt to match the best performance for the in-plane response for TM and TE polarised waves, see Figure 4.4 on page 52.

The structure was examined twice with differing assumptions concerning the medium from which the plane waves are launched. Firstly the transmission response is shown for waves launched from air and then from silicon. Incidence is controlled by the k-vector, angular scans have been carried out from normal incidence $(k_x, k_y)=(0,0)$, to oblique incidence for the two reference mediums, $(k_x, k_y)=(0.5,0.5)$ for air, and $(k_x, k_y)=(1.7,1.7)$ for silicon. Normalisation issues related to the k-vector are presented in Appendix A on page 175.

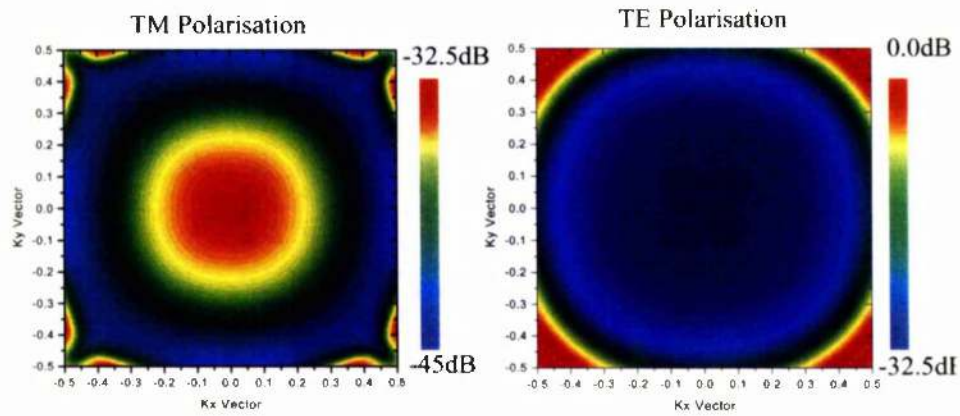
Incidence from air

Figure 4.10 Transmission response for plane waves launched from air.

TM (TE) polarised wave transmission response shown on the left (right) for waves incident onto the top of the structure assuming that the waves are launched from an air medium. The structure consists of the optimised bragg stack, $h_y/a=0.38$, made from silicon and kapton, $\epsilon_{\text{silicon}}=11.7$, $\epsilon_{\text{kapton}}=3.4$, with a square lattice of air holes drilled through the structure with a radius to lattice spacing ratio $r/a=0.30$ for a normalised frequency of $fa/c=0.25$.

Figure 4.10 shows the TM and TE polarised wave transmission response for incidence onto the forward hemisphere of the drilled structure. The two-fold symmetry along the $k_x=0$ and $k_y=0$ lines is immediately apparent. The trends in transmission as the incidence moves from normal incidence to increasingly oblique incidence are in agreement with those found in “Full angular transmittance characterisation of the Bragg Stack” on page 28. For the TM polarised wave, the transmission is at a maximum at normal incidence and decreases as the incidence becomes increasingly oblique; however at $|k_x (k_y)|=(0.3)$ when $|k_y (k_x)|=\pm 0.5$ then there is an increase in transmitted level. For the TM polarisation this increase does not negate the full angular band gap. In contrast the TE polarised wave has a transmission minimum at normal incidence and increases as the incidence angle becomes more oblique. However for the same values of k -vector, $|k_x (k_y)|=(0.3)$ when $|k_y (k_x)|=\pm 0.5$, there is a marked increase in transmitted level through the structure such that the structure completely transmits.

If the waves are launched from a silicon bulk medium then the performance of the structure will degrade further such that both polarisations will result in full transmission. This is exactly what occurs in Figure 4.11

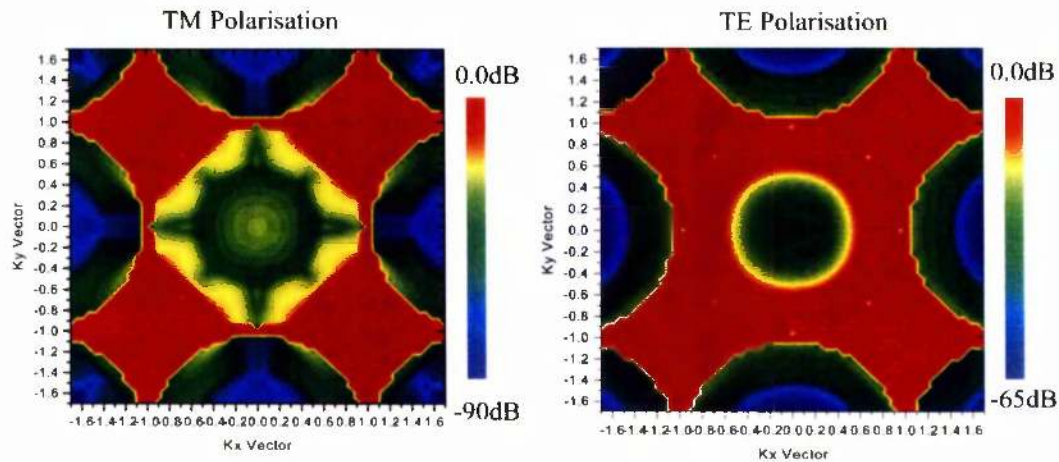


Figure 4.11 Transmission response for plane waves launched from silicon.

TM (TE) polarised wave transmission response shown on the left (right) for waves incident onto the top of the structure 8 periods thick with the assumption that the waves are launched from silicon. The structure consists of the optimised Bragg stack, $h_2/a=0.38$, made from silicon and kapton, $\epsilon_{\text{silicon}}=11.7$, $\epsilon_{\text{kapton}}=3.4$, with a square lattice of air holes drilled through the structure with a radius to lattice spacing ratio $r/a=0.30$ for a normalised frequency of $fa/c=0.25$.

Conclusion

The results show that for a normalised operational frequency of $fa/c=0.25$ for a square lattice of air cylinders $r/a=0.30$ drilled through an optimised Bragg stack there is not omnidirectional reflectance from the structure. Transmission through the structure is possible for a small range of incidence control vectors when the waves are launched from air onto the structure. When the plane waves are assumed to start from a silicon reference medium there is a larger set of angles for which the structure transmits.

Once holes are drilled through the Bragg stack the transmittance through the structure increases dramatically for certain angles for the TE polarisation. For the sizes of air cylinders examined there is not a value where a full, complete photonic band gap exists both internally and externally to the stack at the same normalised frequency. This finding is in agreement with other work done on ‘homogeneous’, i.e. non stratified 2-dimensional-photonic band gap lattices where no complete PBG was found.

The overall aims between this chapter and the chapter “Photonic Crystal Sandwich” on page 31 are the same, to produce a photonic crystal with a complete band gap for both

polarisations. The difference between the chapters concerns the 2-dimensional lattice that has been introduced into the structure, hexagonal and square lattices of holes. It has now been shown that for the materials, feature sizes and investigative frequencies studied that the introduction of either a square or hexagonal lattice into effectively or properly stratified media does not open a complete photonic band gap. These systems can be classified as 2+1 systems where the numbers are representative of the combination of structure symmetry. Such 2+1 systems may well be suited to applications that do not require a complete 3-dimensional band gap such as planar waveguide structures where the +1 confinement could be used to help suppress leakage in the third dimension.

In the next chapter the interleaving of 2-dimensional photonic crystals is presented which form true 3-dimensional structures known generically as the “logpile” or “woodpile” structure which do possess a complete 3-dimensional photonic band gap [24].

*Interleaved 2D lattices creating
fully 3D Photonic Crystals*

Overview

A 2-dimensional lattice consists of an inhomogeneous dielectric medium which has periodic variations of permittivity along two linear directions, and is uniform in the third dimension. This chapter considers a class of 3-dimensional photonic band gap materials formed by the interleaving of a pair of 2-dimensional lattices whose uniform directions are mutually orthogonal, the so-called ‘woodpile’ geometry. It is shown by numerical calculations that the strong polarisation discrimination exhibited by the constituent 2-dimensional sub-lattices in their respective stop-bands leads to a completely 3-dimensional photonic band gap crystal in all polarisations when the two sub-lattices are interleaved. For a general class of such synthetic crystals, having arbitrary 2-dimensional distributions in the sub-lattices, many properties of the 3-dimensional interleaved crystal can be predicted directly from a knowledge of the properties of the sub-lattices, thereby radically reducing the computational cost of their determination.

5.1: Introduction

Three dimensional periodic structures, known as photonic crystals, have generated substantial interest in various fields. Within the microwave and sub-millimetre regime, where fabrication is much simpler than in the optical regime, several 3-dimensional structures have been suggested [25,26]. The periodicity in 3-dimensions of these structures leads to the possibility of complete Bragg reflection in all propagation directions which can actually be attained in a number of known structures, generally of quite high contrast in dielectric constant between dielectric and air regions in the unit cell of the crystal. The requirement for a complete bandgap in all propagation directions and all polarisations is a very strong condition, and cannot be met in all structures with 3-dimensional periodicity; only those with a high dielectric contrast and whose unit cell belongs to restricted symmetry classes will exhibit the phenomenon.

Millimetre-wave applications utilising photonic crystals as substrates for planar microwave circuits and antennas demand complete band rejection over all angles, as well as over a range of frequencies. It is generally part of the design process that the bandgap performance must be predicted in advance before fabrication, which requires numerical modelling of the electromagnetic problem of the wave propagation within the interior of the crystal. Ideally the model should also incorporate the antenna as the performance of both sub systems is not mutually exclusive but this problem is yet to be properly tackled and will provide challenging future research. The numerical modelling of the 3-dimensional crystal is itself a complex and computationally demanding task requiring substantial amounts of time. Unfortunately, there are at present no simple ways of predicting the stop-band frequency range, and it is difficult to gain the physical insight necessary which might provide such simple design methods.

A widely-studied class of PBG crystals for microwave applications is the so-called 'woodpile' geometry consisting of stacked layers of identical parallel dielectric rods with rectangular cross section, with a quarter-turn rotation between successive layers in the stack, and (optionally) a half-period spatial translation between every second layer. These are of interest because they are relatively easy to fabricate, even up to the millimetre-wave and recently infra-red ranges using wet-etch micro-machining of silicon wafers and other

deposition and etch techniques. Using this technology, PBG woodpile crystals have been demonstrated with stop bands up to 25 THz centre frequency [27,28].

Although the stop bands of woodpile geometry crystals are both experimentally and theoretically proven, there are many possible variants in the possible dimensions and materials. Therefore the choice and reasoning required for the structure, apart from fabrication considerations, is non trivial, nor is it easy to demonstrate the propagation characteristics without elaborate 3-dimensional numerical computations, which are very costly to carry out. Alternative geometries and constructions have been previously suggested by Sozuer et al. [24], but in this paper we examine a specific geometrical characteristic of these structures, namely that they consist of an interleaved pair of 2-dimensional sub-lattices each consisting of parallel rods arranged in parallel layers with a space between layers, and with orthogonal orientations for the direction of translation invariance of each sub-lattice. It turns out that significant properties of the 3-dimensional crystal are determined principally by the characteristics of the 2-dimensional sub-lattices, and computation of the latter properties is much less costly than computing those of the 3-dimensional crystal directly.

5.2: Interleaved 2-dimensional lattices

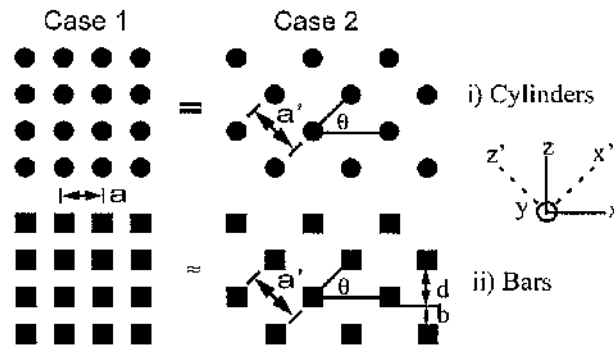


Figure 5.1 2-dimensional square lattices

Figure 5.1 shows 2-dimensional square lattice configurations for cylinders and bars with lattice spacing a . By altering the view point of the lattice by rotating about the y axis, we observe a square lattice that has half-lattice-spacing shifts between consecutive layers. The lattice spacing is chosen so that $a=a'$, $\theta=45^\circ$, so the spacing between the cylinders or bars in the z -direction will allow another to be interleaved. The condition for the correct interleaving is that $d=2b$, where b is the diameter of the cylinders, or the height of the bars

for their respective lattices. In effect we have fixed one dimension of the dielectric bar structure, or the diameter of the cylinder. Woodpile structures as suggested and fabricated by Ozbay [25,26,27] are built by successive stacking and rotation of wafers of similar thickness. In each of the structures [25,26,27] the wafer thickness is b and is application dependent, while θ ranges in value from 50.7 to 59.5 depending on the structure. All of the structures maintain the $d=2b$ relation and the half lattice spacing shifts for the Case 2 lattices before interleaving.

5.3: Numerical results

Using the transfer matrix method we show that the characteristics gained from 2-dimensional analysis can be used to design a 3-dimensional photonic crystal. The vast decrease in processing time for a 2-dimensional structure allows a more extensive analysis of the structures before interleaving to create optimised 3-dimensional crystals.

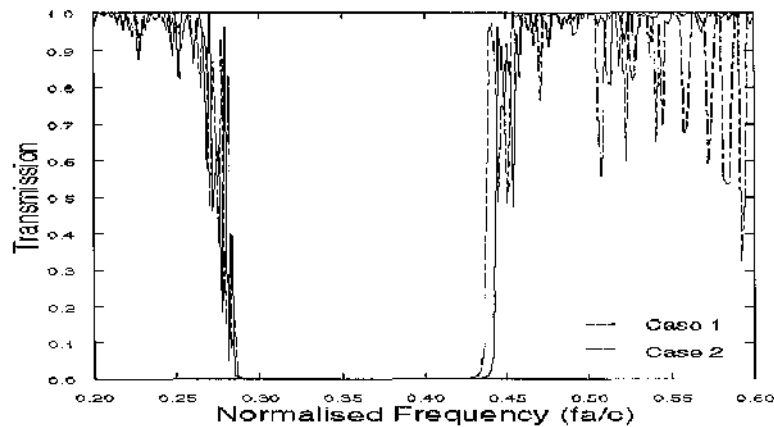


Figure 5.2 Maximum transmission for 2-dimensional bar lattices

Figure 5.2 relates the transmission co-efficient of the multi-layer 2-dimensional crystal to normalised frequency for the two lattice cases of dielectric bars ($\epsilon = 11.4$) shown in Figure 5.1. The transmission plotted in Figure 5.2 is the maximum in the xz and $x'z'$ plane, found by scanning the incidence angle of the plane wave onto the structure in the 2-dimensional plane orthogonal to the direction of translation invariance. The transmission response related to the normalised k_x vector ($0 < k_x < 1$ relates normal ($k_x=0$) to oblique ($k_x=1$) incidence) and frequency is shown in Figure 5.3. In order to preserve a consistent fill ratio of 10.8%, the 45° rotation about the y -axis required to transform Case 1 to Case 2 also requires a 45° rotation of the bars; this has caused a slight upward shift in the bandgap

region of the crystal, although it has not degraded the width of the gap. Only the E -polarisation or transverse magnetic (TM) response is shown, as there is no substantial complete 2-dimensional interaction for the H -polarised or transverse electric (TE) wave. We define E (H) polarised waves as those which have their magnetic (electric) field confined to the xz plane, that is to say the electric (magnetic) field is parallel to the y -axis.

The slight upward shift in mid-gap frequency may be attributed to the decrease in the physical spacing between features due to the 45° bar rotation. The distance between bar edges in the xy direction for the Case 1 lattice and the $x'y'$ direction for the Case 2 lattice narrows by 3% due to the 45° rotation. This narrowing means that the interaction wavelength for band gap region will decrease causing a slight rise in central frequency for the Case 2 lattice.

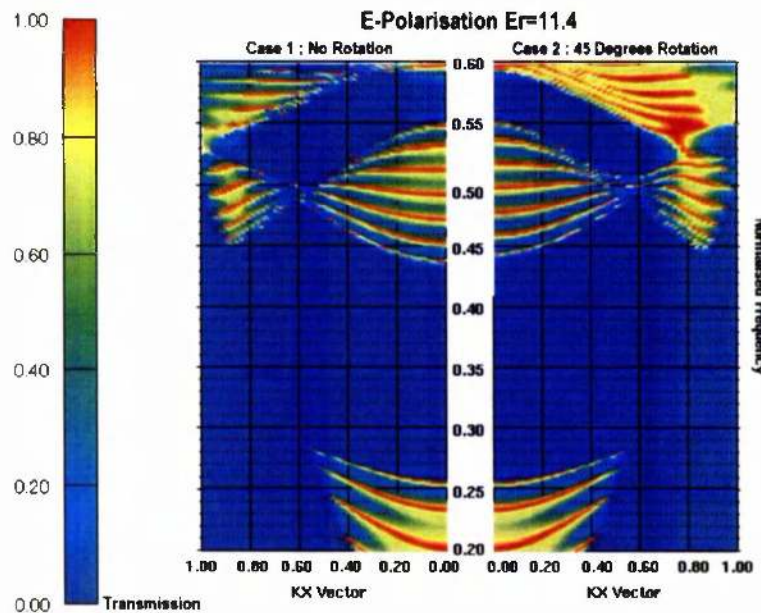


Figure 5.3 Transmission for Angular Sweep of Case 1 & Case 2 Lattices

To investigate the response of the band gap for other values of θ in the Case 2 lattice a super-cell methodology was adopted. The square super-cell of dimension $4b$ (unity aspect ratio), contained two bars, one static bar and one bar free to move in the x direction to allow θ to change as illustrated within the inset of Figure 5.4. For the choice of super-cell, angles below 32.5° were not attainable due to the physical dimensions of the cell.

Near-optimal interleave response is obtained when $\theta = 45^\circ$, and there is a progressive narrowing of the band gap as θ tends to 90° . For a small range of interleave angles, around

$\theta=80^\circ$ there is no 2-dimensional band gap for E -polarised waves. Previously constructed woodpiles utilise alternate interleave angles but cannot be compared with Figure 5.4 unless the super-cell is square, however it has been demonstrated that these other instances do give rise to complete 3-dimensional band gap behaviour when the lattices are interleaved[24-28].

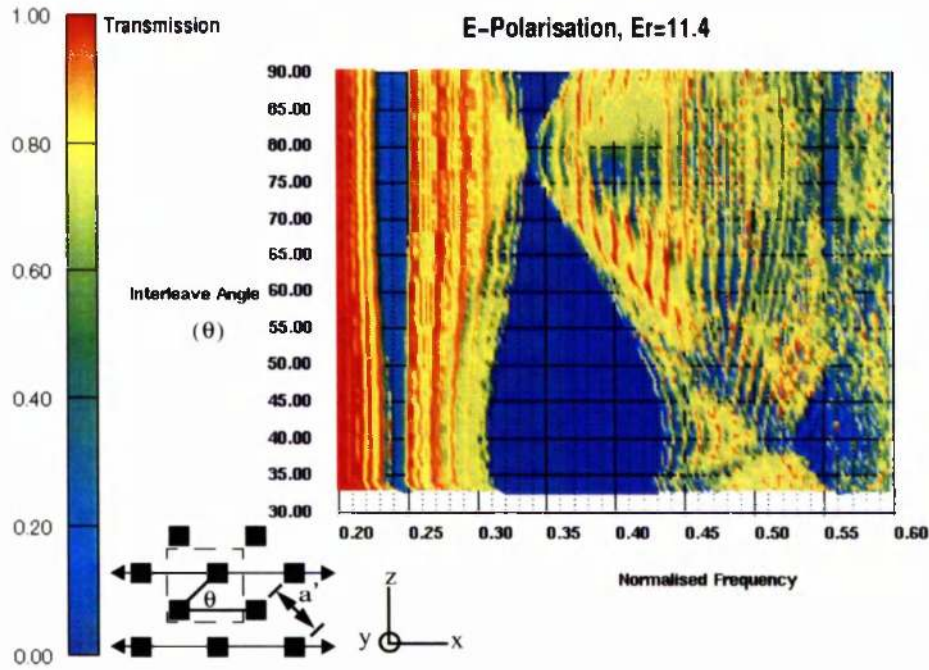


Figure 5.4 Optimum Angle of Interleave

Interleaving two Case 2 bar lattices orthogonal to each other's respective 2-dimensional plane while maintaining the interleaving condition creates a new definition for woodpile structure. Figure 5.5 shows the unit cell for this structure for silicon bars with $\epsilon = 11.4$. Normalised k_x and k_y vector components control the incidence angle of the plane wave onto

the woodpile structure, while the transfer analysis is conducted in the z -direction. Normal incidence of the plane wave onto the structure is achieved when $k_x = k_y = 0$.

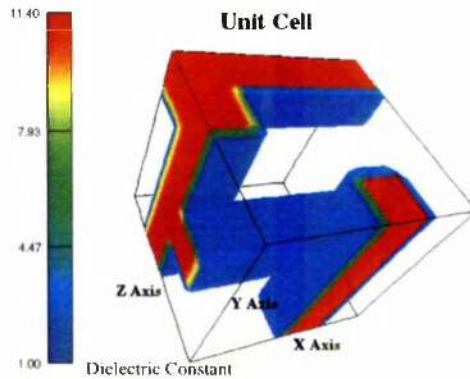


Figure 5.5 Interleaved Bar Unit Cell

Transmission through the new description of the woodpile structure is shown in Figure 5.6 for both E - and H -polarisations. Interleaving a second lattice which is rotated with respect to that of the first, results in a lattice structure which displays photonic band gap behaviour in both polarisations. We have created a photonic band gap response for H -polarised waves by interleaving a structure responsive to H -polarised waves into a structure responsive to E -polarised incident plane waves. The plots in Figure 5.6 show the maximum transmission versus frequency for nested sweeps of the k_x and k_y incidence control vectors. Both polarisations share a common mid-gap frequency of 0.317. The shift in mid-gap frequency is only small with respect to the non-interleaved lattice although the width of the band has narrowed. These factors are related to the change in average dielectric constant as a direct result of interleaving. The new description of the woodpile structure has achieved a bandgap width of approximately 12% of the mid gap frequency.

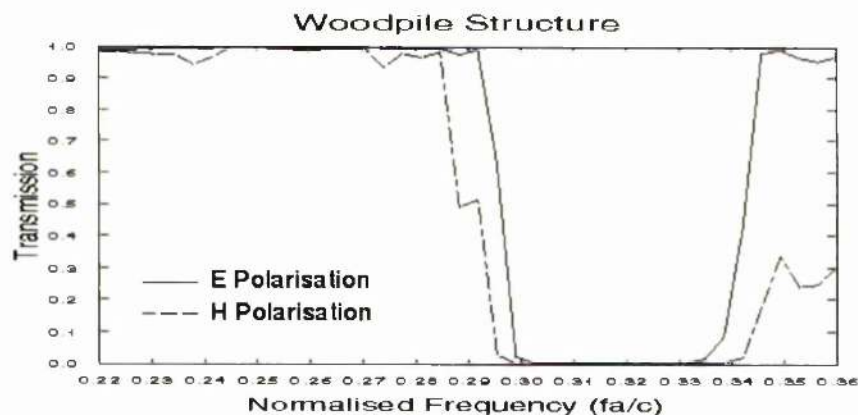


Figure 5.6 Woodpile Frequency Response

Verification of the complete photonic bandgap was carried out with high resolution sweeps of the incidence angle plane wave control vectors. As k_x and k_y are normalised, scans from $-1 < k_x \text{ or } k_y < 1$ relate to incidence angles from -90 to $+90$ in the x or y plane respectively. These scans cover the forward hemisphere of incidence directions at a normalised mid-gap frequency of 0.317. Figure 5.7 shows negligible transmission for both E - and H -polarisations for a crystal eight cells thick. Maximum transmission through the structure is approximately 0.1%, resulting from H -polarised waves. The orientation of the first set of parallel bars as seen by the incident plane wave, (responsive to E -polarised waves for our structure) results in the maximum E -polarisation transmission response being even less than that of the H , some 0.005%. This is in good agreement with the findings of Ozbay[25] who also found polarisation dependence due to the orientation of the first layer of parallel bars.

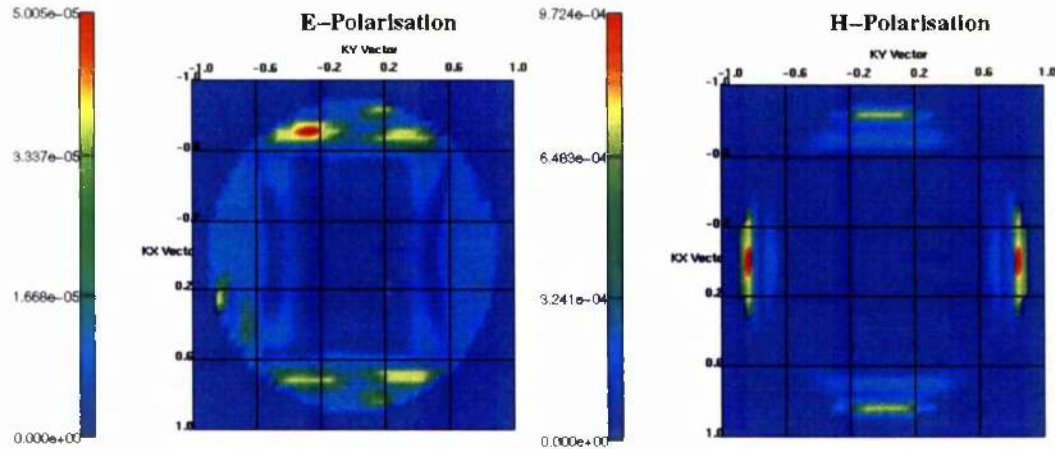


Figure 5.7 Woodpile Mid Gap Transmission

5.4: Characterisation and application of a 94GHz Woodpile

Further investigation of the woodpile crystal for applications at 94GHz was carried out by fabricating the structure as suggested by Ozbay [25]. Figure 5.8 shows a picture of the assembled woodpile made from sixteen stacked silicon wafers to form 4 unit cells of the structure. The woodpile structure is made from high resistivity silicon bars $\epsilon_{\text{silicon}}=11.7$, $340 \times 390 \mu\text{m}$ in the x - and z - directions respectively, and the bars have a periodic spacing of $1275 \mu\text{m}$ in the xy - plane. Each layer of bars is formed by etching straight through a silicon wafer which, with careful thought over the alignment marks, will stack together correctly to form the woodpile structure utilising correctly positioned guiding pins. The layers

are held together using small clips so that alteration of the structure is facilitated. Small deviations in alignment and stacking were not found to alter the experimentally measured response significantly.

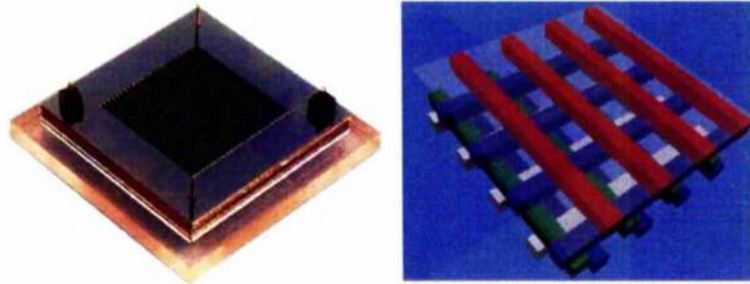


Figure 5.8 Photograph & Schematic of the 94GHz Woodpile

Left: The structure is made from silicon bars, $340 \times 390 \mu\text{m}$, $\epsilon_{\text{silicon}} = 11.7$. The bars have a period of $1275 \mu\text{m}$, each layer has been rotated by 90° to the preceding layer and parallel layers are half period shifted such that four layers are required for one period. *Right:* Schematic illustrating the repeat pattern of the woodpile structure with a semi transparent membrane over the top surface of the crystal.

Theoretical analysis of the structure for normal incidence predicts a band gap from 79 to 117GHz. For thin crystals, only a few cells thick, the attenuation is polarisation dependent, but as the crystal becomes thicker both polarisations confirm a central band gap frequency of approximately 100GHz, see Figure 5.9. With over 12dB attenuation attainable for one cell of the structure, depending on the impinging wave polarisation, and over 17dB per cell for thicker structures this woodpile geometry has strong attenuation characteristics. This is in excellent agreement with the findings of Ozbay [25].

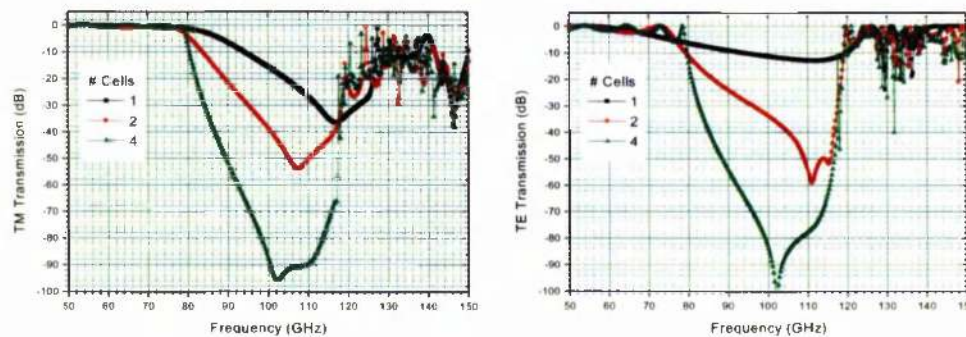


Figure 5.9 Theoretical Transmission Response

TM (TE) polarised wave transmission response shown on the left (right) for 1, 2, and 4 cells of the woodpile crystal.

Measured Response

The TE polarisation transmission response through the structure was measured using a vector network analyser and the measured results and theoretical predictions were found to be in good agreement. Figure 5.10 shows the transmission response at normal incidence

onto the surface plane of the woodpile crystal which was 4, 8, and 16 wafers thick corresponding to 1,2 and 4 unit cells respectively.

The measurements confirm the predictions and the finite size of the crystal can be seen in the ripple leading up to the lower band edge. Due to the measuring limit of the W-band network analyser frequencies higher than 110GHz could not be measured. The higher frequency ripple in the measurements may be attributed to the perspex substrate on which the crystal has been stacked and the consequent Fabry-Perot resonance it introduced into the measurement.

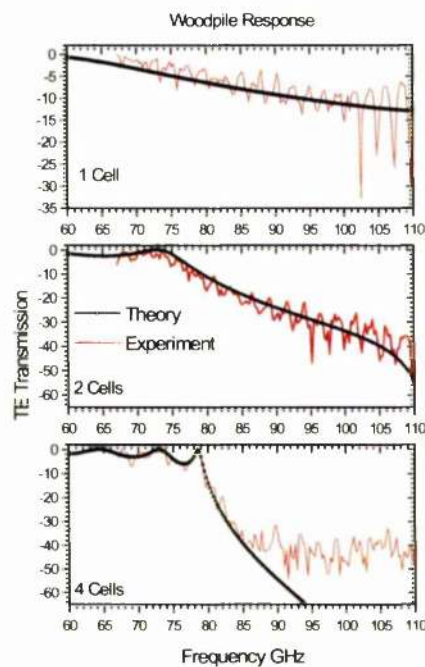


Figure 5.10 Measured & Theoretical Response for the 94GHz Woodpile.

Measured and theoretical predictions for TE polarised wave transmission through the woodpile crystal. The top, middle and bottom inset correspond to the response for 1,2 and 4 cells of the crystal. Each inset shows the measured response, red line, against the theoretical response, black line with symbol. The measured responses have been corrected for the free space loss measurement.

5.5: Angular Performance

A full angular scan of the crystal was performed at 94GHz to ensure the existence of the complete photonic band gap. The angle of incidence was scanned to cover the full forward hemisphere of the structure, see Figure 5.11.

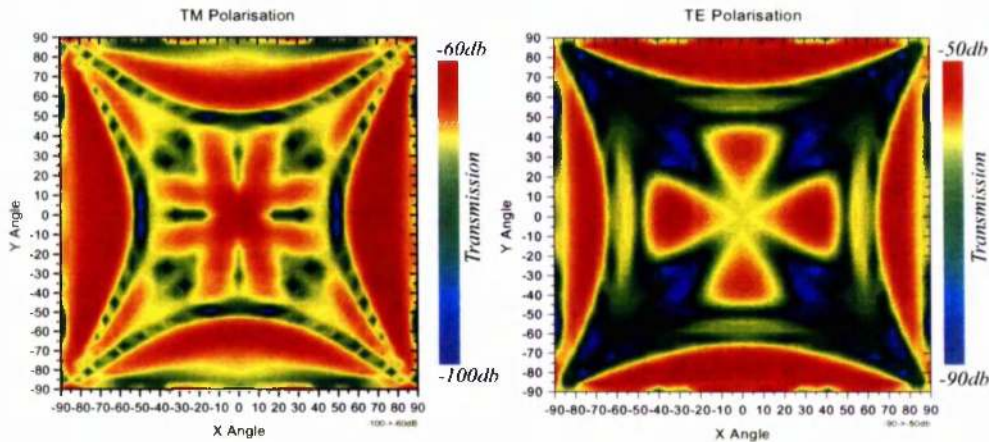


Figure 5.11 Angular response for 4 Cells @94GHz: Waves impinge from air

The TM (TE) polarised wave transmission response shown on the left (right) as a function of incidence angle for the 100GHz woodpile structure. Analysis has been carried out at 94GHz to match the radiation frequency of a slot antenna used in conjunction with the woodpile in the next section. The waves were assumed to impinge onto the crystal from an air medium.

Figure 5.11 shows for the angular analysis for the TM polarised waves, that for incidence angles relatively close to oblique and normal incidence onto the surface of the crystal give rise to the maximum transmission through the crystal. As the incidence angle is scanned between these two extremes the transmitted level drops.

The TE polarised wave does not have maximum transmission for normal incidence onto the surface of the crystal. Maximum transmission for the TE polarised wave occurs for various ranges of angle away from normal incidence. However, both polarisations show strong attenuation, the maximum transmission level is -50dB, resultant from the TE polarised wave. Launching the plane waves from a bulk silicon medium removes any restrictions placed by Snell's law and a full angular scan similar to that presented in Figure 5.11 is shown in Figure 5.12.

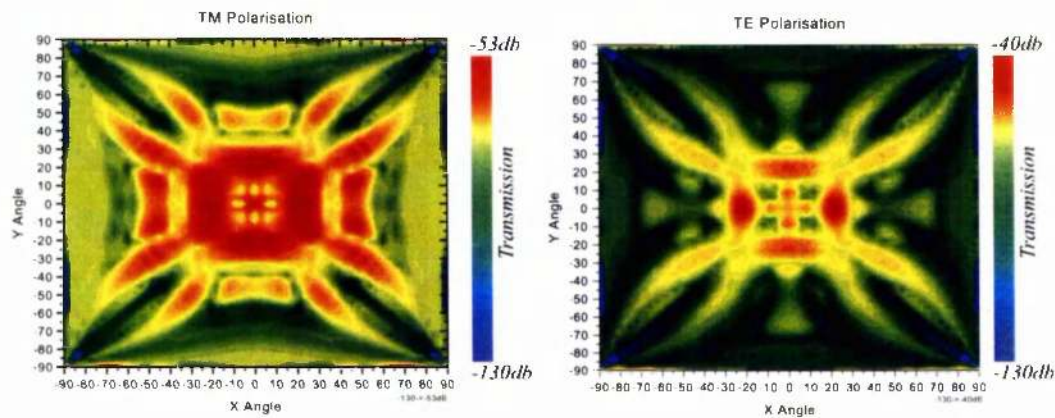


Figure 5.12 Angular response for 4 Cells @94GHz: Waves impinge from silicon

The TM (TE) polarised wave transmission response shown on the left (right) as a function of incidence angle for the 100GHz woodpile structure. Analysis has been carried out at 94GHz to match the radiation frequency of a slot antenna used in conjunction with the woodpile in the next section. The waves were assumed to impinge onto the crystal from a bulk silicon medium.

From the insets for TM and TE polarisations shown in Figure 5.12 for waves that were launched from a bulk silicon medium the transmitted levels do not exceed -40dB for either polarisation. There is a small rise in transmitted level for both polarisations as a result of transmission achieved through angles that were not attainable from when the waves impinged from air. The increase does not return the transmission to a high level, -40dB maximum, consequently it is fair to state that for the 100GHz woodpile photonic crystal studied that it does have a complete 3-dimensional photonic band gap. Depending on the application higher levels of attenuation may be required, this can be increased simply by increasing the finite thickness of the crystal.

5.6: Antenna Radiation Response

Theoretical analysis and measured demonstration of the woodpile crystal [25] verify the existence of the complete photonic band gap and some optimal design parameters [29] also exist. One of the possible applications of the woodpile photonic crystal is for a substrate for antennas; Brown et al. demonstrated the idea by placing a bow tie antenna on Yablonovite, successfully demonstrating the suppression of radiation into the photonic crystal and enhanced radiation into air [30]. Since then the idea has been further researched and patented by several research groups [31-36]. Previous work has measured the response of the woodpile and antenna systems in the 12-15GHz range [29,36-38]. A slot dipole antenna

with an optimal radiation frequency of 94GHz was fabricated on a thin, 100 μ m silicon membrane, and the radiation performance measured for various positions and orientations on the surface of the woodpile photonic crystal¹.

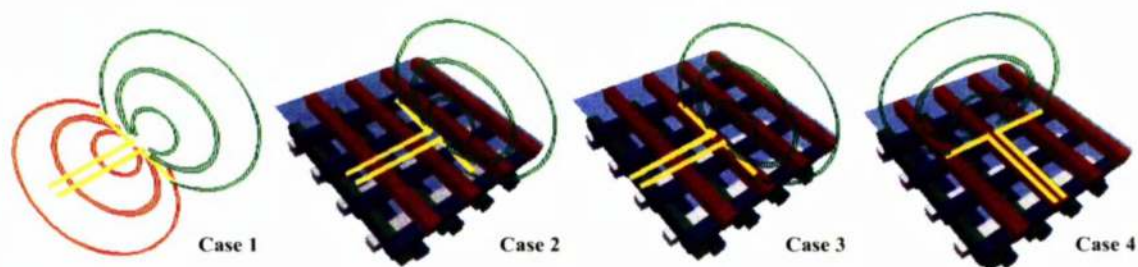


Figure 5.13 Schematic of the measurement scenarios.

The figures show the position and orientation of the antenna relative to a generic visualisation of a woodpile structure. Neither the woodpile nor the antenna is to scale.

Figure 5.13 shows schematically the four measurement scenarios. The antenna radiation response is measured in isolation without the photonic crystal and then measured in three different positions and orientations with the photonic crystal. The slot antenna had a slot length of 601 μ m, the equivalent approximate length to a half wavelength at a dielectric/air boundary at 94GHz. The antenna is fed by a coplanar waveguide, CPW, which enabled on-wafer probing using a Cascade ACP100 W-band probe. The positional data relative to the illustrations in Figure 5.13 is summarised in Table 5.1.

Position:	Description:
Case 1.	Slot antenna without PBG crystal.
Case 2.	Slot antenna and CPW aligned on gap of PBG crystal.
Case 3.	Slot antenna aligned with dielectric bar of top wafer of the PBG crystal, feed aligned with air gap of top wafer.
Case 4.	Slot antenna perpendicular to dielectric rod on top wafer of the PBG crystal with the CPW feed aligned along one of the dielectric bars.

Table 5.1 Summary of antenna orientations

Summary of Measured Response

Case 1: Antenna without PBG

Figure 5.14 on page 78 shows the *E*-plane and *H*-plane radiation patterns for the four measurement scenarios at 94GHz. The Case 1 results show that the antenna radiates in both the forward and backward directions with a preferential radiation in the backward direction.

1. I would like to thank Harold Chong for his time and patience in designing and measuring the performance of the antenna system on the woodpile photonic crystal. I would also like to thank Alex Ross for all his technical expertise in assisting with this work.

This is not unexpected as the antenna prefers to radiate into the substrate medium rather than air by a factor of $\epsilon^{3/2}$, where ϵ is the substrate dielectric constant [5]. This means that for a bulk silicon substrate only about 4% of the power is radiated into free space. The introduction of the woodpile substrate crystal alters the radiation properties of the antenna significantly, forbidding the backward propagation and enhancing the forward radiation.

For all of the following cases, which use the photonic crystal woodpile substrate, the backward radiation has been suppressed as the antenna driving frequency of 94GHz is within the band gap region of the structure, see Figure 5.9 on page 71.

Case 2: Antenna & feed aligned over gap

With the antenna and CPW feed aligned over the gap between the bars of the top wafer in the woodpile structure the *H*-plane power level has increased by approximately 3dB while the *E*-plane power levels remain the same.

Case 3 & Case 4

For either measurement situation the measured radiation power for either the *E*-plane or *H*-plane was found to be lower than that of the Case 2 situation. Indeed the radiated power levels were found to be less than for the Case 1 scenario when no PBG substrate was used.

Summary

These findings are contradictory to our expectations and may be attributable to the following observations. There is a positional dependence of the effective dielectric constant observed by the antenna. In both the Case 3 and Case 4 situations the antenna was in close proximity to a dielectric bar which may have de-tuned the resonance frequency. This in turn may cause a rapid deterioration in the radiation efficiency of the slot explaining the reduced measurement power levels.

As the antenna has been fabricated on a planar 100 μ m silicon membrane structure it is not clear how this structure will interact with the substrate, or whether the combination may result in either or both substrate modes or evanescently bound surface mode states, of which both are parasitic loss mechanisms. This topic is explored further in the following chapter entitled "Membrane Analysis" on page 81. The manufacturing tolerances will certainly effect the response, the extent of which has yet to be explored.

The directivity of the antenna can easily be improved by introducing a defect into the crystal into which the antenna can be placed. The introduction of a planar cavity defect into a woodpile crystal is facilitated by the simple layer by layer construction. The defect cavity can be tuned to a specific frequency by altering the width, and the response of the cavity has incidence angle excitation dependence. Consequently antenna radiation is only supported for a narrow range of angles [32], assuming that the cavity has been carefully designed such that the cavity itself does not act as a waveguide. The angular properties of a planar cavity defect introduced into a 2-dimensional photonic crystal are explored in the chapter entitled: "Tuning Planar Cavity" on page 101.

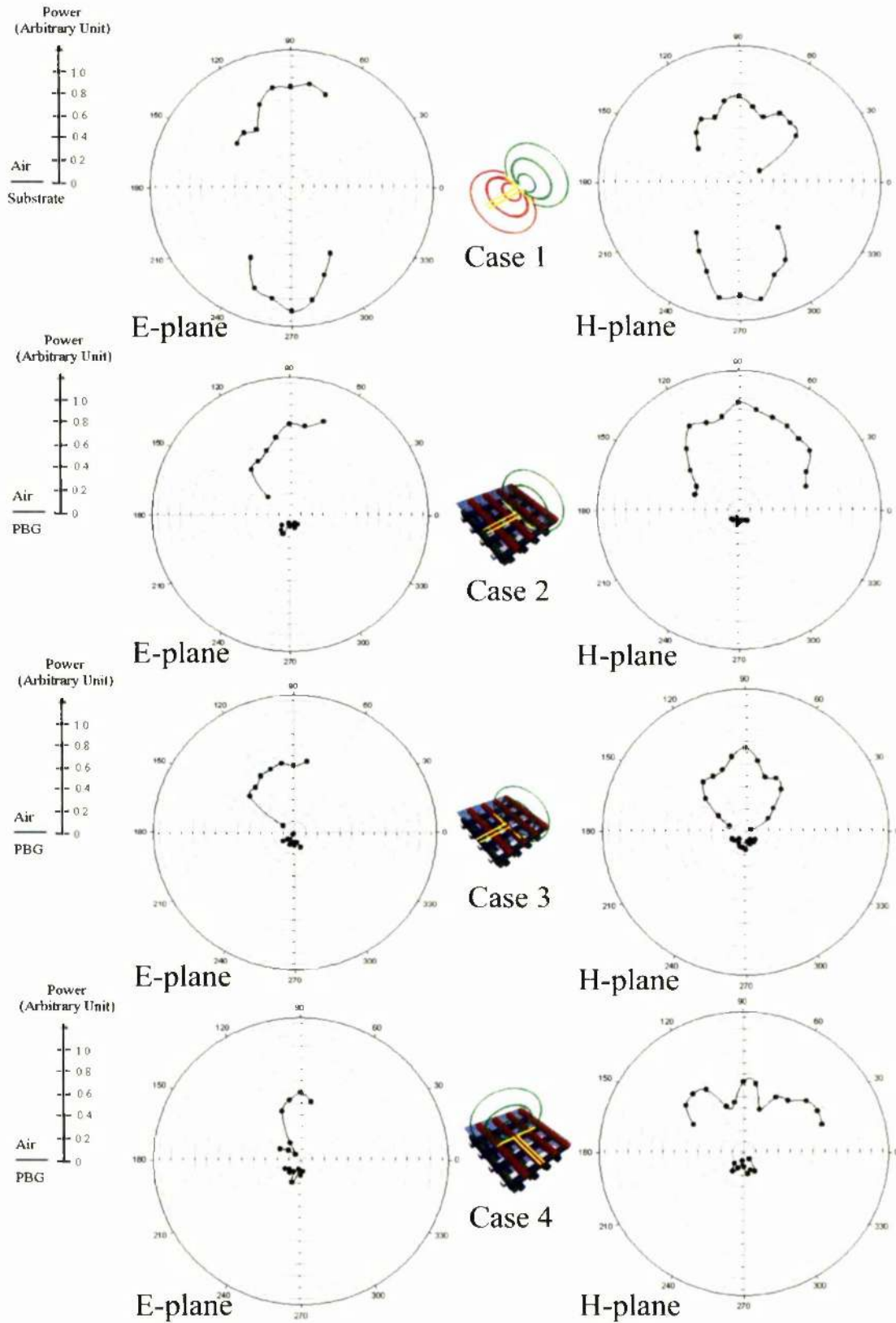


Figure 5.14 Measured Antenna Responses at 94GHz

See Table 5.1 on page 75 for an explanation of the position and orientation of the antenna on the woodpile substrate.

5.7: Conclusion

Through careful thought, construction and analysis two 2-dimensional lattices can be interleaved to create a full 3-dimensional photonic band gap material. The polarisation response for the E -polarisation for the 2-dimensional lattice is sufficient to create a similar response for the H -polarisation when a second 2-dimensional lattice is rotated and interleaved with respect to the first structure. The decrease in processing time of a 2-dimensional lattice allows optimization of the structures before interleaving allowing the construction of band optimised 3-dimensional photonic band gap materials. The optimum aspect ratio of the super cell used before interleaving as well as the interleave angle itself merit further investigation; this methodology may also be applicable to other structures such as the hexagonal lattice.

Fabrication and measurement of the 94GHz woodpile provides further confidence in the theoretical prediction capability as the agreement between the two is excellent. The integration of planar slot dipole antenna onto the surface of the woodpile crystal has shown promising results for enhancing the radiation characteristics of the antenna, as has other published material [35,36,38]. Further work is underway in the researching and optimization of our design and measurement system.

Introduction

To place antennae on the surface of a photonic band gap crystal presents a challenge as many structure surfaces consist primarily of air [25,26,27]. Studies have shown that the radiation response is dependent on the antenna orientation [5] and support for the antennae is required if they span regions of air. Membranes may therefore be used to support the antenna structure although the membrane will affect the performance of the crystal, especially for a crystal only a few periods thick.

The influence of various membranes as a function of thickness and constituent material is examined for membrane placement on the front surface of a 2-dimensional silicon photonic crystals which display full TM photonic band gap. The crystals studied are those which can then be interleaved to construct the 3-dimensional woodpile system as suggested by Ozbay [25,27] for operation at 94GHz and 500GHz. The examination of membranes includes both silicon $\epsilon_{\text{silicon}}=11.7$ and kapton $\epsilon_{\text{kapton}}=3.4$ materials.

It is well known that thick membranes can support substrate modes. The higher the application frequency and the refractive index of the material used as a membrane, the easier it becomes to excite substrate modes. Therefore the characteristics of a membrane on a PBG crystal must be thoroughly checked so that this loss mechanism is not inadvertently added to the system.

Unlike the plane wave technique [10], the transfer matrix method [21] is well suited to examining finite thickness structures that incorporate defects such as membranes. The good agreement between measured and theoretical results reinforces the applicability and usability of the transfer matrix method in examining structures incorporating defects.

6.1: 2-Dimensional Lattices with Membranes

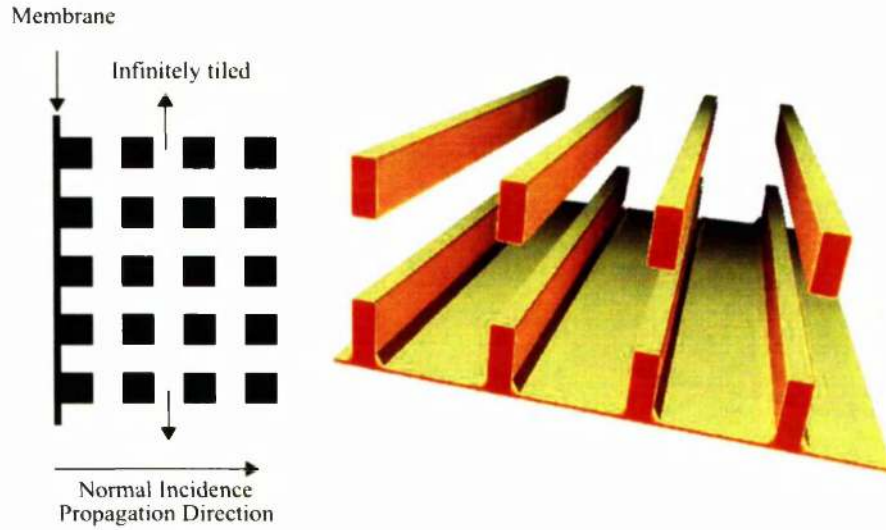


Figure 6.1 General visualisation of a membrane placed over a lattice of 2-dimensional dielectric bars.

Figure 6.1 shows the application of a membrane placed over 2-dimensional dielectric bars. The membrane is transverse to the direction of propagation and is assumed to be infinite within the translational symmetry plane.

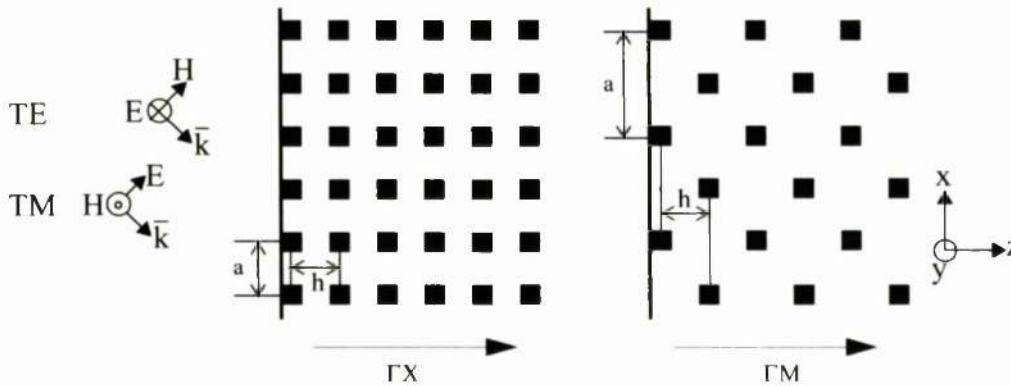


Figure 6.2 Polarisation & Lattice Definitions

Membranes are applied to the first layer within the structure only, both examples show structures that are six layers thick.

The influence of two-membrane materials is examined as a function of membrane thickness for kapton and silicon, $\epsilon_r=3.7$ and $\epsilon_r=11.7$ respectively. The membrane is placed over the illuminated surface of 2-dimensional PBG crystal consisting of dielectric bars of

silicon, $\epsilon_r=11.7$. Figure 6.2 shows the 2-dimensional lattice configurations used, the normal incidence condition defining the crystal orientation, ΓX and ΓM [39]. A general ΓM lattice with every second row displaced by a fractional part of the lattice constant a , can be interleaved [40] to form the layer by layer or woodpile crystal, [24,25,26,27,28]. Our structure interleaves to form the woodpile as suggested by Ozbay in [25] which possess a full 3-dimensional PBG. The PBG crystals studied in this chapter have $a=1275\mu\text{m}$ and for the 2-dimensional lattices discussed $h=780\mu\text{m}$, the silicon bars have dimensions $340\times 390\mu\text{m}$ in the x,z directions respectively.

Finally we note the definition of TE or E - (TM or H -) polarised waves as those which have their E - (H -) field confined to the xz plane, that is to say the H - (E -) field is parallel to the y -axis, see Figure 6.2.

The analysis that follows presents results frequently tabulated in terms of layers, each layer relates to an infinite periodic plane of dielectric bars transverse to the z -direction and periodic in the x -direction. For example, the lattices shown in Figure 6.2 for the ΓX and ΓM systems are both shown as six layers thick *in the z -direction*. To avoid confusion within the angular response analysis the crystals studied are also named by their normal incidence orientation, ΓX and ΓM .

While the application of a membrane on the structure degraded the performance of the PBG in certain areas it also enhanced the response in others. For comparative purposes both silicon and a secondary material, kapton, were used to investigate the influence of membrane types. Thereafter thicker crystal analysis was carried out in both the ΓX and ΓM directions for a varying number of layers. For the calculations the dielectric constants used were $\epsilon_{\text{silicon}}=11.7$ and $\epsilon_{\text{kapton}}=3.7$. The membranes that were studied were 25, 50 and $100\mu\text{m}$ thick. Relevant information regarding relative wavelengths within the different materials is shown in Table 6.1 while Figure 6.3 shows the information graphically.

Material	Dielectric Constant	Refractive Index	Wavelength		# Wavelengths within membrane		
			@100GHz	@500GHz	25um	@100GHz @500GHz 50um	100um
Free Space	1	1	3mm	600um	8.3×10^{-3}	16.6×10^{-3}	33.3×10^{-3}
Silicon	11.7	3.42	0.877mm	175um	41.6×10^{-3}	83.3×10^{-3}	166.6×10^{-3}
Kapton (i)	3.7	1.924	1.559mm	312um	28.5×10^{-3}	57.0×10^{-3}	114.0×10^{-3}
Kapton (ii)	4.0	2.0	1.5mm	300um	142.8×10^{-3}	285.7×10^{-3}	571.4×10^{-3}
					16.0×10^{-3}	32.1×10^{-3}	64.14×10^{-3}
					80.1×10^{-3}	166.7×10^{-3}	320.5×10^{-3}
					16.6×10^{-3}	33.3×10^{-3}	66.6×10^{-3}
					83.3×10^{-3}	166.7×10^{-3}	333.3×10^{-3}

Table 6.1 Material properties and relative wavelengths quoted for 100GHz and 500GHz.

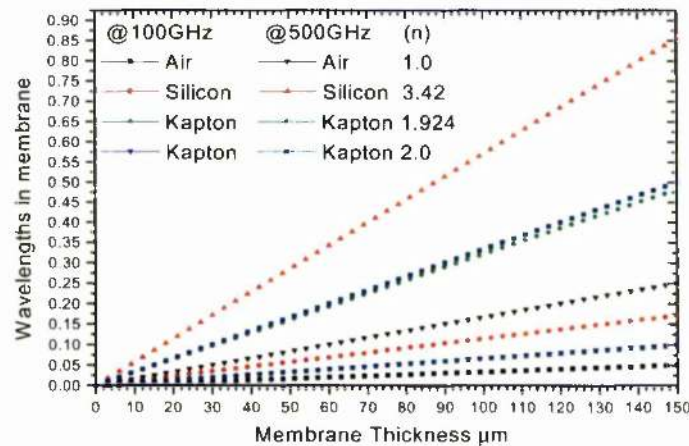


Figure 6.3 Number of wavelengths inside a membrane for Air, silicon and kapton.

The number of wavelengths that will be found inside a membrane for various materials plotted as a function of membrane thickness. Analysis has been carried out at 100GHz and 500GHz as these frequencies are most relevant to the structures under study.

For both 100GHz and 500GHz we see that the lines relating to the silicon membrane contain the largest number of wavelengths for all thickness of membrane. This is a direct consequence of the refractive index of silicon being larger than the other material studied.

6.2: Substrate Modes

The application of membranes on the surface of a photonic crystal may lead, through external excitation, to substrate modes within the membrane. This is a particularly relevant loss mechanism to any radiating element that may be placed on the surface or within the

photonic crystal. Below a certain thickness membranes will not support the guiding of a wave through total internal reflection and the membrane is considered to be a waveguide operating at a frequency which is said to be “cut-off”, i.e. no guided modes are allowed. To a first approximation the cut-off frequency of the guided modes, f_c , can be predicted by Equation 6.1 [41,42] where n is an integer multiplier, h is the thickness of the substrate, c is the speed of light in a vacuum, and ϵ is the dielectric constant of the membrane material.

$$f_c = \frac{nc}{4h\sqrt{\epsilon - 1}} \quad (6.1)$$

Figure 6.4 shows the first four modes that will propagate along either silicon or kapton membranes plotted as a function of the membrane thickness. For sub-millimetre wave applications in the range of 500GHz then *isolated* silicon membranes come dangerously close to supporting substrate modes for membrane thickness in the region of 50 μ m.

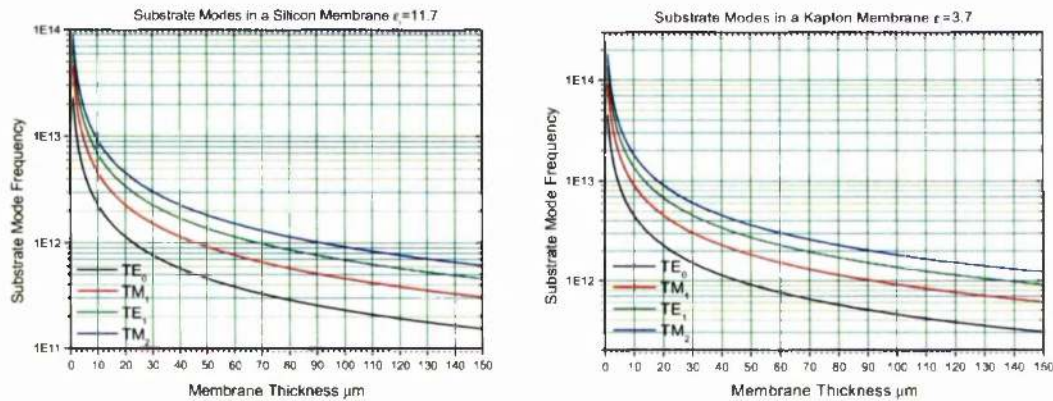


Figure 6.4 Substrate Modes in silicon and kapton Membranes.

The first four substrate mode cut off frequencies (Hz) plotted as a function of membrane thickness for silicon $\epsilon_r=11.7$ and kapton $\epsilon_r=3.7$ membranes shown on the left and right respectively. Note that this analysis assumes that the membrane is grounded on one side.

The analysis assumes that the membranes are excited in isolation from the photonic crystal. For given operational parameters, intended application frequency and membrane material and thickness, it may be safe to assume that the membrane does not support substrate modes itself, however the membranes will influence the performance of the crystal. By placing a membrane onto the surface of a photonic crystal the combination may form a grating coupler, an effect that is investigated later. In many ways the membrane can be considered as a defect on the surface of the crystal.

6.3: 94GHz 2-Dimensional System: Single Layer

Silicon Membranes: Normal Incidence

Several thicknesses of silicon membrane were studied by placing them on a single layer of dielectric bars of a 94GHz woodpile system. Analysis was carried out for normal incidence onto the membrane, since for a single layer of dielectric bars there is no associated crystal propagation direction.

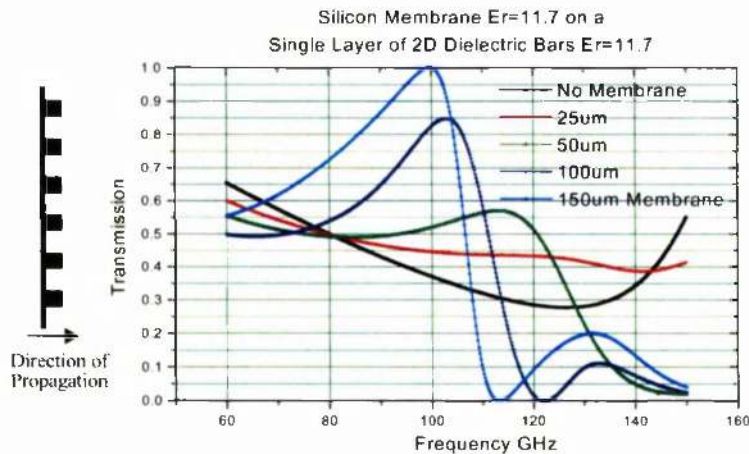


Figure 6.5 Various silicon membranes placed on a single layer of periodic dielectric bars for 94GHz system. TM polarisation transmission response for various membrane thickness' placed on top of a single layer of periodically spaced dielectric bars embedded in air. The period of the bars is $1275\mu\text{m}$ and the dimensions are $340 \times 390\mu\text{m}$ in the x and z direction respectively. The dielectric constant of the bars and membrane were assumed to be $\epsilon_r=11.7$.

Figure 6.5 shows the TM transmission response for 0, 50, 100 and $150\mu\text{m}$ silicon membranes placed on a single layer of periodically spaced silicon bars. As the membrane thickness increases there is a marked increase in the transmitted level in the expected and wanted band gap region of 80-120GHz. There is an evident development of the lower band edge with increasing membrane thickness. For the $150\mu\text{m}$ silicon membrane transmission curve the response of the structure has degraded by increasing to a transmitted value of 1 around 100GHz. For membranes thicker than $50\mu\text{m}$ the transmission through the structure has decreased for frequencies higher than 130GHz enhancing the reflection properties of the substrate.

Kapton Membranes: Normal Incidence

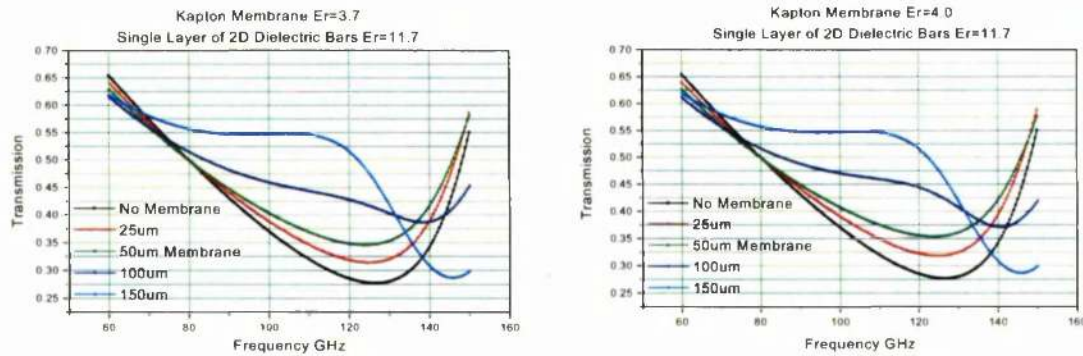


Figure 6.6 Kapton membrane analysis

The TM transmission response for various thicknesses of kapton applied to a single layer of silicon bars $\epsilon_r=11.7$. The bar dimensions were $340 \times 390 \mu\text{m}$ in the x and z directions respectively. See Figure 6.2 on page 82. Two types of kapton membrane were analysed, $\epsilon_r=3.7$ response is shown on the left and $\epsilon_r=4.0$ on the right.

The TM transmission response for 25, 50, 100 and $150 \mu\text{m}$ membranes for two values of kapton $\epsilon_r=3.7$ and $\epsilon_r=4.0$ are shown in Figure 6.6. As the membrane thickness increases the transmission response through the structure is increasingly perturbed. The perturbation level is not as strong for kapton membranes when compared to similar thicknesses of silicon membranes, a positive attribute for the kapton membrane. However the kapton membrane also degrades the PBG by increasing the transmitted level through the structure. In contrast to the silicon membrane the kapton membrane requires a much larger thickness to significantly alter the response.

Comparative performance: single layer kapton & silicon membranes

The small difference in dielectric constant between $\epsilon_r=3.7$ and $\epsilon_r=4.0$ causes a small change in the transmission properties through the crystal. The difference is increasingly apparent with thicker values of membrane. Figure 6.7 shows the difference for TM polarisation transmission levels between various membrane thicknesses placed on a single layer of silicon bars and the transmission response for the same structure without the membrane present. The analysis covers both silicon $\epsilon_r=11.7$ and kapton $\epsilon_r=3.7$ membranes for 25, 50, 100 and $150 \mu\text{m}$ membranes. Negative deviation is shown by a decrease in transmitted level, positive deviation relates to an increase in transmission through the crystal.

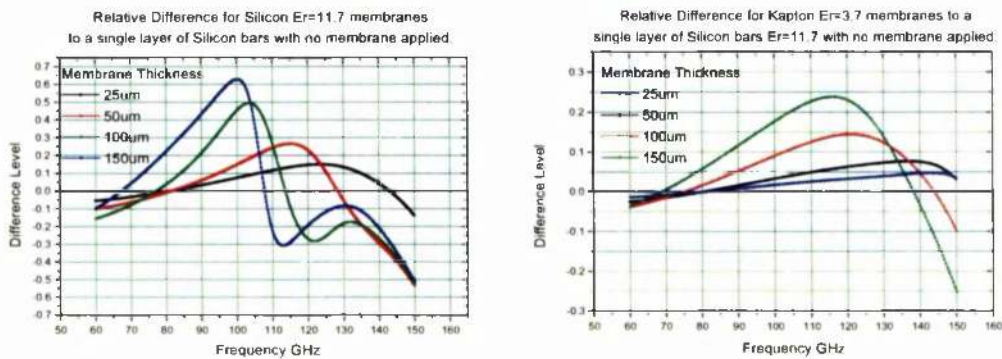


Figure 6.7 Relative Difference curves for silicon and kapton membranes.

The difference in TM transmission between a single layer of silicon bars $\epsilon_r=11.7$ without a membrane and various membrane thicknesses for both silicon, $\epsilon_r=11.7$ and kapton $\epsilon_r=3.7$. The silicon membrane curves are shown on the left, the kapton curves shown on the right. Both plots show membrane thicknesses of 25,50,100 and 150 μm .

As the membrane thickness increases the maximum deviation from the zero difference level increases for both the silicon and kapton membranes. The gradients of the lines at the zero point crossings also increase with the membrane thickness. For the silicon membranes, and to a lesser extent the kapton membranes, the curves return to similar gradient values at higher frequency values. Consequently for frequency operation at the zero point crossings membrane application narrows the operation point bandwidth.

From Figure 6.8 the silicon membranes affect the TM transmission response much more than the kapton membranes. The gradients of the lines close to the zero point difference nodes are much larger for silicon than for kapton. This is the expected response as the thinner the membrane and the lower its dielectric constant then the less the transmission performance of the crystal will be perturbed.

There are regions of operation *for normal incidence* onto the crystal where the application of a membrane enhances the performance of the photonic band gap by decreasing the transmitted level through the structure. This is particularly apparent for the 50 μm and 100 μm silicon membranes in the >100GHz region for one period of the structure studied. While the membrane has been shown to affect the transmitted level through one layer of periodic dielectric bars, the addition of further layers of PBG will also play an important part in characterising the structure. Further analysis for thicker crystals and other incident angles is required. The angular response must ensure that no substrate modes are excited within the membrane before definitive analysis can be presented.

Consequently the transmission response for a crystal with various membranes was analysed for both single layer and thicker PBG substrates. Angular analysis was performed to characterise the crystal response within the periodic plane for 25 μm kapton and 100 μm silicon membranes.

Convergence

Within the modelling code, structural representation is limited by the resolution that can be achieved by the discretising mesh. While the mesh can be increased to ensure correct representation of the finer details of a structure, the computation time involved increases substantially. In order to gauge the difference in transmission level at the thinnest mesh thickness, a 25 μm membrane of kapton $\epsilon_r=3.7$ was analysed using two different mesh sizes. The 94GHz system cell has dimension 1275x780 μm and contains a silicon bar 340x390 μm with a membrane, dimensions are quoted in x,z respectively and the cell tiles infinitely in the x -direction. The left inset of Figure 6.8 shows the representation of the cell obtained with the 54x33 mesh. The mesh is chosen so that the inter-point spacing is as similar as possible for the x - and y - directions although the code corrects for minor deviations.

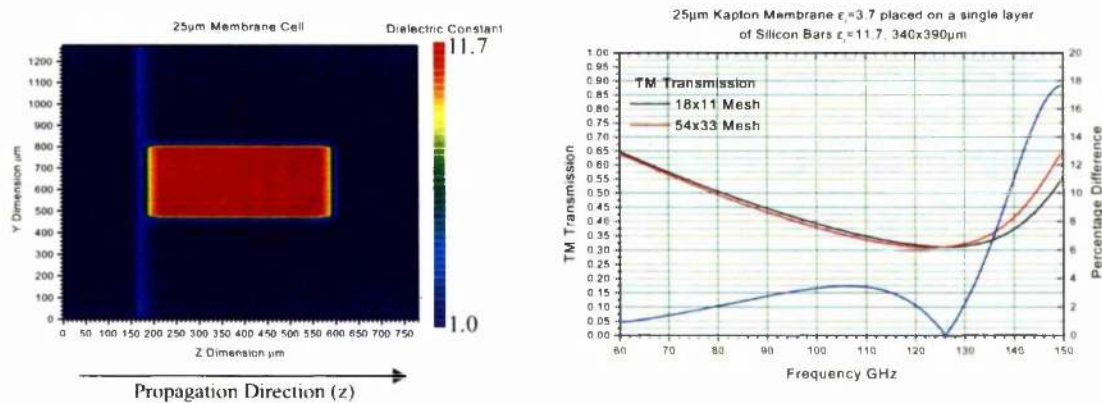


Figure 6.8 Cell & Convergence Plot for a 25 μm kapton membrane using different meshes.

Note that the hard boundary edge of the silicon bar is softened slightly by the sampling mesh.

The TM transmission response is shown for the two different mesh analyses for the same cell. For increasing frequency there is a small difference in the transmitted level through the system. The difference is at maximum for the highest frequency shown of 150GHz; expressed as a percentage relative to the 54x33 mesh, the difference is approximately 18% in transmitted level. The larger differences are found only in the higher frequency range of study and for the region leading up to 130GHz convergence is expected to be better than

4%. (The experimental set-up is limited to an upper operational measurement frequency of 110GHz).

6.4: *Experimental Verification*

Theoretical and experimental analysis of the 2-dimensional crystal with and without membrane has been carried out between 67 and 110GHz, the limit of the W-band analyser. A silicon membrane 100 μ m thick and a 25 μ m kapton sheet were independently analysed on the surface of both the Γ X and Γ M orientated 2-dimensional lattices. The S-parameters were measured with a Wiltron 360B Vector Network analyser and the Load-Reflection-Load, LRL method was used for calibration.

Figure 6.9 overleaf shows good agreement between the theoretical predictions and measurements made on the Γ X orientated lattice. As the crystal thickness was increased there was a steady increase in the attenuation of the transmitted normally incident plane wave through the structure. For increasing crystal thickness, L , the gradual formation of the lower band edge, expected at 84GHz and measured at 82.5GHz for a crystal $L=8h$, i.e. 8 periods thick, was observed.

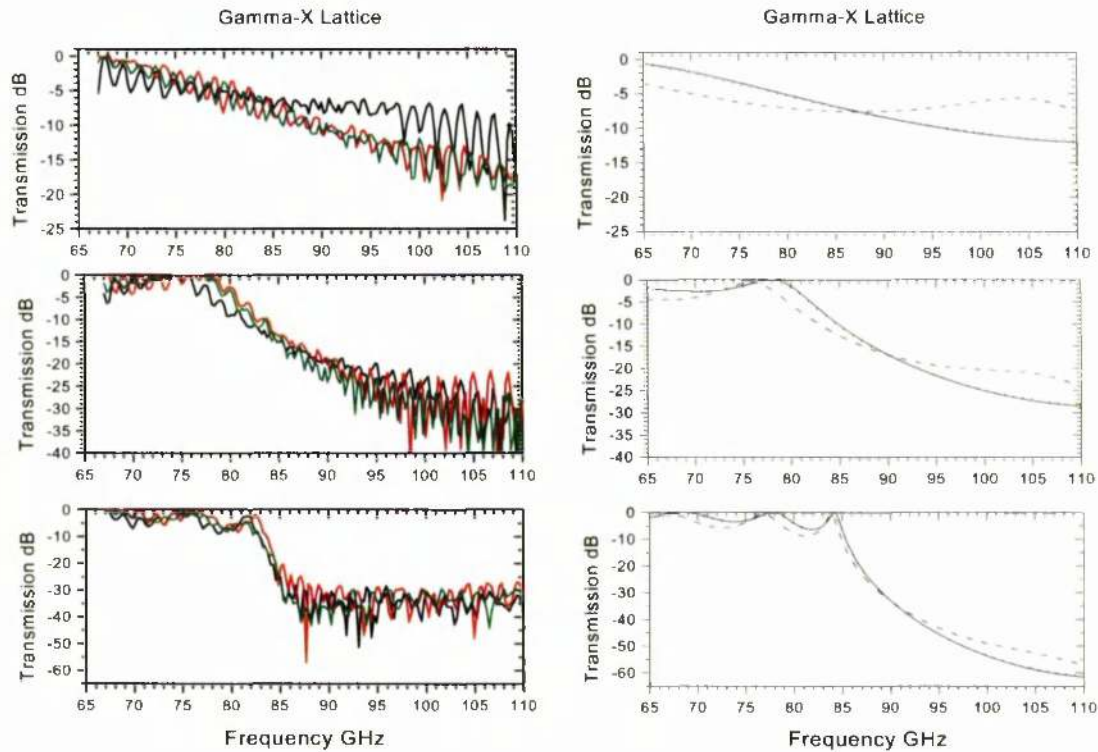


Figure 6.9 Γ X Lattice: Measured and theoretical TM response.

Top, middle and bottom plots correspond to the TM transmission response for a crystal thickness where $L=2h$, $4h$ and $8h$ thick. Plots on the left, red, green and black correspond to the no membrane case, $25\mu\text{m}$ kapton membrane and $100\mu\text{m}$ silicon membrane respectively. Plots on the right, solid, dot, dash correspond to the theoretical response for the no membrane case, $25\mu\text{m}$ kapton membrane and $100\mu\text{m}$ silicon membrane, respectively.

Measurements were limited by the noise floor of the measurement set-up of -35dB . The influence of the membrane is more prominent for the thinner PBG crystals with the $100\mu\text{m}$ silicon membrane than for the thicker crystals. Transmission through the $L=2h$ crystal is decreased with a $100\mu\text{m}$ silicon membrane in the $65\text{-}85\text{GHz}$ region before increasing the transmission response over the $85\text{-}110\text{GHz}$ region. The $25\mu\text{m}$ kapton membrane has little effect on the response for all crystal thicknesses. The $100\mu\text{m}$ silicon membrane slightly down shifts the lower band edge for all crystal thicknesses for the Γ X orientated lattice, out-with the measurable range for the $L=2h$ lattice, from 78GHz to 76GHz for the $L=4h$ lattice and from 82.5 to 81.5GHz for the $L=8h$ lattice, figures that are in excellent agreement with the theoretical predictions. As the underlying PBG substrate thickens the perturbing influence of the membrane is masked by the dominating PBG behaviour.

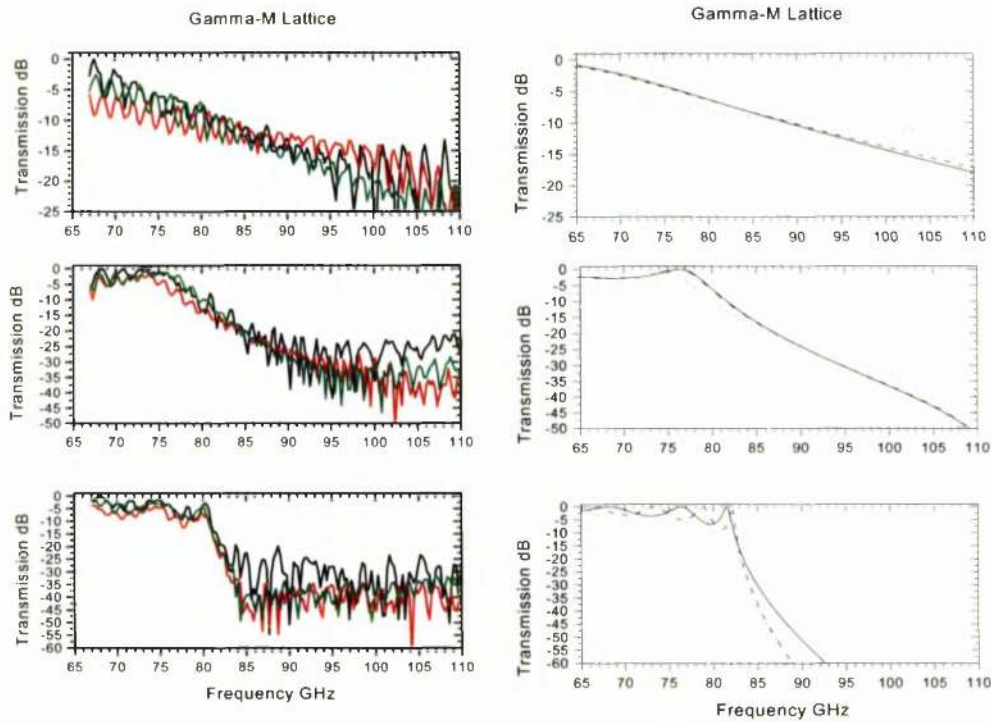


Figure 6.10 Γ M Lattice: Measured and theoretical TM response.

Top, middle and bottom plots correspond to the TM transmission response for a crystal thickness where $L=2h$, $4h$ and $8h$ thick. Plots on the left, black, green and red correspond to the no membrane case, $25\mu\text{m}$ kapton membrane and $100\mu\text{m}$ silicon membrane respectively. Plots on the right, solid, dash, dot correspond to the theoretical response for the no membrane case, $25\mu\text{m}$ kapton membrane and $100\mu\text{m}$ silicon membrane, respectively.

Similar trends are observed with the Γ M lattice as shown in Figure 6.10. The $25\mu\text{m}$ kapton membrane has little effect on the transmission measurements relative to the PBG crystal without a membrane present. The $100\mu\text{m}$ silicon membrane again shifts the lower band edge frequency, but shows convergent behaviour with the non membrane case as the crystal thickens, as was observed for the Γ X orientated crystal. From the theoretical calculations the attenuation for the Γ M lattice per layer thickness is nearly twice as large as that of the Γ X orientated crystal, although the experimental noise floor of the system prevented experimental verification for the thicker crystals. Membranes have the interesting effect of enhancing the lower band edge cut-off gradient, an effect most noticeable for both the kapton and silicon membranes for the $L=8h$ Γ M oriented crystal. This is echoed in the measurements which show the kapton and silicon response curves attaining transmission levels in the noise floor before the crystal with no membrane.

6.5: Angular Response FX Orientated Crystal

Perfect Crystal: no membrane

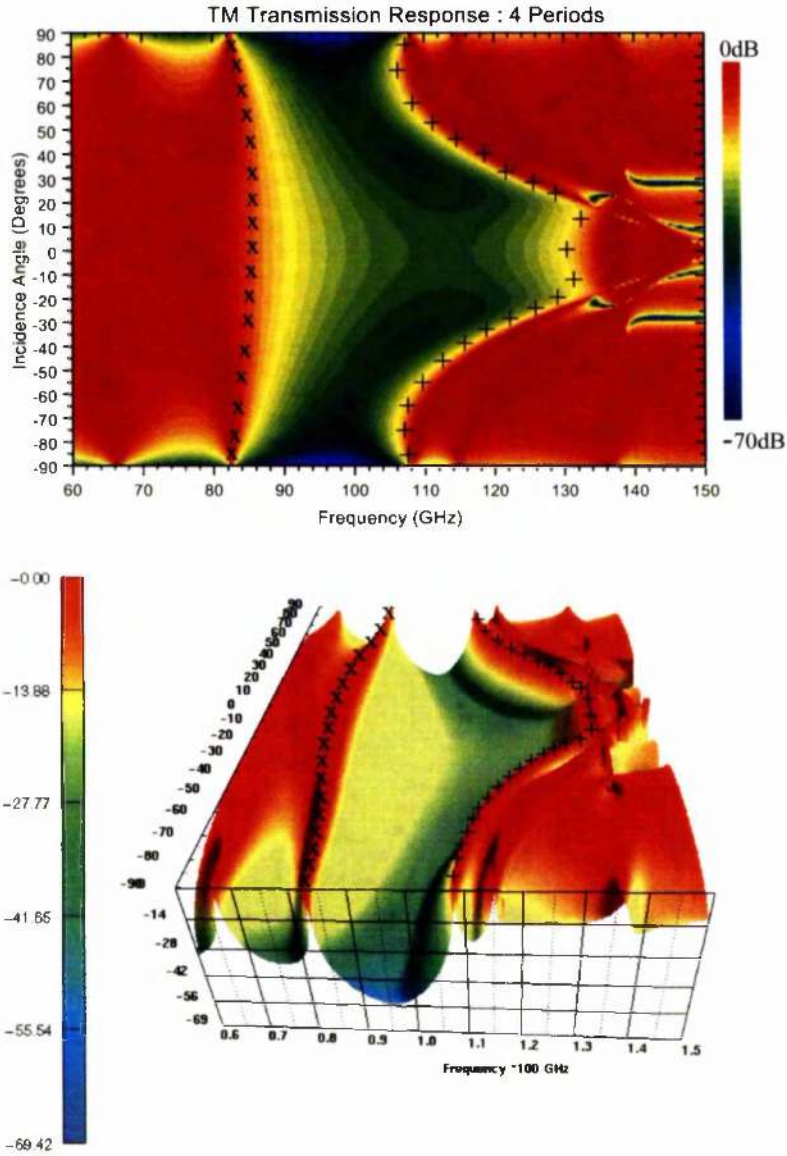


Figure 6.11 Perfect crystal angular transmission response

The transmission response of the perfect crystal as a function of frequency and incidence angle. The response is shown for a crystal four periods thick in the z-direction. The crystal is made from silicon bars, 340x390µm, with a period of 1275x780µm in the x- and z- directions respectively. The upper (lower) band edge envelope has been marked with the '+'('x') symbol to guide the eye. Same information shown in both plots but from a different visualisation perspective.

By scanning the incidence angle of the impinging plane waves to cover all available incidence angles within the 2-dimensional periodic plane of the structure, the angular transmission response is characterised. From Figure 6.11 the normal incidence condition, angle=0° sets the upper frequency limit of the lower band edge while the lower frequency edge of the upper band is found close to oblique incidence. Increasing the number of layers

serves to increase the attenuation within the band gap and steepen the gradient of the transmission curves close to the band edges. The total band gap lies between 84 and 108GHz, a range that is also echoed by the band structure calculation for the same but infinite crystal: see Figure 6.12.

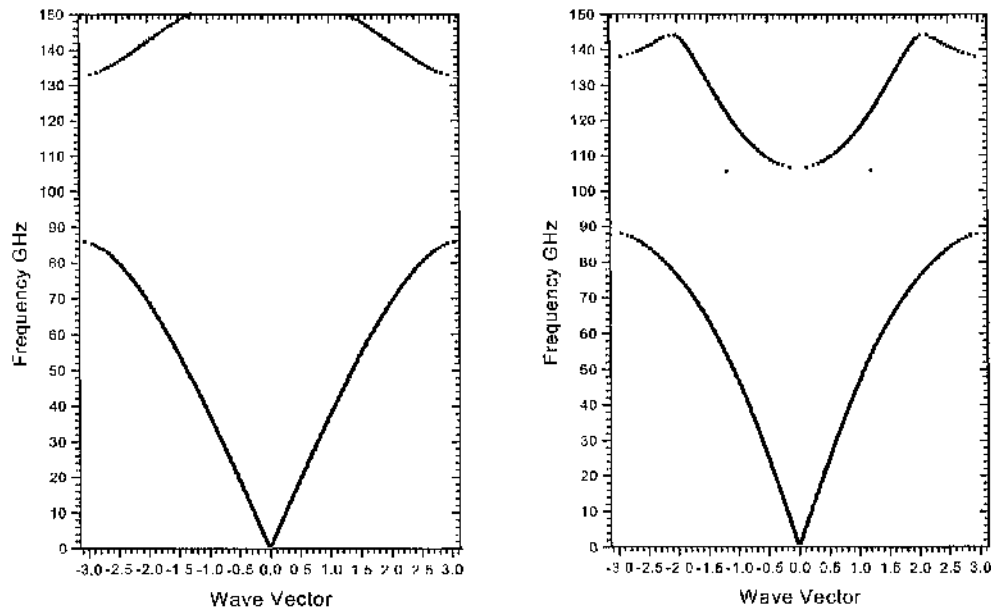


Figure 6.12 TM band structure.

Left: Normal incidence; *Right:* Oblique incidence (90°); onto an infinite crystal of silicon bars, $340 \times 390 \mu\text{m}$, with a period of $1275 \times 780 \mu\text{m}$ in the x - and z - directions respectively. The normal (oblique) incidence condition sets the upper (lower) frequency limit of the lower (upper) band edge.

Influence of kapton & silicon membranes

The introduction of a $25 \mu\text{m}$ kapton membrane over and touching the front surface of the otherwise perfect crystal has a marginal effect on the response of the structure. This was reflected in the measurement data where the normal incidence transmission data for the perfect crystal and kapton membrane crystal were also virtually indistinguishable. However the introduction of a $100 \mu\text{m}$ silicon membrane markedly alters the response of the structure.

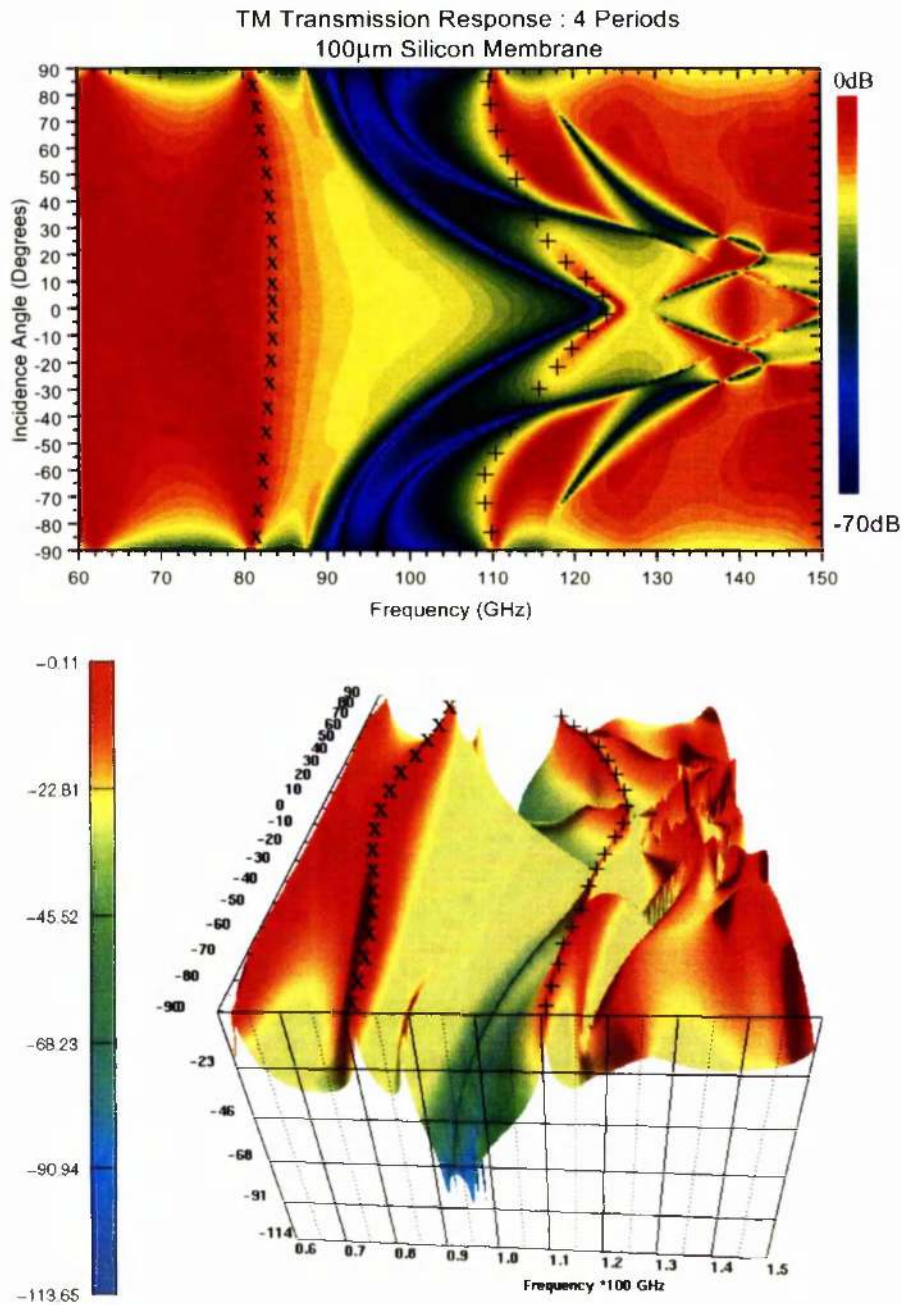


Figure 6.13 100 μ m silicon Membrane response on the otherwise perfect crystal

The transmission response of the perfect crystal as a function of frequency and incidence angle. The response is shown for a crystal four periods thick in the z-direction. The crystal is made from silicon bars, 340x390 μ m, with a period of 1275x780 μ m in the x- and z- directions respectively. The envelope of the upper (lower) band edge has been marked with '+'('x') to guide the eye.

Figure 6.13 shows the angular response of four periods of the crystal with a 100 μ m silicon membrane placed over the front surface. The upper and lower band edge envelopes

have been highlighted with '+' and 'x' symbols to guide the eye. When compared to the angular response for a similar thickness perfect crystal, shown in Figure 6.11, there are evident differences. For angles close to normal incidence the upper band edge has dropped from 130GHz to 120GHz. There is also considerable alteration in the higher frequency region with the effect that the upper band envelope has changed considerably when compared to the perfect crystal case. The distinctive pattern of the upper band edge envelope for the perfect crystal is due to the asymmetry of the unit cell. The unit cell is $1275 \times 780 \mu\text{m}$ with the silicon bar, $340 \times 390 \mu\text{m}$ in respective x - and z - directions, centred in the cell. The choice of cell and bar correspond to the experimental conditions but are not optimum.

It is noteworthy that the lowest frequency limit of the upper band edge is located at a slightly higher frequency, 110GHz, when compared to the perfect crystal response of 108GHz. However the upper frequency limit of the lower band edge, still defined by the normal incidence condition at 0° , is now less well defined and has moved upwards in frequency.

Comparative Performance & Conclusion

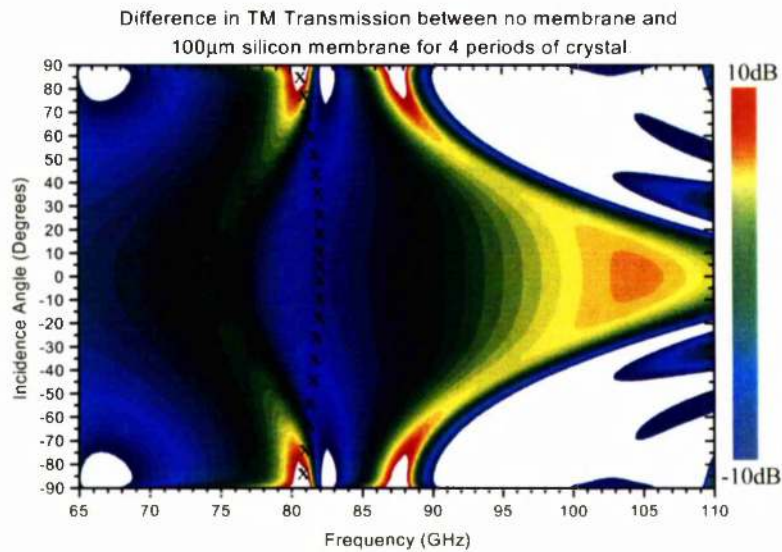


Figure 6.14 Difference in TM Transmission

The difference in the TM transmission response is shown between the no membrane case and the 100 μ m case for a lattice that is four periods thick in the z-direction. The crystal is made from silicon bars, 340x390 μ m, with a period of 1275x780 μ m in the x- and z- directions respectively. Regions that have a larger deviation than 10dB are shown in white. The lower band edge has been projected onto the figure with the symbol 'x'.

Figure 6.14 shows the difference in the TM polarisation transmitted level between the perfect crystal lattice and the same lattice with the 100 μ m silicon membrane included. The plot has been limited only to show a 10dB deviation from the no membrane response, areas which have a deviation larger than 10dB are shown in white. The range of frequencies analysed has been limited to those which could be examined experimentally so that comparison can be made with the insets of Figure 6.9 on page 91. For the regions with large deviations in transmission within the band gap, (the regions at 80.5 and 82.5GHz are within the lower band edge), the deviation assists the band gap behaviour as it reduces the transmitted level through the crystal. There is a small region that increases the transmitted level through the crystal at 87.5GHz, but when the same region is examined in Figure 6.13 on page 95 the total transmitted level is not above -25dB.

Limiting the discussion to the complete TM band gap region, between 85 and 110GHz, the utilisation of a 100 μ m silicon membrane does not display attributes that significantly degrade the performance of the crystal. The main concern is the possible existence of surface waves that may exist within the membrane in conjunction with the top layer(s) of

bars. Such waves are noted by the transfer matrix by a characteristic resonance in transmission and reflection.

The combination of the first layer of bars and the membrane presents an effective index to the impinging wave and therefore can be thought of as a waveguide, albeit transverse to a normally incident wave. However such a wave can couple to the effective waveguide with the coupling mechanism being the bars.

Waves within the effective waveguide can be excited in various manners, not least of which could involve placing a source close to the surface. Waves could then couple through the evanescent fields. However, in our scenario the structure is being exciting with plane waves assuming that the source is far from the crystal surface. Concern lies in the possibility that waves within the effective waveguide may be excited through diffraction.

Excitation of waves within the guide can occur before the onset of conventional diffraction due to the larger effective index of the waveguide than that of air. The effective index of the waveguide lies between the refractive index of air and the refractive index of silicon, which form the dielectric bars and the membrane. Therefore for a given operational frequency, the k -vector within the effective waveguide is larger than that in air as, $\omega n = c_0 k$, (Equation 1.3 on page 7), where ω is the angular frequency, n in this instance, is the effective index, c_0 is the speed of light in a vacuum and k is the k -vector.

For waves to be excited within the effective waveguide, the k -vector within the guide, must coincide with a reciprocal lattice vector of the grating formed by the periodic bars. To illustrate the problem, three cases for normal incidence have been studied.

Figure 6.15 on page 99 shows the TM transmission response for the constituent parts of the structure, a single layer of periodic silicon bars $340 \times 390 \mu\text{m}$ with a period of $1275 \mu\text{m}$, a $100 \mu\text{m}$ silicon membrane, and their combined response. The transmitted level has been plotted against normalised frequency where the lattice constant, $a = 1275 \mu\text{m}$. Conventional diffraction commences at a normalised frequency of $fa/c = a/\lambda = 1.0$. Frequencies between 60

and 150GHz are found between normalised frequencies of 0.255 and 0.6375 respectively, stated so that comparison with Figure 6.5 on page 86 can be made.

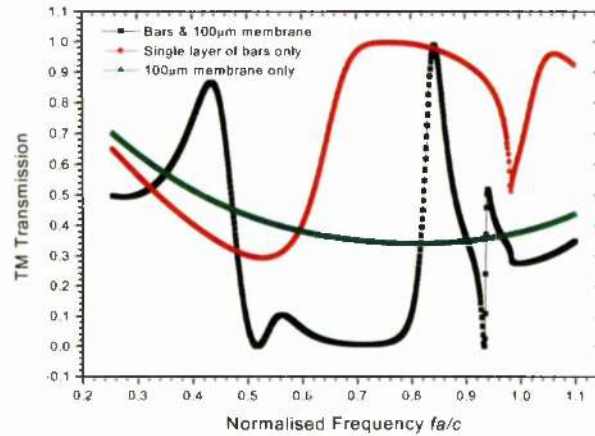


Figure 6.15 Surface wave excitation.

The response for the isolated membrane is as expected, the transmission through the membrane shows no anomalous behaviour, illustrated by the smooth slowly changing profile. The response for the single layer of periodic bars is more interesting with a notable resonance in the transmitted level just before the onset of conventional diffraction at a normalised frequency of 0.98. This resonance is attributable to the excitation of the guided waves within the effective waveguide as discussed. Once the membrane is integrated onto the surface of the bars the effective index of the guide increases, consequently the k -vector increases in magnitude with the results that the resonance moves down in normalised frequency to a value of 0.93. Given the bar period of $a=1275\mu\text{m}$, a normalised frequency of 0.93 relates to a frequency of approximately 218GHz. Therefore using a $100\mu\text{m}$ membrane as a support structure for our intended operational frequency of 94GHz, should not be cause for concern.

Consequently for the membrane materials and thicknesses examined, it has been shown both through theoretical investigation and experiment that it is safe to use a thin membrane on the surface of 2-dimensional photonic crystals to support an antenna structure. The thinner the membrane and the lower its dielectric constant the less chance there is of exciting guided modes within the membrane structure or forming a grating coupler with the top layer of the photonic crystal.

By careful fabrication it is possible to fabricate the membrane structure and the top layer of the photonic crystal from a single wafer. The benefits to this are two fold; firstly thinner membranes can be made which, as demonstrated in this chapter, are required for higher frequency applications, secondly, it will inherently strengthen the top layer, especially if the membrane is thin. Fabricating the top layer in this way facilitates the integration of an antenna, such as a patch antenna, and associated circuitry onto the wafer due to the reduced fragility. The wafer can also be reused, an added benefit, as once thin membrane structures are placed onto the surface of a crystal there is often no way of moving or removing them. Through rotation and repositioning, the wafer can be used to investigate the orientation dependence of the antenna to the underlying photonic crystal, or simply be removed for replacement with other designs.

Abstract

The introduction of defects into a crystal either at single or multiple lattice points can be achieved by adding, removing or distorting material in the crystal. Defects break the crystal symmetry and may give rise to a defect state or allowed frequency within the PBG region of the perfect crystal. Such defect states appear as resonances in the PBG transmission response. In this chapter a planar cavity defect is introduced into an otherwise perfect 2-dimensional photonic crystal lattice of dielectric bars. The introduction of planar cavities has been explored in 1, 2 and 3-dimensional photonic crystals [43,44,45]. Planar cavities have been shown to enhance the performance of detectors placed within the cavity [53] and increase the directivity of antenna radiation [32]. In this chapter the defect frequency is investigated as a function of plane wave incidence excitation angle.

7.1: Introduction

As photonic crystals act as mirrors with reflectance, R , which depends on the crystal thickness, reflectivity values in excess of 95% have been reported [46,47]. A planar cavity between two such mirrors can be likened to a Fabry-Perot interferometer. The modes that are supported by the cavity at normal incidence are given by the phase matching condition:

$$2nL \approx 2\pi / \lambda = 2m\pi \quad (7.1)$$

where L is the total cavity length $L=L_c+2L_p$, L_c is the cavity spacing, L_p the penetration depth and m is an integer, and n is the refractive index of the cavity material. The width of the supported mode, Equation (7.2) is related to the quality factor, Q -, Equation (7.3) and the frequency of the mode, f . The quality factor of the cavity is related to the cavity finesse by F , defined as the ratio of separation of adjacent maxima to the half width of the individual fringes [48].

$$\Delta f = f/Q \quad (7.2)$$

$$Q = mF \quad (7.3)$$

Finesse is related to the mirror reflectivity, R by:

$$F = \pi \sqrt{R} / (1-R) \quad (7.4)$$

Consequently high Q - and F - factors can be achieved for defect states in resonant cavities. However the Q -factor does saturate, such that it reaches a maximum value due to dielectric losses, and any further increase in the thickness of photonic crystal has little effect on the Q -factor beyond saturation [49].

7.2: Structure

The crystal was made from silicon dielectric bars $\epsilon_r=11.7$. The bars are $340 \times 390 \mu\text{m}$ in the x - and z - dimensions respectively with a periodic spacing of $1275 \mu\text{m}$ in the x -direction and $790 \mu\text{m}$ in the y -direction. A schematic of the crystal and a photo of part of the experimental set-up are shown in Figure 7.1.

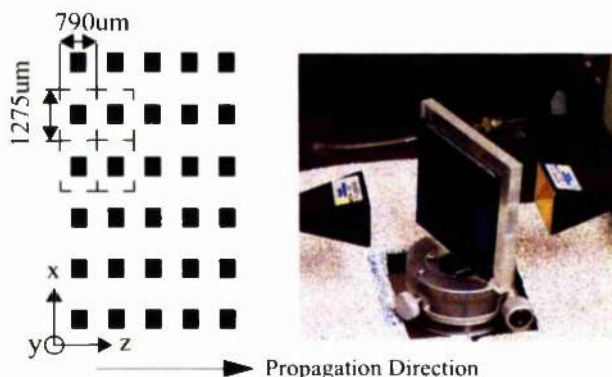


Figure 7.1 Schematic & picture of the photonic crystal.

Each vertical column of the crystal represents a single wafer or layer of silicon bars. The bars were fabricated by a wet etch process, the dimensions chosen to facilitate the construction of the layer-by-layer or woodpile structure[24] as published by Ozbay[25].

The transmission response for the perfect crystal was examined, both theoretically and experimentally. Experimental analysis was carried out between 67 and 110GHz, the limitation range of the W-band system. Full 2-port S-parameters of the structures were measured in the frequency range 67-110 GHz using an Anritsu 360B Vector Network Analyser. The VNA has short WR-10 waveguide sections at the test ports to which standard gain horns were connected. The horn separation was around 80 mm, with the membrane/PBG structure between.

The measurement system was calibrated using the Line-Reflect-Line (LRL) method using a Flann Microwave bronze WR-10 waveguide calibration kit which comprises a quarter-wavelength offset, a fixed termination, flush short circuit and through waveguide section. After calibration, the measurement reference planes are situated at the flanges of the short sections of waveguide at the test ports of the VNA to which the standard gain horns were subsequently attached. Thus 0 dB transmission loss refers to the situation when the short lengths of waveguide at the VNA test ports are joined. A small additional loss and uncertainty will be introduced by attaching the horns after calibration but this will be relatively small compared with the internal VNA system losses whose influence is removed by this calibration procedure.

7.3: Perfect Crystal

The transmission response for the perfect crystal was examined for various crystal thicknesses. The transfer matrix method, TMM, was utilised for the theoretical calculations[21,50]. The calculations assumed that the crystal has a finite thickness in the z -direction but was infinite in the xy -plane.

Due to the limited frequency range of the experimental set-up only the lower band edge results are presented as the upper band edge is outwith the measurable range. As the number of periods increases in the propagation direction the PBG behaviour strengthens. This causes the lower band edge gradient to increase, a result predicted and echoed in the experiment. The TM transmission results are shown in Figure 7.2 for normal incidence in the z -direction.

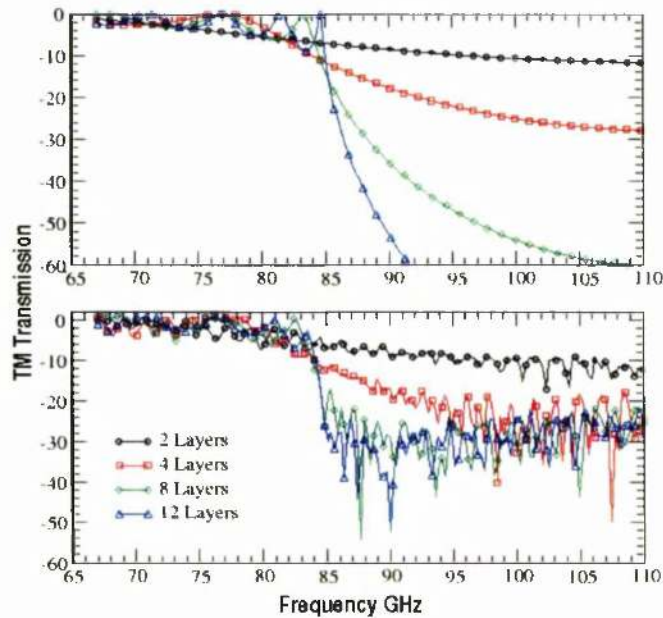


Figure 7.2 Perfect crystal response.

TM transmission response versus frequency as a function of the number of layers of dielectric bars. The response has been shown for a crystal that is 2,4,8 and 12 layers thick by using a circle, square, diamond and triangle respectively.

The noise floor in the experimental set up limits the transmission measurements to an a minimum level around -30dB. For a finite thickness crystal the number of periods influences both the upper and lower band edges. As the number of periods increases the lower band edge moves upwards in frequency as the photonic band gap effect strengthens; in this instance the lower band edge develops around 85GHz. The characteristic Fabry-Perot resonances associated with finite size structures can be seen as ripple in both the

theoretical curves and in the measured results at lower frequencies leading up to the lower band edge.

The band structure is shown in Figure 7.3 for a TM polarised wave incident onto the same, but infinite, crystal. Figure 7.3 shows that the lower band edge is at 86GHz and the upper to be at 131GHz. The unit cell has been normalised in units of π/a , where a is the lattice constant. The wave vector is in units of cell length.

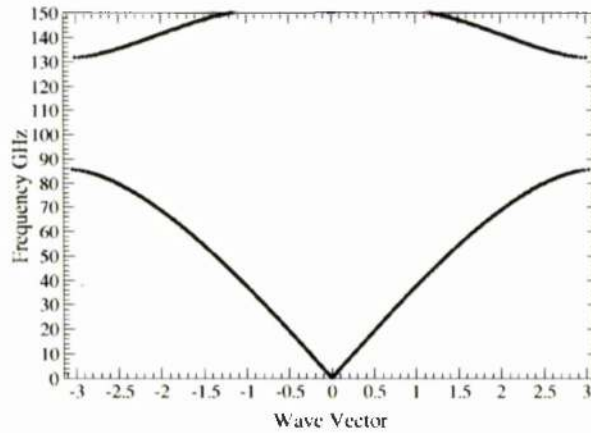


Figure 7.3 TM Band structure, perfect crystal.

Allowed bands for the infinite photonic crystal, normal incidence.

Changing the external incidence angle from normal incidence in the xz - or yz - planes degrades the width and attenuation within the gap region as shown in Figure 7.4. At close to oblique incidence within the periodic plane the band gap is located between 84 and 108GHz, some 25% bandwidth with a maximum attenuation of 97dB compared with 42% bandwidth and an attenuation of approximately 25dB for normal incidence. Consequently increasingly oblique incidence decreases the bandwidth of the gap while increasing the attenuation through the structure due to the asymmetry of the structure cell.

Altering the incidence angle in the yz - plane degrades both the bandwidth and attenuation of the band gap region. This is caused by the increasingly compromised periodicity as the incident wave angle deviates from the periodic plane. This finding has also been reported by Sigalas[51] for a periodic hexagonal lattice. As the incidence angle in the yz - plane becomes more oblique there is a rapid upward frequency shift in the lower band edge. When the yz - incidence angle is 50° the PBG region has moved to approximately 100-138GHz, some 32% bandwidth with a maximum attenuation of 20dB.

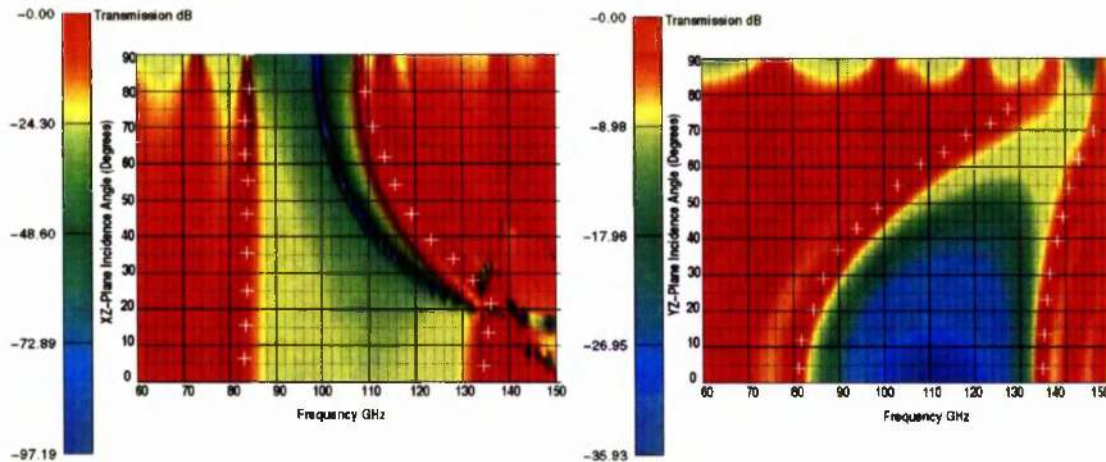


Figure 7.4 In & Out of Plane Angular Response.

The TM transmission response for an angular scan within *Left*: the periodic xz -plane, *Right*: the yz -plane. The upper and lower band edges have been marked with the '+' symbol.

7.4: Planar Cavity Defect

The planar cavity defect in the crystal is created by removing the central row of bars perpendicular to a normally incident propagating plane wave. Figure 7.5 shows the theoretical transmission response for the defect and perfect crystal case. Both crystals have a total thickness of 3.95mm equivalent to 5 silicon bar layers plus 5-spacing elements required to generate the periodic pattern. An inset has been included in Figure 7.5 to show the planar cavity defect crystal and cavity length L_c .

The planar cavity causes a defect state to appear within the PBG region of the crystal at 106GHz. The frequency of the defect can be tuned by altering the length of the defect cavity, L_c to accurately tune the defect mode [46]. For the defect case depicted in Figure 7.5 the upper and lower band edges have moved apart when compared to the perfect crystal case. This is due to the combined effect of the introduced defect and a reduction in the total number of periods within the crystal.

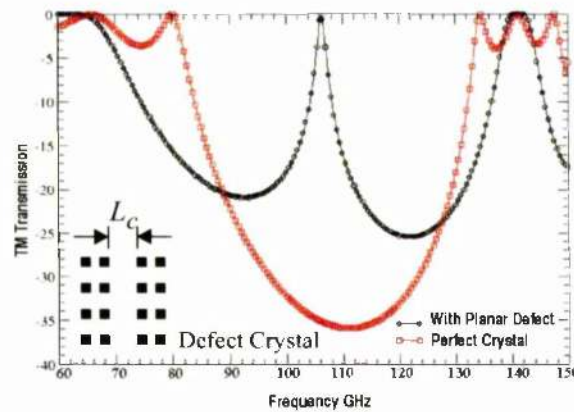


Figure 7.5 Cavity transmission, normal incidence.

TM transmission response for a perfect 5 layer photonic crystal (*squares*) and for a planar cavity defect introduced centrally into the crystal (*circles*). The inset shows the planar cavity within the crystal with cavity length L_c .

Utilising the defect frequency for normal incidence, the total cavity length including the penetration depth can be derived from Equation (7.1) as $L=1.415\text{mm}$. From the crystal geometry and the actual cavity length of $L_c=1.19\text{mm}$ the penetration depth is calculated to be $L_p=112\mu\text{m}$ at both ends of the cavity.

As the external incidence angle is varied theoretical calculations predict that the frequency of the defect state rises for increasingly oblique incidence. Figure 7.6 shows the transmission response for both the xz - and yz - planes for the crystal with the planar cavity defect as a function of plane wave incidence angle. The defect frequency is found at 106GHz for normal, 0° , incidence for both planes.

For increasing incidence angle in the xz - plane there are two notable characteristics, firstly that the defect mode frequency moves upwards in frequency, and secondly that the lower band edge has dropped in frequency. The sensitivity in the lower band edge frequency arises from reduction in the number of periods of the crystal, an effect that is exaggerated in this instance as the crystal is only a few periods thick.

The increasing central frequency of the defect, as the incidence angle within the periodic plane is altered, occurs as the effective length of the planar cavity is correspondingly reduced. The effective cavity length is given by $L_{\text{ceff}} = L_c \cos\phi$, where ϕ is the angle of incidence but the penetration length L_p also changes. As the cavity length decreases the resonance frequency of the cavity increases. Recent work by Centeno has also shown this

tuning effect for changing incidence angle for localised defects within photonic crystals [52].

For the xz - plane the defect mode merges with the upper band edge at an incidence angle of approximately 50° at a frequency of 113 GHz. For the yz - plane the defect mode gradually merges with the band edges at approximately 70° incidence angle.

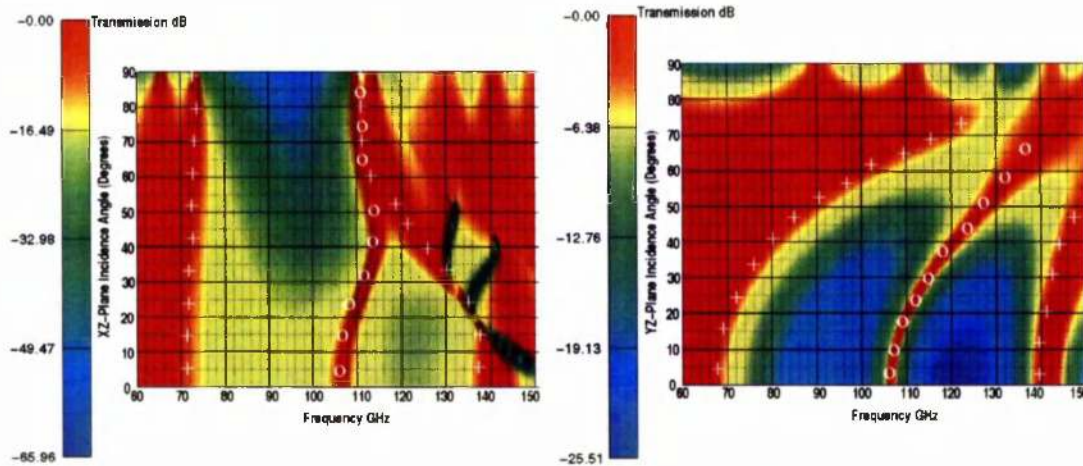


Figure 7.6 TM Defect In- & Out of plane response.

Left: In-plane *Right:* Out of Plane TM transmission response for a planar cavity defect in the centre of the crystal as a function of external incidence angle. For normal incidence, 0 degrees, the defect can be seen at 106GHz. The upper and lower band edges have been marked with the + symbol, the defect with an 'o' to aid the eye.

Using the same experimental set-up, the TM transmission response for a planar cavity defect centrally located within the crystal was measured. The measured results for several discrete angles in the xz - plane are shown with the corresponding theoretical curves in Figure 7.7. The agreement between theory and measurement is excellent. For the given experimental set-up TE polarised waves are completely transmitted through the structure and consequently are not examined.

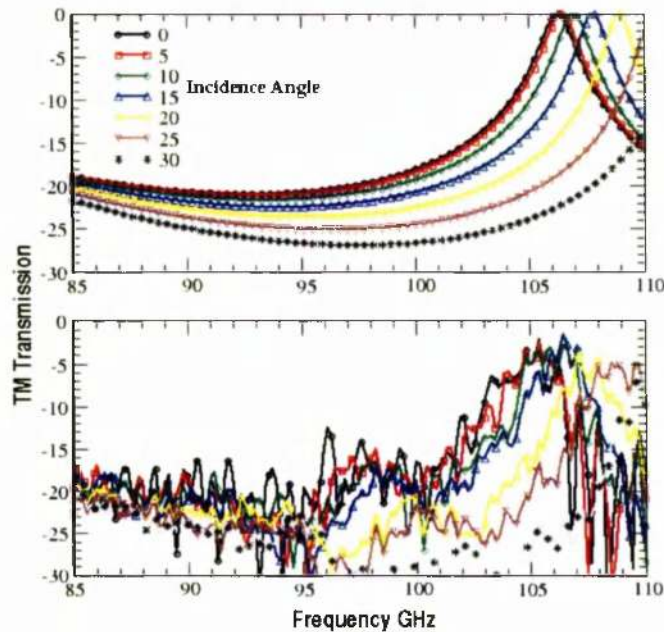


Figure 7.7 Angular xz -plane transmission response.

Top: Theoretical response for the defect transmission as a function of external incidence angle. Bottom: Measured results.

7.5: Conclusion

A 2-dimensional photonic crystal has been characterised using the transfer matrix method for both in-plane and out of plane propagation for the defect and perfect crystal case. Experimental results from a crystal made for operation at microwave frequencies are presented and found to be in excellent agreement with the theoretical results.

The defect mode frequency generated by introducing a planar cavity defect into the crystal was found to be angular-dependent. The angular dependence of the defect state may play an important role in directional and tunable filters for both microwave and integrated optics applications. By using a wide band emitter in conjunction with a crystal with a planar cavity, an angular filter with thickness controlled quality factor, Q , can be created. The angular dependence of a planar cavity introduced into a woodpile crystal has been demonstrated by Temelkuran [32] by measuring the radiation pattern of an antenna that was inserted into the cavity. The radiation pattern was found to be highly directional.

Localised Defects in Hexagonal Photonic Crystals

Introduction

In the previous chapter the introduction of a planar cavity defect into a square lattice photonic crystal gave rise to a defect state into the transmission response of the crystal. While previous work has examined photonic crystals with the introduction of more than one localised defect as a function of distance [54], in this a superlattice of defects is introduced into an otherwise perfect hexagonal lattice of air holes in dielectric. The effect of localisation is investigated by altering the number of lattice constants between neighbouring defects.

The defects are introduced into the hexagonal lattice by altering the size of one or more of the constituent features of the lattice. This hexagonal lattice is created by placing air cylinders into dielectric material. The defects were created by completely in-filling a superlattice of periodically spaced air cylinders within the crystal. By placing defects periodically throughout the crystal, the creation of mini bands within the photonic band gap occurs. A mini-band is created by two or more allowed bands in close proximity to each other. If they are located within a band gap region then the transmission response shows a region of transmission with two or more peaks rather than a single localisation frequency.

The dependence of the defect mode or mini-band width and position is investigated as a function of the cross-talk or coupling between defects

within the lattice. Cross-talk minimisation or defect isolation was achieved at a much faster rate than was at first expected. The defect mode band was found to have directional and width dependence as a function of the distance between defects for the two lattice directions, ΓK and ΓM , studied.

8.1: Motivation

It has been shown that perfect photonic crystals have application as reflectors for a wide range of applications ranging from antenna systems to their already current usage as reflective optical coatings. In general these applications assume that the crystal is being used as a complementary device in their application and as such is not an integral part of the device.

As photonic crystals have rejection bands which specifically forbid propagation, they also forbid spontaneous emission. By controlling spontaneous emission, or suppressing it completely, the opportunity to control and enhance the efficiency of optical devices such as light emitting diodes (LEDs), and lasers is enormous. Efficiency close to 100% have been theoretically predicted. Defects introduced into a photonic crystal have very particular properties and their frequency dependence and quality factor, (Q), amongst other properties can be engineered to suit their intended application.

Within LEDs defects can be used as emitters with the surrounding PBG lattice suppressing propagation and enhancing the emission characteristics. If an array of emitters can be used then the emitted power of the “chip” can be increased. Therefore insight into the effects of cross-coupling between defects would be interesting and also act as a gauge as to how close together the emitters can be placed.

Previous work [8] has shown an interesting application of particular photonic crystals as waveguides where a continuous channel of crystal has been removed in an otherwise perfect 2-dimensional crystal to form the waveguide. Such systems have been made from square lattices of dielectric cylinders such that the waveguide has been made from air. Bends of 90° have been introduced into the waveguide but suffer consequential insertion loss due to reflection [55,56]. Such systems also have light containment problems in the third or vertical direction and serious device integration, coupling and fragility problems. If a hexagonal lattice is employed rather than a square lattice then reflection at the bend still

occurs and once again parasitic loss mechanisms are introduced into the system. By employing the inverse lattice, such that air holes are introduced into a dielectric material, then a similar waveguide can be formed by in-filling a chain of holes or by separating two pieces of similar crystal, see Figure 8.1.

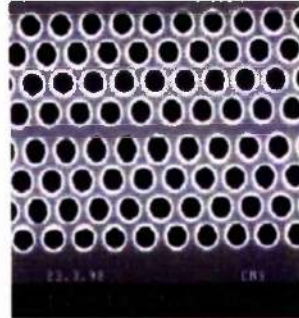


Figure 8.1 A planar defect introduced into a hexagonal lattice photonic crystal.

With the kind permission of Dr. Christopher Smith.

Such systems then guide within the dielectric channel and have the added benefit that guiding is maintained within the periodic plane by total internal reflection, which was not the case for the guide made from air. Compatibility with other semiconductor devices relative to integration and coupling issues is also overcome. However these dielectric guiding systems also suffer from reflections at bends introduced into the waveguide, consequently performance comparisons should be kept in mind with conventional waveguide corner techniques.

By altering a continuous dielectric guide to be a periodic chain of lattice sites that have been either completely or partially in-filled then the coupling properties of the defects can be used to form coupled resonance optical waveguides, CROWs. Light can still be guided within the crystal and bends can be introduced into the waveguide path by taking advantage of the crystal's inherent lattice symmetry, without consequential bend reflection loss [57,58]. Experimental verification of wave guiding has successfully been demonstrated for various photonic crystals in the microwave regime by Bayindir, Temelkuran et al.[56,59-61]

8.2: Hexagonal Lattice Definitions

The perfect crystal

A section of the hexagonal lattice studied is shown in Figure 8.2 and the two main crystal directions are labelled within the figure. The refractive index of the material was chosen to be $n_{\text{material}}=2.81$ resulting in a dielectric constant of $\epsilon_r=7.9$, figures representative of the effective index of a GaAs waveguide that is $\lambda/2$ thick and that has oxidised AlGaAs on one side, $n_{\text{AlOx}}=1.6$, and air on the other for application at $1.5\mu\text{m}$. The air cylinders in the material were chosen to have a ratio of radius, r , to lattice constant, a , of $r/a=0.35$ to emulate the fabrication scenario.

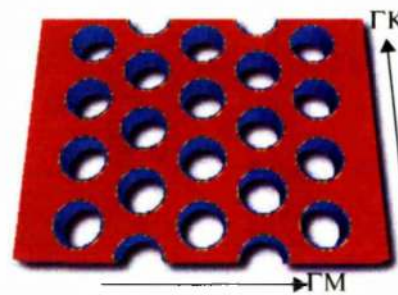


Figure 8.2 Section of Hexagonal lattice showing the two propagation directions studied.

Periodic defects

The results presented are frequently shown with evolutionary curves for the number of cells of photonic crystal over which the transmission analysis has been carried out. A cell is defined as the smallest building block that self-repeats to generate the crystal, some examples of the “cells” including periodic defects are shown in Figure 8.3.

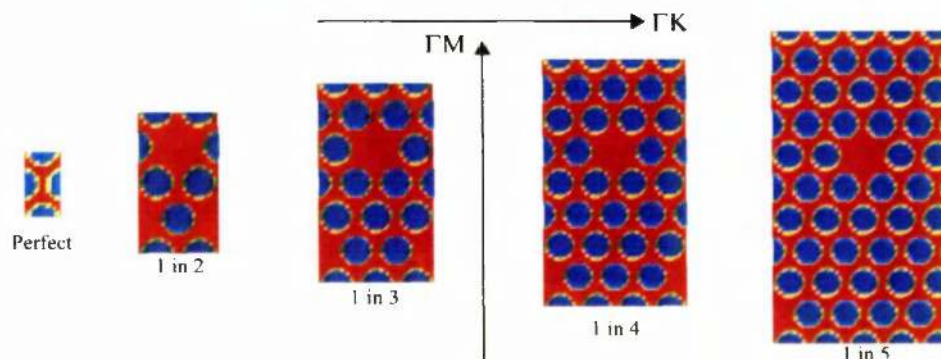


Figure 8.3 “Cells” used to build the perfect and hexagonal lattices.

Shown from left to right are the cells used to build the perfect hexagonal lattice, the defect lattices, one in two, one in three, one in four, and one in five for analysis in either the ΓK or ΓM directions as shown in the figure.

Perfect Crystal Results

Before defects were introduced into the crystal, transmission analysis for TE polarised waves was carried out for the perfect crystal in both the ΓK and ΓM directions. For the range of normalised frequency studied the TM polarised waves do not display photonic band gap behaviour and therefore are not studied.

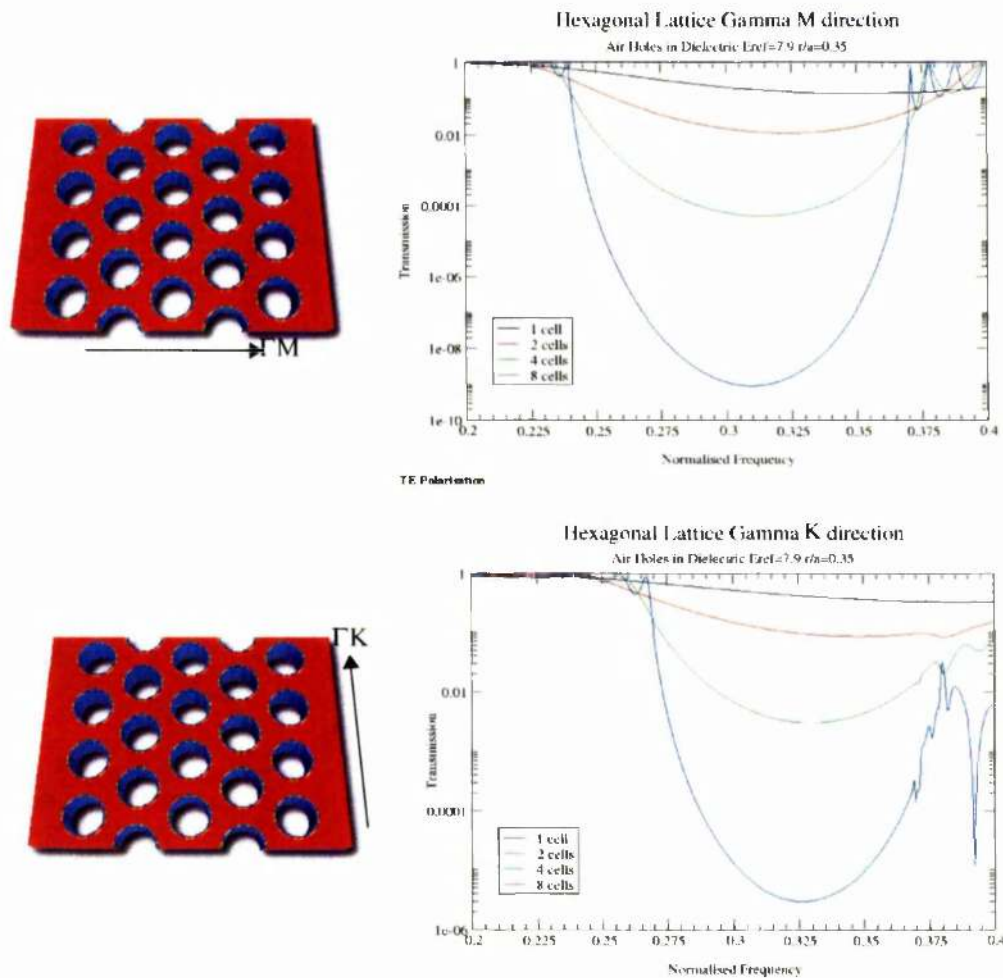


Figure 8.4 Perfect Crystal: TE Polarisation Response for the ΓM and ΓK directions.

The TE Polarisation transmission response for photonic crystals 1,2,4, and 8 cells thick.

The response for the perfect crystal displays the expected parabolic attenuation response within the stop band of the crystal. The ΓK response shows less attenuation for the same number of cells compared to the ΓM direction; this is not unexpected due to the symmetry of the lattice.

8.3: Defects: One in every two, ΓK & ΓM

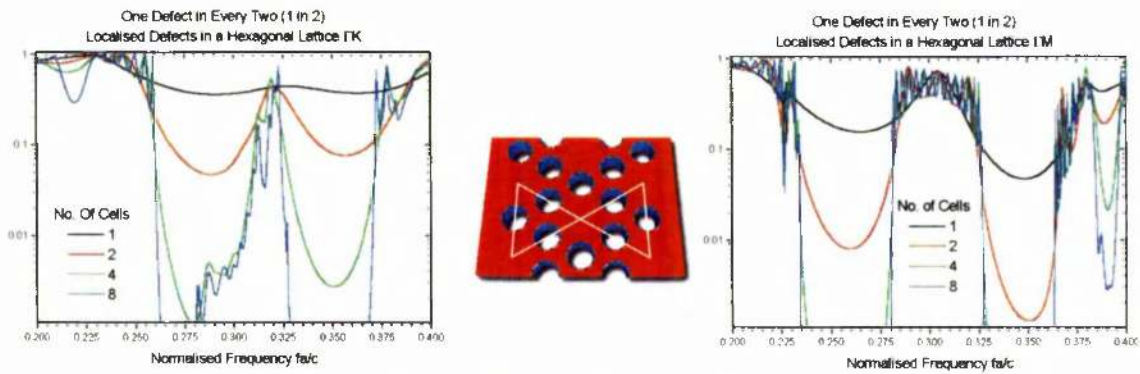


Figure 8.5 Periodic Defects: One in every two, ΓK & ΓM .

The transmission response of a TE polarised wave as a function of normalised frequency and crystal thickness expressed in terms of the number of cells through which the wave has been propagated, definitions of cells given in *Figure 8.3 on page 114*. Defects have been introduced periodically along the high symmetry axis of the crystals one in every two lattice spacings. *Left: ΓK response. Right: ΓM response. Centre: Cell schematic showing filled in lattice sites one in every two in the high symmetry lattice directions.*

Figure 8.5 shows the TE polarised wave response as a function of normalised frequency for various crystal thicknesses and for a superlattice of defects introduced once in every two lattice spacings. By filling every second lattice site in the high symmetry axis directions, a defect band is immediately obvious in both lattice directions although the width of the mini bands which are formed is substantially different. For the ΓK direction the introduction of the defect causes the appearance of a considerably narrower mini band than for the ΓM direction.

The defect band for the ΓK direction is found at a normalised frequency of approximately 0.325. The mini band forms slowly as a function of crystal thickness, mildly visible for a single cell, considerably more pronounced for two cells and then well localised for further increases in crystal thickness. The mini-band for the ΓM direction is already notable for one cell of the structure and is centred at a normalised frequency closer to 0.30. In strict contrast to the ΓK direction, as the thickness of the crystal increases in the ΓM direction, the mini-band covers a range of normalised frequency from 0.280 to 0.325. Consequently the coupling in the ΓM direction when defects are introduced one in every two lattice spacings is stronger than that for the ΓK direction. This is a finding that can be used to our advantage if a wide band response is required, an application idea which is expanded later in this chapter.

8.4: Defects: One in every three, ΓK & ΓM

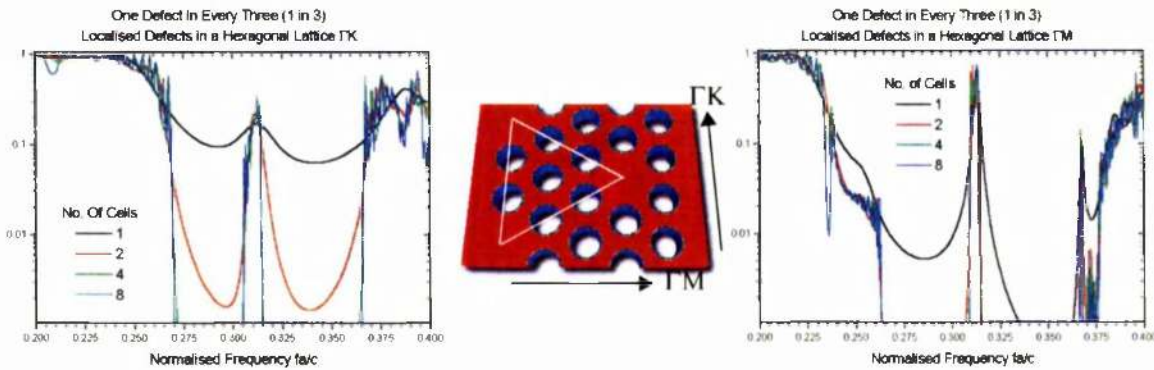


Figure 8.6 Periodic Defects: One in every three, ΓK & ΓM .

The transmission response of a TE polarised wave as a function of normalised frequency and crystal thickness expressed in terms of the number of cells through which the wave has been propagated, definitions of cells given in *Figure 8.3 on page 114*. Defects have been introduced periodically along the high symmetry axis of the crystals one in every three lattice spacings. *Left: ΓK response. Right: ΓM response. Centre: Cell schematic showing filled in lattice sites one in every three in the high symmetry lattice directions.*

When the defects are introduced into the lattice by filling in every third lattice site in the high symmetry directions both ΓM and ΓK directions show a high degree of localisation. *Figure 8.6* shows the TE polarised wave transmission response versus normalised frequency as a function of crystal thickness in terms of cells. Note that due to the definition of the cells, (see “Periodic defects” on page 114), that the actual physical length per cell in the propagation direction is larger for the defects introduced one in every three than for the one in two lattices. The “one in three” inset from *Figure 8.3 on page 114* shows the cell that is used for the calculations.

The transmission response for either lattice direction show marked localisation at a normalised frequency of $fa/c=0.31$. This localisation is even present for a single cell but this is attributable to the increased number of lattice periods required to build the cell. As the number of cells increases the localisation frequency does not alter significantly and the mini-band forms as expected, see *Figure 8.7*. The mini-band formed is however much narrower than that of the “one in two” defect superlattice as presented in *Figure 8.5*.

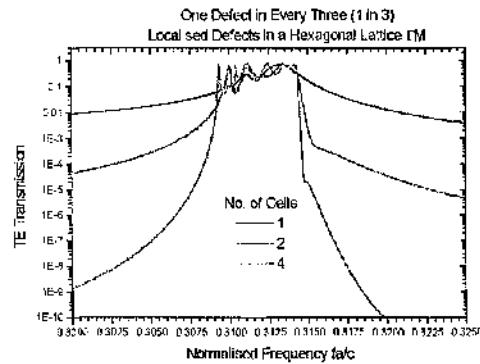


Figure 8.7 Closer look at 1 in 3 defects in the ΓM lattice direction.

The TE polarised wave transmission response for a superlattice of defects introduced into the lattice by in-filling every third lattice site in the high symmetry directions of the lattice. The response is plotted against normalised frequency as a function of the number of cells through which the plane wave has been propagated.

There is asymmetry present in the transmission response shown in Figure 8.7 which may be attributed to possible plane wave coupling issues. It is noteworthy that the number of oscillation peaks present in the mini band is directly attributable to the number of defects encountered by the plane wave.

For any given superlattice of defects, the single cells shown in Figure 8.3 on page 114 each incorporate the lattice sites of three defects. This is necessary to cover the primitive cell that has been highlighted with a triangle in the central insets of either Figure 8.5 or Figure 8.6 with an orthogonal discretisation mesh. For example a plane wave propagating in either lattice direction for the “one in three” cell shown in Figure 8.3 encounters successive columns of air holes, two of which contain defects. Therefore for the single cell response shown for the “one in three” defect superlattices in Figure 8.6 the transmission response contains two peaks in the mini band region. For the two cell response, two single cells must be bolted together. For the ΓM direction this results in three columns which now contain defects, as a defect site is shared between cells; hence there are three peaks in the two cell mini band transmission response. This finding is true for any number of coupled defects.

8.5: Superlattice evolution

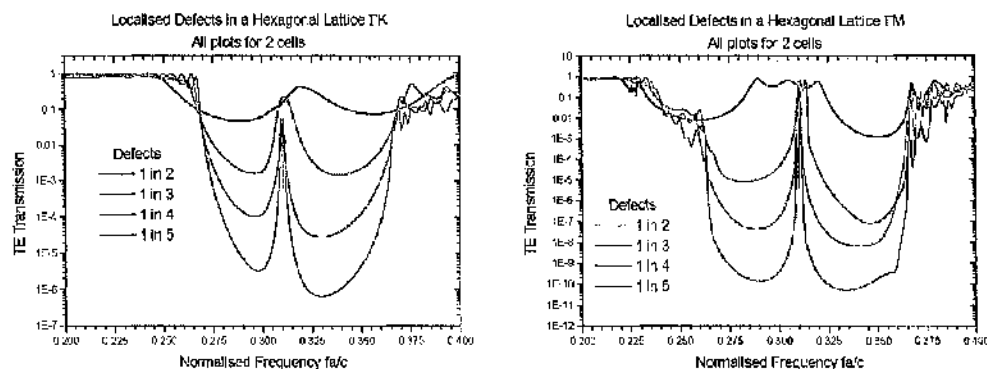


Figure 8.8 Evolution for superlattice spacing.

The TE polarised wave response against normalised frequency as a function of the neighbour to neighbour defect superlattice spacing.

The TE transmission response as a function of the neighbour to neighbour defect superlattice spacing is shown in Figure 8.8 for transmission through two cells of structure. The plots clearly show convergence of the defect mode localisation frequency as the distance between the defects increases. The most noteworthy curve is for the ΓM direction for a defect superlattice of “one in two” shown in the right inset of Figure 8.8. As discussed previously the mini-band formed by this defect lattice is wide band when compared to the next defect lattice of “one in three”, or to the same defect superlattice for transmission in the other crystal direction. This means that the defects are coupling strongly to each other. When the distance is increased to “one in three” rather than “one in two” between neighbouring sites the coupling decreases, the width of the mini-band formed is substantially decreased.

Both lattice directions show localisation towards a normalised frequency of $fa/c=0.310$ as the distance between defects is increased. The quality factor of the defect state is also improved by increasing the distance between defects which results in an increased reflectivity between defect sites, an effect already discussed in the chapter entitled “Tuning Planar Cavity” on page 101 within the introductory remarks. This means that for certain applications the quality factor, Q , of the system can be engineered to match either the wanted Q or to increase the coupling efficiency between the photonic crystal chip and other emitting components.

Applications

In summary, future devices would benefit greatly from using coupled defects to guide electromagnetic radiation. Bends in coupled defect chains can be introduced along the crystal's inherent symmetry axis with no insertion loss i.e. mode mismatch due to bends in straight wave guiding does not occur. The Q-factor of the defect state can be tuned to suit the intended application as can the localisation frequency by altering the type of defect introduced into the lattice. It is noteworthy that the defects introduced into a lattice need not necessarily be a superlattice themselves, nor involve the complete filling of lattice sites. Chains of defects in a straight line with a periodic pattern will suffice to guide a signal through a photonic crystal chip.

For example, a frequency splitting or combining Y junction could be formed by employing a wide band guiding system which then splits into two directions each supporting a different localisation frequency, see Figure 8.9. Defects introduced one in every two lattice sites for TE polarised waves show for the Γ M direction a wide "mini" pass band. By then using the hexagonal lattice's inherent symmetry this chain could then be split into two, with different chains of defect lattice used in each of the branches supporting different defect localisation frequencies and Q-factor, engineered as required. In much the same way, planar waveguide filters could also be realised. This is an idea worthy of future research both experimentally and theoretically.

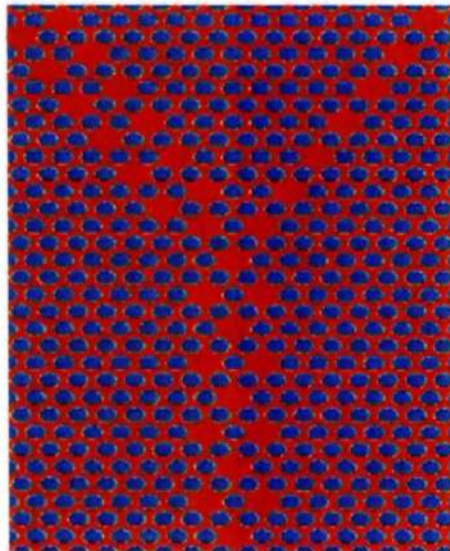


Figure 8.9 An idea for a Y-Splitter

Introduction

It is now well acknowledged that periodic systems can be used to control the propagation of electromagnetic radiation [1,2,8,62,63]. These systems can be made with relative ease for low frequency applications while the fabrication of their optical counterparts is considerably more complex due to the vast reduction in the crystal size and lattice period [64]. This has been the main motivational factor in the study of self-ordered systems such as colloidal crystals, three dimensional arrays of periodically ordered structures which can be made from dielectric spheres [65,66]. The synthetic opals studied here are made from either silica, SiO_2 , or PMMA spheres that self organise into an ordered face centred cubic, f.c.c., lattice.

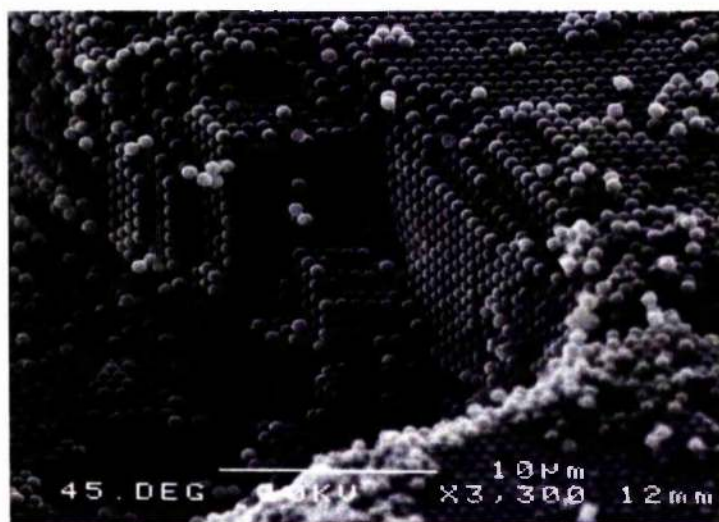


Figure 9.1 SEM Micrograph of a shear ordered PMMA Opal
Reproduced with kind permission from the authors [67]

9.1: Motive

Fabrication of artificial opal can be achieved via various techniques. However all methods build on the property that the dielectric spheres, the constituent particles of the crystal, self-organise themselves into a face centred cubic, f.c.c. crystal, see Figure 9.2 .

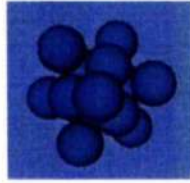


Figure 9.2 The face centred cubic cell.

After fabrication the opal may then be post processed. The resultant opal may display either partial or complete photonic band gap behaviour depending on the size and constituent material of the particles and the host medium within which they are embedded. With small enough spheres and lattice period the photonic band gaps can be observed at optical wavelengths, thereby opening opportunities for telecommunications and other applications.

In simple form a bare opal is made from silica spheres in air and has a weak refractive index contrast, (1.5:1). Such opals do not possess complete gaps even when the voids between the spheres are in-filled with semiconductor material [68-75]. However inverted opals¹, which have the inverse dielectric matrix to that of bare opals, can now be realised due to advances in fabrication technology [76,77]. Band structure calculations have shown that inverted opals have complete photonic band gaps between the eighth and ninth bands[78]. The existence of the complete band gap is conditional on the refractive index contrast ratio between the spheres and embedding medium. If the ratio contrast between the embedding medium and the spheres is greater than 2.9, assuming that the voids are completely in-filled, then a complete gap exists [75].

The main challenge still lies in the fabrication process of the crystals where large crystal sizes and crystal purity remain important issues. Crystal impurity degrades the performance of the crystal. Normal deposition and etch techniques for three dimensional photonic crystals are expensive and become increasingly complicated for structures that operate in the optical domain. Self-organising colloidal crystals are however, comparatively cheap.

1. fabrication issues concerning opals are discussed briefly see "Crystal types" on page 124

There are still many questions to be answered over device application and integration, but the reproducibility and purity of opal crystals remains an important issue.

Through the theoretical study of colloidal crystals a greater understanding of their possible performance can be obtained. This not only provides insight and allows prediction but also arms the experimentalists with guidelines and a set of absolutes to help enhance the performance of their colloidal crystals.

Aims & Objectives

The initial phase of the European funded PHOBOS project investigated the performance of opals in terms of both band structure and transmission. These were then investigated as functions of direction of propagation, filling factor and other fabrication related properties such as inversion, coating and sintering. Sintering is a post fabrication thermal process which partly merges the constituent spheres adding mechanical stability to the structure. Evidently the combinations of these are rather extensive so the study was limited to particular ‘types’ of opal, some simple combinations, and the two main common crystal directions of propagation, the [100] and [111] directions, see Figure 9.3.

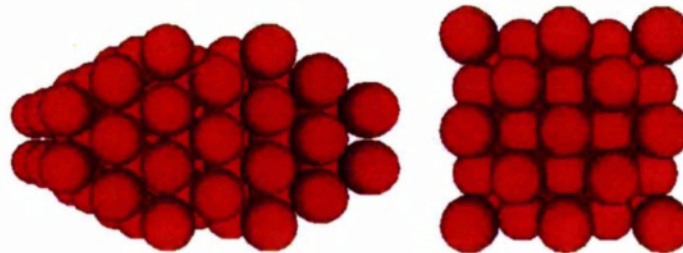


Figure 9.3 Opal [111] and [100] surface truncations.

The definitions of the surface plane truncations as seen by a plane wave arriving into the page.

In collaboration with the University of Montpellier II, as part of the PHOBOS project, Dr. David Cassagne performed plane wave expansion calculations to determine the band structure of opals and also developed an order-N code to investigate the evolution of the bands as functions of coating and sintering effects. With his kind permission some of those calculations are included to provide a comparison to the results calculated using the transfer matrix method.

9.2: Crystal types

Normal / Bare opal

Normal opals consist of dielectric spheres packed into an embedding medium; these systems self-assemble and may take the form of close packed, face centred cubic, f.c.c., lattice. This bare opal is often the template that is used in fabricating inverted, coated and sintered opal systems. There are two forms of the pure f.c.c. lattice available, the ABC and ACB repeat pattern lattices, where each letter refers to a single monolayer. In pure form the differences are in definition only. For all variants of opal the properties can be adjusted by altering the filling ratio, the materials used for the spheres, coatings, and host medium and by adjusting the level of sintering.

Inverted opal

These systems are the dielectric inverse of a normal opal. They may consist of air spheres embedded in a background dielectric medium. Their fabrication follows that of a normal opal, after which the opal is completely infiltrated with a background medium. After completion of the infiltration the original opal is removed by the usage of an etch step resulting in air spheres in a background medium [76].

Coated opal

Coated opals come in both inverted and normal form. Fabrication is similar for both with normal opal, dielectric spheres in the background medium being fabricated first. After completion of this step, the background medium, which may have been a fluid is drained and replaced with another. This later infiltration of the opal can either be complete or incomplete. The result is a coating which is applied over all non-touching parts of dielectric spheres. Thereafter, if required, another etch step to remove the dielectric spheres can be carried out resulting in an inverted, coated opal. The coatings assumed in these calculations try to reflect the fabrication process; they cover only non touching areas of the spheres and are assumed to be uniform in thickness.

Sintered opal

Sintered opals are created through heat treatment of the various other opal systems. The effect of the heating is to cause the dielectric spheres to merge slightly, in effect causing a circular cross section between neighbouring spheres. Sintering results in better connectivity between the spheres while simultaneously reducing the fragility of the structure. In these

calculations sintering is assumed only to shrink the lattice spacing while fixing the radius, no shape distortion of the sphere is included, see Figure 9.4. Shape distortion is likely to alter the response to a marginal extent, the performance of the colloid being more sensitive to the lattice type and material rather than the individual atoms.

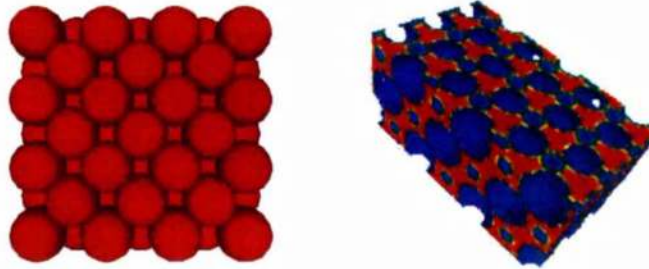


Figure 9.4 Sintered & Inverted opal

Example of a Sintered opal (100) (left) and an Inverted opal (111) (right). Note the small overlapping areas between the spheres for the sintered opal. For the inverted opal red areas (dark) represent areas of high dielectric constant and scale down through the colour spectrum to blue (light) representing air. The pure air spheres have been removed to aid understanding of the visualisation.

Throughout the calculations, unless stated otherwise, the refractive index of the spheres was assumed to be $n_{\text{sphere}}=1.5$, coatings when applied were assumed to have an index of $n_{\text{coating}}=3.0$.

9.3: Unit Cell Approach

Conventional Cell

One of the inherent difficulties with modelling the opal system is that the simplest cubic unit cell used to make a face centred cubic, f.c.c. lattice configuration contains volumetric sections of dielectric spheres. To construct an f.c.c. lattice, spheres are centrally positioned on each vertex and face of the cube. This requires a total of fourteen individual spheres to build the cell. In order to achieve a good representation of the cell a large sampling matrix is consequently required, making theoretical modelling a complicated and time consuming task.

The images within Figure 9.5 overleaf depict the cells required to build a realistic block of the opal crystal for analysis in the [100] direction. The central cell can be repeated as required to provide a block of opal although without the addition of the front and rear interfaces for the block the representation of the opal is somewhat unrealistic. However, usage of an initial front interface, a block of crystal, and then a final rear interface does not

drastically alter the performance of the crystal and can be ignored for crystals that are larger than a few conventional cells thick.

As with many photonic crystals there are a few vital formulae that are used. We can define the filling ratio for the cell, Equation 9.1 but this is only valid for values of radius where the close packed condition, Equation 9.2 is not exceeded, i.e. $radius\ r \leq Radius_{Close\ Packed}$

$$\text{Filling Ratio} = \frac{16\pi r^3}{3a^3} \quad (9.1)$$

For the close packed system, the radius of each sphere is related to the lattice constant through the relation:

$$\text{Close Packed Condition: } a = 2r\sqrt{2} \quad (9.2)$$

For the close packed situation the filling ratio is 74.04%. Reduction in the filling ratio from 74%, the condition for a close packed lattice, results in an ever increasing distance between neighbouring spheres, breaking the connectivity of the lattice. The simplest way of creating an opal is shown below in Figure 9.5, the front interface cell, central conventional cell and rear interface cell are shown.

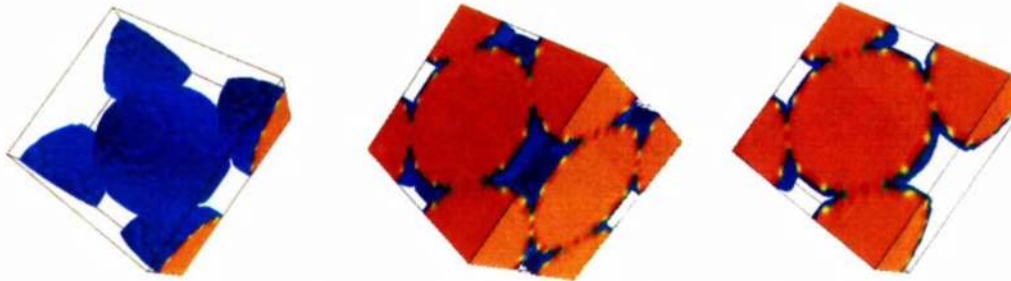


Figure 9.5 Front, Conventional, and Rear Cells to construct opal [100]

The colour scale ranges from air (blue) to pure material (orange). Pure air has been removed to aid visualisation.

When using the conventional unit cell a large matrix is required to represent the central cell in the figure above and numerical instabilities within the code can arise. To further complicate the matter the analysis of coatings and sintering demands a mesh that will sufficiently discretise the cell such that the effects are noted; a larger discretisation mesh is therefore required. It was decided to exploit the inherent symmetry within the central cell and to split the cell calculation in two, overcoming some inherent numerical problems, and allowing a slightly finer discretisation mesh to be employed.

Split Cell

Within the general unit cell the unit cell was split in half in order to obtain better resolution and representation of the opal cell. The front and rear interfaces remain the same as shown in Figure 9.5, while the new cells constituting the conventional cell are shown in Figure 9.6.

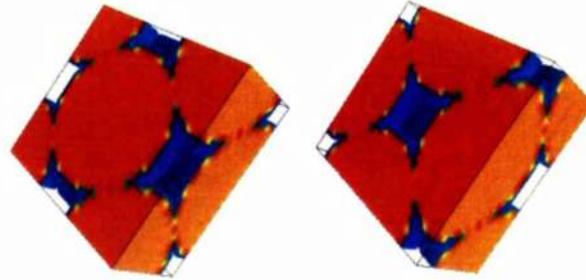


Figure 9.6 Split Cell opal [100]

With the split central cell larger matrices can be employed to sample the structure and hence the effect of thin coatings can be studied more accurately. The usage of larger central matrices also results in better convergence of the results. There is however one problem with using the split cell method; because the matrix sizes are large it was not possible to include the front and rear interfaces for the calculations as at the time there was insufficient computer memory. Comparative calculations in 2-dimensions demonstrated that the front and rear interface cells have little influence on the performance of the crystal once the thickness is above a few crystal periods.

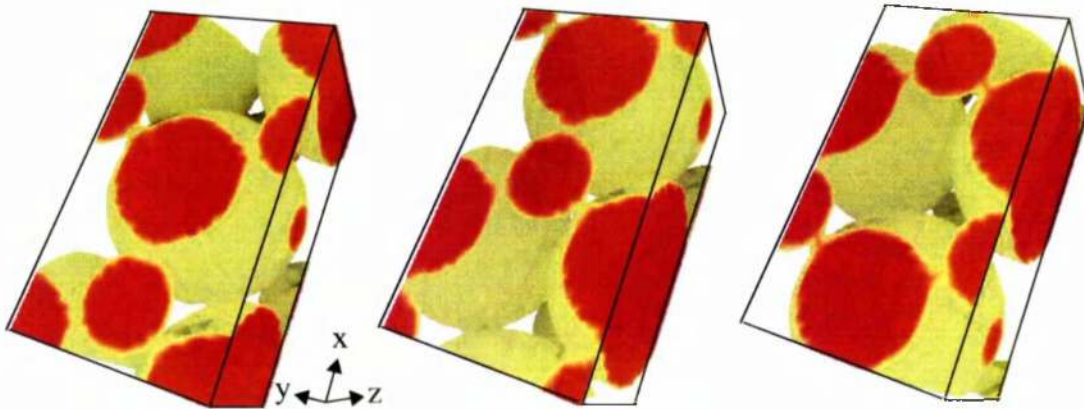


Figure 9.7 Split Cell opal [111]

The three constituent layers that are used to build the ABC repeat pattern for normal incidence in the [111] direction.

The split cell method was also used to change normal incidence to the [111] direction. Figure 9.7 shows the three cells that were used to build the ABC repeat pattern to form the

f.c.c. lattice. A hexagonal close packed lattice, h.c.p. can also be formed in a similar way and requires only two cells to achieve the required periodicity.

Matrix Processing Time Considerations

While there is no limit to the number of points that can be used in the mesh to represent a structure, the representational structure matrix determines the size of the transfer matrix employed in the calculation. For 3-dimensional systems the computational time is a serious consideration, a matrix size of $14 \times 14 \times 7$, ($18 \times 10 \times 7$) used to sample the cell in the x, y and z directions respectively for [100], ([111]) opal requires a considerable amount of time to run. Present day computer systems take between 20-30 minutes for one frequency point depending on the thickness of crystal analysed. Therefore the computational demand for such calculations is severe and the utilisation of parallel super computing is beneficial. The utilisation of multiple processors on a super computer can cut the time for the same calculation considerably. To this end the transfer matrix code was made parallel using the Message Passing Interface, MPI, and run on an IBM SP2 super computer.²

9.4: Bare Opal

Transmission along the [100] direction

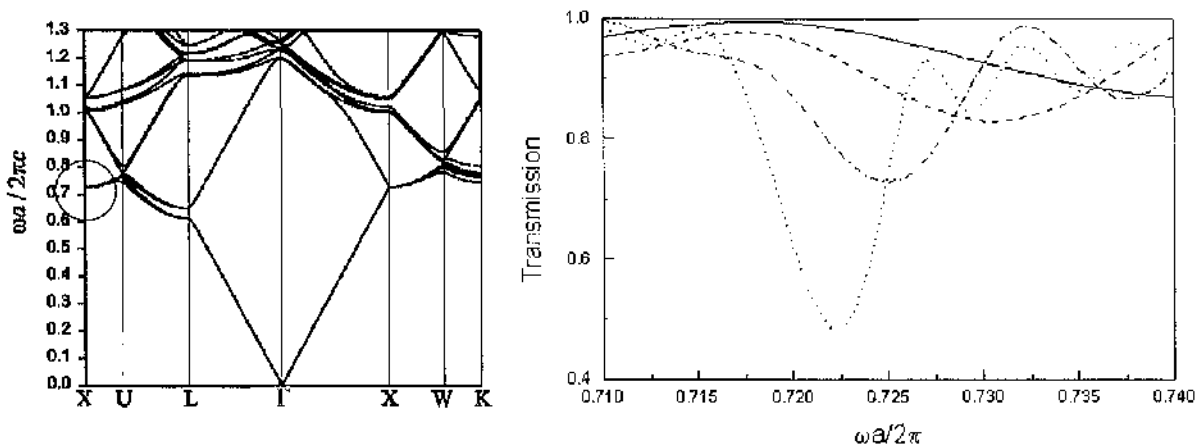


Figure 9.8 Band structure & [100] transmission response.

Left: Band structure diagram of a bare opal showing the high symmetry points in the Brillouin zone. The Γ point corresponding to the [100] direction has been highlighted with a circle. *Right:* Transmission as function of number of lattice planes in the [100] direction for the opal crystal. Thicknesses shown are for 8,16,32,64 layers annotated by solid, dash, dash-dot and dot. Both insets assume a close packed f.c.c. lattice of silica spheres, $n_{\text{silica}}=1.5$ in air corresponding to a filling ratio of 74%.

The transmission response in the [100] or Γ X direction for a face centred cubic, f.c.c., close packed opal is shown in the right inset of Figure 9.8. The gap studied is the first order

2. I would like to acknowledge the extremely beneficial use of the CNUSC super computing facility.

pseudo gap, which is both very narrow and incomplete for other directions as can be seen from the band structure diagram, the left inset of Figure 9.8. The position of that gap calculated by the T.M.M. method is found to be in good agreement with the plane wave method, P.W.M., with the central gap frequency converging on a normalised frequency just below 0.723. The results are presented in terms of normalised frequency, $\omega a/2\pi c = a/\lambda$, where ω is the angular frequency, a is the lattice constant, and c is the speed of light in a vacuum.

Several planes of crystal in the [100] direction were required for the band gap effect to manifest and there is a characteristic shift in central band gap frequency as the crystal becomes thicker. The shift is not unexpected and may be analogous to impedance mismatch such that the thicker the crystal the less mismatch. While the central band gap frequency moves, the amount of shifting decreases as the number of layers increases, converging in the infinite limit to the same value highlighted by the circle in the left inset of Figure 9.8 as considered automatically by the P.W.M. calculation.

In summary, the attenuation in the [100] direction through a bare opal photonic crystal is weak even for a large number of layers. The information from the band diagram backs this finding as the gap between the first order bands is small. Therefore the first order pseudo band gap for a bare, close packed opal [100] is not of great interest until the crystal is of a substantial thickness.

Transmission along the [111] direction.

To study the transmission of the [111] direction the split crystal cell for the [111] opal was utilised, see Figure 9.7. Three cells were used, each one defining one layer of the ABC

repeat pattern found within an f.c.c. lattice of close packed spheres. Each cell incorporates the influence of the preceding and following layer.

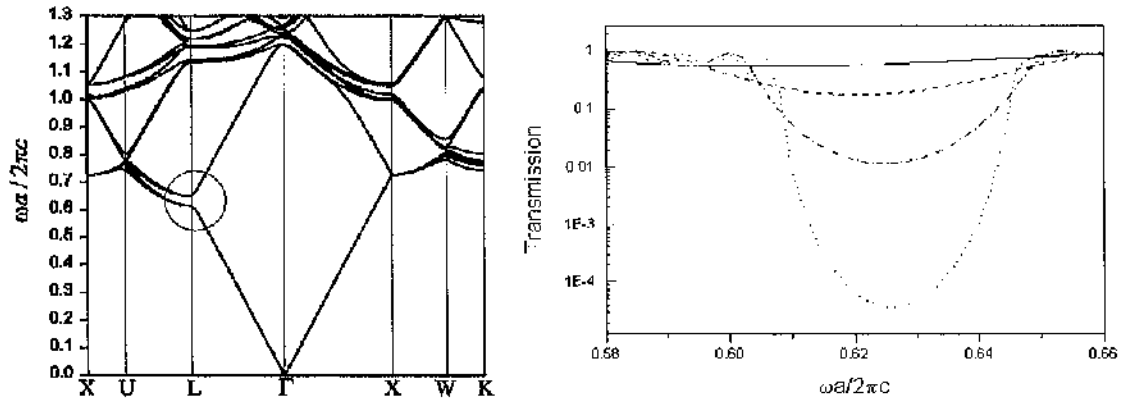


Figure 9.9 Band structure & [111] transmission response.

Left: Band structure diagram of a bare opal showing the high symmetry points in the Brillouin zone. The Γ point corresponding to the [111] direction has been highlighted with a circle. *Right:* Transmission as a function of the number of crystal planes in the [111] direction. Thicknesses shown are for 4, 8, 16, 32 planes corresponding to solid, dash, dash-dot and dot curves. To convert into a thickness related to the lattice constant a the number of layers should be multiplied by $\sqrt{3}$. Both insets assume a close packed f.c.c. lattice of silica spheres, $n_{\text{silica}}=1.5$ in air corresponding to a filling ratio of 74%.

In contrast to the findings in the [100] direction we find that the transmission in the [111] direction, Γ L, is considerably less for a similar comparison of crystal thickness. For 16 crystal planes in the [111] direction, corresponding to a crystal thickness of $27.7a$ there is less than 1% transmission through the structure. The central gap frequency once again shifts in frequency with an increasing number of layers, converging on a value of normalised frequency of approximately 0.64, confirmed by the P.W.M. analysis.

Comparison of response in the [100] and [111] directions

Figure 9.8 on page 128 and Figure 9.9 show the calculated transmission for plane waves impinging at normal incidence onto the $\langle 100 \rangle$ and $\langle 111 \rangle$ surfaces respectively. The figures show the evolution of the transmission co-efficient as a function of normalised frequency and for N number of layers in each particular direction. The distance between two identical layers for the [111] direction is $a\sqrt{3}$ while for the [100] direction it is simply a , where a is the lattice spacing.

For the [111] direction a gap minimum appears at a normalised frequency of 0.63, a figure also predicted by the band structure calculation at the Γ L point. As the crystal thickness is increased the transmission through the structure weakens and reaches a level of 10^{-4} for a slab thickness of $L=50a$. While the gap is incomplete the attenuation is

significant. For the [100] direction the gap minimum is at a higher frequency of 0.73, corresponding to the ΓX point in the band structure. It is remarkable that at a thickness of $L=64a$ 50% of the incident plane wave is transmitted, a vast difference compared to the [111] direction.

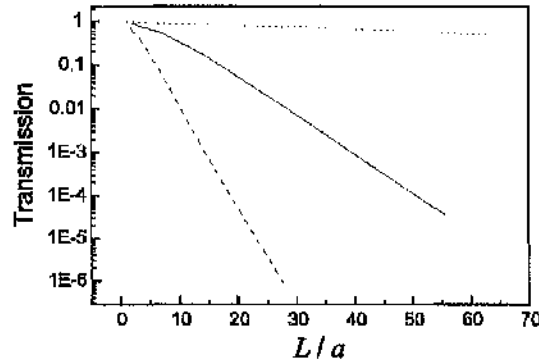


Figure 9.10 Transmission as a function of thickness

The minimum transmission as a function of slab thickness L . The solid line is for normal incidence on the (111) surface of bare opal. The dotted line is for normal incidence on the (100) surface of bare opal. Finally the dashed line plots the transmission response for a bare opal that has been fully in-filled with a dielectric material with a refractive index $n_{\text{infill}}=3.0$.

From the transmission response curves presented in Figure 9.8 on page 128 and Figure 9.9 on page 130 for incidence in the [100] and [111] directions respectively it is not immediately evident that the attenuation has an exponential dependence on the thickness of the crystal. By plotting the transmission minima as a function of the number of layers on a logarithmic scale, Figure 9.10, the response becomes linear for either the [100] direction, dotted line, or the [111] direction, solid line. The slopes of the lines correspond to the attenuation lengths, $\Lambda_{[111]}=3.4a$ and $\Lambda_{[100]}=87.4a$. For the sake of comparison Figure 9.10 also shows the response of a bare opal fully in-filled with a dielectric material with a refractive index of $n_{\text{infill}}=3.0$. In summary, to achieve the same attenuation with bare opal as for the in-filled opal presented in Figure 9.10 requires approximately twice the number of monolayers.

9.5: Coated Opal

Comments on Coatings

The application of a coating over the already close packed spheres provides a completely connected network of higher dielectric material. The transfer matrix method uses a discretisation sampling technique to define the average refractive index seen at a mesh sampling point, hence the accuracy of the representation of coatings is mesh dependent.

While the coating is expressed in an absolute ratio relative to a pre-defined condition, the actual coating thickness as seen by the T.M.M. code will be somewhat blurred due to the averaging effects of the sampling lattice.

The range of coatings that can be covered in simulation is not necessarily representative of those which can be achieved experimentally. The range of values of coating investigated theoretically probably exceed the current capabilities of the laboratory, but the findings and trends are important none the less. Forthcoming advances in fabrication technology justify the inclusion of data for structures that currently present fabrication challenges.

Transmission along the [100] direction

Application of thin coating to the spheres previously placed in a close packed lattice for plane wave incidence in the [100] direction results in a pronounced enhancement of the first order pseudo band gap of the opal. The coatings are applied such that they only cover non-touching areas of the spheres and are uniform in their extent of coverage. The coating thickness is expressed as a percentage of the ratio of the coating thickness to the radius required to achieve a close packed lattice before coating, Equation 9.3.

$$\text{Coating Thickness \%} = \frac{\text{Coating Thickness}}{\text{Close Packed Radius } R_{CP}} \times \frac{100}{1} \quad (9.3)$$

The application of a thin coating, $n_{\text{coating}}=3.0$, to a bare silica opal greatly enhances the performance of the gap. Figure 9.11 shows the response for a bare opal with a 10% coating for varying crystal thicknesses. There is a marked decrease in the transmission through the

crystal for the coated opal when compared to the bare opal response shown in Figure 9.8 on page 128.

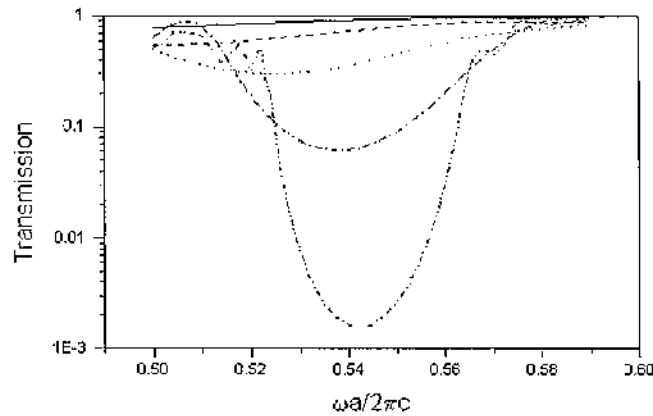


Figure 9.11 10% Coated opal [100]

Transmission through a Close Packed 10% coated opal in the [100] direction for various thicknesses. Solid, dash, dot, dot-dash and dot-dot-dash correspond respectively to 1,2,4,8,16 a where a is the lattice spacing.

The evolution of the transmission for varying coating thicknesses was studied for the range of 0-10% by the T.M.M. and found to enhance the gap, see Figure 9.12. The band evolution curve, the left inset of Figure 9.12, shows that the gap gradually opens with increased coating thickness to a maximum gap width at value of approximately 12% before slowly tapering. It is also noteworthy that the central band gap frequency decreases with increased coating thickness, a direct result of the increasing effective index of the structure. The band evolution predictions are echoed by the transmission response shown in the right inset of Figure 9.12 with a small deviation in central gap frequency for similar coating values.

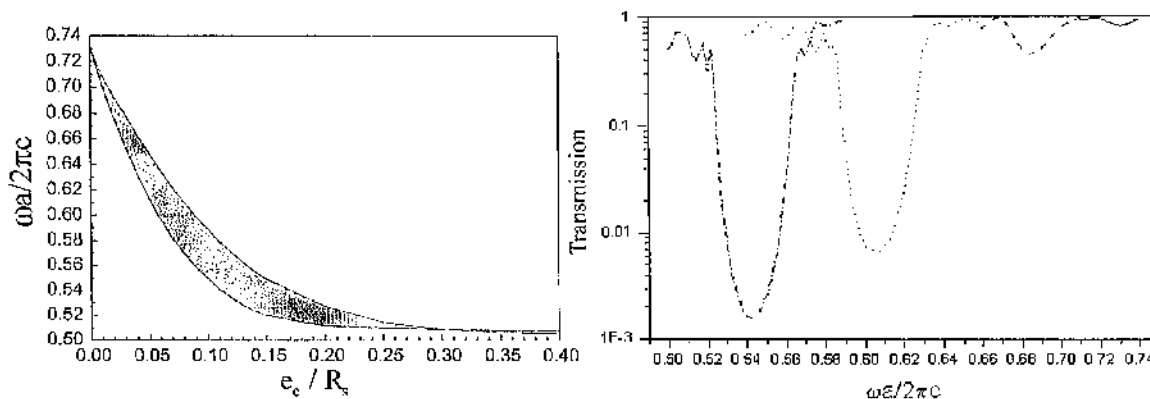


Figure 9.12 [100] Evolution for various coating thicknesses

Left: The lowest two bands calculated using the order-N method showing normalised frequency against the ratio of coating thickness, e_c , to the sphere radius, R_s . *Right:* Transmission as a function of coating thickness for a close packed opal in the [100] direction. Solid, dash, dot and dash dot lines correspond to 0,1,5,10% coatings. All data shown is for a similar thickness of crystal, $16a$ where a is the lattice constant.

When the evolution of the transmission is plotted as a function of the crystal thickness, shown in Figure 9.13 for 0,1,5 and 10% coatings, for the range of coatings studied the photonic band gap properties are enhanced due to the marked decrease in the transmitted levels.

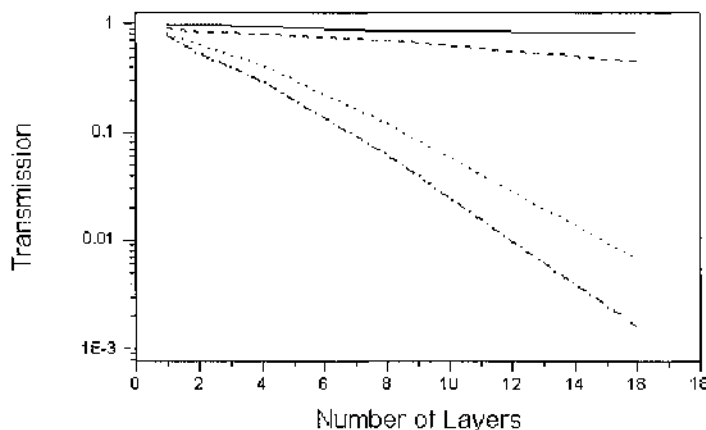


Figure 9.13 [100] Transmission against thickness for various coatings.

The evolution of the transmission against crystal thickness for close packed opal in the [100] direction. The thickness is expressed in terms of lattice constant a for various coatings, solid, dash, dot and dash dot lines correspond to 0,1,5 and 10% coatings.

Transmission along the [111] direction

The application of a coating results in some interesting behaviour for the transmission through the opal in the [111] direction. In contrast to the performance in the [100] direction, the application of a thin coating first *enhances* the transmission through the crystal. For values of coatings less than 5% the transmission through the crystal increases in comparison with the non-coated bare case before decreasing for coating values larger than 5%. Simulations for coating values of 1,5,10% were carried out for a fixed crystal thickness and the transmission level as a function of normalised frequency is shown in the right inset of Figure 9.14.

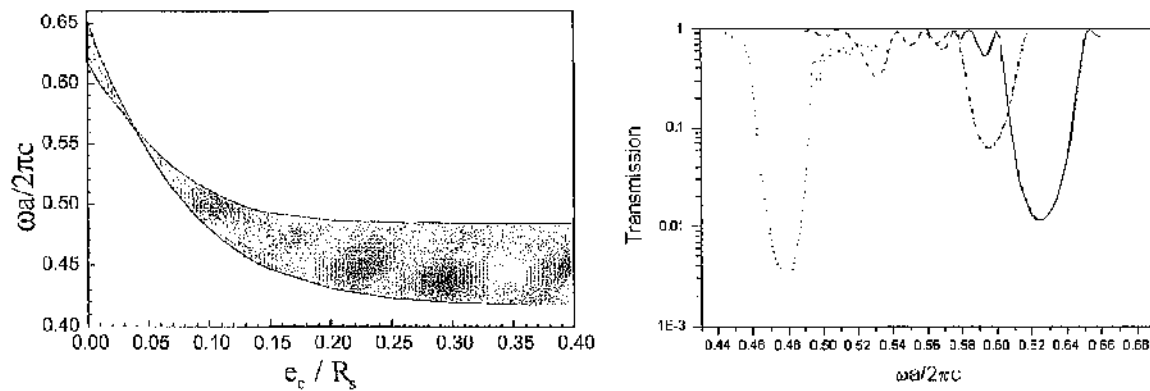


Figure 9.14 [111] Evolution as a function of coating thickness.

Left: The lowest two bands calculated using the order-N method showing normalised frequency against the ratio of coating thickness, ϵ_c , to the sphere radius, R_s . *Right:* Transmission as a function of coating thickness for an opal crystal $27.7a$ thick, where a is the lattice constant. Solid, dash-dot, dash and dotted curves relate to 0,1,5 and 10% coatings respectively. The refractive index of the spheres was assumed to be $n=1.5$, coating $n=3.0$.

The evolution of the transmission for the central band gap frequency as a function of crystal thickness is shown in Figure 9.15. The arrow is to guide the eye from the non-coated case through the 1,5 and 10% coatings to the completely in-filled case. The application of a coating causes the transmission response to increase for thin values of coating.

The increase in transmission is caused by a redistribution of the energy within the structure such that thin coatings can be thought of as a matching layers. Impinging waves prefer to distribute their energy in the highest refractive index of the structure [8]. For thin values of coating the energy contained in the coating is likely to be similar to that within the spheres. Therefore an impinging wave encounters a medium which appears more as a bulk medium rather than a periodic structure. As the coating value increases further the energy continues to redistribute such that becomes increasingly distributed in the coating. At this

stage, the propagating wave once again sees the periodicity of the structure and the band gap behaviour reappears as a noticeable drop in transmitted level through the structure. Further increases in the coating thickness eventually result in the voids of the structure being completely filled with coating material. In this instance the dielectric contrast between the coating material and the dielectric spheres is larger than that of the bare opal before in-filling, consequently the band gap region has stronger attenuation and down shifts in frequency due to the increased effective index. These trends are shown in Figure 9.15, which shows the transmission through the structure for the initial bare opal through a few coating thicknesses to the completely in-filled case.

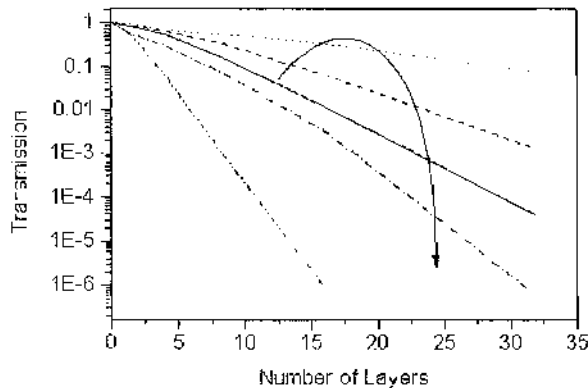


Figure 9.15 [111] Transmission versus thickness for various coatings.

The evolution of the transmission through a close packed opal in the [111] direction as a function of coating thickness. Solid, dash, dot, dash dot, and dot-dot dash lines correspond to 0, 1, 5, 10% coatings and completely in-filled opal respectively. The refractive index of the spheres was assumed to be $n=1.5$, coating $n=3.0$. The arrow is only to guide the eyes through the evolution of coatings from the non-coated to completely in-filled case.

9.6: Sintered Opal

Comments on implementation

Sintering is a post fabrication thermal step that causes a slight shrinkage of the lattice constant. For a close packed lattice sintering slightly merges neighbouring spheres resulting in a circular cross section connection between spheres. The level of sintering is expressed as a percentage of the ratio relating the difference between the actual radius sphere size and the consequent close packed³ radius size due to the lattice shrinkage to the same close packed sintered radius size, Equation 9.4.

$$\text{Sintering Level (\%)} = \frac{\text{Sphere Radius} - R_{\text{CP Sintered}}}{R_{\text{CP Sintered}}} \times \frac{100}{1} \quad (9.4)$$

3. See Equation 9.2 on page 126

Transmission along the [100] direction

We find that the effect of sintering in the [100] direction enhances the photonic band gap as the transmission through the crystal decreases. Figure 9.16 shows the effect of sintering for an opal crystal $16a$ thick for 0, 5 and 10% sintered. Whilst causing a decrease in transmission through the crystal, sintering also down shifts the central band gap frequency, an effect possibly explained through the average refractive index of the crystal which will undoubtedly increase per conventional cell upon sintering. Figure 9.17 on page 138 shows the effect of the crystal thickness as a function of the same sintering levels as shown in Figure 9.16, the exponential dependence on thickness can easily be recognised by the straight line on a log scale.

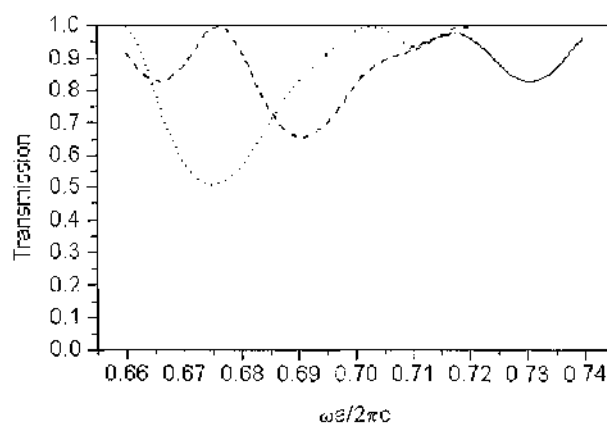


Figure 9.16 [100] The effect of Sintering

Transmission response as a function of sintering for initially close packed opal $L=16a$. The solid, dash, and dot lines correspond to normal bare opal, 5 and 10% sintered opals respectively. The refractive index of the spheres was assumed to be $n_{\text{sphere}}=1.5$ embedded in air.

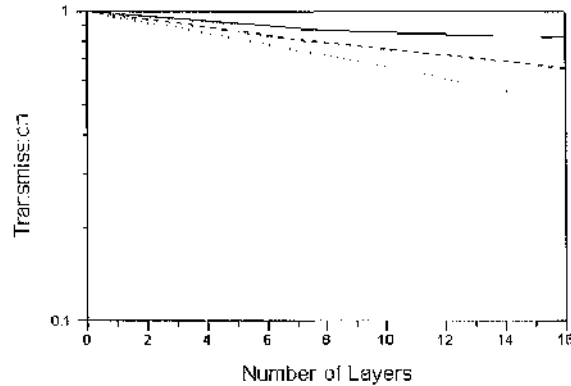


Figure 9.17 [100] Transmission versus thickness as a function of sintering.

The transmission response as a function of thickness for various levels of sintering in the [100] direction. The number of layers corresponds exactly to the thickness of the crystal in terms of a , the lattice constant. Solid, dashed and dotted lines correspond to 0, 5, 10% levels of sintering respectively. The spheres were assumed to have a refractive index of $n_{\text{sphere}}=1.5$ and were embedded in air.

Transmission along the [111] direction

In contrast to the results for the [100] direction, the effect of sintering on the transmission in the [111] direction degrades the photonic band gap. For the sake of similar comparison the results presented cover 0, 5 and 10% levels of sintering.

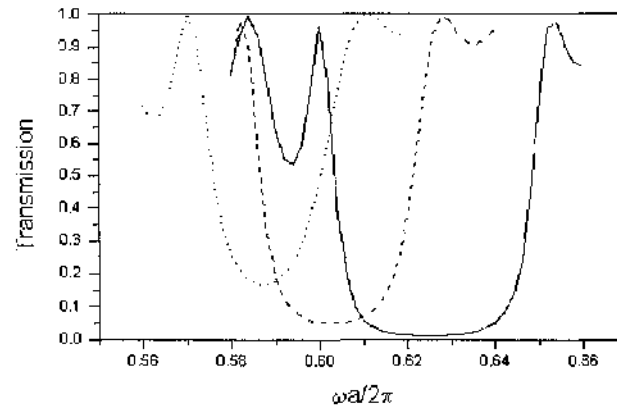


Figure 9.18 [111] Evolution of Transmission as a function of sintering level.

The transmission through an opal in the [111] direction versus normalised frequency as a function of the level of sintering. Solid, dashed, and dotted lines correspond to 0, 5 and 10% levels of sintering respectively. Note that the increasing level of sintering degrades the photonic band gap by increasing the level of transmission. All data for a crystal 16 [111] lattice planes thick i.e. $27.7a$ where a is the lattice constant.

Figure 9.18 shows the transmission response versus normalised frequency for 0, 5 and 10% levels of sintering for an opal in the [111] direction. Increasing the sintering levels from the close-packed, non-sintered case, causes the photonic band gap to degrade both in width and in attenuation level. This is also seen in Figure 9.19 on page 139 where sintering

clearly decreases the gradient of the line relating the transmission through the crystal to the thickness expressed in lattice constants for the close packed condition.

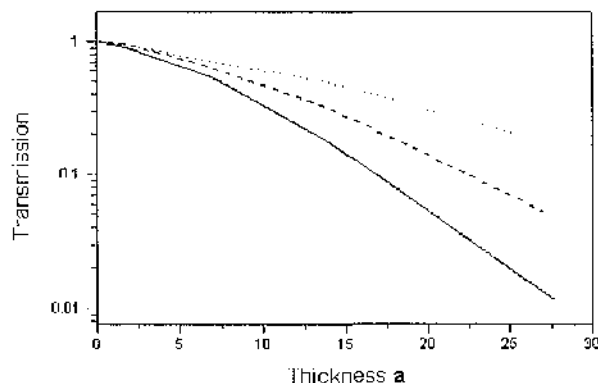


Figure 9.19 [111] Transmission versus crystal thickness as a function of the sintering level.

The transmission as a function of crystal thickness expressed in terms a , where a is the lattice constant defined by the close packed condition. Solid, dashed, and dotted lines correspond to 0, 5 and 10% levels of sintering respectively. As can be clearly seen the effect of sintering progressively decreases the transmission through the crystal.

9.7: Conclusion

The transmission response for opal photonic crystals for two of the main directions of interest has been investigated. Furthermore, the photonic band gap behaviour changes significantly as a function of sintering and of coating and the response to these functions is highly direction dependent.

The application of a coating to a close-packed lattice of silicon spheres in the [100] direction causes substantial enhancement of the photonic band gap behaviour of the crystal. The continued thickening of the coating serves only to enhance the photonic band gap for the [100] direction, no saturation behaviour has been seen for the ranges of coatings studied. In strict contrast the application of coatings in for [111] incidence initially degrades the photonic band gap before reinforcing it for larger coating values.

The effect of sintering also effects the photonic band gap in different ways for different incidence directions. For the [111] direction sintering cause degradation of the photonic band gap both in bandwidth and through an increase in transmission magnitude. This behaviour is not unexpected as sintering of the close-packed [111] plane will reduce the interstitial void volume between the spheres. This reduction increases the average refractive index presented to the incident wave and explains the downward shift in frequency of the centre of the photonic band gap whilst simultaneously closing the gap as the crystal starts to look more and more like a bulk piece of material for continued sintering.

Conversely the same levels of sintering for the [100] direction enhance the photonic band gap by increasing the width of the gap and decreasing the transmission magnitude through the crystal. While the downward shift of the central gap frequency follows the reasoning for that of the [111] direction, the decrease in transmission is explained through the packing of the [100] plane. The [100] plane is less densely packed than that of the [111] plane and an increase in the plane packing through sintering enhances the gap for the values studied. Carried to extremes the effect of sintering will also close the gap in the [100] direction for the same reasons outlined for the [111] direction.

The combined effects of coating and sintering have still to be investigated, and with shape distortion and tolerances incorporated the models will reflect the experimental situation more realistically. As the effects of coating and sintering have opposing trends, depending on the lattice orientation, a trade off in performance is expected.

Optical characterisation of shear ordered colloidal crystals

Introduction

In the process of physically making colloidal crystals there is a very large chance that stacking faults and defects will occur during fabrication. Stacking faults can alter the repeat pattern from one type of face centred cubic, f.c.c., crystal to another if they do not randomise the structure completely. Assuming that the colloid constructs itself properly, there are two types of pure f.c.c. crystal; one is the ABC crystal and the other is ACB, where each letter corresponds to one monolayer and the letter order corresponds to the stacking sequence. The stacking sequence is most easily visualised when the $\langle 111 \rangle$ plane is the surface truncation plane.

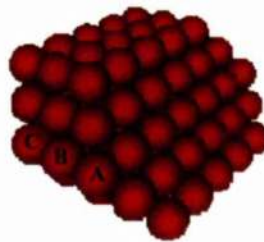


Figure 10.1 Generic ABC Colloid

Thin crystals, several tens of monolayers, can be easily fabricated using the process of shear ordering to form either ABC or ACB colloids by lateral oscillation in the $\langle 111 \rangle$ surface plane. By laterally shifting either the top or bottom $\langle 111 \rangle$ surface plane with respect to the other, the crystal can be switched between the two stacking orders. For thicker crystals stacking faults may occur, changing the stacking sequence which can result in the

crystal being a mixture of the two pure f.c.c. lattice types, or having a completely random stacking sequence. As demonstrated within the previous chapter the properties of the colloids are very sensitive and any information that can be obtained concerning the purity of the sample is beneficial. Fortunately the stacking sequence of thin colloidal crystals can be characterised by examining the intensity of diffracted Bragg spots and further information regarding the purity of the sample can be gleaned by examining the intensity of the diffracted spots as a function of incidence angle.

10.1: Building The Crystal

Theoretical representation of the crystal

For incidence onto the $\langle 111 \rangle$ surface plane the transfer matrix code discretises the cell in an orthogonal Cartesian co-ordinate basis, which utilises a non primitive cell. Figure 10.2 shows the $\langle 111 \rangle$ surface plane relative to the face centred cubic cell.

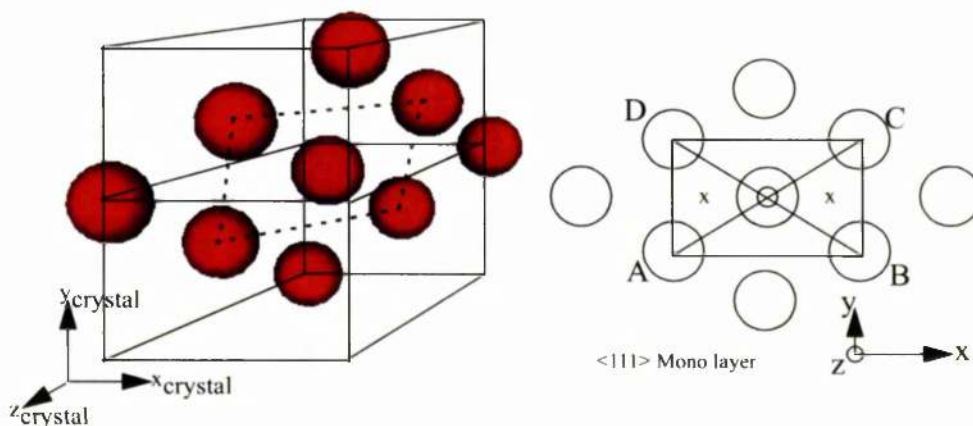


Figure 10.2 $\langle 111 \rangle$ plane within the cubic crystal lattice

The x-markers on the mono layer illustrated on the right show the translational shift required from point O to form the two different mono layers that are used to build an f.c.c. cell. The labelling of A,B and C for each mono layer can be chosen at will so long as the definitions remain consistent.

By considering the perpendicular bisectors of triangle AOD or BOC the shift that is required from point O, located centrally in the right inset of Figure 10.2, to either x point is one third of the distance AB. Within the modelling tool this fact is used to our advantage such that only one monolayer is defined and then shifted by the relevant amount to form either the ABC or ACB repeat patterns. The model uses one cell for each monolayer incorporating the influence of the previous and next monolayers. Renditions of each layer used for impinging wave incidence onto the $\langle 111 \rangle$ opal surface plane have already been shown in Figure 9.7 on page 127.

Fabrication using shear alignment

The technique of shear alignment allows the fabrication of large domain colloids. In the experiment PMMA spheres, approximately 785nm in diameter, are mixed with octanol such that a 54% filling ratio mixture results. The mixture is then placed on a microscope slide. 10 μ m diameter spacer beads are placed on other areas of the slide to control the thickness of the crystal and then a second microscope slide is placed as a top cover over the sample. The crystal is then formed by laterally oscillating one of the slides forcing the spheres to self-organise. Once the crystal has formed continued oscillation switches the lattice repeat pattern from ABC to ACB.

For two layers of the $\langle 111 \rangle$ crystal there are certain directions in which each layer will slide relative to the other. By moving the top slide one monolayer will slip over the layer below and then lock. For thicker crystals the first two layers now being locked together will then slip over the third, lock, and the process continues down through the crystal. Once the maximum extent of the lateral shift has been reached the oscillatory motion then reverses the process and the crystal repeat pattern is then reversed. The crystal can therefore be changed from ABC to ACB or vice versa, see Figure 10.3.

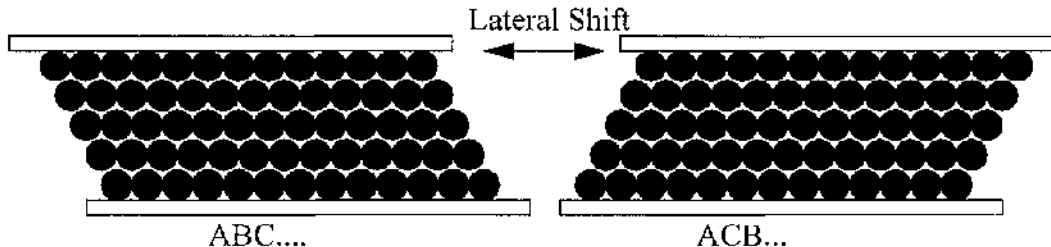


Figure 10.3 Shear Alignment

A cross section of the crystal during the process of shear alignment for the two extremes of the lateral oscillation. The $\langle 111 \rangle$ surface is shown in cross section for 5 monolayers of the crystal.

When compared with conventional deposition and evaporation techniques the domain size and purity of shear ordered opals is superior. If the shear ordered opal is left such that the host medium can evaporate then domain granulation and cracking does occur.

Emulating the experiment

The colloid used in the experiment consists of a 54% suspension of PMMA spheres $n_{\text{sphere}}=1.49$ in octanol $n_{\text{octanol}}=1.43$. The diameter of the PMMA balls has been estimated at 785nm with the first order gap to be found at 1941nm. Due to the small index difference between the materials a thick crystal is required for the photonic band gap effect to become

apparent. Figure 10.4 shows the transmitted intensity as a function of normalised frequency for various crystal thicknesses calculated theoretically and measured experimentally.

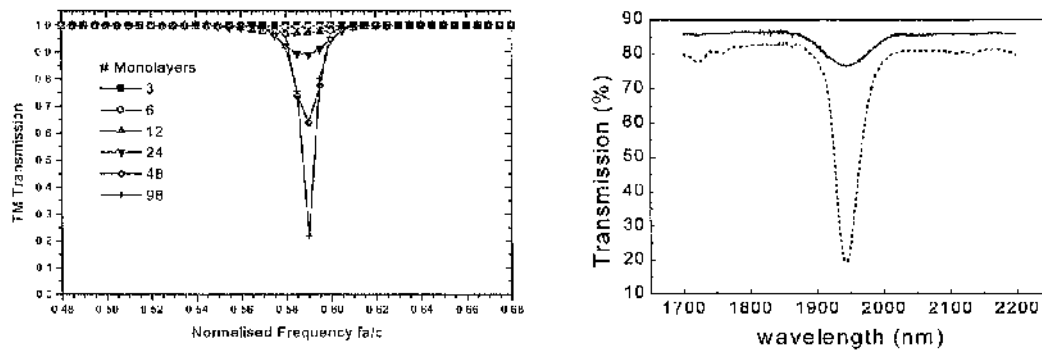


Figure 10.4 PMMA & Octanol <111> surface transmission

Left: The TM polarised wave transmission assuming that the waves impinging from the crystal start from octanol.
Right: The transmission at normal incidence as a function for a 10 μm thick (solid) and a 115 μm thick (dotted) PMMA-octanol colloidal crystal. The first order band gap is evident as a reduction in transmission at 1941 nm. (With kind permission from the authors of [67])

From Figure 10.4 the band gap is located at a normalised frequency of $fa/c=0.59$. Recalling the expression for the filling ratio for colloids, Equation 9.1 on page 126, and given the approximate radius of the spheres of 785 nm and the filling ratio of 54%, the lattice constant can be derived to be approximately $a=1150$ nm. Using these parameters to convert the predicted normalised frequency first order band gap at $fa/c=0.59$ to wavelength, the model predicts a first order band gap located at 1949 nm, figures that are in good agreement with the measurements.

10.2: Diffraction

The interaction of electromagnetic waves and periodic structures can lead to diffraction, a well known effect that plays an important role in the characterisation of structures and devices. Photonic colloidal crystals can also cause incident radiation to diffract, the onset of diffraction being determined by the diffraction limit or cut off frequency for the structure. There are many texts that deal exclusively with X-ray diffraction through crystals. One of the most notable being written by Sir William Lawrence Bragg [79], and another by Woolfson [80] both of which extensively cover diffraction through crystal structures. Examples of diffraction through hexagonal crystal planes, also examined here, along with other structures can be found on page 318 of Woolfson.

Diffraction Limit

For many of the common photonic crystal structures the effects of diffraction need not be considered, as operation within the first order band gap occurs at frequencies where no diffraction occurs. Once the frequency of interest exceeds the diffraction cut-off frequency for the structure then diffraction starts to occur and plays an important role in characterising the structure. To verify the integrity of the transfer matrix code in predicting diffraction within PBG structures, a return to simple grating structures is required. Diffraction starts to occur when the lattice, or grating periodicity, a , is equivalent to the free space wavelength of the incident plane wave for normal incidence, λ .

$$\text{Diffraction Cut-Off: } \lambda = a$$

The famous analogy is in fact the experiment carried out by Young, in the ‘Young’s Slit’ experiment. This experiment shows that diffraction starts to occur only when the periodicity and wavelength relation outlined is fulfilled. If the frequency is increased further then higher orders of diffraction are seen.

Normal Incidence

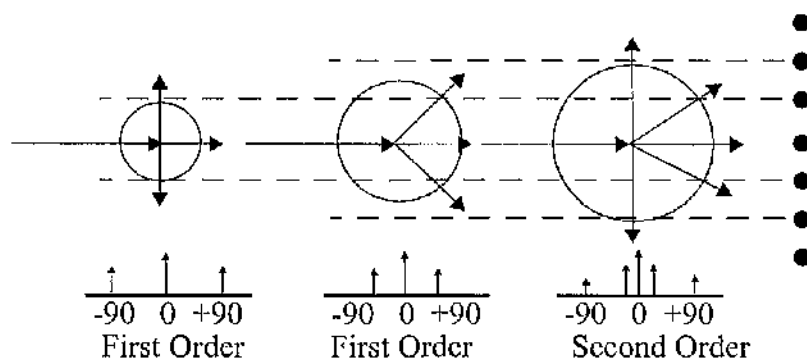


Figure 10.5 Diffracted Orders resultant from a normally incident wave.

The transmitted / diffracted orders resultant from a single normally incident plane wave. From left to right the illustrations show *Left*: the condition at the diffraction limit, *Centre*: beyond the diffraction limit (but only first order diffraction), *Right*: second order diffraction.

The orders of diffraction are defined in relation to the main plane wave passing through the structure. For an incident wave that is normal to the vertical periodicity of a two dimensional grating that just satisfies the criterion for diffraction, two diffracted orders are found in addition to the zero order non diffracted wave. This is illustrated in the left-hand diagram of Figure 10.5, one order is diffracted upwards, and one downwards and the zero order diffracted order passes through the grating. The two diffracted orders are a direct result of the symmetry of the structure, the condition of normal incidence and the

relationship that derives the position of the diffracted orders, discussed next. The angles of propagation of the diffracted orders can be simply found by considering the frequency or wavelength of the incident plane wave and an integer number, n , of the reciprocal lattice grating vectors in conjunction with the component of the incident wave vector parallel to the grating.

$$k_{\text{allowed}\parallel} = k_{\text{incident}\parallel} + \frac{2n\pi}{a_{\text{grating}\parallel}} \quad (10.1)$$

Figure 10.5 shows normal incident plane waves for three different frequencies arriving on the same grating. The black dots represent the reciprocal lattice points of the grating and the circle is representative of the k of the incident plane wave, the higher the frequency of the wave the larger the diameter of the circle. For frequencies where the circle does not encompass any of the reciprocal lattice points there is no diffraction and the system is below the cut-off frequency.

The choice of normal incidence on the system ensures that there are no parallel components of the wave vector on the grating, and this simplifies the explanation of the diffracted orders. To calculate the allowed diffraction orders, horizontal lines are drawn through the reciprocal lattice grating vectors, see Figure 10.5. The intersection of these lines with the k -circle relating to the operational frequency through the relation $\omega = c_0 k$, where ω is the angular frequency and c_0 is the speed of light, defines the allowed diffraction orders.

At the onset of diffraction, the first example on the left of Figure 10.5, the diffracted orders exist at angles oblique to the incident plane wave, that is to say ± 90 degrees. These are the first diffracted orders and they are symmetrical about the main transmitted 'zero' diffracted order. As the frequency of the incident wave continues to increase then these diffracted first order waves will move consistently closer to the main transmitted beam, and if the k -circle overlaps a second set of parallel lines, then second order diffracted beams occur. If the power into the system is normalised then the summation over the main transmitted order (zero order) and any existing diffracted orders, evanescent waves and reflected orders should be unity.

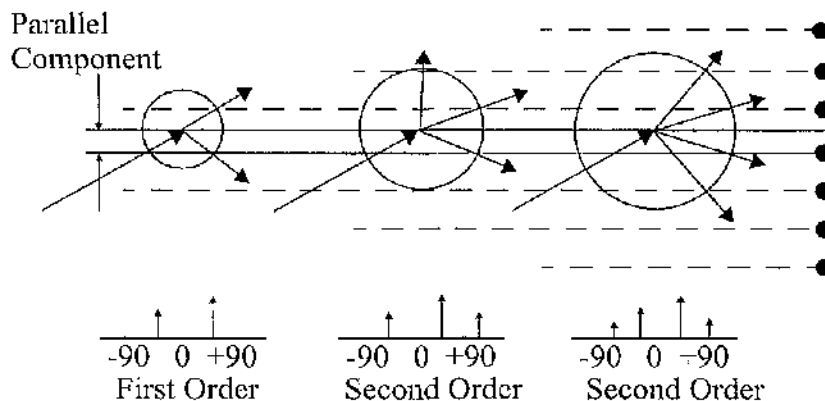
Off-Normal Incidence

Figure 10.6 Off normal incidence diffraction.

On moving away from normal incidence there is a component of the k -vector which now exists for the direction perpendicular to normal incidence, the parallel component of the k -vector to the grating, which has to be considered. The reciprocal lattice vectors of the grating must be displaced by this parallel component, which can lead to a situation where only one diffracted order exists, and there is not the symmetry about the main transmitted order as was found for the normal incidence scenario. The asymmetry occurs when the incident angle results in a component of the k -vector parallel to the grating, which upon the addition or subtraction of a reciprocal lattice grating vector, see Equation 10.1 on page 146, allows only one diffracted order after the zero order. When higher orders of diffraction are allowed then there will be angles where there will be even total numbers of diffracted orders rather than a odd number as was the case for normal incidence.

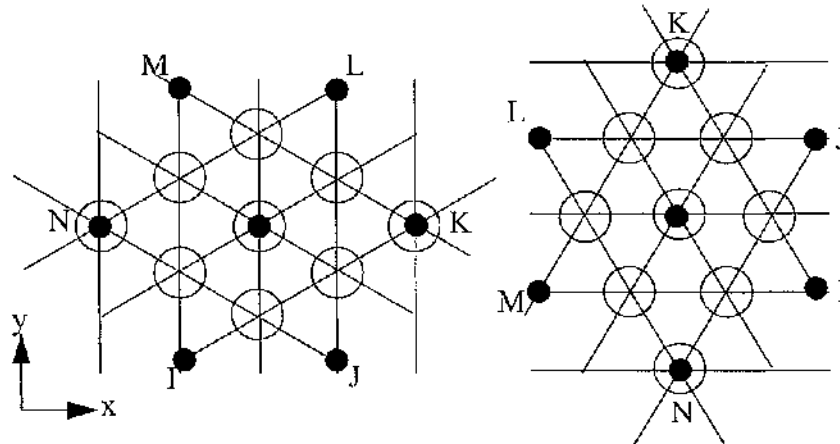
10.3: Diffraction resultant from the $\langle 111 \rangle$ surface plane

Figure 10.7 Two possible orientations of the $\langle 111 \rangle$ surface plane.

The empty circles represent the actual spherical atoms that constitute the lattice while the solid circles represent transmitted orders. Within the insets the zero order (main transmitted beam) is the central black dot while the surrounding six dots are the first order diffracted spots. The insets assume that the probing beam is normal to the $\langle 111 \rangle$ surface plane shown and that the normalised frequency is over unity such that there is diffraction.

By considering the atoms that constitute the $\langle 111 \rangle$ surface a set of lines can be drawn that form a geometrically tiled pattern of isosceles triangles due to the three fold symmetry of the surface plane. Two vectors drawn from one point to any two different nearest neighbour points define the direct lattice vectors. Due to the three fold symmetry of the surface plane, the reciprocal lattice is simply related to the direct through Equation 10.2 where \mathbf{b} is the direct lattice vector, \mathbf{d} is the reciprocal lattice vector and δ is the Kronecker delta unity matrix.

$$\mathbf{b}_i \cdot \mathbf{d}_j = 2\pi\delta_{ij} \quad (10.2)$$

A rotation through ninety degrees of either inset of Figure 10.7 generates the other, such that either could be the direct or reciprocal lattice with respect to each other. Three sets of parallel lines are drawn along the high symmetry directions of the lattice defining the diffraction planes which give rise to the diffracted orders. The diffracted orders are equidistant relative to the main zero order transmitted beam, assuming a normally incident impinging probe beam onto the $\langle 111 \rangle$ surface plane. The three sets of diffraction planes result in six first order diffracted spots for the surface layer. The existence and deviation of the diffracted orders from the zero order beam is a function of the frequency of the probing wave.

The f.c.c. structure repeats every three mono layers in the $[111]$ direction with each layer consecutively shifted to the previous layer to form either the ABC or ACB stacking sequence. These stacking sequences cause the six diffracted spots to split into two pairs of three. Three of these spots are more intense than the others, either IKM, or JLN. Each group of three dots itself form an isosceles triangle. Depending on the f.c.c. type the opposite three dots are more intense, therefore by experiment the lattice stacking sequence can be determined.

As the f.c.c. crystal structure thickens, such that it is several tens of monolayers thick, it is very likely that the resultant colloid will be a mixture of the two lattice types arising from stacking faults. The diffracted order intensity can also be used to obtain an idea of the disorder within the colloid.

Diffraction through the colloid

A normalised frequency of 1.7674 was chosen for the diffraction calculations to emulate the Helium-Neon, HeNe, laser that was used in the experiment. Both forms of pure f.c.c. lattice were examined and the diffraction data for both ABC and ACB lattice types was computed. For thin crystals all six Bragg spots can be measured in the experiment and they are also generated by the model. Figure 10.8 shows the diffraction spot angles in the xy -plane for a normally incident plane wave. The transmitted beam which passes straight through the crystal is located at an angle of $(90,90)$, shown in the centre of the figure. The diffracted spots which form the expected hexagon shape are joined together by the black line. Due to the rectangular nature of the non-primitive representative cell there are also spurious diffracted spots which have been joined to form a diamond shape highlighted by the red line. These dots are related to the artificial boundaries of the 3-dimensional rectangular cell that has been used to represent the structure in the calculation and do not relate to the physical properties of the crystal in any way, and consequently they can be ignored.

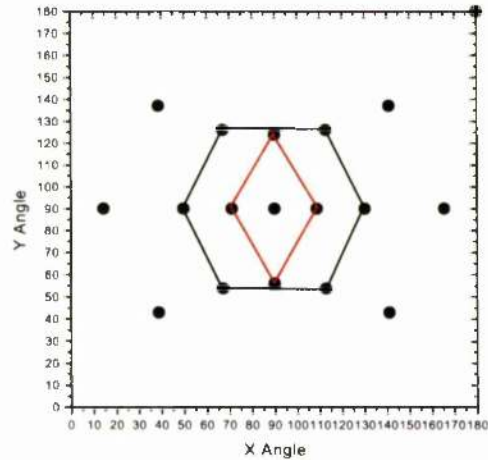


Figure 10.8 Code generated diffracted orders.

The diffracted orders as calculated by the code plotted in the xz - plane for a normal incidence plane wave at a normalised frequency of 1.7674 on the $\langle 111 \rangle$ plane.

The data files for the ABC and ACB simulations were then sorted to extract the most intense diffracted spots to give the results in Figure 10.9.

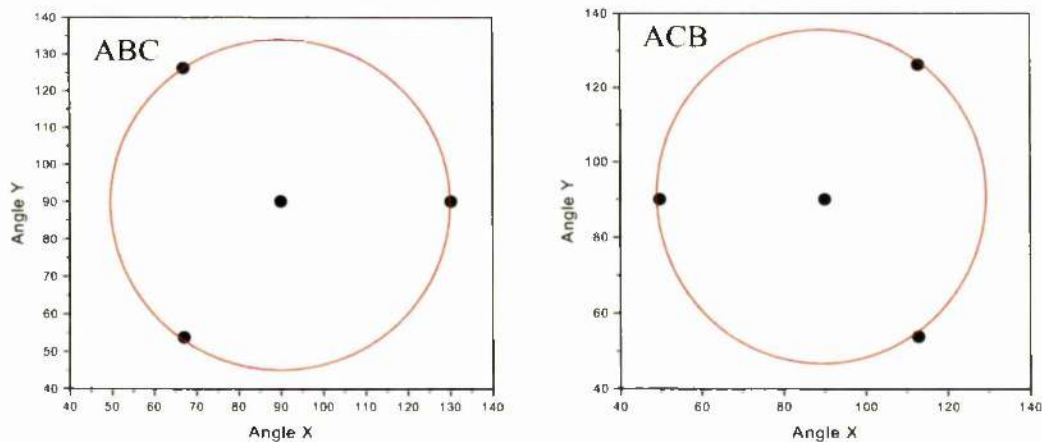


Figure 10.9 Diffraction patterns for ABC and ACB f.c.c colloids

The experimental results for a disordered crystal, a large shear crystal and the two types of f.c.c. lattice for the PMMA / octanol opal defined in “Fabrication using shear alignment” on page 143 are shown in Figure 10.10.

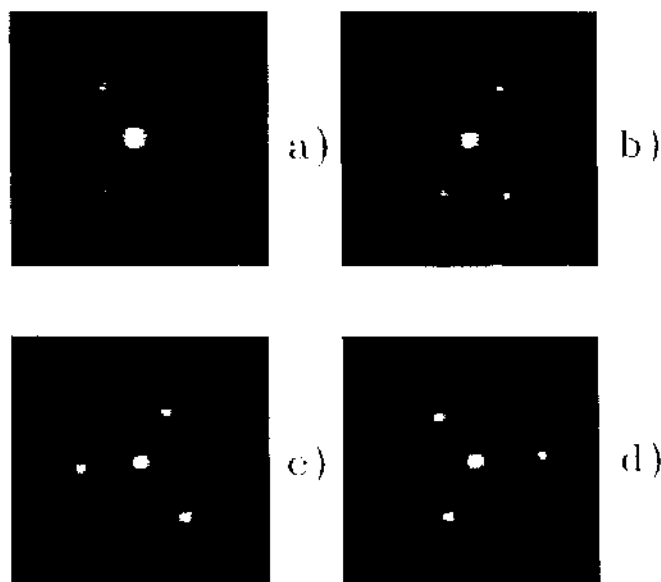


Figure 10.10 Measurements on shear aligned opals

The observed diffracted Bragg spots from a) a disordered crystal, b) a crystal aligned with a large scale shear, c) face-centred cubic crystal structure and d) the alternative face-centred cubic structure. Figure reproduced with kind permission from Dr. Richard Amos, DERA.

Figure 10.9 and insets c) and d) of Figure 10.10 illustrate that the stacking sequence clearly affects which of the three diffracted orders are primarily excited. The measurement results and theoretical predictions agree. For completeness, Figure 10.11 illustrates the difference in diffracted order intensity between the three main excited diffracted orders and the others for an ABC lattice 96 monolayers thick.

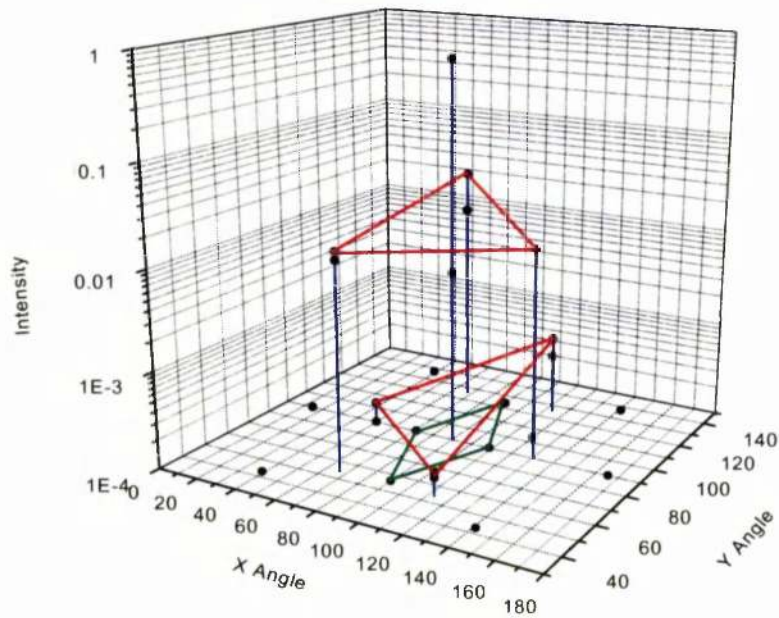


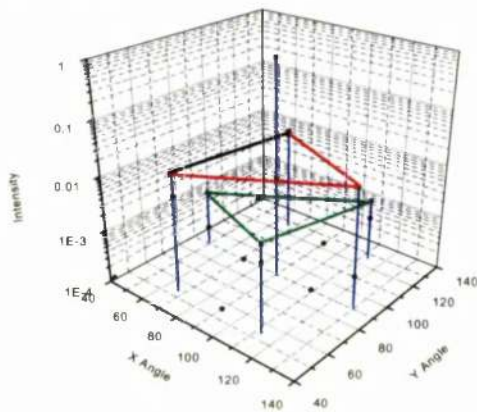
Figure 10.11 Diffracted order intensity for an ABC colloid.

The diffracted order intensity for a TM polarised normally incident plane wave. Colloid is 96 monolayers thick. Analysis at a normalised frequency of 1.7674. The main transmitted order related to normal incidence is found at an angle of $(x,y)=(90,90)$

Twinned Opal

A twinned opal consists of a mixture of the two pure f.c.c. lattice types. Analysis was carried out for evenly twinned opals, the first half of each opal being ABC, and the second half being ACB, and vice versa.

ABC/ACB



ACB/ABC

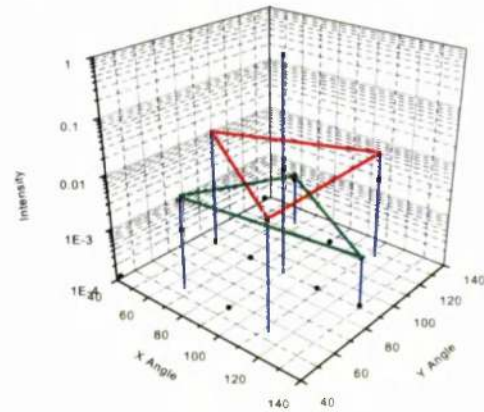


Figure 10.12 Twinned Opal Intensity responses.

Both simulations assumed a normalised frequency of 1.7674 and normal incidence onto the $\langle 111 \rangle$ surface plane. The main transmitted order related to normal incidence is found at an angle of $(x,y)=(90,90)$

Both simulations assumed the following structure: 48 monolayers of one type of crystal, a single change-over layer, and then 48 layers of the other crystal type. Therefore the overall thickness of the crystal is 97 monolayers. Comparing the transmission response to that of the pure f.c.c. results shown in Figure 10.11 it is interesting to note the differences in the diffracted order spot intensity. The three most intense dots depend on which type of crystal is first encountered by the incoming wave. The other three diffracted spots, while less intense than others, when compared in intensity level to the less intense orders of a pure f.c.c. lattice for similar circumstance and thickness, are considerably more intense. Consequently there is a recognisable signature for either a twinned or pure f.c.c. colloid which can be examined optically.

10.4: Optical characterisation of a shear ordered colloidal crystal

Further information concerning the stacking sequence and purity of the sample can be obtained by examining the intensity of the diffracted spots as a function of impinging laser beam angle. By scanning the incidence angle of the laser beam onto the sample an intensity profile for the diffracted spots can be obtained, see Figure 10.13. An impinging laser beam with a sufficiently long wavelength will generate six diffracted beams and a main transmitted beam when the laser beam is normally incident onto the sample, i.e. $\theta=0^\circ$ in Figure 10.13. The spots can be paired using the diffraction grating planes that generate them, from Figure 10.7 on page 148, the pairs are I and L, K and N, and J and M.

By ensuring that both diffracted spots of one pair, generated at normal incidence, lie within the angular plane that can be swept by the experimental set-up, the surface orientation of the crystal is known (previously discussed in “Diffraction resultant from the $\langle 111 \rangle$ surface plane” on page 148).

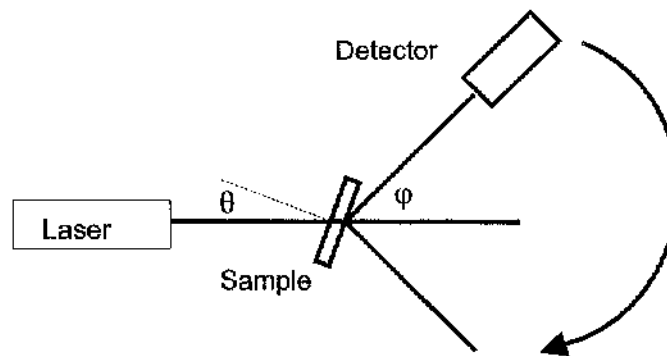


Figure 10.13 The experimental set-up

The modelling tool should emulate any required rotation on the $\langle 111 \rangle$ surface plane that is used in the experimental set-up, see Appendix C on page 195. Through careful choice of unit cells that are used to represent incidence onto the $\langle 111 \rangle$ surface plane of the colloid, limiting the incidence scan in the xy -plane suffices to theoretically characterise the diffracted spot intensity as a function of incidence angle and emulate the experimental set-up.

By scanning the incidence angle an intensity profile of a diffracted Bragg spot can be obtained. With the kind permission from the authors of [67], the intensity profiles for one of the diffracted Bragg spots for both types of shear ordered pure f.c.c. opal that were calculated using Mie scattering theory are shown in Figure 10.14. Note that the colloid modelled within Figure 10.14 was also made from PMMA and octanol but with a different volume concentration to that used in our experiment, consequently the incidence angles associated with the Bragg peaks of our sample are different. However, the findings are applicable nonetheless.

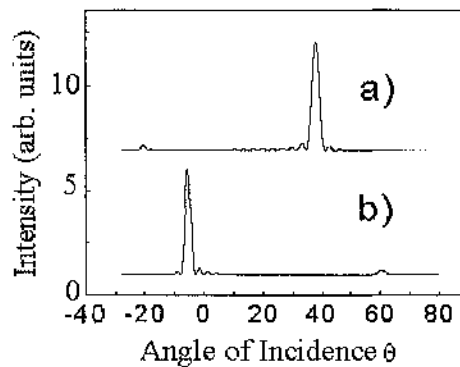


Figure 10.14 Bragg spot intensity profiles as a function of incidence angle.

The theoretical scattered intensity of one of the Bragg spots as a function of the angle of incidence for a) a pure f.c.c. structure with a stacking sequence of ABCABC, b) a pure f.c.c. structure with a stacking sequence of ACBACB. All plots are for 20 layers of colloid suspended between two glass plates. They have been scaled and offset for clarity. Figure and caption reproduced with the kind permission from the authors of [67].

From Figure 10.14 it can be seen that the type of f.c.c. crystal clearly affects the intensity profile. The two pure f.c.c. crystal intensity profiles, insets a) and b) show a strong and clearly different incidence dependence with noteworthy peaks for particular angles of incidence. These peaks are related to the satisfaction of the three dimensional Bragg condition for the colloid, such that for a given incidence angle the wave propagating within the structure encounters a periodic modulation of refractive index enhancing the reflection.

Similar analysis was carried out for a twinned f.c.c. opal, and is shown in Figure 10.15 again with the kind permission of the authors of [67]. The twinned structure shows two distinct Bragg resonances, one attributable to ABCABC-stacking sequence and the other related to the other f.c.c. crystal ACBACB-stacking sequence. The transfer matrix was then used in an attempt to verify the findings for a similar shear ordered colloidal crystal made from PMMA and octanol.

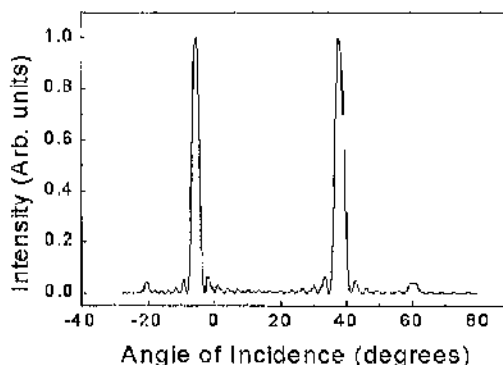


Figure 10.15 Bragg spot intensity profile for a twinned f.c.c. as a function of incidence angle.

The theoretical scattered intensity of one of the Bragg spots as a function of the angle of incidence for a twinned f.c.c. structure based on 10 layers of ABCABC-type stacking and 10 layers of ACBACB-type stacking. Figure and caption reproduced with the kind permission from the authors of [67].

The measurement set-up

The colloidal crystal measured was made with a solution of 720nm diameter PMMA spheres dispersed in octanol with a volume concentration between 49 and 54%. The colloidal crystal was ordered using the shear ordering technique and optical characterisation was performed using a laser beam of 441nm confirming the ordering of the sample. The laser beam showed six spots which were observed to oscillate between the two bright sets of three spots as the shear direction changed, as discussed in the previous section. On removal of the shear the sample relaxed to six spot configuration corresponding to a twinned f.c.c. structure. Glue was then used between the slides such that it also encompassed the sample to prevent further movement of the slides or evaporation of the octanol.

The structure was then characterised by monitoring the intensity of all of the transmitted and reflected orders, including the diffracted orders. This was achieved by placing the sample on a rotation stage with an impinging laser beam of wavelength 543nm as shown in Figure 10.13. A silicon photo-diode detector was mounted on a second rotation whose centre of rotation was coincident to the sample. Both stages were then scanned through

computer control to characterise the angular performance of the sample. Polariser were inserted in front of the sample and the detector so that differentiation between input and output polarisation could be made. The scattered light for normal incidence onto the sample for both the transmitted and reflected orders is shown in Figure 10.16 for the twinned f.c.c. structure. Information concerning the transmitted orders is shown between $\pm 90^\circ$ while reflection data is shown from $+91^\circ$ to 270° . Note that due to physical limitations of the experimental set-up the detector mechanism blocks the reflection measurement when the sample angle and detector angle are coincident.

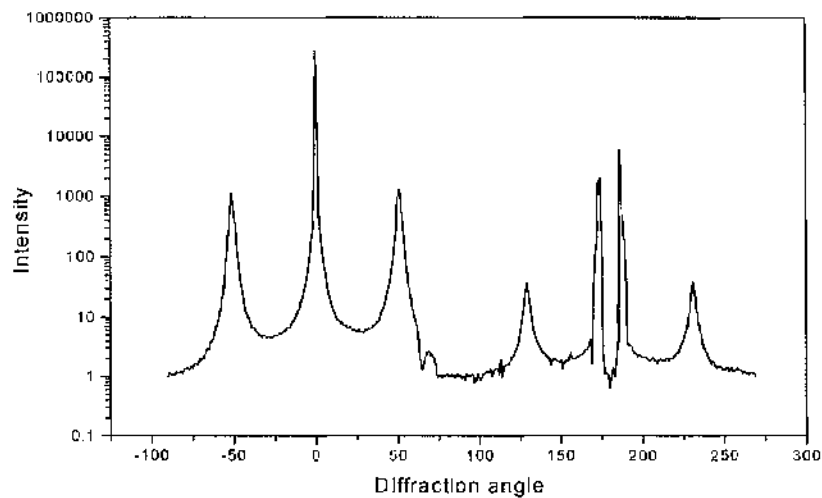


Figure 10.16 Experimental data for the twinned f.c.c. PMMA colloid in Octanol

The transmission and reflection data shown for normal incidence in arbitrary units for a twinned f.c.c. colloidal crystal made using the shear ordering technique. The transmission data is shown in the angular range from -90° to $+90^\circ$ while the reflection data is shown from $+90^\circ$ to 270° . The main transmitted (reflected) order can be seen at 0° (180°). The transmitted (reflected) Bragg spots can be seen at $+50^\circ$ (130° and 230°). Note that the dip in the main reflected beam is caused by the blockage of the beam by the detector mechanism.

The computer was then set to perform iterative measurements of both the reflected and transmitted orders as the sample angle was changed. Figure 10.17 on page 157 shows a gray scale map of the optical scattering for the sample as a function of the incidence angle against the angle measured with respect to the sample surface normal, white relates to high intensity. Note that the angle conventions adopted in Figure 10.16 on page 156 have been reversed for Figure 10.17. The transmission data is shown on the right-hand side of the figure, from 90° to 270° while the reflection data is shown on the left-hand side from -90° to $+90^\circ$. Figure 10.18 shows the same data in 3 dimensions in colour, showing the intensity change in the scattering as a function of incidence angle more clearly.

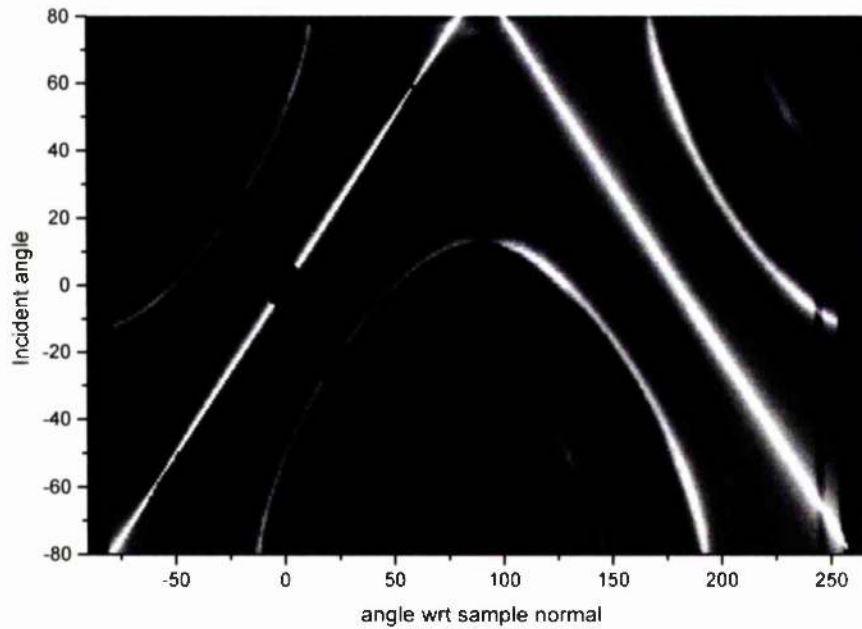


Figure 10.17 Gray scale map of the optical scattering of a twinned f.c.c. colloidal crystal.

Reflected light corresponds to angles from -90° to $+90^{\circ}$ while transmitted light corresponds to angle from 90° to 270° . The diagonal straight lines correspond to the zero order transmitted and reflected beams. The first and second order Bragg spots can be seen as the incidence angle is varied. White relates to high intensity, black relates to low intensity.

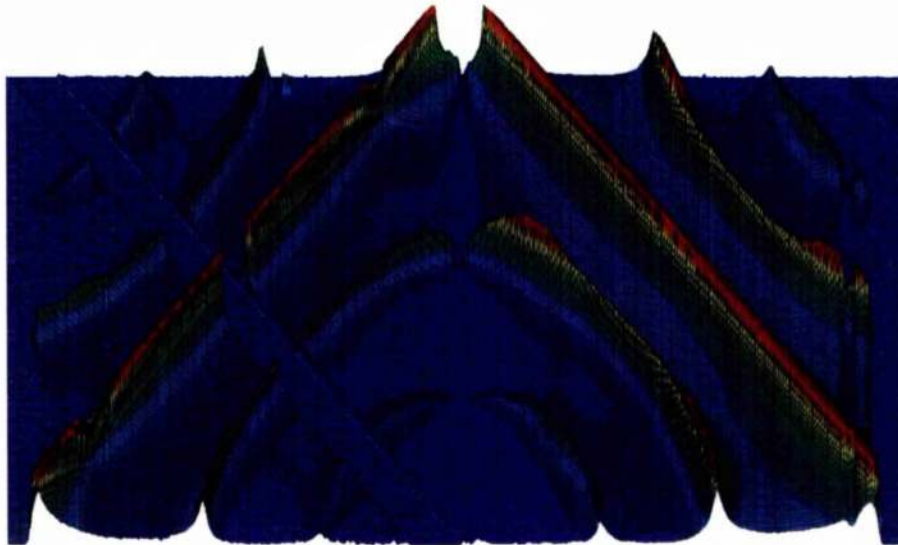


Figure 10.18 3-dimensional colour map of the optical scattering of a twinned f.c.c. colloidal crystal.

Same caption as for Figure 10.17, with the information shown on a colour scale showing the intensity variation more clearly.

The transfer matrix code was set up to emulate the colloidal crystal and the measurement scenario, the diffracted order angles for the zero, first and second orders along with their associated intensity were calculated as a function of incidence angle. Figure 10.19 shows the order's incident angle plotted against the propagation angles measured with respect to the sample normal.

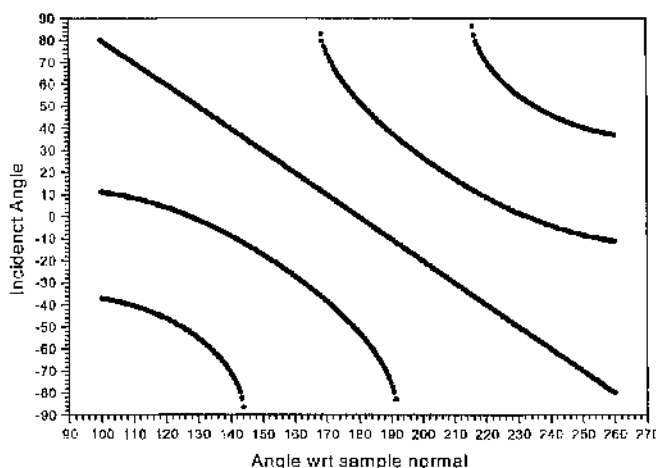


Figure 10.19 The zero, first and second TM orders predicted by the TMM code.

The angular information in Figure 10.19 from the model can be compared with the right-hand side of Figure 10.17 on page 157 for the experiment and is found to be in good agreement.

The experimental data was processed such that the intensity of the first order diffracted spot could be plotted as a function of incidence angle, see Figure 10.20 on page 159. As can be seen from the figure the intensity for the first order transmitted Bragg spot peaks when the impinging incidence angle reaches approximately 55° . The peak is somewhat broader than expected, but can be attributed to the variation in the PMMA sphere radius size, approximately 5%, and the angular resolution of the detector.

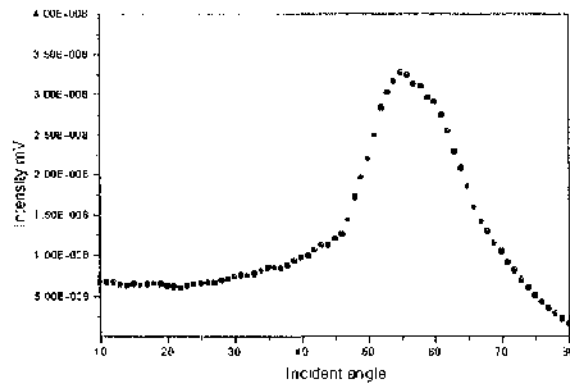


Figure 10.20 Experimental Intensity of the first order Bragg spot.

The experimental intensity as a function of incident angle of the first order transmitted Bragg spot.

Considerable time and effort was put into modelling the structure, various discretisation meshes were investigated as the mesh sizes used to predict the location of the first order band-gaps in the [111] direction were found to be insufficient to accurately resolve the angular positions of the diffracted orders. Consequently the discretisation mesh size was increased to a level where the diffracted order intensity for one of the Bragg spots peaked at the same angular value as measured in the experiment. At this level of representation the demands on computer resources are considerable, such that given the limitations of the machine used for the modelling only pure f.c.c. opal was investigated with several hours required to calculate the response for a single angle of incidence. The results for the intensity of the first order transmitted Bragg spot for three different discretisation meshes are shown in Figure 10.21.

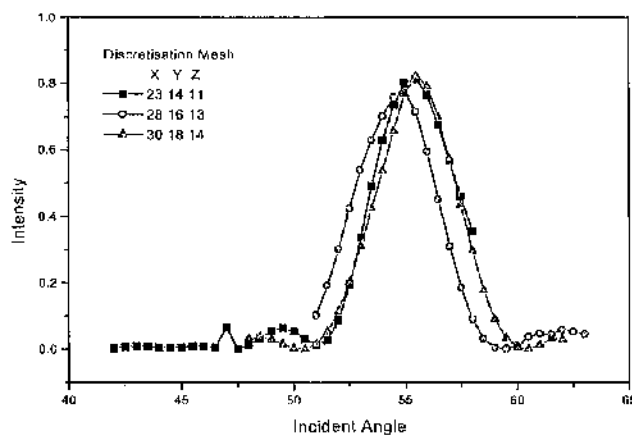


Figure 10.21 Theoretical intensity of the first order Bragg spot.

The theoretical intensity as a function of incident angle of the first order transmitted Bragg spot.

The agreement between theory and experiment is good but the computation times, forethought and care involved in obtaining the results in Figure 10.21 are substantial.

10.5: Conclusion

By examining the intensity of the first order Bragg spots for colloidal crystals which are a few tens of monolayers thick information concerning the stacking sequence can be obtained. For normal incidence onto the $\langle 111 \rangle$ surface plane an impinging plane wave of sufficient frequency will generate six first order diffracted spots due to the three fold symmetry of the $\langle 111 \rangle$ surface plane. There are two types of pure f.c.c. lattice, ABCABC and ACBACB where each letter corresponds to one monolayer of the stacking sequence. From the six diffracted orders generated two isosceles triangles can be constructed. Depending on which pure f.c.c. lattice type is being examined three spots that form the vertices of one of the triangles are much more intense than the other three. The situation reverses for the other type of pure f.c.c. lattice. Consequently there exists a method for optically characterising the f.c.c. lattice type.

Optical characterisation is particularly suited to the examining the properties of opal colloidal crystals that have been ordered using the shear ordering technique. The shear ordering technique uses a suspension of particles in a liquid sandwiched between two glass microscope slides. Spacer beads are used between the two slides such that a minimum spacing between them is assured. The top slide is then laterally oscillated and the crystal then self orders into one type of f.c.c. crystal, on reversal of the lateral shift the stacking sequence is altered and the other type of crystal is formed. However once the lateral oscillation is stopped the suspension relaxes into a mixture of the two pure lattice types called twinned opal.

By examining the intensity of one of the diffracted spots as a function of the impinging wave incidence angle there are distinct optical signatures. The pure f.c.c. lattice types display a marked increase in intensity for a particular, but different incidence angle depending on the lattice type. For the twinned structure two peaks are generated due to the mix of the two lattice types. The peaks in the response are resultant from the three dimensional Bragg condition. When the Bragg condition is satisfied the diffracted beams that are generated by each monolayer add together in amplitude and phase. As the thickness

of the crystal, in terms of monolayers, increases the range of angles which satisfy the Bragg condition becomes increasingly smaller. Both experimental measurement and theoretical models have confirmed the optical characteristics of the colloids. This demonstrates that the information contained in the diffracted spots, when they are scanned as a function of incidence angle, can provide definitive information concerning the internal structure of the colloidal crystal.

The agreement between the measurement and theoretical results demonstrates the applicability of the transfer matrix method in modelling the diffraction properties of colloids. However considerable computer resources and patience are required to model the diffraction properties of the crystals. Careful thought must also be exercised over the choice of discretisation mesh that is employed in building the dielectric matrix used to represent the colloidal structure.

Summary, Conclusions and Future Considerations

Summary & Conclusions

After the introductory chapter, chapters 2 to 5 characterised the performance of 1-, 2- and 2+1-dimensional photonic crystals. The objective was to find a design for an omni-directional reflector, a structure that should not allow propagation for any polarisation or incidence angle for a range of frequencies.

Chapter 2 demonstrated, through the limitations imposed by Snell's Law, that a 1-dimensional Bragg stack under particular circumstances can display omni-directional reflection. However the circumstances under which these conditions apply are limited, and it was shown that upon removal of these conditions omni-directional reflectance was no longer sustainable.

Chapter 3 built on the idea of using a Bragg stack as the base mechanism for a proper 3-dimensional reflector. By sandwiching a slab of high refractive index material, perforated with an optimised 2-dimensional hexagonal lattice of air holes, between two pieces of the same bulk material a pseudo 2+1-dimensional structure was formed. The refractive index contrast between the bulk material and the effective index of the perforated layer was shown to be insufficient to open a full 3-dimensional photonic band gap.

Chapter 4 extended the thinking of chapter 3 by using two different materials to form the Bragg stack and extended the holes straight through the stack. For the materials examined and for the range of frequencies studied, it

was concluded that the 2+1-dimensional structures examined in chapters 3 and 4 had insufficient symmetry to display a full 3-dimensional photonic band gap.

Chapter 5 demonstrated that interleaving two, 2-dimensional photonic crystal lattices to make a woodpile structure resulted in the successful creation of a full 3-dimensional photonic band gap. Many of the properties of the resultant 3-dimensional photonic crystal could be predicted directly from a knowledge of the properties of the 2-dimensional sublattices. This radically reduced the computational overhead in terms of the time and cost involved in the determination of their properties. Examination of the properties of a previously published woodpile structure demonstrated the existence of a full 3-dimensional photonic band gap, confirmed both experimentally and theoretically. An increase in the performance of a slot antenna placed onto the surface of the crystal was also presented. It was concluded that the woodpile was a truly 3-dimensional photonic band gap material which showed promise as a substrate for integrated antenna systems.

Chapter 6 examined the influence of placing various dielectric membranes over the top layer of an underlying 2-dimensional photonic crystal. It was demonstrated that concerns over surface wave excitation due to the combination of the membrane and top layer of photonic crystal were justified, but concluded that for our operational frequency such surface waves were not of concern.

Chapter 7 introduced a planar cavity defect into an otherwise perfect 2-dimensional photonic crystal. The supported mode in the cavity displayed strong impinging wave incidence angle dependence. Both theory and measurement confirmed the angular filter dependence. It was suggested that by placing an antenna, with a resonant frequency supported by the cavity, into the cavity, the directivity of the antenna could be vastly improved providing further explanation of recently published work.

Chapter 8 examined the coupling between defects that were introduced as superlattices into an otherwise perfect hexagonal lattice of air holes in dielectric. The coupling between neighbouring defects was examined as a function of distance and direction of propagation. The coupling was strong for defects that were close to each other, and as the distance between the defects was increased the coupling between them reduced at a significant rate. Waveguides made from coupled defects were discussed; these present the opportunity to guide light around corners without the inherent loss encountered by conventional

techniques. In the conclusion of the chapter a simple idea for a wavelength dependent optical waveguide splitter was presented.

Chapters 9 and 10 examined the properties of opal colloidal crystals. These crystals are mainly fabricated by taking advantage of the fact that the crystals self organise to form face centred cubic lattices. Chapter 9 examined the transmitted level through the crystal for different surface truncations as a function of various crystal parameters. The influence of dielectric coatings and sintering, a thermal process that shrinks and stabilises the crystal, were examined as functions of crystal thickness.

Chapter 10 presented analysis of the information that can be obtained optically by examining the diffracted orders generated by a laser beam probing a thin colloidal crystal. The intensity of the diffracted orders and their angular dependence defined optical signatures for the structure being probed, providing useful information concerning the stacking sequence and purity of the colloidal crystal.

Future considerations

The transfer matrix technique has been clearly demonstrated to be a useful modelling tool and confidence has been built in the technique through experimental verification. Photonic crystals are set to be an important partner in their marriage to current mm-wave and optical devices. As yet there are many structures and properties still to be investigated. The accurate modelling of antennas incorporated onto the surface of photonic crystals and the integration of active material into optical photonic crystals is yet to be properly undertaken and will certainly provide a challenging task for the future.

- 1) Spectral Properties of Opal-based photonic crystal with SiO₂ matrix.
A.L.Reynolds, F. Lopez-Tejeira, D. Cassagne, F. J. Garcia-Vidal, C. Jouanin, J. Sanchez-Dehesa.
Physical Review B, 15th October 1999.
- 2) Interleaving two-dimensional lattices to create three dimensional photonic band structures.
A. L. Reynolds, J. M. Arnold.
I.E.E. Proceedings Optoelectronics Part J., Vol 145, No. 6, December 1998.
- 3) Analysis of membrane support structures for integrated antenna usage on 2-dimensional photonic band gap structures.
A. L. Reynolds, H. Chong, I. G. Thayne, J. M. Arnold, P. J. I. de Maagt
Presented at the NATO ASI summer school on photonic band gap materials and light localisation, Greece, June 2000.
- 4) Analysis of membrane support structures for integrated antenna usage on 2-dimensional photonic band gap structures.
A.L. Reynolds, H. Chong, I. G. Thayne, J. M. Arnold, P. de Maagt
Accepted for publication in IEEE transactions on Microwave Theory and Techniques, in press.
- 5) Optical Properties of bare, sintered and coated Opal based photonic crystals.
A. L. Reynolds, D. Cassagne, C. Jouanin, J. M. Arnold.
Fourth International Topical Conference on Optical Probes of Conjugated Polymers and Photonic Crystals, 15th-19th February 2000, Salt Lake City, Utah, USA - currently in press will appear in journal of Synthetic Metals.
- 6) Transmission response for in plane and out of plane propagation for a 2D photonic crystal with a planar cavity defect.
A. L. Reynolds, H. Chong, I. G. Thayne, J. M. Arnold, P. J. I. de Maagt.
Fourth International Topical Conference on Optical Probes of Conjugated Polymers and Photonic Crystals, 15th-19th February 2000, Salt Lake City, Utah, USA - currently in press will appear in journal of Synthetic Metals.
- 7) Photonic crystals based on Opal structures
A. L. Reynolds, C. Jouanin, D. Cassagne
Presented at Photonic North: International Conference on the application of photonic technology, 12-16th June 2000 Quebec City, Quebec, Canada.
- 8) Angular frequency dependence for a planar cavity defect introduced into a 2D photonic crystal.
A.L. Reynolds, H. Chong, I.G. Thayne, P.J.I. de Maagt, J. M. Arnold
CLEO Europe / IQEC, Nice, September 2000.
- 9) Transmission response for defect localization in a 2-dimensional hexagonal photonic band gap crystal.
A. L. Reynolds, T. F. Krauss, J. M. Arnold
CLEO/QELS, San Francisco, May 2000.

Consequent publications

- 10) 2D & 3D photonic band gap materials, theoretical modelling and experimentation for application in the mm, sub-mm and far infra-red regimes
Andrew L. Reynolds
Presented at the summer school on Confined Photon Systems, Cargese, Corsica, 1998
- 11) 3D Millimetrewave Photonic Crystal as a Reflector for a Slot Antenna.
H. Chong, A. L. Reynolds, J.M. Arnold, I. G. Thayne, P. J. I. de Maagt.
24th Antenna Symposium on "Millimetrewave Applications", London, 18th April 2000.
- 12) Photonics Crystal Antennas.
P. de Maagt, R. Gonzalo, A. Reynolds, G. Crone.
IEE E11 Antennas Newsletter, Summer 1999.
- 13) PBG Crystals: a smart way to control c.m. waves.
P. de Maagt, Ramon Gonzalo, Andrew L. Reynolds.
Microwave Engineering Europe, October 1999.
- 14) Integrated Antenna Technology for Millimetre and Sub-Millimetre Waves.
P. J. I. de Maagt, W. Luinge, R. Heeres, M. van der vorst, M. Herben, A. Neto, S. Maci, L. Borselli,
A. Reynolds, J. Arnold, I. Thayne.
ESA's Preparing for the Future Vol. 8 No. 2 June 1998.
- 15) Effect of internal Reflections on the Radiation Properties and Input impedance of Integrated Lens antennas:
comparison between theory and measurement,
M. van der Vorst, P. de Maagt, A. Neto, A. Reynolds, R. Heeres, W. Luinge, M. Herben,
submitted to IEEE transactions on Microwave Theory and Techniques.
- 16) Some 2-D and 3-D Photonic Bandgap structures for Antenna Applications
R. Gonzalo, J. Vazquez, P. de Maagt, A. Reynolds, M. Sorolla
proc. JINA'98 Int. Symp. Antenna, 17-19 November 1998, Nice France, pp.129-132.
- 17) Photonic defect states in imperfect coated opals,
J. Manzanares-Martinez, A. Reynolds, D. Cassagne, and C. Jouanin
Presented at the NATO ASI summer school on photonic band gap materials and light localisation,
Greece, June 2000.
- 18) Modelling of 3D photonic crystals based on opals,
D. Cassagne, A. Reynolds, and C. Jouanin,
Presented at the International Workshop on Optical waveguide Theory and Numerical Modelling,
23-25 September 1999, Saint-Etienne, France.
- 19) Modelling of 3D photonic crystals based on opals,
D. Cassagne, A. Reynolds, and C. Jouanin,
Optical and Quantum Electronics Vol. 32, pp. 923-933, August 2000.

- 1) Yablonovitch, E., Inhibited spontaneous emission in solid-state physics and electronics, *Phys. Rev. Lett.* 58, 2059 1987.
- 2) John, S., Strong localization of photons in certain disordered dielectric superlattices, *Phys. Rev. Lett.* 58, 2486 1987.
- 3) De Maagt, P. J. I., Luinger, W., Heeres, R., Van der Vorst, M., Herben, M., Neto, A., Maci, S., Borselli, L., Reynolds, A., Arnold, J., Thayne, I., *Integrated Antenna Technology for Millimetre and Sub-Millimetre Waves, ESA's Preparing for the Future Vol. 8 No. 2 June 1998.*
- 4) De Maagt, P., Gonzalo, R., Reynolds, A., Crone, G., *Photonic Crystal Antennas, I.E.E. E11 News, Summer pp. 5-7 1999.*
- 5) Cheng, S. D., Biswas, R., Ozbay, E., McCalmont, S., Tuttle, G., Ho, K. M., *Optimized dipole antennas on photonic band gap crystals, Applied Physics Letters, 67 23, pp. 3399-3401, 1995.*
- 6) Purcell, E. M., *Phys. Rev. Vol 69, p 681, (1941)*
- 7) Krauss, T. F., De La Rue, R. M., *Photonic crystals in the optical regime - past, present and future, Progress in Quantum Electronics 23, pp 51-96, 1999.*
- 8) Joannopoulos, J. D., Meade, R. D., Winn, J. N., *Photonic Crystals Molding the Flow of Light, Princeton University Press ISBN 0-691-03744-2.*
- 9) Brillouin, L., *Wave propagation in periodic structures, McGraw-Hill Book Company, Second Edition, 1946, ISBN 486-60034-3*
- 10) Kweon, G., Lawandy, N.M., 'Quantum electrodynamics in photonic crystals', *Optics Communications, 15 July 1995.*
- 11) Ward, A. J., Pendry, J. B., *Calculating Photonic Green's Functions Using a Non-Orthogonal Finite Difference Time Domain Method., Phys. Rev. B, 58, 7252, 1998.*
- 12) Born, M., Wolf, E., *Principles of Optics, Pergamon, Bath, 1959*
- 13) Berling, P. H., *Physics of Thin Films, Vol. 1, 69, 1963*
- 14) MacLeod, H. A., *Thin film optical filters, Hilger, Bristol, 1986*
- 15) Knittl, Z., *Optics of thin films, Wiley, London, 1976*
- 16) Winn, J. N., Fink, Y., Fan, S., Joannopoulos, J. D., *Omnidirectional reflection from a one-dimensional photonic crystal, Optics Letters, Vol. 23, No.20, Oct. 15, 1998*
- 17) Fink, Y., Winn, J. N., Fan, S., Chen, C., Michel, J., Joannopoulos, J. D., Thomas, E. L., *A Dielectric Omnidirectional Reflector, Science, Vol 282, 27 Nov 1998.*
- 18) Chigrin, D. N., Lavrinenko, A. V., *Existence of an omni-directional photonic band gap in one-dimensional periodic structures, Journal of Condensed Matter, 22 Oct 1998*
- 19) Chigrin, D. N., Lavrinenko, A. V., Yarotsky D.A., Gaponenko, S. V., *Observation of total omnidirectional reflection from a one-dimensional dielectric lattice, Journal of Condensed Matter, 5 Nov 1998*

- 20) Dowling J.P., Mirror on the Wall: You're Omnidirectional After All? *Science* Vol. 282, 04 December 1998, 1841-1842.
- 21) Bell, P. M., Pendry, J. B., Ward, A. J., A program for calculating photonic band structures and transmission coefficients of complex structures, *Computer Physics Commun.* 85, 306 1995.
- 22) Baba, T., Matsuzaki, T., Theoretical Calculation of Photonic Gap in Semiconductor 2-Dimensional Photonic Crystals with Various Shapes of Optical Atoms, *Journal of Applied Physics*, Vol. 34 1995, pp. 4496-4498
- 23) Agi, K., Brown, E. R., McMahon, O. B., Dill, C., Malloy, K. J., Design of ultrawideband photonic crystals for broadband antenna applications, *Electronics Letters*, Vol 30, No. 25, 8th December 1994
- 24) Sozuer, H. S., Dowling, J. P., Photonic band calculations for woodpile structures, *J. Mod. Opt.* 41, 231 1994.
- 25) Ozbay, E., Michel, E., Tuttle, G., Biswas, R., Sigalas, M., Ho, K.-M.: 'Micro-machined millimetre wave photonic band gap crystals,' *Appl. Phys. Lett.*, 1994, **64**, 16., pp. 2059-2061.
- 26) Ozbay, E., Temelkuran, B., Sigalas, M., Tuttle, G., Soukoulis, C.M., Ho, K.M.: 'Defect structures in metallic photonic crystals,' *Appl Phys. Lett.*, 1996, **69**, 25., pp. 3797-3799
- 27) Ozbay, E., Michel, E., Tuttle, G., Biswas, R., Ho, K.-M., Bostak, J., Bloom, D.M., 'Terahertz spectroscopy of three-dimensional photonic band-gap crystals,' *Optics Lett.*, 1994, **19**, 15., pp. 1155-1157.
- 28) Lin, S.Y., Flemming, J.G., Hetherington, D.L., Smith, B.K., Biswas, R., Ho, K.M., Sigalas, C.M., Zubrzycki, W., Kurtz, S.R., Bur, J., 'A three-dimensional photonic crystal operating at infrared wavelengths', *Nature*, 1998, **394**, pp. 251-253.
- 29) Ho, K. M., Chan, C. T., Soukoulis, C. M., Biswas, R., Sigalas, M., Photonic band gaps in three dimensions: New layer-by-layer periodic structures, *Solid State Communications*, 89, No. 5, pp 413-416, 1994.
- 30) Brown, E. R., Parker, C. D., and Yablonovitch, E., Radiation properties of a planar antenna on a photonic-crystal substrate, *J. Opt. Soc. Am. B* 10, 404 1993.
- 31) Brown, E. R. and McMahon, O. B., High zenithal directivity from a dipole antenna on a photonic crystal, *Appl. Phys. Lett.* 68, 1300 1996.
- 32) Temelkuran B., Bayindir M., Ozbay E., Biswas R., Sigalas M. M., Tuttle G., Ho K. M., Photonic crystal based resonant antenna with a very high directivity, *J. Appl. Phys.* 87, 603, 2000.
- 33) Agi, K., Brown, E. R., McMahon, O. B., Dill, C., Malloy, K. J., Design of ultrawideband photonic crystals for broadband antenna applications, *Elec. Lett.* 30, 2166 1994.
- 34) Kesler, M. P., Maloney, J. G., Shirley, B. L., Antenna design with the use of photonic band-gap materials as all-dielectric planar reflectors, *Microwave & Opt. Tech. Lett.* 11, 169 1996.
- 35) Sigalas, M. M., Biswas, R., Ho, K. -M., Theoretical study of dipole antennas on photonic band-gap materials, *Microwave and Optical Technol. Lett.* 13, 205 1996.
- 36) Sigalas, M. M., Biswas, R., Li, Q., Crouch, D., Leung, W., Jacobs-Woodbury, Russ, Lough, Brian, Nielsen, Sam, McCalmont, S., Tuttle, G., and Ho, K.M., Dipole antennas on photonic band-gap crystals: Experiment and simulation, *Microwave and Optical Technol. Lett.* 15, 153 1997.
- 37) Ozbay, E., Abyeita, A., Tuttle, G., Trigides, M., Biswas, R., Chan, C. T., Soukoulis, C. M., Ho, K. M., Measurement of a three dimensional photonic band gap in a crystal structure made of dielectric rods, *Physical Review B*, Vol 50, Number 3, pp. 1945-1948, 15 July 1994
- 38) Leung, W. Y., Biswas, R., Cheng, S. D., Sigalas, M. M., McCalmont, J. S., Tuttle, G., Ho, K. M., Slot antennas on photonic band gap crystals, *IEEE Transactions on Antennas and Propagation*, Vol 45, No. 10, pp. 1569-1570, 1997.
- 39) Anderson, C.M., Giapis, K.P. "Symmetry Reduction in group 4mm photonic crystals", *Phys Rev B*, 1997, **54** 12,
- 40) Reynolds, A. L., Arnold, J. M., Interleaving two-dimensional lattices to create three-dimensional photonic band gap structures. *IEE Proc.-Optoelectronics*, Vol, **145**, No 6, December 1998.
- 41) Bharta, P., Rao, K.V.S, Tomar, R.S., Millimeter-Wave Microstrip and Printed Circuit Antennas, Artech House, ISBN 0-89006-333-8
- 42) James J. R., Henderson, A., High-Frequency behaviour of microstrip open-circuit terminations, *IEE J. Microwaves, Optics and Acoustics*, Vol. 3, pp.205-218. 1979.
- 43) Lin, S.-Y., Hietala, V. M., Lyo, S. K., Zaslavsky, A., Photonic band gap quantum well and quantum box structures: A high-Q resonant cavity, *Appl. Phys. Lett.* 68, 3233 1996.
- 44) Lin, S. Y., and Arjavalingam, G., Photonic bound states in two-dimensional photonic crystals probed by coherent-microwave transient spectroscopy, *J. Opt. Soc. Am. B* 11, 2124 1994.

Bibliography

- 45) Karathanos, V., Modinos, A., Stefanou, N., Planar defects in photonic crystals, *J. Phys. Condens. Matter* 6, 6257 1994.
- 46) Smith, C.J.M., De la Rue, R.M., Benisty, H., Oesterle, U., Krauss, T.F., Labilloy, D., Weisbuch, C., Houdre, R., In-plane microcavity resonators with two-dimensional photonic bandgap mirrors, *IEE Proc. Optoelectron.* 145: 6, 373-378 DEC 1998.
- 47) Ozbay, E., Temelkuran, B., Reflection properties and defect formation in photonic crystals, *Appl. Phys. Lett.* 69, 743 1996.
- 48) Pedrotti, F. L., Pedrotti, L. S., Introduction to optics, Prentice-Hall, Inc., Englewood Cliffs, New Jersey 07632, 1987
- 49) Sigalas MM, Ho KM, Biswas R, Soukoulis CM, Theoretical investigation of defects in photonic crystals in the presence of dielectric losses, *PHYS REV B* 57: 7, 3815-3820 FEB 15 1998.
- 50) Pendry, J. B., MacKinnon, A., Calculation of photon dispersion relations, *Phys. Rev. Lett.* 69, 2772 1992.
- 51) Sigalas, M.M., Biswas, R., Ho, K. M., Soukoulis, C. M., Theoretical investigation of off-plane propagation of electromagnetic waves in two-dimensional photonic crystals, *PHYS REV B* 58: 11, 6791-6794 SEP 15 1998.
- 52) Centeno E., Felbacq, D., Characterization of defect modes in finite bidimensional photonic crystals, *J OPT SOC AM A* 16: 11, 2705-2712 NOV 1999.
- 53) Temelkuran, B., Ozbay, E., Kavanaugh, J.P., Tuttle, G., Ho, K.M., Resonant cavity enhanced detectors embedded in photonic crystals, *Appl. Phys. Lett.* 72: 19, 2376-2378 MAY 11 1998.
- 54) Tayeb, G., and Maystre, D., Rigorous theoretical study of finite-size two-dimensional photonic crystals doped by microcavities, *J. Opt. Soc. Am. A* 14, 3323 1997.
- 55) Mekis, A., Chen, J. C., Kurland, I., Fan, S., Villeneuve, P. R., Joannopoulos, J. D., High transmission through sharp bends in photonic crystal waveguides. *Phys. Rev. Lett.* 77, 3787 1996.
- 56) Temelkuran, B., Ozbay, E., Experimental demonstration of photonic crystal based waveguides, *Appl. Phys. Lett.* 74: 4, 486-488 JAN 25 1999.
- 57) Stefanou, N. and Modinos, A., "Impurity bands in photonic insulators", *Phys. Rev. B* 57, 12127 1998.
- 58) Yariv A, Xu Y, Lee RK, Scherer A, Coupled-resonator optical waveguide: a proposal and analysis, *Opt. Lett.* 24: (11) 711-713 JUN 1 1999.
- 59) Bayindir M, Temelkuran B, Ozbay E, Tight-binding description of the coupled defect modes in three-dimensional photonic crystals *Phys. Rev. Lett.* 84: 10, 2140-2143 March 6 2000.
- 60) Bayindir M., Temelkuran B., Ozbay E., Propagation of photons by hopping: A waveguiding mechanism through localized coupled-cavities in three-dimensional photonic crystals, *Phys. Rev. B* 61, R11855 2000.
- 61) Bayindir M, Ozbay E Heavy photons at coupled-cavity waveguide band edges in a three-dimensional photonic crystal *Phys Rev B* 62: 4, R2247-R2250 JUL 15 2000
- 62) Photonic Bandgaps and Localization, edited by C. M. Soukoulis plenum, New York, 1993.
- 63) Photonic Band Gap Materials, edited by C. M. Soukoulis Kluwer Academic, Dordrecht, 1996.
- 64) Cheng, C. C., Scherer, A., Fabrication of photonic band-gap crystals, *J. Vac. Sci. Technol. B* 13, 2696 1995.
- 65) Tarhan, I. I., Watson, G. H., Photonic band structure of fcc colloidal crystals, *Phys. Rev. Lett.* 76, 315 1996.
- 66) Romanov, S. G., Sotomayor-Torres, C. M., in Handbook of Nanostructured Materials and Nanotechnology, edited by H. S. Nalwa Academic Press, New York 1999.
- 67) Amos, R. M., Shepherd, T. J., Rarity, J. G., Tapster, P., Kitson, S. C., Fabrication of large area face centred cubic hard sphere colloidal crystals by shear alignment, *Phys. Rev E*, 61, pp 2929-2935 2000.
- 68) Astratov, V. N., Vlasov, Yu. A., Karimov, O. Z., Kaplyan-skii, A. A., Musikhin, Y. G., Bert, N. A., Bogomolov, V. N., Prokofiev, A. V., Photonic Band Gaps in 3D Ordered FCC Silica Matrices, *Phys. Lett. A* 222, 349 1996.
- 69) Bogomolov, V. N., Gaponenko, S. V., Germanenko, I. N., Kapitonov, A. M., Petrov, E. P., Gaponenko, N. V., Prokofiev, A. V., Ponyavina, A. N., Silvanovich, N. I., Samoilovich, S. M., Photonic band gap phenomenon and optical properties of artificial opals, *Phys. Rev. E* 55, 7619 1997,
- 70) Vlasov, Yu. A., Astratov, V. N., Karimov, O. Z., Kaplyanskii, A. A., Bogomolov, V. N., Prokofiev, A. V., Existence of a photonic pseudogap for visible light in synthetic opals, *Phys. Rev. B* 55, R13 357 1997.
- 71) Romanov, S.G., Johnson, N.P., Fokin, A.V., Butko, V.Y., Yates, H.M., Pemble, M.E., Torres, C.M.S., Enhancement of the photonic gap of opal-based three-dimensional gratings, *Appl. Phys. Lett.* 70, 2091 1997.
- 72) Romanov, S.G., Fokin, A.V., Alperovich, V.I., Johnson, N.P., De La Rue, R.M., The effect of the photonic stop-band upon the photoluminescence of CdS in opal, *Phys Status Solidi A* 164: 1, 169-173 NOV 16 1997.

Bibliography

- 73) Miguez, H., Blanco, A., Meseguer, F., Lopez, C., Yates, H.M., Pemble, M.F., Fornes, V., Mifsud, A., Bragg diffraction from indium phosphide infilled fcc silica colloidal crystals, *PHYS REV B* 59: 3, 1563-1566 JAN 15 1999.
- 74) Blanco, A., Lopez, C., Mayoral, R., Miguez, H., Meseguer, F., Mifsud, A., Herrero, J., CdS photoluminescence inhibition by a photonic structure, *APPL PHYS LETT* 73: 13, 1781-1783 SEP 28 1998.
- 75) Cassagne, D., *Ann. Phys. Paris*, **23** 4, 1 1998,
- 76) Wijnhoven, J.E.G.J., Vos, W. L., Preparation of photonic crystals made of air spheres in titania, *SCIENCE* 281: 5378, 802-804 AUG 7 1998.
- 77) Anvar A. Zakhidov, Ray H. Baughman, Zafar Iqbal, Changxing Cui, Ilyas Khayrullin, Socrates O. Dantas, Jordi Marti, and Victor G. Ralchenko, *Science* 282, 897 1998
- 78) Sozuer, H. S., Haus, J. W., and Inguva, R., Photonic bands: Convergence problems with the plane-wave method, *Phys. Rev. B* 45, 13962 1992.
- 79) Bragg, W. L., Claringbull, G. F., *Crystal structures of minerals* by Sir Lawrence Bragg and G. F. Claringbull, The crystalline state v.4 1965.
- 80) Woolfson, M. M., *An introduction to X-Ray crystallography*, Cambridge University Press, 1970, ISBN 521-074401
- 81) Lin, S. Y., and Arjavalingam, G., Tunneling of electromagnetic waves in two-dimensional photonic crystals, *Optics Lett.* 18, 1666 1993.
- 82) Pendry, J. B., Calculating photonic band structure, *J. Phys. Condens. Matter* pp 1086-1108, 1996.
- 83) Pendry, J. B., Bell, P. M., *Transfer Matrix Techniques for Electromagnetic Waves*, NATO Advanced Study Institute on Photonic Band Gap Materials, June 1996
- 84) Ward, A. J., Pendry, J. B., Refraction and geometry in Maxwell's equations, *J. Mod. Opt.* 43, 773 (1996).

A.1 The Dispersion Relation

The free space dispersion relation is given by Equation A.1.1. For a given frequency this equation allows the external incidence angle of a plane wave incident from air onto a PBG crystal.

$$\omega^2 = k_x^2 + k_y^2 + k_z^2 \quad \text{A.1.1}$$

The code assumes that the period in the x-direction relates to the dimension of the first Brillouin zone, (FBZ) and normalises this dimension to π/a . The light line defined by Equation A.1.2 can then be used in conjunction with Equation A.1.1 to scan the relevant values of the k-vector to cover all external angles of incidence, where n is the refractive index of the material, c_0 is the speed of light in vacuo and ω is the angular frequency and k is the k-vector,

$$\omega n = c_0 k \quad \text{A.1.2}$$

The diagram on the left of Figure A.1 shows the k_x and k_z components for several fixed frequencies in a 2-dimensional plane assuming that $k_y=0$, i.e. it is the graphical solution of Equation A.1.1. The normalised boundaries of $\pm\pi/a$ have also been marked on the diagram in the k_x direction. For any given k value this can be broken down into the constituent k_x and k_y parts and the incidence angle θ taken using the $k_z=0$ plane as a reference.

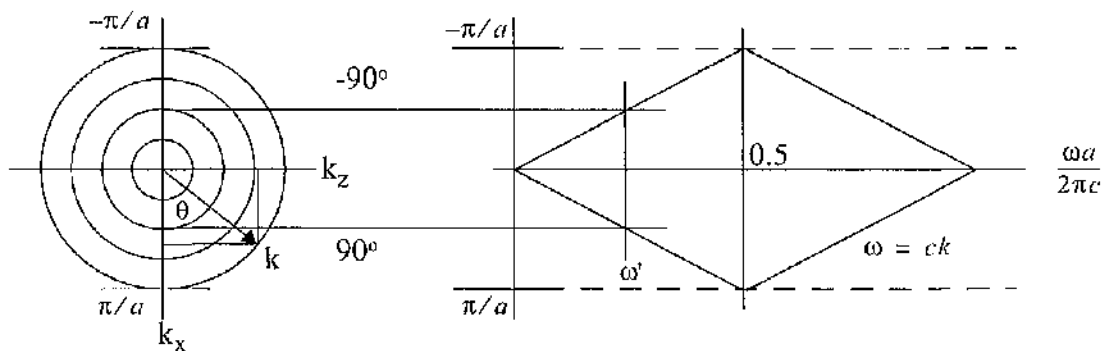


Figure A.1 The light line

When the light line is plotted against normalised frequency as on the right hand side of Figure A.1, the repetitive diamond structure is seen. This diamond structure is a result of the periodicity introduced in the k_x direction, the free space mode defined by the light line

continues to propagate by folding back within the k_x zone as shown. For a given normalised frequency below a value of 0.5 scanning the k_x vector between $\pm\pi/a$ covers all incidence angles from -90° to $+90^\circ$ degrees across the face of the crystal. This has been shown in Figure A.1 for a particular frequency ω' . Values of k_x that result in a complex k_z relate to evanescent waves in the structure.

Point of Interest

Inside the program the k-vector has been normalised to units of π/a . Consequently for the largest value of normalised frequency the oblique incidence value of the k -vector is found using Equation 13.1.

$$\begin{aligned}\omega n &= ck \\ 2\pi f n &= ck' \frac{\pi}{a} \\ k' &= 2n \left(\frac{fa}{c} \right)\end{aligned}$$

(13.1) Calculating the relevant k-vector.

Where ω is the angular frequency, $\omega=2\pi f$, the k-vector is k , the speed of light in vacuo is c , the lattice constant is denoted by a , and the refractive index of the ambient medium is n .

The transfer matrix method for analysing the reflection and transmission characteristics of stacks of layers which are 2D-periodic in the plane of the layers under plane wave incidence from outside the stack has been described by Pendry, Bell and Ward [21,50,63,82,83,84]. This appendix presents an overview of the main techniques used within the program, which has been extensively modified from the original version distributed by Professor Bell, Professor Pendry and Dr. Ward from the Condensed Matter Group of Imperial College's Science Technology and Medicine, (ICSTM), Imperial College, London.

In essence the fields on one interface of the stack are expanded in Fourier series with respect to the spatial coordinates along the layer plane. Each spatial harmonic is the projection on the plane of a sum of upward- and downward-propagating plane waves in the layer medium, so the Fourier coefficients of the spatial harmonics on opposite interfaces of each layer are related by a scattering matrix which describes the inhomogeneity of the layer between the interfaces.

By cascading the scattering matrices for each layer, Fourier coefficients can be propagated down through layers by successive matrix multiplications. A boundary condition, that there can be no inward propagating wave in the half-space beyond the stack not illuminated by the illuminating plane wave, is applied, and this is sufficient to determine the transmission coefficient of the plane wave which exits from the stack propagating parallel to the

incident plane wave direction, along with the amplitudes of all its associated diffraction orders.

B.1 The Transfer Matrix & Co-ordinate Definitions

The transfer matrix technique relates the electric and magnetic fields from one co-ordinate plane in space to another through knowledge of the dielectric profile of the material between the planes. Defining a Cartesian co-ordinate system, shown in Figure B.1, the fields can be propagated in the z-axis from the $z=0$ plane to another plane, $z=c$.

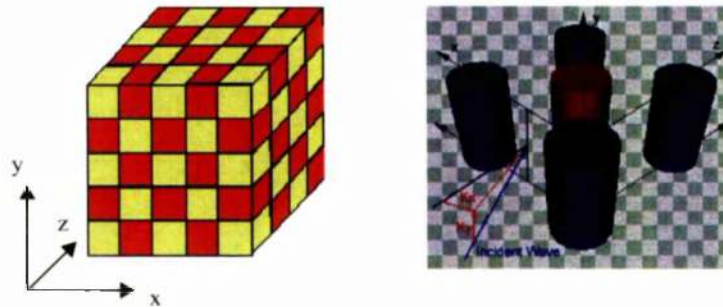


Figure B.1 Cartesian co-ordinate system for a generic periodic structures.

Once the initial electric and magnetic fields have been defined in the $z=0$ plane then by using the transfer matrix, T , the new fields can be calculated at the $z=c$ plane. The transfer matrix relates how the electric and magnetic fields cross a slab of material and therefore if the calculation is set up correctly and normalised the transmission and reflection co-efficients can be derived directly from the resultant transfer matrix.

$$\begin{aligned}
 \mathbf{F}(z=0) &= [E_x(z=0), E_y(z=0), H_x(z=0), H_y(z=0)] \\
 \mathbf{F}(z=c) &= T(c,0)\mathbf{F}(z=0)
 \end{aligned}
 \tag{B.1.1}$$

B.2 Formulating the calculation

Before the transfer matrix technique can provide results a methodology of application is required for a computer. One strategy is to sample the dielectric structure intended for study with a mesh, a technique also commonly used for Finite Element, (F.E.), and Finite Difference Time Domain (F.D.T.D.), techniques. These strategies require that Maxwell's equations are discretized onto such a mesh, facilitating a computer solution. The transfer matrix method, (T.M.M.), also discretizes Maxwell's equations and for the transmission and reflection co-efficient calculation adopts a Finite Difference Frequency Domain, (F.D.F.D.) approach.

To outline the operation of the code, Figure B.1 shows the general process flow chart. The band structure calculation side of the code has not been developed while extra features and capabilities have been added to the transmission and reflection coefficient part of the program. The code now handles the seamless integration of multiple 'cells', each cell containing a different structure and if required dissimilar z-dimension. Each 'cell' represents a piece of the crystal structure allowing the user more freedom to introduce defects and higher resolution meshes.

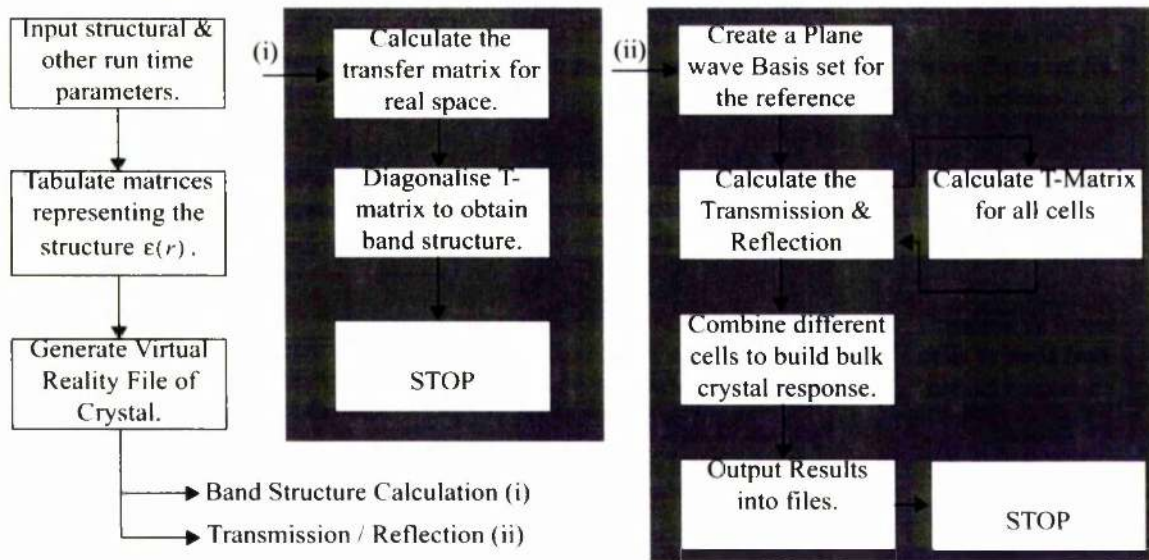


Figure B.1 Simplified Flow Chart of Program Operation.

B.2.1 Discretizing Maxwell's equations

Maxwell's equations in SCI form are shown in Equation B.2.1 where \mathbf{D} is the electric displacement vector, \mathbf{B} is the magnetic flux density, \mathbf{E} is the electric field vector, \mathbf{H} is the magnetic field vector, ρ is the charge density and \mathbf{j} is the electric current density.

$$\begin{aligned}
 \nabla \cdot \mathbf{D} &= \rho & \nabla \cdot \mathbf{B} &= 0 \\
 \nabla \times \mathbf{E} &= -\frac{\partial \mathbf{B}}{\partial t} & \nabla \times \mathbf{H} &= \frac{\partial \mathbf{D}}{\partial t} + \mathbf{j}
 \end{aligned}
 \quad \text{B.2.1}$$

As the code uses a finite difference frequency domain approach operation is carried out in the frequency domain. The quantities that are used within Maxwell's equations are written in Equation B.2.2 with their time and frequency dependence, in following the convention used by Imperial College is adopted, and it must be noted that this follows the style adopted by physicists rather than engineers.

$$\begin{aligned}
\mathbf{D}(\mathbf{r},t) &= \mathbf{D}(\mathbf{r})\exp(-i\omega t) & \mathbf{E}(\mathbf{r},t) &= \mathbf{E}(\mathbf{r})\exp(-i\omega t) \\
\mathbf{B}(\mathbf{r},t) &= \mathbf{B}(\mathbf{r})\exp(-i\omega t) & \mathbf{H}(\mathbf{r},t) &= \mathbf{H}(\mathbf{r})\exp(-i\omega t) \\
\rho(\mathbf{r},t) &= \rho(\mathbf{r})\exp(-i\omega t) & \mathbf{j}(\mathbf{r},t) &= \mathbf{j}(\mathbf{r})\exp(-i\omega t)
\end{aligned}
\tag{B.2.2}$$

Returning these expressions into Maxwell's equations in Equation B.2.1, performing the partial derivatives, defining the electric displacement vector, the magnetic flux and current density defines the scope of the problem which is expressed in Equation B.2.3.

$$\begin{aligned}
\nabla \cdot \mathbf{D} &= \rho & \nabla \cdot \mathbf{B} &= 0 \\
\nabla \times \mathbf{E} &= i\omega\mathbf{B} & \nabla \times \mathbf{H} &= (-i\omega)\mathbf{D} + \mathbf{j} \\
\mathbf{D} &= \epsilon\epsilon_0\mathbf{E} & \mathbf{B} &= \mu\mu_0\mathbf{H} & \mathbf{j} &= \sigma\mathbf{E}
\end{aligned}
\tag{B.2.3}$$

Further simplification is made such that there are no embedded electric currents or magnetic sources allowing us to assume that ρ and \mathbf{j} are zero. By substituting our expressions for \mathbf{D} and \mathbf{B} back into Equation B.2.3 it is then elementary to obtain the expressions in Equation B.2.4

$$\begin{aligned}
\nabla \cdot \mathbf{D} &= 0 & \nabla \cdot \mathbf{B} &= 0 \\
\nabla \times \mathbf{E} &= i\omega\mu\mu_0\mathbf{H} & \nabla \times \mathbf{H} &= -i\omega\epsilon\epsilon_0\mathbf{E}
\end{aligned}
\tag{B.2.4}$$

Fourier Transforms

As much of the transfer matrix work is carried out in \mathbf{k} -space it is also necessary to Fourier transform Maxwell's equations. The expressions for the electric and magnetic field can be simply rewritten from Equation B.2.3 by implementing the Fourier transform. The generic Fourier transform translates functions from time to frequency or vice versa.

$$\begin{aligned}
F(\mathbf{k}, \omega) &= (2\pi)^{-1} \int_{-\infty}^{\infty} \int_{-\infty}^{\infty} f(\mathbf{r}, t) \exp(i\omega t) \exp(-i\mathbf{k} \cdot \mathbf{r}) d\mathbf{r}^2 dt \\
f(\mathbf{r}, t) &= (2\pi)^{-1} \int_{-\infty}^{\infty} \int_{-\infty}^{\infty} F(\mathbf{k}, \omega) \exp(-i\omega t) \exp(-i\mathbf{k} \cdot \mathbf{r}) d\mathbf{k}^2 d\omega
\end{aligned}
\tag{B.2.5}$$

To apply the Fourier transform to the Maxwell equations expressed in Equation B.2.3 the quantities in Equation B.2.2 are expanded via their position vector, \mathbf{r} . When the Fourier transform from position and time to frequency and \mathbf{k} -space is applied the differential operator yields a factor of $i\mathbf{k}$ for the expressions for the electric and magnetic field and the

time differential introduces a multiplicative factor of $-i\omega$ for the electric displacement vector and the magnetic flux. Both the time and frequency electric and magnetic Maxwell equations are expressed in Equation B.2.6.

$$\begin{aligned} \mathbf{D}(\mathbf{r}, t) &= D \exp(i(\mathbf{k} \cdot \mathbf{r} - \omega t)) & \mathbf{E}(\mathbf{r}, t) &= E \exp(i(\mathbf{k} \cdot \mathbf{r} - \omega t)) \\ \mathbf{B}(\mathbf{r}, t) &= B \exp(i(\mathbf{k} \cdot \mathbf{r} - \omega t)) & \mathbf{H}(\mathbf{r}, t) &= H \exp(i(\mathbf{k} \cdot \mathbf{r} - \omega t)) \end{aligned}$$

$$\nabla \times \mathbf{E}(\mathbf{r}, t) = -\frac{\delta \mathbf{B}(\mathbf{r}, t)}{\delta t} \quad \nabla \times \mathbf{H}(\mathbf{r}, t) = \frac{\delta \mathbf{D}(\mathbf{r}, t)}{\delta t} \quad \text{B.2.6}$$

Fourier transform to give:

$$i\mathbf{k} \times \mathbf{E}(\mathbf{k}, \omega) = i\omega \mathbf{B}(\mathbf{k}, \omega) \quad i\mathbf{k} \times \mathbf{H}(\mathbf{k}, \omega) = -i\omega \mathbf{D}(\mathbf{k}, \omega)$$

Approximating the k -vector

The free space dispersion relation can be expressed exactly and is adjusted simply for alternative media by including the relevant refractive index, Equation B.2.7. However when discretising Maxwell's equations on a mesh it is necessary to approximate the k -vector.

$$\begin{aligned} \omega &= ck & \text{Free Space Dispersion Relation} \\ \omega n &= ck & \text{Generic Expression for any medium} \end{aligned} \quad \text{B.2.7}$$

With a little thought over the choice of how the k -vector is represented the approximation can be used to help in the discretisation process. The discretisation process should ideally relate fields at one point to another via some difference relation. Recalling the shift property of Fourier transforms, a positional shift of ' a ' in real space relates to a modulation in k -space, then this property can be used with the k -vector approximation to help set up a set of difference equations. At this point it is now not necessary to move Fourier transform into k -space as a set of difference equations can be written directly, however the transformation to k -space and then back to real space included below for the sake of completeness. The reader may jump directly to the section entitled "Real space difference equations" on page 183

In the process of Fourier transforming from (\mathbf{r}, t) to (\mathbf{k}, ω) space for both the electric and magnetic field equations expressed in Equation B.2.6 the differential operator results in a multiplicative factor. Therefore the approximation for k should be divided by this same factor to ensure that the two cancel. Finally k is approximated such that when a Taylor expansion is used for the exponential all terms higher than second order are neglected.

Written in x,y,z components the k -vector approximation is summarised in Equation B.2.8 where a,b,c are the discretisation lengths in the x,y,z directions respectively.

$$\left. \begin{aligned} k_x &\equiv \frac{1}{ia}(\exp((ik_x a) - 1)) \\ k_y &\equiv \frac{1}{ib}(\exp((ik_y b) - 1)) \\ k_z &\equiv \frac{1}{ic}(\exp((ik_z c) - 1)) \end{aligned} \right\} = \kappa_E \quad \left. \begin{aligned} -k_x &\equiv \frac{1}{ia}(\exp((-ik_x a) - 1)) \\ -k_y &\equiv \frac{1}{ib}(\exp((-ik_y b) - 1)) \\ -k_z &\equiv \frac{1}{ic}(\exp((-ik_z c) - 1)) \end{aligned} \right\} = \kappa_H \quad \text{B.2.8}$$

Expanded Maxwell's equations

With the approximations for k now defined and returning to the expressions for the Fourier transformed Maxwell equations expressed in Equation B.2.6 the expanded expressions are shown in Equation B.2.9

$$\begin{aligned} k_y E_z - k_z E_y &= \omega B_x & k_y H_z - k_z H_y &= -\omega D_x \\ k_z E_x - k_x E_z &= \omega B_y & k_z H_x - k_x H_z &= -\omega D_y \\ k_x E_y - k_y E_x &= \omega B_z & k_x H_y - k_y H_x &= -\omega D_z \end{aligned} \quad \text{B.2.9}$$

Now substituting for k using κ_E for the E and κ_H for the H equations the equations are:

$$\begin{aligned} \frac{1}{ib}(\exp((ik_y b) - 1))E_z - \frac{1}{ic}(\exp((ik_z c) - 1))E_y &= \omega B_x \\ \frac{1}{ic}(\exp((ik_z c) - 1))E_x - \frac{1}{ia}(\exp((ik_x a) - 1))E_z &= \omega B_y \\ \frac{1}{ia}(\exp((ik_x a) - 1))E_y - \frac{1}{ib}(\exp((ik_y b) - 1))E_x &= \omega B_z \end{aligned} \quad \text{B.2.10}$$

$$\begin{aligned} -\frac{1}{ib}(\exp((-ik_y b) - 1))H_z + \frac{1}{ic}(\exp((-ik_z c) - 1))H_y &= -\omega D_x \\ -\frac{1}{ic}(\exp((-ik_z c) - 1))H_x + \frac{1}{ia}(\exp((-ik_x a) - 1))H_z &= -\omega D_y \\ -\frac{1}{ia}(\exp((-ik_x a) - 1))H_y + \frac{1}{ib}(\exp((-ik_y b) - 1))H_x &= -\omega D_z \end{aligned} \quad \text{B.2.11}$$

Recalling the shift property of Fourier transforms that has been discussed previously Equation B.2.10 and Equation B.2.11 can be transformed to real space to obtain the following real space difference equations.

B.2.2 Real space difference equations

$$\begin{aligned}
 \frac{1}{ib}(E_z(r+b) - E_z(r)) - \frac{1}{ic}(E_y(r+c) - E_y(r)) &= \omega B_x(r) \\
 \frac{1}{ic}(E_x(r+c) - E_x(r)) - \frac{1}{ia}(E_z(r+a) - E_z(r)) &= \omega B_y(r) \\
 \frac{1}{ia}(E_y(r+a) - E_y(r)) - \frac{1}{ib}(E_x(r+b) - E_x(r)) &= \omega B_z(r)
 \end{aligned} \tag{B.2.12}$$

$$\begin{aligned}
 \frac{-1}{ib}(H_z(r-b) - H_z(r)) + \frac{1}{ic}(H_y(r-c) - H_y(r)) &= -\omega D_x(r) \\
 \frac{-1}{ic}(H_x(r-c) - H_x(r)) + \frac{1}{ia}(H_z(r-a) - H_z(r)) &= -\omega D_y(r) \\
 \frac{-1}{ia}(H_y(r-a) - H_y(r)) + \frac{1}{ib}(H_x(r-b) - H_x(r)) &= -\omega D_z(r)
 \end{aligned} \tag{B.2.13}$$

Recalling the definitions of \mathbf{B} and \mathbf{D} from Equation B.2.3 and using the z-components from Equation B.2.12 and Equation B.2.13 an expression for the z-components for \mathbf{E} and \mathbf{H} can be written as

$$\begin{aligned}
 \frac{1}{ia}[E_y(r+a) - E_y(r)] - \frac{1}{ib}[E_x(r+b) - E_x(r)] &= \omega\mu_0\mu(r)H_z(r) \\
 \frac{-1}{ia}[H_y(r-a) - H_y(r)] + \frac{1}{ib}[H_x(r-b) - H_x(r)] &= -\omega\varepsilon_0\varepsilon(r)E_z(r)
 \end{aligned} \tag{B.2.14}$$

The expressions for the E and H fields on the next plane $z+c$ relative to the current plane z , can then be easily derived by substituting for the z-components of the following equations by using the expressions in Equation B.2.14. Note that in deriving the expressions for the x- and y- components of H that $r+c$ has been substituted for r in Equation B.2.13.

$$\begin{aligned}
 E_x(r+c) &= E_x(r) + ic \left[\omega\mu_0\mu(r)H_y(r) + \frac{1}{ia}[E_z(r+a) - E_z(r)] \right] \\
 E_y(r+c) &= E_y(r) - ic \left[\omega\mu_0\mu(r)H_x(r) + \frac{1}{ib}[E_z(r+b) - E_z(r)] \right] \\
 H_x(r+c) &= H_x(r) - ic \left[\omega\varepsilon_0\varepsilon(r+c)E_y(r+c) + \frac{1}{ia}[H_z(r+c-a) - H_z(r+c)] \right] \\
 H_y(r+c) &= H_y(r) + ic \left[\omega\varepsilon_0\varepsilon(r+c)E_x(r+c) + \frac{1}{ib}[H_z(r+c-b) - H_z(r+c)] \right]
 \end{aligned} \tag{B.2.15}$$

Substituting for the z- components of E and H from Equation B.2.14 gives Equation B.2.16

$$\begin{aligned}
 E_x(r+c) &= \begin{pmatrix} E_x(r) + ic\omega\mu_0\mu(r)H_y(r) + \frac{ic}{a\omega\epsilon_0\epsilon(r)} \left[a^{-1}[H_y(r-a) - H_y(r)] \right] \\ \frac{-ic}{a\omega\epsilon_0\epsilon(r+a)} \left[a^{-1}[H_y(r) - H_y(r+a)] \right] \end{pmatrix} \\
 E_y(r+c) &= \begin{pmatrix} E_y(r) - ic\omega\mu_0\mu(r)H_x(r) + \frac{ic}{b\omega\epsilon_0\epsilon(r)} \left[a^{-1}[H_x(r-a) - H_x(r)] \right] \\ \frac{-ic}{b\omega\epsilon_0\epsilon(r+b)} \left[a^{-1}[H_x(r-a+b) - H_x(r+b)] \right] \end{pmatrix} \\
 H_x(r+c) &= \begin{pmatrix} H_x(r) - ic\omega\epsilon_0\epsilon(r+c)E_y(r+c) + \\ \frac{ic}{a\omega\mu_0\mu(r-a+c)} \left[a^{-1}[E_y(r+c) - E_y(r-a+c)] \right] \\ \frac{-ic}{a\omega\mu_0\mu(r+c)} \left[a^{-1}[E_y(r+a+c) - E_y(r+c)] \right] \end{pmatrix} \\
 H_y(r+c) &= \begin{pmatrix} H_y(r) + ic\omega\epsilon_0\epsilon(r+c)E_x(r+c) + \\ \frac{ic}{b\omega\mu_0\mu(r-b+c)} \left[a^{-1}[E_x(r+c) - E_x(r-b+c)] \right] \\ \frac{-ic}{b\omega\mu_0\mu(r+c)} \left[a^{-1}[E_x(r+a+c) - E_x(r+c)] \right] \end{pmatrix}
 \end{aligned} \tag{B.2.16}$$

These equations can then be further simplified by introducing the reduced magnetic field and recalling that the speed of light in a vacuum, c_0 , can be derived from the dielectric permittivity and magnetic permeability. Note that c is a discretisation length.

$$\begin{aligned}
 H &= \frac{i}{c\omega\epsilon_0} H \\
 c_0^2 &= \frac{1}{\epsilon_0\mu_0}
 \end{aligned} \tag{B.2.17}$$

$$\begin{aligned}
E_x(r+c) &= \begin{pmatrix} E_x(r) + \frac{c^2 \omega^2}{c_0^2} \mu(r) H_y(r) + \frac{c^2}{a \epsilon(r)} \left[a^{-1} [H_y(r-a) - H_y(r)] \right] \\ \frac{-c^2}{a \epsilon(r+a)} \left[a^{-1} [H_y(r) - H_y(r+a)] \right] \\ -b^{-1} [H_x(r-b) - H_x(r)] \\ -b^{-1} [H_x(r+a-b) - H_x(r+a)] \end{pmatrix} \\
E_y(r+c) &= \begin{pmatrix} E_y(r) - \frac{c^2 \omega^2}{c_0^2} \mu(r) H_x(r) + \frac{c^2}{b \epsilon(r)} \left[a^{-1} [H_y(r-a) - H_y(r)] \right] \\ \frac{-ic}{b \omega \epsilon_0 \epsilon(r+b)} \left[a^{-1} [H_y(r-a+b) - H_y(r+b)] \right] \\ -b^{-1} [H_x(r-b) - H_x(r)] \\ -b^{-1} [H_x(r+a-b) - H_x(r+a)] \end{pmatrix} \\
H_x(r+c) &= \begin{pmatrix} H_x(r) + \epsilon(r+c) E_y(r+c) + \\ \frac{c_0^2}{a \omega^2 \mu(r-a+c)} \left[a^{-1} [E_y(r+c) - E_y(r-a+c)] \right] \\ -b^{-1} [E_x(r-a+b+c) - E_x(r-a+c)] \\ \frac{c_0^2}{a \omega^2 (r+c)} \left[a^{-1} [E_y(r+a+c) - E_y(r+c)] \right] \\ -b^{-1} [E_x(r+b+c) - E_x(r+c)] \end{pmatrix} \\
H_y(r+c) &= \begin{pmatrix} H_y(r) - \epsilon(r+c) E_x(r+c) + \\ \frac{-c_0^2}{b \omega^2 \mu(r-b+c)} \left[a^{-1} [E_y(r+a-b+c) - E_y(r-b+c)] \right] \\ -b^{-1} [E_x(r+c) - E_x(r-b+c)] \\ \frac{c_0^2}{b \omega^2 \mu(r+c)} \left[a^{-1} [E_y(r+a+c) - E_y(r+c)] \right] \\ -b^{-1} [E_x(r+b+c) - E_x(r+c)] \end{pmatrix}
\end{aligned} \tag{B.2.18}$$

The equations that relate the electric and magnetic field values on a plane relative to another are now defined. This now allows the transform relation from one position to another to be defined, the ‘Transfer Matrix’.

$$\begin{bmatrix} E_x(r+c) \\ E_y(r+c) \\ H_x(r+c) \\ H_y(r+c) \end{bmatrix} = \sum_{r'} \begin{bmatrix} T_{11}(r, r') & T_{12}(r, r') & T_{13}(r, r') & T_{14}(r, r') \\ T_{21}(r, r') & T_{22}(r, r') & T_{23}(r, r') & T_{24}(r, r') \\ T_{31}(r, r') & T_{32}(r, r') & T_{33}(r, r') & T_{34}(r, r') \\ T_{41}(r, r') & T_{42}(r, r') & T_{43}(r, r') & T_{44}(r, r') \end{bmatrix} \begin{bmatrix} E_x(r') \\ E_y(r') \\ H_x(r') \\ H_y(r') \end{bmatrix} \tag{B.2.19}$$

B.3 Boundary conditions

During the calculation there are instances when the code requires fields outwith the defined scope of the cell. As photonic crystals are periodic materials the Bloch condition can be imposed on the calculation in the directions transverse to the integration direction.

With the transfer matrix the total thickness of the crystal can be controlled to a finite value while the other two dimensions are assumed to be infinite.

The Bloch condition states that the fields at one point in a periodic material must be the same as those which are an integer number of periods distant with a multiplicative phase factor. In calculating the reflection and transmission coefficients the Bloch condition is applied only in the x - and y - directions, the xy -plane being assumed to be infinite while the crystal has a finite thickness in the z -direction.

When the band structure calculation is wanted the code also implements the Bloch condition in the third dimension, the z -direction such that the crystal is assumed to be infinite in all three dimensions. Assuming that the distance c , is the periodic lattice constant and the dimension of the cell in z , then the Bloch condition in the z -direction states:

$$\exp(ik_z c)F(z=0) = F(z=c) = T(c,0)F(z=0) \quad \text{B.3.1}$$

The band structure $\kappa(\omega)$ can be obtained by calculating the eigen values of the real space transfer matrix \mathbf{T} .

B.4 Polarisation & the plane wave basis.

In “Formulating the calculation” on page 178 the flow process of the program is discussed and Figure B.1 on page 179 shows the block diagram. There are many elements involved in the calculation of the transmission and reflection co-efficients but one of the most important is the initial set-up of the plane wave basis. Before the transfer matrix routines can be used we must determine the plane wave basis for the reference medium and incorporate the effects of incidence angle and polarisation.

Polarisation relative to the surface normal

There are two distinguishing cases that must be differentiated within the basis set, normal incidence and off-normal incidence. In defining polarisation a surface normal to the crystal is introduced, and it is relative to this surface normal that polarisation is defined. Between the two incidence conditions it is normal incidence that is the simpler of the two but has the catch that for either s- (TE) or p- (TM) polarised waves the dominant electric or magnetic field component could lie at any position within the surface plane of the crystal.

In brief returning to Maxwell's equations for the electric and magnetic fields and making the substitutions for the magnetic flux density \mathbf{B} , the electric displacement vector \mathbf{D} , and performing the partial derivative, the expressions in Equation B.4.1 are obtained.

$$\begin{aligned} \nabla \times \mathbf{E} &= \frac{\partial \mathbf{B}}{\partial t} & \nabla \times \mathbf{H} &= \frac{\partial \mathbf{D}}{\partial t} \\ \nabla \times \mathbf{E} &= i\mu\mu_0\omega\mathbf{H} & \nabla \times \mathbf{H} &= i\epsilon_{ref}\epsilon_0\omega\mathbf{E} \end{aligned} \quad \text{B.4.1}$$

Recalling the reduced magnetic field from Equation B.2.17 on page 184 it is then possible to write Equation B.4.2, the expressions therein are then Fourier transformed into k-space.

$$\nabla \times \mathbf{E} = \frac{\omega^2}{c_0^2} a \mathbf{H} \quad \nabla \times \mathbf{H} = \frac{\epsilon_{ref}}{a} \mathbf{E} \quad \text{B.4.2}$$

$$\begin{aligned} ik \times \mathbf{E} &= \frac{\omega^2}{c^2} a \mathbf{H} & (a) & & ik \times \mathbf{H} &= \frac{\epsilon_{ref}}{a} \mathbf{E} & (b) \\ i\kappa_E \times \mathbf{E} &= \frac{\omega^2}{c^2} a \mathbf{H} & (c) & & i\kappa_H \times \mathbf{H} &= \frac{\epsilon_{ref}}{a} \mathbf{E} & (d) \end{aligned} \quad \text{B.4.3}$$

$$\left. \begin{aligned} k_x &\equiv \frac{1}{ia} (\exp(ik_x a) - 1) \\ k_y &\equiv \frac{1}{ib} (\exp(ik_y b) - 1) \\ k_z &\equiv \frac{1}{ic} (\exp(ik_z c) - 1) \end{aligned} \right\} = \kappa_E \quad \left. \begin{aligned} -k_x &\equiv \frac{1}{ia} (\exp(-ik_x a) - 1) \\ -k_y &\equiv \frac{1}{ib} (\exp(-ik_y b) - 1) \\ -k_z &\equiv \frac{1}{ic} (\exp(-ik_z c) - 1) \end{aligned} \right\} = \kappa_H \quad \text{B.4.4}$$

The expressions for the \mathbf{k} -vector have already been defined, see Equation B.2.8 on page 182 and for convenience are rewritten above. From here onwards we assume that the mesh used to discretise the structure is uniform such that $a=b=c$.

General polarisation definitions

For both normal and off-normal incidence polarisation is defined relative to the crystal surface normal \mathbf{n} . Both s- (TE) or p- (TM) polarised waves are assumed to be orthogonal to the surface normal and to each other, a condition enforced using the cross product where \mathbf{g} is the reciprocal lattice vector.

$$\begin{aligned} S_{polarisation} &= \frac{[(\mathbf{k} + \mathbf{g}) \times \mathbf{n}]}{\sqrt{[(\mathbf{k} + \mathbf{g}) \times \mathbf{n}] \cdot [(\mathbf{k} + \mathbf{g}) \times \mathbf{n}]}} \\ P_{polarisation} &= \frac{[(\mathbf{k} + \mathbf{g}) \times ((\mathbf{k} + \mathbf{g}) \times \mathbf{n})]}{\sqrt{[(\mathbf{k} + \mathbf{g}) \times ((\mathbf{k} + \mathbf{g}) \times \mathbf{n})] \cdot [(\mathbf{k} + \mathbf{g}) \times ((\mathbf{k} + \mathbf{g}) \times \mathbf{n})]}} \end{aligned} \quad \text{B.4.5}$$

From expressions (c) and (d) in Equation B.4.3 the E -field is perpendicular to κ_H and the H-field is perpendicular to κ_E . Thus

$$\begin{aligned}
 E_S &= \kappa_H \times n & (a) & & H'_S &= \frac{ic^2}{a\omega^2} \kappa_E \times (\kappa_H \times n) & (b) \\
 H'_P &= \kappa_E \times n & (c) & & E_P &= \frac{ia}{\epsilon_{ref}} \kappa_H \times (\kappa_E \times n) & (d)
 \end{aligned}
 \tag{B.4.6}$$

B.4.1 Normal incidence

For normal incidence the k_x and k_y components of κ_E and κ_H are respectively zero. For each polarisation plane waves are incident from an infinite distance from the left and the right side of the crystal.

S- or TE- Polarisation waves from + infinity

For the TE- polarised waves the electric field is completely directed along the x -direction. Therefore the reduced magnetic field only has only one non-zero valued component.:

$$\begin{aligned}
 ik \times E &= \frac{\omega^2}{c^2} a H \\
 \begin{bmatrix} x & y & z \\ 0 & 0 & \frac{1}{a}(e^{-ik_x a} - 1) \\ 1 & 0 & 0 \end{bmatrix} &= \frac{\omega^2}{c^2} a H^S & \text{B.4.7} \\
 H_y^S &= \frac{c^2}{\omega^2 a^2} (e^{-ik_x a} - 1)
 \end{aligned}$$

P- or TM- Polarisation waves from + infinity

For the TM- polarised waves the analysis is similar but this time the electric field is directed along the y- axis. This is due to the orthogonal nature between the TE and TM polarisations as defined by Equation B.4.5 on page 187.

$$ik \times E = \frac{\omega^2}{c_0^2} a H^p$$
$$\begin{bmatrix} x & y & z \\ 0 & 0 & \frac{1}{a}(e^{-ik_z a} - 1) \\ 0 & \frac{-1}{ia}(e^{-ik_z a} - 1) & 0 \end{bmatrix} = \frac{\omega^2}{c_0^2} a H^p \quad \text{B.4.8}$$
$$H_x^p = \frac{c_0^2}{\omega^2 a^2} (e^{-ik_z a} - 1)(e^{-ik_z a} - 1)$$

Waves arriving from - infinity

The same analysis is performed from waves arriving from -infinity for both TE and TM polarised waves by changing the sign on the k -vector in the exponential.

B.4.2 Off-normal incidence

When the off-normal incidence condition is considered there are no simple assumptions that can be made concerning either TE or TM polarised waves.

S- or TE- Polarisation waves from + infinity

The analysis is similar to that of the normal incidence condition but this time there are no simplifications for the E-field:

$$\mathbf{k}_H + \mathbf{g} \times \mathbf{n} = \begin{bmatrix} x & y & z \\ k_x^H & k_y^H & k_z^H \\ 0 & 0 & 1 \end{bmatrix} = \begin{bmatrix} k_y^H \\ -k_x^H \\ 0 \end{bmatrix} = \mathbf{E}_s \quad \text{B.4.9}$$

Equation B.4.3 on page 187 part (a) can then be used in conjunction with the full expression for \mathbf{E} -field derived in Equation B.4.9:

$$\begin{aligned} & \begin{bmatrix} x & y & z \\ \frac{1}{a}(e^{ik_x a} - 1) & \frac{1}{a}(e^{ik_y a} - 1) & \frac{1}{a}(e^{ik_z a} - 1) \\ \frac{-1}{ia}(e^{-ik_x a} - 1) & \frac{1}{ia}(e^{-ik_y a} - 1) & 0 \end{bmatrix} = \frac{\omega^2}{c_0^2} a \mathbf{H}^S \\ & \begin{bmatrix} \frac{-1}{ia^2}(e^{-ik_x a} - 1)(e^{ik_z a} - 1) \\ \frac{-1}{ia^2}(e^{-ik_y a} - 1)(e^{ik_z a} - 1) \\ \frac{1}{ia^2}[(e^{-ik_x a} - 1)(e^{ik_x a} - 1) + (e^{-ik_y a} - 1)(e^{ik_y a} - 1)] \end{bmatrix} = \frac{\omega^2}{c_0^2} a \mathbf{H}^S \end{aligned} \quad \text{B.4.10}$$

which provides verification of the expression given in part b) of Equation B.4.6 on page 188.

P- or TM- Polarisation waves from + infinity

As was the case for the normal incidence condition Equation B.4.6 is used to derive the components of the P- or TM- polarised H-field:

$$\mathbf{k}_E + \mathbf{g} \times \mathbf{n} = \begin{bmatrix} x & y & z \\ k_x^E & k_y^E & k_z^E \\ 0 & 0 & 1 \end{bmatrix} = \begin{bmatrix} k_y^E \\ -k_x^E \\ 0 \end{bmatrix} = \mathbf{H}_P \quad \text{B.4.11}$$

Thereafter part d) of Equation B.4.3 on page 187 provides verification of the expression for the E- components for the P- or TM- polarised field which is also expressed in part d) of Equation B.4.6 on page 188:

$$\begin{aligned} & \begin{bmatrix} x & y & z \\ \frac{-1}{a}(e^{-ik_x a} - 1) & \frac{-1}{a}(e^{-ik_y a} - 1) & \frac{-1}{a}(e^{ik_z a} - 1) \\ \frac{1}{ia}(e^{ik_y a} - 1) & \frac{-1}{ia}(e^{ik_x a} - 1) & 0 \end{bmatrix} = \frac{\epsilon_{ref}}{a} \mathbf{E}_P \\ & \begin{bmatrix} \frac{-1}{ia^2}(e^{ik_x a} - 1)(e^{-ik_z a} - 1) \\ \frac{-1}{ia^2}(e^{ik_y a} - 1)(e^{ik_z a} - 1) \\ \frac{1}{ia^2}[(e^{-ik_x a} - 1)(e^{ik_x a} - 1) + (e^{-ik_y a} - 1)(e^{ik_y a} - 1)] \end{bmatrix} = \frac{\epsilon_{ref}}{a} \mathbf{E}_P \end{aligned} \quad \text{B.4.12}$$

Waves arriving from - infinity

The same analysis is performed from waves arriving from -infinity for both TE and TM polarised waves by changing the sign on the \mathbf{k} -vector in the exponential.

B.5 Calculating the reflection and transmission coefficients

B.5.1 Unitary transformation

At the end of the section “Formulating the calculation”, Equation B.2.19 on page 185 defined the transfer matrix for propagation through a slab of finite material thickness. The equation can be rewritten,

$$\mathbf{F}(z + c) = \mathbf{T}(z)\mathbf{F}(z) \quad \text{B.5.1}$$

where

$$\mathbf{F}(z) = \begin{bmatrix} E_y(r) \\ E_x(r) \\ E_y(r) \\ H_x(r) \\ H_x(r) \\ H_y(r) \end{bmatrix} \quad \text{B.5.2}$$

is a vector containing information relating to the electric and magnetic fields in the slice located at z . If the waves are propagating in free space such that ϵ and μ are unity then the eigen vectors of matrix \mathbf{T} from Equation B.5.1 define electromagnetic waves in free space. Since the transfer matrix \mathbf{T} is not Hermitian then the left and right Eigen vectors are distinct such that,

$$\begin{aligned} \mathbf{T}_{free} \mathbf{F}_{ij}^{free}(z) &= \mathbf{F}_{ij}^{free}(z+c) = \exp(ik_j^{free}c) \mathbf{F}_{ij}^{free}(z) \\ \bar{\mathbf{F}}_{ij}^{free}(z) \mathbf{T}_{free} &= \bar{\mathbf{F}}_{ij}^{free}(z+c) = \exp(ik_j^{free}c) \bar{\mathbf{F}}_{ij}^{free}(z) \end{aligned} \quad \text{B.5.3}$$

Therefore a unitary transformation can be defined using Equation B.5.3 to define \mathbf{S} ,

$$\mathbf{S} = \sum_j \mathbf{F}_{ij}^{free}(z) \bar{\mathbf{F}}_{ij}^{free}(z) \quad \text{B.5.4}$$

assuming that the Eigen vectors have been normalised.

$$\mathbf{F}_{ij}^{free} \cdot \bar{\mathbf{F}}_{ij}^{free} = \delta_{ij} \quad \text{B.5.5}$$

Therefore by using our transfer matrix the transmitted wave can be related to the reflected and impinging wave through Equation B.5.8.

$$\begin{bmatrix} t^+ \\ I \end{bmatrix} = \begin{bmatrix} \tilde{T}^{++}(z) & \tilde{T}^{+-}(z) \\ \tilde{T}^{-+}(z) & \tilde{T}^{--}(z) \end{bmatrix} \begin{bmatrix} 0 \\ t^- \end{bmatrix} \quad \text{B.5.8}$$

From matrix algebra it follows that

$$\begin{aligned} \tilde{T}^{+-}(z) &= t^+(t^-)^{-1} \\ \tilde{T}^{-+}(z) &= (t^-)^{-1} \end{aligned} \quad \text{B.5.9}$$

The other two components of the unitary transformed transfer matrix given in Equation B.5.7 are found by starting the wave on the left hand side of the slab, see Figure B.2

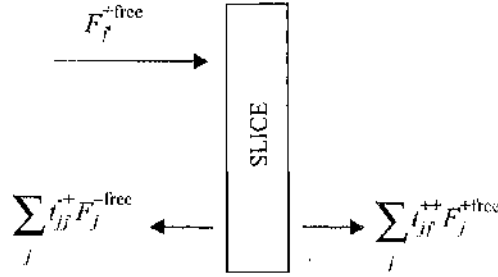


Figure B.2 A wave incident on to the left side of a slice of material

Such that

$$\begin{bmatrix} t^{++} \\ 0 \end{bmatrix} = \begin{bmatrix} \tilde{T}^{++}(z) & \tilde{T}^{+-}(z) \\ \tilde{T}^{-+}(z) & \tilde{T}^{--}(z) \end{bmatrix} \begin{bmatrix} I \\ t^+ \end{bmatrix} \quad \text{B.5.10}$$

From Equation B.5.10 it is now possible to derive expressions for the other components of the transfer matrix, and using the expressions for the already derived components from Equation B.5.9 we can then write Equation B.5.11

$$\begin{aligned} \tilde{T}^{++}(z) &= t^{++} - \tilde{T}^{+-}(z)t^+ = t^{++} - t^+(t^-)^{-1}t^+ \\ \tilde{T}^{-+}(z) &= -\tilde{T}^{--}(z)t^+ = -(t^-)^{-1}t^+ \end{aligned} \quad \text{B.5.11}$$

Pulling the components from Equation B.5.9 and Equation B.5.11:

$$\tilde{T}(z) = \begin{bmatrix} \tilde{T}^{++}(z) & \tilde{T}^{+-}(z) \\ \tilde{T}^{-+}(z) & \tilde{T}^{--}(z) \end{bmatrix} = \begin{bmatrix} t^{++} - t^+(t^-)^{-1}t^+ & t^+(t^-)^{-1} \\ -(t^-)^{-1}t^+ & (t^-)^{-1} \end{bmatrix} \quad \text{B.5.12}$$

B.5.3 Transmission and reflection from a block.

A block consists of several slices, and as the transfer matrix translates the electric and magnetic field for one slice to go through a slab it is simply a matter of iteratively performing the transfer matrix operation. The result is a transfer matrix for the block of material, Equation B.5.13.

$$\tilde{T}(L_z) = \prod_{z=1}^{N_z} T(z) \quad \text{B.5.13}$$

Transforming to the free wave basis to perform the unitary transformation yields the equivalent equations for a block of material as per the slice, Equation B.5.7 becomes Equation B.5.14.

$$ST(L_z)S^{-1} = \tilde{T}(L_z) = \begin{bmatrix} \tilde{T}^{++}(L_z) & \tilde{T}^{+-}(L_z) \\ \tilde{T}^{-+}(L_z) & \tilde{T}^{--}(L_z) \end{bmatrix} \quad \text{B.5.14}$$

$$\tilde{T}(L_z) = \begin{bmatrix} t_{L_z}^{++} - t_{L_z}^{+-}(t_{L_z}^{-})^{-1} & t_{L_z}^{+-} t_{L_z}^{+}(t_{L_z}^{-})^{-1} \\ -(t_{L_z}^{-})^{-1} t_{L_z}^{+} & (t_{L_z}^{-})^{-1} \end{bmatrix}$$

Due to numerical stability problems, in so far as wave fields may grow with an exponential dependence as they are integrated through the slab, there is a finite number of slices that can be used to form a block before numerical accuracy of the machine is swamped and the results are useless. This problem is overcome by using a numerically stable multiple scattering algorithm to combine the transfer matrices for blocks. In this way different transfer matrices can be combined together such that the response for a system with dissimilar blocks can be found.

Polarmetric scattering from opal colloid photonic crystals

Acknowledgements:

I would like to thank Dr. John Roberts from DERA whose time, explanation, patience and documentation were fundamental in the preparation of this Appendix.

C.1 Motivation

For the ideal f.c.c. colloidal crystal the crystals are frequently named after the ordering of the monolayers which form the crystal. There are two types, one ordering is named ABC such that the colloid repeats ABCABC through the crystal while ACB ordering repeats ACBACB. Each letter relates to one monolayer within the crystal. For thin crystals, several tens of monolayers, which can be easily fabricated using the process of shear ordering, and the resultant crystal can be switched between the two stacking orders. For thicker crystals stacking faults can result in the crystal being a mixture of the two lattice types. The purity of colloidal crystals can be estimated by examining the intensity of diffracted Bragg spots and further information can be gleaned by also examining the intensity of the diffracted spot as a function of incidence angle.

The transfer matrix method is well suited to calculate the transmission, reflection and diffraction intensity properties of photonic crystals. However care must be taken with the method due to the definitions of the crystal itself

and polarisation. Within the code the crystal unit cell is non-primitive as the version of code limits the discretisation of the crystal to orthogonal Cartesian space. The situation for polarisation is further complicated as there are two distinct cases to be considered, normal incidence and off-normal incidence. The transfer matrix code defines polarisation relative to the crystal surface normal. At normal incidence both s- (TM) and p- (TE) are orthogonal to the surface normal and mutually orthogonal, therefore we are free to choose the directions within the surface plane of the s- and p- polarised waves. When the incidence direction is off-normal the situation becomes more complex. Depending on the experimental and code coordinate frame definitions it may be necessary to implement coordinate transforms to ensure that the laboratory co-ordinate frame is modelled correctly within the code or vice-versa.

C.1.1 Polar Spherical Co-ordinates

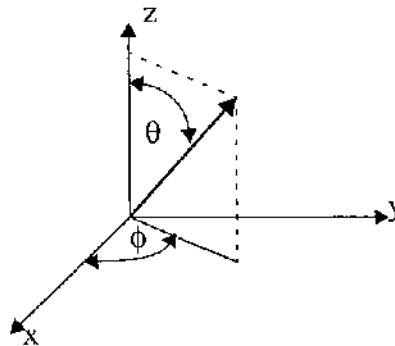


Figure C.1 Spherical Polar Co-ordinates.

Where r is the position vector, θ is the polar angle and ϕ is the meridian.

The projections of a position vector r onto the x, y, z cartesian axis are listed in Equation C.1.1 In the experiment the crystal surface is aligned in the xy - plane such that ϕ is 0° .

$$\begin{pmatrix} x \\ y \\ z \end{pmatrix} = \begin{pmatrix} r \sin \theta \cos \phi \\ r \sin \theta \sin \phi \\ r \cos \theta \end{pmatrix} \quad \text{C.1.1}$$

C.2 The experimental set-up

In the experiment the laser beam is incident onto the photonic crystal with a surface normal \hat{n} . The laser beam is incident in the Oz direction and s - and p - polarisations are defined as being along the Ox and Oy directions respectively. Within the experiment the incidence direction of the impinging laser beam can be altered to probe various properties. This incidence angle is within the xy - surface plane of the photonic crystal. A deviation angle, θ , can be defined from the surface normal direction of the photonic crystal. Retrospectively the surface normal of the crystal can be defined from the deviation angle using the projection equations in Equation C.1.1,

$$\hat{n} = \begin{pmatrix} \sin\theta \\ 0 \\ \cos\theta \end{pmatrix} \quad \text{C.2.1}$$

In the experiment the intensity of one of the diffracted orders is examined as a function of incidence angle. However the experimentalists are free to choose an orientation of the crystal in the surface plane such that the diffracted order lies in the same plane as the incidence angle scan. Consequently one of the Bragg spots is projected into the xz - plane such that there are no y - components. Any spot can be analysed by considering the Miller index, such that if there are no components in the y - direction then:

$$(p\hat{x}_{crystal} + q\hat{y}_{crystal} + r\hat{z}_{crystal}) \cdot \hat{y} = 0 \quad \text{C.2.2}$$

The crystal vectors, $x_{crystal}$, $y_{crystal}$, $z_{crystal}$ are the primitive lattice vectors for the cubic cell that contains the f.c.c. structure. However the transfer matrix code uses a different co-ordinate frame to analyse incidence onto the $\langle 111 \rangle$ surface such that a co-ordinate transform is required.

$$\begin{bmatrix} \hat{x}' \\ \hat{y}' \\ \hat{z}' \end{bmatrix} \text{Transfer Matrix} = \begin{bmatrix} M_{11} & M_{12} & M_{13} \\ M_{21} & M_{22} & M_{23} \\ M_{31} & M_{32} & M_{33} \end{bmatrix} \begin{bmatrix} \hat{x}_{crystal} \\ \hat{y}_{crystal} \\ \hat{z}_{crystal} \end{bmatrix} \quad \text{C.2.3}$$

Equation C.2.3 relates a co-ordinate transform from one orthogonal co-ordinate axis to another. The matrix M is therefore itself orthogonal which means that $M^T=M^{-1}$. To relate the crystal vectors to the transfer matrix frame, simple matrix algebra yields Equation C.2.4.

$$\begin{bmatrix} \hat{x}_{crystal} \\ \hat{y}_{crystal} \\ \hat{z}_{crystal} \end{bmatrix} = \begin{bmatrix} M_{11} & M_{21} & M_{31} \\ M_{12} & M_{22} & M_{32} \\ M_{13} & M_{23} & M_{33} \end{bmatrix} \begin{bmatrix} \hat{x}' \\ \hat{y}' \\ \hat{z}' \end{bmatrix} \quad \text{C.2.4}$$

Transfer Matrix

Returning to Equation C.2.2 and substituting the expressions for the crystal vectors obtained in Equation C.2.4, the projected Bragg spot in xz -plane can then be written as Equation C.2.5.

$$(pM_{11} + qM_{12} + rM_{13})(\hat{x}' \cdot \hat{y}') + (pM_{21} + qM_{22} + rM_{23})(\hat{y}' \cdot \hat{y}') + (pM_{31} + qM_{32} + rM_{33})(\hat{z}' \cdot \hat{y}') = 0 \quad \text{C.2.5}$$

Recall that the surface normal of the crystal has been defined such that $\hat{n} = \hat{z}'$ where $\hat{z}' = \hat{x} \sin \theta + \hat{z} \cos \theta$. However to define the \hat{x}' and \hat{y}' vectors we recall that the rotation about the surface normal of the crystal is allowed to align diffracted spots within the xz - plane. This rotation amounts to another co-ordinate transform.

C.2.1 Rotation in a plane.

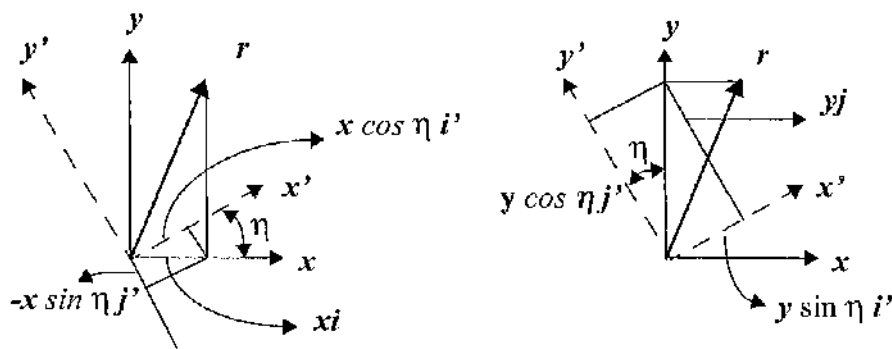


Figure C.1 Rotation in a plane

Unit vectors in x (x') & y (y') are i (i') & j (j') respectively. The vector r can be represented by the summation of the axial contribution vectors.

The projection of the original position vector r onto the various axes allows us to obtain an expression for r in terms of the original and rotated co-ordinate frames.

$$\begin{aligned} xi &= x \cos \eta i' - x \sin \eta j' \\ yj &= y \sin \eta i' + y \cos \eta j' \end{aligned} \quad \text{C.2.6}$$

In the original co-ordinate system $r = xi + yj$. Using the expressions from Equation C.2.6 the expression in Equation C.2.7 for the position vector can be obtained. The terms in the brackets relate to the components in the rotated co-ordinate axis, (x',y') .

$$\begin{aligned}
 r &= x \cos \eta i' - x \sin \eta j' + y \sin \eta i' + y \cos \eta j' \\
 r &= (x \cos \eta + y \sin \eta) i' + (y \cos \eta - x \sin \eta) j' \\
 x' &= x \cos \eta + y \sin \eta \\
 y' &= -x \sin \eta + y \cos \eta
 \end{aligned}
 \tag{C.2.7}$$

C.2.2 Rotation in the plane relative to the colloid

The (x',y') components related to the rotated co-ordinate frame are known in relation to the original (x,y) frame through Equation C.2.7. Expressions for the x' and y' values can be derived utilising the cross product and the crystal's surface normal, Equation C.2.1 on page 197.

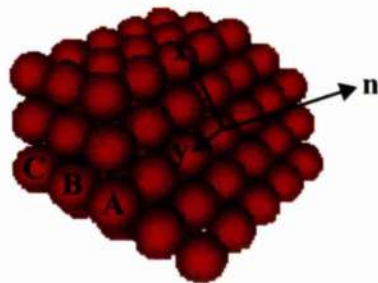


Figure C.2 Schematic of an Opal Colloid <111> Surface

$$\begin{aligned}\hat{x}' &= \cos\eta\left(\frac{\hat{n}\times\hat{x}}{|\hat{n}\times\hat{x}|}\right) + \sin\eta\left(\frac{\hat{n}\times(\hat{n}\times\hat{x})}{|\hat{n}\times(\hat{n}\times\hat{x})|}\right) \\ \hat{y}' &= -\sin\eta\left(\frac{\hat{n}\times\hat{x}}{|\hat{n}\times\hat{x}|}\right) + \cos\eta\left(\frac{\hat{n}\times(\hat{n}\times\hat{x})}{|\hat{n}\times(\hat{n}\times\hat{x})|}\right)\end{aligned}$$

$$\hat{n}\times\hat{x} = \begin{bmatrix} x & y & z \\ \sin\theta & 0 & \cos\theta \\ 1 & 0 & 0 \end{bmatrix} = [0 \ \cos\theta \ 0] \cdot \frac{\hat{n}\times\hat{x}}{|\hat{n}\times\hat{x}|} = [0 \ 1 \ 0] = \hat{y}$$

$$\hat{n}\times\hat{y} = \begin{bmatrix} x & y & z \\ \sin\theta & 0 & \cos\theta \\ 0 & 1 & 0 \end{bmatrix} = [-\cos\theta \ 0 \ \sin\theta] \cdot \frac{\hat{n}\times\hat{y}}{|\hat{n}\times\hat{y}|} = [-\cos\theta \ 0 \ \sin\theta]$$

$$\begin{aligned}\therefore\hat{x}' &= \cos\eta\hat{y} + \sin\eta(\sin\theta\hat{z} - \cos\theta\hat{x}) \\ \therefore\hat{y}' &= -\sin\eta\hat{y} + \cos\eta(\sin\theta\hat{z} - \cos\theta\hat{x})\end{aligned}$$

$$\hat{x}' = \begin{bmatrix} -\sin\eta\cos\theta \\ \cos\eta \\ \sin\eta\sin\theta \end{bmatrix} \quad \hat{y}' = \begin{bmatrix} \cos\eta\cos\theta \\ \sin\eta \\ \cos\eta\sin\theta \end{bmatrix} \quad \hat{z}' = \begin{bmatrix} \sin\theta \\ 0 \\ \cos\theta \end{bmatrix}$$

C.2.8

With generic values for the rotated co-ordinate frame now defined the expressions can now be substituted into Equation C.2.5 on page 198. We must now define our matrix M.

$$(pM_{11} + qM_{12} + rM_{13})\cos\eta + (pM_{21} + qM_{22} + rM_{23})\sin\eta = 0 \quad \text{C.2.9}$$

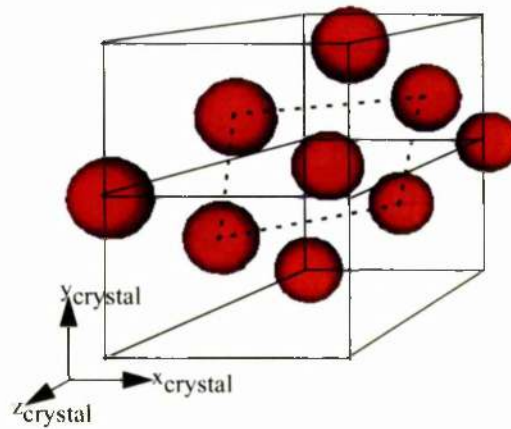


Figure C.3 <111> plane within the cubic crystal lattice

The initial crystal cubic lattice vectors define the f.c.c. structure that is shown in Figure C.3 with 2 cubic cells which have been outlined with thin black lines. To examine the <111> plane within the code a new unit cell is defined and in Figure C.3 the $x'y'$ plane primitive cell is shown with a dotted line. With no assumptions concerning the x' or y' cell direction lengths and by picking a right-handed set of co-ordinates for the new x',y',z'

directions, a definition of the new lattice vectors in relation to the cubic crystal lattice vectors can be written.

$$\begin{aligned}
 a_1 &= a\left(\frac{1}{2}\hat{x}_{crystal} - \frac{1}{2}\hat{y}_{crystal}\right) = a\frac{1}{\sqrt{2}}x' \\
 a_2 &= a\left(\frac{1}{2}\hat{x}_{crystal} + \frac{1}{2}\hat{y}_{crystal} - \hat{z}_{crystal}\right) = a\sqrt{\frac{3}{2}}y' \\
 a_3 &= a(\hat{x}_{crystal} + \hat{y}_{crystal} + \hat{z}_{crystal}) = a\sqrt{3}z'
 \end{aligned}
 \tag{C.2.10}$$

By manipulating this matrix to find expressions for x', y', z' the transformation matrix M can then be found, Equation C.2.11. Using the relevant values of the matrix in Equation C.2.9 then allows us to formulate a general formula for $\{p, q, r\}$ Bragg scattering. Note that the scattering is expressed in terms of the Miller indices relative to the original f.c.c. cubic co-ordinate frame.

$$M = \begin{bmatrix} \frac{1}{\sqrt{2}} & -\frac{1}{\sqrt{2}} & 0 \\ \frac{1}{\sqrt{6}} & \frac{1}{\sqrt{6}} & -\frac{\sqrt{2}}{\sqrt{3}} \\ \frac{1}{\sqrt{3}} & \frac{1}{\sqrt{3}} & \frac{1}{\sqrt{3}} \end{bmatrix}
 \tag{C.2.11}$$

$$\begin{aligned}
 \left(p\frac{1}{\sqrt{2}} - q\frac{1}{\sqrt{2}}\right)\cos\eta + \left(p\frac{1}{\sqrt{6}} + q\frac{1}{\sqrt{6}} - r\frac{\sqrt{2}}{\sqrt{3}}\right)\sin\eta &= 0 \\
 \frac{1}{\sqrt{2}}(p - q)\cos\eta + \frac{1}{\sqrt{6}}(p + q - 2r)\sin\eta &= 0
 \end{aligned}
 \tag{C.2.12}$$

All the equations are now defined to allow us to solve for Bragg scattering in the new transfer matrix frame given any Miller index of a diffracted Bragg spot in the original crystal frame. To control the incidence direction onto the laboratory frame θ can be changed. The incidence angle is chosen by altering the k -vector. The projection of the k -vector onto the x' and y' axis is required as it is the x' and y' components of k that are conserved going into the crystal.

$$\begin{aligned}
 k_{\parallel} &= \frac{\omega}{c}[(\hat{z} \cdot \hat{x}')\hat{x}' + (\hat{z} \cdot \hat{y}')\hat{y}'] \\
 &= \frac{\omega}{c}\sin\theta(\sin\eta\hat{x}' + \cos\eta\hat{y}')
 \end{aligned}
 \tag{C.2.13}$$

Experimentalists alter the angle η to ensure that the Bragg spot of interest is in the same plane that is being scanned. Equation C.2.12 can be manipulated to express $\sin\eta$ and $\cos\eta$ in terms of the transformation matrix using standard trigonometric expressions.

$$\begin{aligned}
 a \cos Q + b \sin Q &= 0 & x(a \cos Q - b \sin Q) \\
 a^2 \cos^2 Q - b^2 \sin^2 Q &= 0 \\
 \text{Route 1 } + (\cos^2 Q) & & \text{Route 2 } + (\sin^2 Q) \\
 a^2 - b^2 \tan^2 Q &= 0 & a^2 \cot^2 Q - b^2 = 0 \\
 a^2 - b^2(\sec^2 Q - 1) &= 0 & a^2(\csc^2 Q - 1) - b^2 = 0 \\
 a^2 + b^2 &= \frac{b^2}{\cos^2 Q} & \csc^2 Q = \frac{a^2 + b^2}{a^2} \\
 \cos^2 Q &= \frac{b^2}{a^2 + b^2} & \sin^2 Q = \frac{a^2}{a^2 + b^2} \\
 \cos Q &= \frac{b}{(a^2 + b^2)^{1/2}} & \sin Q = \frac{a}{(a^2 + b^2)^{1/2}}
 \end{aligned} \tag{C.2.14}$$

Using the expressions for $\cos Q$ and $\sin Q$ from Equation C.2.14 in conjunction with Equation C.2.12, the expression for the parallel k -vector, Equation C.2.13 becomes:

$$k_{\parallel} = \frac{\omega}{c} \sqrt{\frac{6}{3(p-q)^2 + (p+q-2r)^2}} \sin \theta \left[\frac{1}{\sqrt{2}}(p-q)\hat{x} - \frac{1}{\sqrt{6}}(p+q-2r)\hat{y} \right] \tag{C.2.15}$$

For the choice of vectors in Equation C.2.10 we can choose $\{p,q,r\}=\{0,0,1\}$ to select one of the diffracted orders. With this choice of Miller index the diffracted order Equation C.2.15 reduces to Equation C.2.16.

$$\begin{aligned}
 k_{\parallel} &= \frac{\omega}{c} \sqrt{\frac{6}{4}} \sin \theta \left[\frac{\sqrt{4}}{\sqrt{6}} \hat{y} \right] \\
 k_{\parallel} &= \frac{\omega}{c} \sin \theta \hat{y}
 \end{aligned} \tag{C.2.16}$$

This reduced equation shows that for this choice of Miller index and crystal definition in the $\langle 111 \rangle$ plane there is a Bragg spot that is within the $y'z'$ -plane. The intensity of this Bragg spot can then be investigated as a function of incidence angle by scanning the k -vector within the $y'z'$ -plane.

C.2.3 Issues related to the Translight program

The choice of the a_1 and a_2 vectors in Equation C.2.10 define the orientation of the $\langle 111 \rangle$ surface in the $x'y'$ -plane which is in fact the reverse of that used in the Translight program. As the vectors in Equation C.2.10 form a right handed set, swapping the a_1 and a_2 vector components to reflect the situation in the code requires that $-a_3$ is used.

$$\begin{aligned} a_1 &= a \left(\frac{1}{2} \hat{x}_{crystal} + \frac{1}{2} \hat{y}_{crystal} - \hat{z}_{crystal} \right) = a \frac{\sqrt{3}}{\sqrt{2}} x' \\ a_2 &= a \left(\frac{1}{2} \hat{x}_{crystal} - \frac{1}{2} \hat{y}_{crystal} \right) = a \frac{1}{\sqrt{2}} y' \\ a_3 &= a (-\hat{x}_{crystal} - \hat{y}_{crystal} - \hat{z}_{crystal}) = a \sqrt{3} z' \end{aligned} \quad \text{C.2.17}$$

Following a similar analysis to that used in deriving Equation C.2.15 a new transformation matrix must be formed.

$$M = \begin{bmatrix} \frac{1}{\sqrt{6}} & \frac{1}{\sqrt{6}} & -\frac{\sqrt{2}}{\sqrt{3}} \\ \frac{1}{\sqrt{2}} & \frac{-1}{\sqrt{2}} & 0 \\ \frac{-1}{\sqrt{3}} & \frac{-1}{\sqrt{3}} & \frac{-1}{\sqrt{3}} \end{bmatrix} \quad \text{C.2.18}$$

Consequently

$$k_{\parallel} = \frac{\omega}{c} \sqrt{\frac{6}{3(p-q)^2 + (p+q-2r)^2}} \sin \theta \left[\frac{1}{\sqrt{6}}(p+q-2r)\hat{x}' - \frac{1}{\sqrt{2}}(p-q)\hat{y}' \right] \quad \text{C.2.19}$$

which, when we choose the same diffracted spot Miller index to study $\{p,q,r\}=\{0,0,1\}$ Equation C.2.19 then reduces to Equation C.2.20.

$$\begin{aligned} k_{\parallel} &= \frac{\omega}{c} \sqrt{\frac{6}{4}} \sin \theta \left[\frac{\sqrt{4}}{\sqrt{6}} \hat{x}' \right] \\ k_{\parallel} &= \frac{\omega}{c} \sin \theta \hat{x}' \end{aligned} \quad \text{C.2.20}$$

With the definitions of the crystal as used by the program the $r=1$ Bragg spot sits in the $x'z'$ - plane. By scanning in the k -vector in the $x'z'$ -plane the intensity as a function of incidence angle of the Bragg spot can be examined.

